# OPTIMIZATION AND APPLICATION OF KILOHERTZ ELECTRICAL STIMULATION NERVE BLOCK TO AUTONOMIC NEURAL CIRCUITS

A Dissertation
Presented to
The Academic Faculty

By

Yogi A. Patel

In Partial Fulfillment
of the Requirements for the Degree
Doctor of Philosophy in
BioEngineering

Georgia Institute of Technology
Emory University

August 2017

# OPTIMIZATION AND APPLICATION OF KILOHERTZ ELECTRICAL STIMULATION NERVE BLOCK TO AUTONOMIC NEURAL CIRCUITS

Approved by:

Dr. Robert J. Butera, Advisor
Department of Biomedical Engineering & School of Electrical and Computer Engineering
*Georgia Institute of Technology*

Dr. Laura O'Farrell
Georgia Tech Research Corporation
*Georgia Institute of Technology*

Dr. Arthur W. English
Department of Cell Biology
*Emory University*

Dr. Christopher J. Rozell
Department of Electrical and Computer Engineering
*Georgia Institute of Technology*

Dr. Thomas J. Burkholder
School of Biological Sciences
*Georgia Institute of Technology*

Date Approved: April 14, 2017

*To my past, present, and future family.*

## ACKNOWLEDGEMENTS

This work was completed with support from a number of individuals that I am grateful for and thank.

First, my advisor, Dr. Robert J. Butera, who provided me the freedom and resources to explore my scientific and engineering curiosities, put up with my stubbornness, and answered my calls/text at odd hours of the day to provide honest input, feedback, and advice. Thank you for believing in me and giving me a chance to develop as a scientist and as a person.

My colleague, Dr. Laura O'Farrell, who has played a critical role in the work presented in Chapter VI and to my professional development. Her willingness to always help with experiments, challenge my understanding and approaches, and push me to think differently have reshaped how I conduct scientific research.

My committee members, Drs. Arthur English, Christopher Rozell, Thomas Burkholder, and the global scientific community - all of whom have played a critical role in the development of the works presented here and in my professional development. Thank you for always answering my cold calls and making time for me.

My friends - Michael, Eric, Andrew, Gareth, Clarissa, Jon, Tarun, Manfred, and Sandip. Each of you has taught me something that has helped me get to where I am today, and for that I truly appreciate you and the time we have spent together.

My best friend and partner, Sarika, who has been patient, supportive, and encouraging throughout this journey. Thank you for bringing out the best in me.

Finally, my family - Mom, Dad, Sneha, Prem, aunts, uncles, and cousins - for everything. Thank you for always asking questions about my work, sending me food, and giving me multiple reasons to laugh everyday. I don't say it enough - but I love you all very much.

## TABLE OF CONTENTS

## LIST OF TABLES

## LIST OF FIGURES

## LIST OF EQUATIONS

## GLOSSARY

| | |
|---|---|
| **Closed-loop** | a process that computes an output based upon an input and feedback signal |
| **Daemon** | a computer process that runs as a background process (e.g., Dropbox, Skype but not Web Browsers or File Managers). |
| **Hard real-time** | guaranteed performance of I/O within specified bound; failure to achieve bounded performance results in a system crash |
| **Jitter** | deviation from the desired real-time period |
| **Kernel** | core of an operating system that enables bi-directional communication between software and hardware |
| **Live CD** | a complete bootable operating system with applications and drivers ready to run from a computer's memory; requires no installation |
| **Open-loop** | a process that computes an output based upon an input only (no feedback signal) |
| **Real-time period** | duration between the real-time thread waking up (becoming active) and going to sleep (becoming idle) |
| **Scheduler** | an operating system component that manages allocation of system resources |
| **Soft real-time** | guaranteed performance of I/O within specified bounds; failure to achieve bounded performance is acceptable and does not effect system stability |
| **Synchronous** | unbuffered data acquisition or processing |
| **Thread** | a sequence of machine instructions for execution |

# ACRONYMS

| | |
|---|---|
| **AC** | Alternating Current |
| **acVNS** | afferent cervical Vagus Nerve Stimulation |
| **AI** | Analog Input |
| **AO** | Analog Output |
| **API** | Application Programming Interface |
| **ASIC** | Application Specific Integrated Circuit |
| **CAP** | Compound Action Potential |
| **cm** | centimeters |
| **CNS** | Central Nervous System |
| **CPU** | Central Processing Unit |
| **CSC** | Charge Storage Capacity |
| **cVN** | cervical Vagus Nerve |
| **cVNS** | intact cervical Vagus Nerve Stimulation |
| **cVNx** | cervical Vagus Nerve transection |
| **DAQ** | Data Acquisition |
| **DC** | Direct Current |
| **DIO** | Digital Input/Output |
| **ecVNS** | efferent cervical Vagus Nerve Stimulation |

**EEG** Electroencephalography

**EMG** Electromyography

**ENG** Electroneurogram

**ESA** Electrochemical Surface Area

**GB** GigaBytes

**GHz** GigaHertz

**GPU** Graphics Processing Unit

**GSA** Geometric Surface Area

**GSN** Greater Splanchnic Nerve

**GSNx** Greater Splanchnic Nerve transection

**GUI** Graphical User Interface

**HDF** Hierarchical Data Format

**HFD** High Fat Diet

**Hz** Hertz

**I/O** Input/Output

**KES** Kilohertz Electrical Stimulation

**kHz** kiloHertz

**m/s** meters per second

**$mA_{peak}$** milliAmps peak

**$mA_{pp}$** milliAmps peak-to-peak

**MIMO** Multiple-Input Multiple-Output

**ml** milliliter

**mm** millimeters

**ms** millisecond

**ND** Normal Diet

**NHP** Non-Human Primate

**OGTT** Oral Glucose Tolerance Test

**PNS** Peripheral Nervous System

**Pt** Platinum

**Pt-Ir** Platinum-Iridium

**RAM** Random Access Memory

**RPM** Revolutions per minute

**RTXI** Real-Time eXperiment Interface

**SINE** Separated Interface Nerve Electrode

**SISO** Single-Input Single-Output

**SNR** Signal to Noise Ratio

**SS** Stainless Steel

**tACS** Transcranial Alternating Current Stimulation

**TiN** Titanium Nitride

**TNF-$\alpha$** Tumor Necrosis Factor-$\alpha$

**V** volts

## SUMMARY

Kilohertz Electrical Stimulation (KES) enables a rapid, reversible, and localized inhibition of peripheral nerve activity. Discovered in the early 1900's, the utility and application of KES nerve block to treat symptoms of various disease states is nearly non-existent. Although a handful of clinical products utilize KES, it is highly debated and unknown if these products provide therapeutic benefit or, if they do, whether they do it by achieving a true conduction block of nerve activity or through other unknown mechanisms of action. Furthermore, many critical questions still remain about the optimal electrodes, waveforms, and approaches necessary for clinical utility of KES nerve conduction block. In this thesis, I investigate multiple facets of KES nerve conduction block. In Part I, I present electrode optimizations that reduce energy requirements and ensure optimal KES nerve conduction block. I describe critical geometry and materials considerations for electrode design, quantify charge characteristics of KES waveforms, and discuss how electrode characteristics can impact clinical device design. In Part II, I demonstrate the utility of KES in a variety of somatosensory and autonomic neural circuits to treat symptoms arising from immune and metabolic disorders. I show that KES nerve block can selectively block conduction in different fiber-types for selective inhibition of motor and sensory information. I then demonstrate the ability of KES nerve block to provide direction-specific stimulation of the vagus nerve for modulation of the innate immune system. Finally, I demonstrate the utility of KES nerve block for modulation of glucose metablism. Collectively, the methods, tools, and results presented in this thesis significantly impact the design and clinical translation of KES therapies.

# Part I

# Optimization of Kilohertz Electrical Stimulation

# CHAPTER I

# KILOHERTZ ELECTRICAL STIMULATION NERVE BLOCK

## *1.1 What is Kilohertz Electrical Stimulation (KES) nerve block?*

Luigi Galvani was the first to observe the effects of electrical charge on to the nervous system in 1780. By accident, he observed that a dead frog's muscles contracted when the sciatic nerve was touched with his scalpel. He postulated that the static charge held by the scalpel activated the nerve, which in turn led to activation of the muscle. Since then, electrical stimulation has been used to investigate neural function as well as control and modulate nervous system activity.

A variety of different stimulation therapies and techniques exist within the domain of electrical stimulation. For example, low frequency (<100 Hz) electrical stimulation is typically used to excite neuronal structures such as cell bodies, axons, or ganglia, resulting in generation of action potentials. Higher frequency (>100 Hz, but <1 kHz) electrical stimulation is used to modulate deep brain structures, the spinal cord, and peripheral nerves. Depending on the structure stimulated, high frequency stimulation can lead to generation of action potentials or depletion of neurotransmitters. Although less understood and investigated, electrical stimulation using kilohertz frequencies (>1 kHz) has gained significant traction for use in neuromodulation therapies in the last decade.

The critical difference between low- or high- frequency electrical stimulation and kilohertz electrical stimulation (KES) is that KES enables a quick, reversible, and

complete *inhibition* of action potential propagation through the stimulated region of tissue, referred to as nerve conduction block. KES nerve block has been demonstrated in a variety of animal models and nerve diameters, including sea slugs (Joseph et al., 2009), frogs (Kilgore et al., 2004; Joseph et al., 2011), rats (Patel et al., 2015; Williamson et al., 2005; Bhadra et al., 2005), cats (Bhadra et al., 2006; Boger et al., 2013), dogs (Lin et al., 2007), goats (Cuellar et al., 2013), pigs (Camilleri et al., 2008), and non-human primates (Ackermann et al., 2011b). These studies and others (Table 3) have demonstrated the ability to achieve a quick, reversible, localized block of peripheral nerve activity.

Experimental investigations using KES nerve block typically modulate two key KES parameters to achieve a complete nerve block  frequency and amplitude. Previous studies have demonstrated that frequencies greater than 5 kHz are required to achieve a true conduction block (Bhadra et al., 2005) that is localized to the site of KES delivery, rather than neuromuscular depletion (fatigue) (Kilgore et al., 2004). Frequencies as high as 70 kHz are effective experimentally (Patel et al., 2015), while frequencies up to 100 kHz have been evaluated in computational studies (Tai et al., 2011). The KES amplitude, typically reported with units of either volts (V) or milliAmps peak ($mA_{peak}$) and milliAmps peak-to-peak ($mA_{pp}$) depending on the mode of stimulation, is determined by the target nerve's anatomy, electrical coupling between the interface and target nerve, resolution of the readout used for validation of KES nerve block, and neural interface geometry and configuration. The lowest amplitude (V or mA) at a given KES frequency that provides block of target nerve activity is referred to as the block threshold, and has been found to increase linearly with frequency for large diameter fibers and non-monotonically for small diameter fibers (Joseph et al., 2009; Joseph et al., 2011; Patel et al., 2015; Bicket et al., 2016).

## *1.2 Why study KES nerve block?*

Many clinical neuromuscular conditions result from neuronal hyperactivity. Undesired motor activity occurs in spasticity conditions and affects patients suffering from spinal cord injuries (Sköld et al., 1999), multiple sclerosis (Beard et al., 2003), cerebral palsy (Flett, 2003) and stroke (O'dwyer et al., 1996). Dystonia, choreas, tics, and intractable hiccups are other conditions that result from extraneous motor neural activity. Unwanted afferent activity also occurs in various conditions associated with chronic pain, like neuromas, neuralgias etc. Arresting or blocking these kinds of superfluous activity through peripheral nerves can be useful for alleviating disease symptoms and eliminating the debilitating nature of these conditions.

Various methods exist for blocking conduction of neural activity include pressure application, temperature changes, and various pharmacological methods. Unfortunately, these methods are not able to provide a quick effect or reversal and can cause serious side effects, including possible nerve destruction. Although effective for selective blocking, these methods are unsuitable for chronic clinical applications. As an alternative, nerve block has been studied in whole nerves through the use of kilohertz frequency Alternating Current (AC) and Direct Current (DC) currents. DC induced conduction block has been shown to block both A- and C- fibers however problems relating to polarization and generation of undesired synchronous and asynchronous activity are significant and remain a barrier to translation. In contrast, kilohertz frequency AC stimulation has been shown to be clinically useful without the complications presented by DC stimulation.

### *1.2.1 How are existing KES therapies benefiting patients?*

The need to investigate KES nerve block stems from existing KES clinical products and their effects on disease states. The ability to achieve a true nerve conduction block

can vary significantly depending upon the frequency, amplitude, electrode, waveform, duration, and anatomy of the target structure. Under inadequate conditions, KES can lead to significant activation or anatomical modification of the target tissue. Clinically, KES is currently used in spinal cord stimulation therapies for treatment of chronic pain without paresthesia (Miller et al., 2016), abdominal vagus nerve stimulation for modulation of satiety and appetite (Apovian et al., 2016), as well as somatic nerve stimulation therapies for treatment of post-amputee pain (Soin et al., 2015). How these therapies are providing therapeutic benefit is highly debated and unknown. Regardless of the mechanisms, how therapeutic benefit is being achieved using KES is critical to mitigating long-term and potentially severe side-effects.

## *1.3 Characteristics of KES nerve block*

In addition to the effect of blocking nerve conduction, application of KES to nerves consists of a number of additional characteristics that have been investigated and are relevant to application of KES to neural circuits. The most relevant characteristics include the onset artifact, fiber-type and directional selectivity, as well as the the carry over effect.

### *1.3.1 Onset artifact*

Upon delivery of KES to a target nerve, a brief period of asynchronous, bi-directional activity is induced in the nerve. This discrete event has been labeled the onset artifact and has previously been measured directly from nerves (Patel et al., 2015). Depending upon the target nerve and the neural circuit it is part of, the onset artifact can lead to activation of muscles, various reflex loops, or pathway specific efferent or afferent signaling resulting in changes in systemic physiology. A key distinction that should be made is that the onset artifact observed from the perspective of the nerve can be

**Table 3:** History of KES nerve block electrodes.

| Publication | Configuration | Contacts | Conductor | Species |
|---|---|---|---|---|
| Cattell et al., 1935 | ND | Wires | Ag/Calomel | Frog |
| Rosenblueth et al., 1939 | Bipolar | Wires | Ag\|AgCl | Cat |
| Reboul et al., 1939 | Bipolar | Wires | Ag\|AgCl | Cat |
| Tanner, 1962 | Bipolar | ND | Pt | Frog |
| Woo et al., 1964 | Bipolar | ND | ND | Frog/Cat |
| Baratta et al., 1989 | Tripolar | Wires | SS | Cat |
| Bowman et al., 1987 | Bipolar | Wire | Pt | Cat |
| Kilgore et al., 2004 | Bipolar | Wire | Pt | Frog |
| Tai et al., 2004 | Tripolar | Wires | SS | Cat |
| Bhadra et al., 2005 | Tripolar | Pads | Pt | Rat |
| Williamson et al., 2005 | Tripolar | Wires | SS | Rat |
| Bhadra et al., 2005 | Tripolar | Pads | Pt | Rat |
| Bhadra et al., 2006 | Tripolar | Pads | Pt | Cat |
| Miles et al., 2007 | Tripolar | Pads | Pt | Rat |
| Boger et al., 2008 | Tripolar | ND | ND | Cat |
| Joseph et al., 2007 | Bipolar | Wires | Ag\|AgCl | Sea Slug |
| Ackermann et al., 2009 | Bipolar | Pads | Pt | Rat |
| Ackermann et al., 2010b | Bipolar | Pads | Pt | Rat |
| Ackermann et al., 2010c | Bipolar | Pads | Pt | Rat |
| Gerges et al., 2010 | Bipolar | Pads | Pt | Rat |
| Ackermann et al., 2010a | Bipolar | Wires | W | Rat |
| Ackermann et al., 2011a | Monopolar | Pads | Pt+Ag\|AgCl | Rat |
| Ackermann et al., 2011b | Bipolar | Pads | Pt | Rat |
| Ackermann et al., 2011d | Monopolar SINE | Pads | Pt | Rat |
| Ackermann et al., 2011c | Bipolar | Pads | Pt | NHP |
| Joseph et al., 2009 | Bipolar | Wires | Ag\|AgCl | Sea Slug |
| Joseph et al., 2011 | Bipolar | Wires | Ag\|AgCl | Sea Slug |
| Liu et al., 2013 | Bipolar | Wires | Ag\|AgCl | Frog |
| Patel et al., 2015 | Tripolar | Pads | PtIr | Rat |
| Yang et al., 2016 | Tripolar | ND | ND | Frog |
| Patel et al., 2017b | Bipolar | Pads | PtIr | Rat |
| Patel et al., 2017a | Bipolar | Pads | PtIr | Rat |

on the order of tens of milliseconds, while the physiological response resulting from the onset artifact can last up to tens of seconds.

In somatosensory neural circuits, the physiological result of the onset artifact is a muscle contraction or force production and has been studied extensively by Kilgore and colleagues (Kilgore et al., 2004; Kilgore et al., 2014). Their investigations focused on minimizing the onset artifact magnitude and duration measured through force production. Their studies elucidated the role of electrode contact spacing in reducing the onset artifact magnitude and duration (Ackermann et al., 2010b). In other cases, Kilgore and colleagues completely abolished the onset artifact by combining both direct and alternating current waveforms (Franke et al., 2014a). Application of KES to nerves part of autonomic neural circuits is less studied, but can result in activation of numerous unwanted pathways or circuit functions. For example, application of KES to the thoracic sympathetic chain in anesthetized pigs has demonstrated a susbtantial elevation of cardiac function that eventually subsides (Buckley et al., 2017).

It is unclear, however, if such onset artifacts exist and are of concern in conscious (unanesthetized) states, where cascades of neural control circuits may prevent the occurrence of detrimental physiological effects. The lack of clinical reports discussing the onset artifact in patients currently implanted with KES devices suggests there may be no significant physiological side effects, however this remains to be thoroughly evaluated. Anecdotal evidence by this author suggests that the onset artifact is a consequence of inhomogenous fields present at the site of KES. By optimizing electrode geometry parameters - such as contact spacing, contact dimensions, and total electrode length - the onset artifact can be substantially reduced and in some cases, completely abolished.

### *1.3.2 Selectivity*

Until recently, KES-induced conduction block had been reported as being "all-or-none", suggesting that all propagating activity in the target nerve was blocked upon delivery of KES. Typically, investigators plot the amplitude of the KES waveform as a function of frequency, resulting in the block threshold curve, which shows the relationship between frequency and amplitude for achieving a nerve conduction block for a given nerve. Previous investigations (Kilgore et al., 2004) have demonstrated that the frequency-amplitude relationship is linear, with the block threshold increasing as the KES frequency increases.

Joseph and Butera were the first to demonstrate that this relationship between frequency and amplitude is not always linear. They characterized KES block thresholds in unmyelinated *Aplysia* nerves and found the relationship between frequency and amplitude to be non-monotonic (Joseph et al., 2009). In their studies, they used suction electrodes to deliver the KES waveforms and record Compound Action Potential (CAP)s from the nerve to evaluate the effects of KES on nerve conduction. To validate these findings in a mixed nerve, Joseph and Butera later conducted investigations in the frog sciatic nerve, which is a mixed myelinated and unmyelinated nerve bundle. Using the same electrophysiology approaches as with the *Aplysia*, Joseph and Butera demonstrated the ability to selectively block myelinated (fast-conducting) and unmyelinated (slow-conducting) axons (Joseph et al., 2011). They found that the frequency-amplitude relationship for myelinated fibers was linear, as had been shown previously, however the frequency-amplitude relationship for unmyelinated fibers was non-monotonic, similar to that of their findings in *Aplysia*. By selecting the frequency-amplitudes appropriately, Joseph and Butera demonstrated the ability to achieve fiber-selective KES block of nerve activity.

### *1.3.3 Carry over*

The onset artifact is present when KES is initially turned on. In contrast, artifacts of KES nerve block present themselves even after turning of KES. The primary artifact that has received investigation is called the carry over block effect, and is a window of time after KES delivery is turned off in which nerve activity is either partially or nearly completely inhibited. The carry over effect has received little attention, primarily in somatosensory circuits such as the sciatic nerve. Bhadra and colleagues demonstrated that the carry over can be observed after as little as 15 minutes of KES nerve block. However experimental unknowns about the true waveform delivered to the nerve make it difficult to hypothesize potential mechanisms underlying the carry over. In addition, it is likely that the KES duration after which a carry over is observed and the duration of the carry over itself are functions of the target nerve's anatomy and physiological functions.

## *1.4 Biophysical mechanisms(s)*

The biophysical mechanism(s) underlying KES nerve block are unknown, however a significant number of computational investigations have been reported and propose a number of different potential mechanisms. Computational studies to date are based on single axon models with a point source for the stimulation electrode. It is currently unknown how well existing single axon models correlate to the axon's true biophysical behavior at kilohertz frequencies. Although not a thorough review of computational investigations to-date, the studies discussed (below) represent the primary hypotheses believed to be a part of KES conduction block. To-date, there are not reported experimental investigations on the mechanisms of KES conduction block.

Bhadra and Kilgore (Kilgore et al., 2004) began to use simulation studies of KES conduction block to visualize the electrophysiological behavior of the nerve membrane.

Their simulations were constructed using the NEURON software package (Hines, 1993) and provided a means to study the mechanism of KES conduction block. Their nerve membrane was modeled using the McIntyre-Richardson-Grill (MRG) model, which is an equivalent electrical circuit for myelinated axons. The blocking electrode was modeled as a single point source centered above the middle node of the axon. The extracellular potential and intracellular currents were calculated at each compartment of the model and a current-controlled sinusoidal waveform delivered by the blocking electrode using frequencies from 3-10 kHz, with the amplitude varying from 0.050-1 $mA_{pp}$ at each frequency. Conduction block was determined as the condition where no action potential was propagated to the node opposite to the stimulating end of the axon. Simulation results proposed that conduction block is a result of tonic depolarization of the nerve membrane (Kilgore et al., 2004).

Further modeling studies by Tai et al (Tai et al., 2005) utilized a Hodgkin-Huxley based lumped circuit model of the unmyelinated axon to study KES conduction block. Simulation results showed that when the stimulation frequency is approximately 4 kHz, axons of various diameters (5-20 $\mu$m) could be blocked. Their simulations also showed that larger diameter axons require a lower amplitude to achieve conduction block. They also showed that frequency dependent pulse-width modulation is more effective compared to fixed pulse-width stimulation. Their simulation results supported the claim that conduction block in unmyelinated nerves was due to activation of potassium channels, rather than inactivation of sodium channels.

Later, Tai et al (Zhang et al., 2006b) studied nerve conduction block in myelinated axons using the Frankenhaeuser-Huxley (FH) model and the Chiu-Ritchie-Rogart-Stagg-Sweeney (CRRSS) model. Simulation results from the FH model showed that constant activation of potassium channels at the node under the block electrode was the mechanism of KES nerve conduction block in myelinated axons and the nerve could recover from block within 1 ms. In contrast, CRRSS model simulations revealed

that complete inactivation of sodium channels next to the block electrode caused the nerve conduction block. Stimulation frequencies (>6 kHz) from FH model simulations agreed with those from animal experiments, but stimulation frequencies from CRRSS model simulations did not (>15 kHz). Tai et al proposed that this difference in stimulation frequency is indicative of the constant activation of potassium channels.

## *1.5 Future of KES Nerve Block*

Recent and on-going scientific discoveries have started to unravel the role of neural control in achieving homeostasis, and prompted a variety of investigations as to why neural control fails in disease states. For example, increased chronic sympathetic output to the visceral organs in obese patients is implicated in the onset, progression, and development of cardiovascular and metabolic disorders such as diabetes and hypertension. In these disease states, it may be desired to inhibit sympathetic output to either treat symptoms or halt disease onset and progression with quick, localized, and reversible inhibition of nerve activity in relevant neural circuits. Kilohertz Electrical Stimulation (KES) induces such a block of nerve activity, and holds significant promise as a potential therapeutic intervention as well as tool for scientific investigation.

A significant number of unknowns remain and are necessary to understand for effective translation of KES and achieve therapeutic benefit. These remaining unknowns however, must be approached with a physiology-first mindset, in which the physiological system to be modulated is thoroughly understood in terms of both anatomy and physiology. Only then can engineering and physiological principles be bridged to optimize and effectively translate KES neuromodulation therapies.

## *1.6 Thesis Organization*

This dissertation is organized into two complementary parts. Part One (Chapters I - III), *Optimization of Kilohertz Electrical Stimulation*, is a sensitivity analysis of individual experiment components part of achieving a true nerve conduction block using KES. Part Two (Chapters IV - VI), *Applications of Kilohertz Electrical Stimulation*, demonstrates the use of KES nerve block in modulating multiple autonomic neural circuits involved in maintenance of immune and metabolic homeostasis.

In Chapter II, *Effects of electrode surface area*, I explore the relationship between the electrode geometric surface area, nerve geometry, and nerve block thresholds. I designed electrode geometries to provide varying degrees of circumferential coverage of the rat tibial nerve and evaluated the nerve block thresholds as a function of the coverage. I demonstrate that although KES nerve block can be achieved with any degree of coverage, the electrical power required to achieve a true nerve conduction block is inversely related to the geometric surface area of the electrode.

In Chapter III, *Effects of electrode material*, I investigate the impact of different electrode materials on the ability to achieve a true nerve conduction block. By using electrode materials with fundamentally different charge injection mechanisms, I show that non-porous and non-coated materials such as Platinum-based alloys minimize the power consumption and provide a safe, reversible, and effective nerve conduction block. I also show that the electrochemical behavior of all electrode materials, regardless of composition and structure, is fundamentally the same at KES frequencies.

In Chapter IV, *Fiber-specific block of nerve conduction*, I investigate the ability of KES nerve conduction block to be fiber-type specific in both somatic and autonomic nerves. First, I characterized the block thresholds for A and C fibers in the sciatic and cervical vagus nerves. I then utilized the frequency-amplitude curves to demonstrate inhibition of both electrophysiological (compound action potential components) and

functional (muscle contractions and sensory perception) activity in the sciatic nerve.

In Chapter V, *Directional selectivity for down-regulation of systemic inflammation*, I collaborate with Tarun Saxena to investigate the utility of KES nerve block for achieving directional stimulation for modulation of the innate immune system. We show that, by pairing KES nerve block and pulsatile electrical stimulation, we can achieve directional activation of the cervical vagus. We demonstrate that this selective stimulation provides for enhanced modulation of the innate immune system in response to induced toxemia. We also investigate and propose a potential side-effect of existing vagus nerve stimulation therapies, which is in stark contrast to leading hypotheses about the mechanism(s) underlying vagus nerve stimulation for modulation of the innate immune system.

In Chapter VI, *Modulation of postprandial glycemia via sympathetic inhibition*, I collaborate with Laura O'Farrell, Jay Pasricha, and Lian Sheng Liu to investigate the role of the sympathetic nervous system in postprandial hyperglycemia. We demonstrate that sympathetic visceral denervation, via transection of the greater splanchnic nerves, significantly reduces postprandial hyperglycemia in healthy and diseased rats. We extend this work by evaluating the use of KES to virtually denervate the greater splanchnic nerve in healthy rats, demonstrating the clinical utility of KES in treatment of postprandial hyperglycemia.

In the Appendix, I describe tools for real-time investigation of neural circuits and novel new electrodes for interfacing with the peripheral nervous system. Appendix A.1, *Hard real-time closed-loop electrophysiology with the Real-Time eXperiment Interface (RTXI)*, provides a technical overview of the Real-Time eXperiment Interface (RTXI), an open source software platform for achieving hard real-time data acquisition and closed-loop control in biological experiments while retaining the flexibility needed for experimental settings. RTXI is the result of work and effort put in by many individuals. My contributions to RTXI include redesigning the hard real-time

scheduler and threading, developing Linux kernel drivers for new data acquisition hardware, and rebuilding the graphical user interface (GUI). RTXI has enabled users to implement complex custom closed-loop protocols in single cell, cell network, animal, and human electrophysiology studies.

Appendix A.2, *Microneedle cuff electrodes*, describes a microneedle ($\mu$Needle) peripheral nerve interface, called the transneural cuff electrode, I developed and evaluated in collaboration with Axion BioSystems (Atlanta, GA). We evaluated the electrode's electrophysiological functionality and histologically evaluated the safety of the interface in chronic studies.

Segments of this thesis have been published or are under review for publication. Chapters based upon published work include a citation and are unchanged from their published form with the exception of minor modifications to typography and style.

# CHAPTER II

# EFFECTS OF ELECTRODE SURFACE AREA

## *2.1 Motivation*

Kilohertz Electrical Stimulation (KES) induces repeatable and reversible conduction block of nerve activity and is a potential therapeutic option for various diseases and disorders resulting from pathological or undesired neurological activity. However successful translation of KES nerve block to clinical applications is stymied by many unknowns such as the relevance of the onset response, acceptable levels of waveform contamination, and optimal electrode characteristics. We investigated the role of electrode geometric surface area on the KES nerve block threshold using 20 and 40 kHz current-controlled sinusoidal KES. Electrodes were electrochemically characterized and used to characterize typical KES waveforms and electrode charge characteristics. KES nerve block amplitudes, onset duration, and recovery of normal conduction after delivery of KES were evaluated along with power requirements for effective KES nerve block. Results from this investigation demonstrate that increasing electrode geometric surface area provides for a more power efficient KES nerve block. Reductions in block threshold by increased electrode surface area were found to be KES-frequency dependent, with block thresholds and average power consumption reduced by >2x with 20 kHz KES waveforms and >3x for 40 kHz KES waveforms.

This work is published as Yogi A. Patel et al. (2017a). "Kilohertz Electrical Stimulation Nerve Conduction Block: Effects of Electrode Surface Area". In: *IEEE Transactions on Neural Systems and Rehabilitation Engineering*. Financial support for this work was provided by Georgia Tech and the National Institutes of Health

(Grant 2R01EB016407-09A1).

## *2.2 Background*

Kilohertz Electrical Stimulation (KES) nerve block has been demonstrated in a variety of animal models and nerve diameters, including sea slugs (Joseph et al., 2009), frogs (Kilgore et al., 2004; Joseph et al., 2011), rats (Patel et al., 2015; Williamson et al., 2005; Bhadra et al., 2005), cats (Bhadra et al., 2006; Boger et al., 2013) dogs (Lin et al., 2007), goats (Cuellar et al., 2013), pigs (Camilleri et al., 2008), and non-human primates (Ackermann et al., 2011b). These studies have demonstrated the ability to achieve a quick, reversible, localized block of peripheral nerve activity.

Experimental investigations using KES nerve block typically modulate two key KES parameters to achieve a complete nerve block  frequency and amplitude. Previous studies have demonstrated that frequencies greater than 5 kHz are required to achieve a true conduction block (Bhadra et al., 2005) that is localized to the site of KES delivery, rather than neuromuscular depletion (fatigue) (Kilgore et al., 2004). Frequencies as high as 70 kHz are effective experimentally (Patel et al., 2015), while frequencies up to 100 kHz have been evaluated in computational studies (Tai et al., 2011). The KES amplitude, typically reported with units of either voltage (volts (V)) or current (milliAmps peak ($mA_{peak}$)) depending on the mode of stimulation, is determined by the target nerve's anatomy, electrical coupling between the interface and target nerve, resolution of the readout used for validation of KES nerve block, and neural interface geometry and configuration. The lowest amplitude (V or mA) at a given KES frequency that provides block of target nerve activity is referred to as the block threshold, and has been found to increase linearly with frequency for large diameter fibers and non-monotonically for small diameter fibers (Joseph et al., 2009; Joseph et al., 2011; Patel et al., 2015; Bicket et al., 2016).

Early studies report that the quality of KES nerve block is significantly impacted by the electrode configuration (Rosenblueth et al., 1939). A few follow up investigations have been conducted recently with a focus on determining the optimal inter-pole spacing within a bipolar cuff electrode that minimizes the block threshold (Ackermann et al., 2009) and the onset response (Ackermann et al., 2010b), which is a measurable burst of asynchronous nerve activation that occurs when KES delivery is initiated. Aside from the few investigations cited here, no systematic investigation has been carried out to understand the effects of electrode characteristics on KES nerve block. Furthermore, almost all published results have reported the use of different interfaces (as shown in Table 3). These reports differ in electrode type, materials, and geometry, as well as animal model and target nerve, with many publications missing sufficient details to enable valuable comparison.

The focus of the present study is to systematically evaluate the effect of electrode contact Geometric Surface Area (GSA) on KES nerve block thresholds and power consumption. The secondary goal of this study is to evaluate the effect of contact GSA on the KES nerve block onset artifact as well as nerve conduction and recovery post-KES nerve block. We created and electrochemically characterized electrode contacts and computed the charge characteristics of KES waveforms with fabricated contacts. Experiments were then carried out to investigate the effects of contact GSA on KES block thresholds. We computed the power consumption of KES nerve block using the electrochemical characterization data and experimental KES nerve block thresholds.

## *2.3 Experimental Methods*

### *2.3.1 Animal Preparation*

All animal research was approved by the Georgia Institute of Technology Institutional Animal Care and Use Committee. Experiments were conducted on tibial nerves from

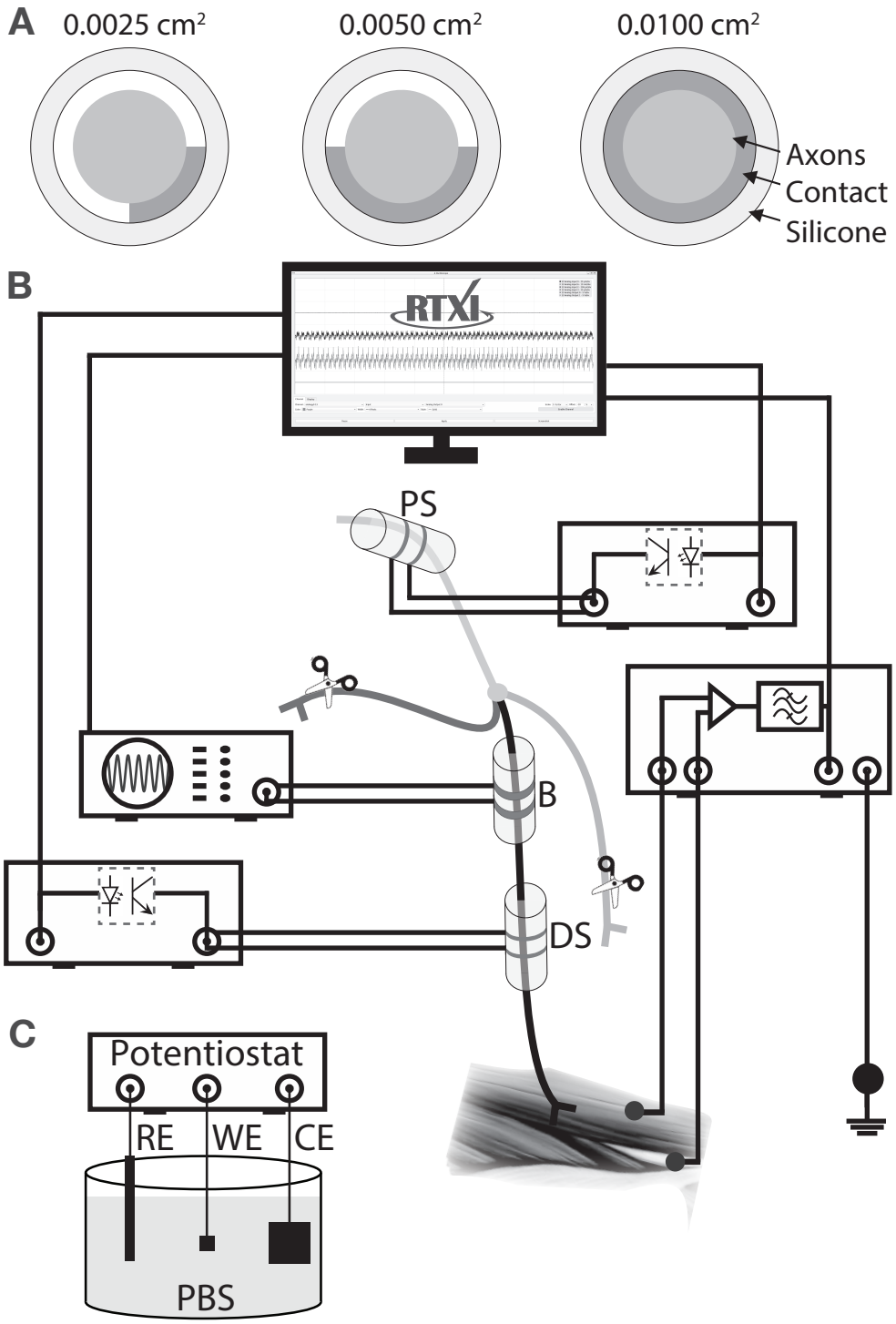


**Figure 1:** Electrophysiology setup and electrode configurations. (A) The nerve was electrically stimulated at the proximal and distal ends using bipolar cuff electrodes. EMG activity was measured from the gastrocnemius muscle using intramuscular fine wire electrodes. KES nerve block was delivered proximal to the distal stimulation electrode using a bipolar cuff electrode. Timing and duration of stimulation events, along with measurement of activity was achieved with RTXI. PS = proximal stimulation electrode, B = Block electrode, DS = distal stimulation electrode (B) Illustration of increasing nerve coverage with increasing contact GSA.

*in vivo* urethane-anesthetized rats (377.3 ± 72g, n = 6 males). Animals were briefly anesthetized using isoflurane in oxygen (5%, 1 liter/min flow rate) prior to delivery of urethane (IP, 1.2 g/kg in 0.9% saline). Anesthetic depth was evaluated 60 - 90 minutes post-injection by pinching the rear footpad and supplemental urethane (0.12 mg/ml) was delivered as necessary until the reflex withdrawal was eliminated. After reaching surgical depth, the animal's back was shaved from the lumbar section down to the distal end of the gastrocnemius muscle. The animal's foot was magnetically clamped to the surgical table to minimize motion during experimental trial. An incision approximately 1 - 1.5 cm in length was made along the length of the biceps femoris muscle and the sciatic nerve exposed via blunt dissection. The tibial branch of the sciatic nerve was identified and isolated from the sciatic notch down to the gastrocnemius muscle under a high magnification dissection scope. The common peroneal, sural, and collateral branches of the sciatic were cut to minimize off-target stimulation. Normal rat ringer's solution (*Normal Rat Ringer's Solution*) was applied throughout the experiment to prevent muscle and nerve tissue dehydration. The animal's body temperature was monitored and maintained at 37 - 40 °C with a rectal temperature probe (Model BAT-12, Physitemp Instruments, Clifton, NJ) and warming pad (COM-11289, SparkFun Electronics, Niwot, CO). Preparations lasted 5 - 6 hours after which animals were euthanized via an IP injection of pentobarbital-based euthanasia drug (0.5 ml/kg, IP). All experiments were conducted at room temperature.

### *2.3.2 Electrophysiology Setup*

The proximal end of the exposed sciatic nerve was stimulated using a bipolar cuff electrode made in-house. Two braided stainless steel wires (#793500, A-M Systems, Sequim, WA) separated by 1 mm were threaded through silicone tubing (#807600, A-M Systems, Sequim, WA). The wires were deinsulated inside the cuff and impedance

measured at 1 kHz in 0.9% saline (Table 4). A second bipolar stimulation cuff electrode was placed approximately 0.2 cm distal to the block electrode in all experiments for delivery of distal test stimuli. Distal test stimuli verified that KES nerve block was localized to the site of the block electrode and did not cause neuromuscular fatigue or neurotransmitter depletion.

Block of the tibial nerve was achieved using Pt/Ir (90/10, 25.4 $\mu$m thick) contact pads (ESPI Metals, Ashland, OR) spot-welded to braided stainless steel wire. Contact pads were cut and measured under a high resolution microscope with digital calipers (Table 4, measurement error = 0.01), wrapped around the tibial nerve under a dissection microscope, and insulated using silicone (Kwik-Cast, WPI, Sarasota, FL). The width of all contacts was 0.5 mm. Contact lengths were chosen to provide $\sim$90°, $\sim$180°, and $\sim$360° coverage (Figure 23B) based upon a tibial nerve circumference of 2.0 - 2.1 mm (Schmalbruch, 1986). Actual contact GSAs were calculated using measured mean contact dimensions. Impedance measurements were made at 1 kHz in room temperature saline stirred at a constant rate. Values shown are mean $\pm$ standard deviation. All calculations requiring contact GSA were conducted using ideal values.

Spacing between the proximal stimulation and block electrodes was approximately 1 cm in all experiments. Electromyography (EMG) activity was differentially measured from the gastrocnemius muscles using bipolar fine wire electrodes (Cooner Wire No. AS631, Chatsworth, CA). EMG measurements were filtered (100 - 300 Hz) and gained (1000x, Brownlee Precision Model 440, San Jose, CA) before being digitized at a rate of 20 kHz using Real-Time eXperiment Interface (RTXI) (RTXI, `http://www.rtxi.org`) with a PCI-6036E data acquisition card (National Instruments, Austin, TX). A stainless steel wire was inserted into the contralateral gastrocnemius muscle and connected to the surgical air table to electrically ground the animal, with the surgical table grounded to the amplifier (building supply ground).

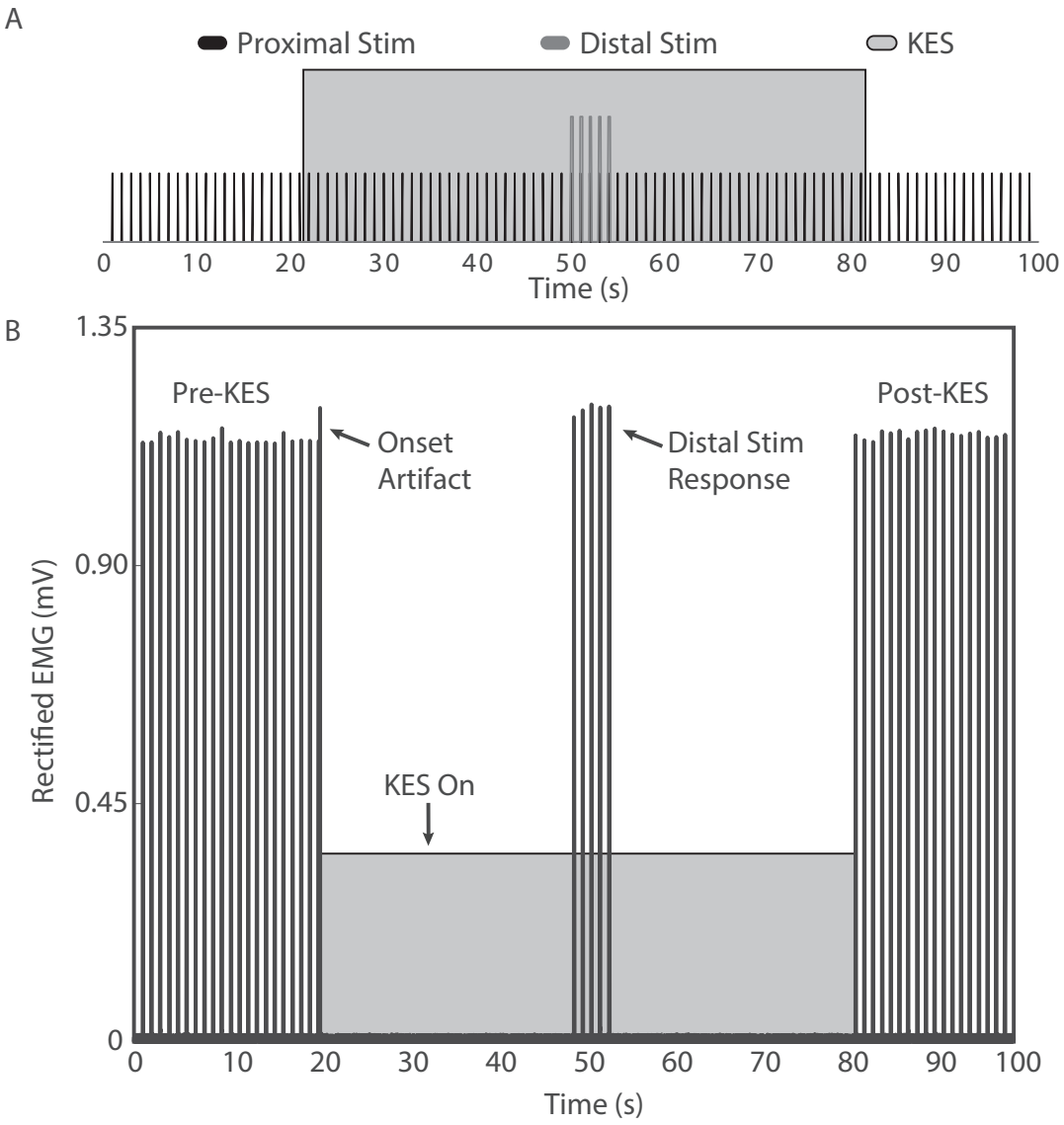


**Figure 2:** Experiment trial protocol and representative data. (A) Each trial lasted a total of 100 seconds, with KES on for 60 seconds. Stimulation pulses were delivered via the proximal stimulation cuff electrode throughout the entire trial. Five stimulation pulses were delivered to the nerve via the distal stimulation electrode to assess the locality of KES nerve block. (B) Representative rectified evoked EMG data.

Figure 23A shows the complete experiment setup.

### *2.3.3 Nerve Activation and KES Block*

Constant current pulses (0.3-0.5 $mA_{peak}$, 0.2 ms, 1 Hz) were generated using the RTXI signal generator module for proximal stimulation and an optically isolated constant current stimulator (DS3, Digitimer, Ft. Lauderdale, FL) for distal stimulation. Proximal stimulation pulses were optically-isolated using linear stimulus isolators (A395, WPI, Sarasota, FL). The KES waveform (current-controlled, continuous sinusoid) was generated using a floating current source function generator (Model 6221, Keithley Instruments, Inc, Clevelend, OH). The 2.1 $mA_{peak}$ and 21.0 $mA_{peak}$ ranges were used for the 20 kHz and 40 kHz KES trials, respectively. Direct current contamination of the KES waveform was randomly measured with a 10 $\Omega$ sense resistor in series with the return electrode and found to be 150 - 500 nA. All stimulus isolation units used were calibrated prior to each experiment and output offsets zeroed by visualization on an oscilloscope. Timing control of stimulation equipment was achieved by using digital I/O triggers generated from RTXI.

### *2.3.4 Experimental Protocols*

The first trial was conducted to determine the block threshold with a given electrode and KES frequency (as previously described in (Patel et al., 2015). The sciatic nerve was stimulated at 1 Hz using the proximal stimulation electrode to elicit supramaximal EMG activity in the gastrocnemius muscle. The threshold was found by increasing the amplitude of the KES waveform in 0.1 $mA_{peak}$ increments until complete block was achieved. Complete block was achieved only when the RMS voltage of the EMG measurement was equivalent to that of the measurement noise. The second trial was conducted at the empirically determined block threshold, with approximately 3

- 5 minutes between each trial. In each trial, a total of 100 stimulation pulses were delivered to the nerve (Figure 2A). The initial 21 stimulation pulses were delivered to the nerve to capture pre-KES EMG activity. KES was delivered to the nerve 900 ms after the $21^{st}$ stimulation pulse at either 20 or 40 kHz with the predetermined block threshold. Test pulses were delivered to the nerve while delivery of KES nerve block for continuous assessment of KES nerve block efficacy. The KES waveform was automatically turned off after 60 seconds (60 stimulation pulses) with continued nerve stimulation to measure post-KES EMG activity (18 stimulation pulses). Figure 2 provides a pictorial description of the experimental protocol for a single trial and representative data.

### *2.3.5 Electrochemical Measurements*

Monopolar cyclic voltammetry (CV) measurements were made for electrode contacts of different GSAs to compute the cathodic charge storage capacity Charge Storage Capacity (CSC) (Figure 12A). Measurements were made using a three electrode setup with a Ag|Ag/Cl reference electrode and a Pt counter electrode (surface area: 0.02 $cm^2$). A potentiostat (VMP3, Bio-Logic) was used to sweep the potential between -0.6 V and 0.8 V with a scan rate of 50 mV/sec while simultaneously measuring the current flow between the working (monopolar test electrode) and counter electrodes. The negative current time integrals were computed for each voltammogram and averaged to obtain the mean cathodic CSC for each contact GSA (Cogan, 2008).

Monopolar electrical impedance spectroscopy (EIS) measurements were made using the same three electrode setup to quantify changes at the electrode-tissue-interface as a function of contact GSA (Figure 12B-C). Measurements were made by sweeping a 10 mV excitation waveform over a frequency range of 1 - $10^5$ kHz. All electrochemical measurements were made in room temperature (25 °C) phosphate buffered saline (PBS, pH = 7.4, Sigma Aldrich, St. Louis, MO) stirred at a constant rate. The

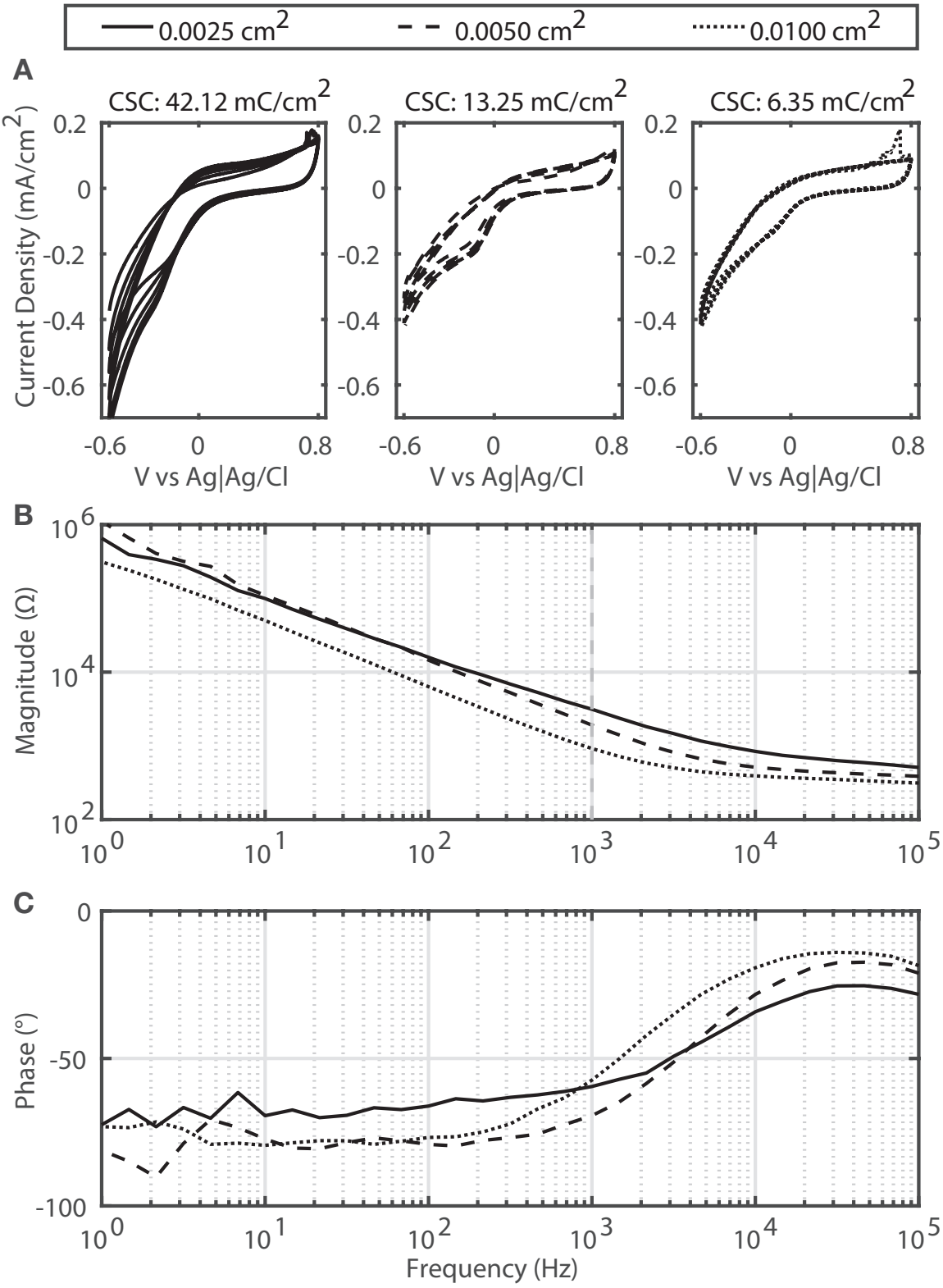


**Figure 3:** Electrochemical characterization of electrodes. (A) Five voltammograms are shown for each contact GSA evaluated (increasing contact GSA from left to right). The cathodic time integral was taken for each voltammogram and averages to calculate the cathodic CSC per contact GSA. Representative electrical impedance magnitude (B) and phase angle (C) are shown for each contact GSA. Impedance magnitudes are reduced with increasing contact GSA, with a nearly linearly response at typical KES frequencies.

measured impedance magnitude and phase at experimentally tested KES frequencies were used for waveform and power computations.

### *2.3.6 Waveform Characterization*

Nearly all investigations to date have presented KES nerve block data in terms of block thresholds only. We analyzed typical KES waveforms for common characteristics including charge density, current density, and charge per phase as a function of KES frequency and contact GSA (Figure 4). One full period of each KES (sinusoidal) current waveform was generated in MATLAB 2016 (MathWorks Inc., Natick, MA) with a sampling rate of 20 MHz (Equation 1). The cathodic phase (Figure 4A) was used for computing waveform characteristics. Charge per phase (Figure 4B), current density (Figure 4C), and charge density (Figure 4D) were calculated using equations 2, 3, and 4, respectively.

$$I(t) = I * sin(2 * \pi * f * t + \phi), 0 \leq t \leq \frac{1}{T_{KES}} \tag{1}$$

$$Q_{phase} = \int_0^{\frac{1}{2}T_{KES}} I(t) \tag{2}$$

$$I_\rho(t) = \frac{I(t)}{GSA}, \quad 0 \leq t \leq \frac{1}{2}T_{KES} \tag{3}$$

$$Q_\rho = \frac{\int_0^{\frac{1}{2}T_{KES}} I(t)}{GSA} \tag{4}$$

### *2.3.7 Power Calculations*

We used EIS magnitude, phase, and mean KES block thresholds (Figure 26) to approximate the energy required to achieve effective KES nerve conduction block with each contact GSA (Figure 6). The mean RMS ($mA_{peak}$) KES block threshold for

each contact GSA was used to generate a single cycle of a 20 and 40 kHz KES current waveform (Equation 1). The EIS magnitude and phase for 20 and 40 kHz were obtained by interpolating between the EIS measurements for each contact GSA. The magnitude was used to generate an equivalent voltage waveform (Equation 5). The phase and generated voltage and current waveforms were then used to calculate the power (Equation 6).

$$V_{RMS} = I_{RMS} * |Z(GSA, KES)| \tag{5}$$

$$Power = V_{RMS} * I_{RMS} * cos(\phi) \tag{6}$$

### *2.3.8 Data Analysis*

All data were analyzed with MATLAB. EMG recordings were detrended and windowed (10 ms bins) to capture evoked EMG activity. The stimulus trigger was used to define the EMG window's left edge. An additional 10 ms window was used to capture baseline noise prior to stimulus delivery. The windowed data was full-wave rectified and the root mean square (RMS) voltage used as a metric for evaluating nerve and muscle activation as well as KES nerve block. The noise RMS voltage was subtracted from the EMG RMS voltage to reduce variance introduced by noise and differences in electrical coupling between experimental setups. Onset artifacts were identified by comparing the RMS voltage of a moving 10 ms window to pre-KES RMS noise values. All box plots show the population mean (center black bar), 95% confidence interval (white region), and one standard deviation (gray region).

**Table 4:** Ideal and actual electrode contact dimensions and geometries.

| **Ideal Dimensions (mm)** | 0.50 x 0.50 | 0.50 x 1.00 | 0.50 x 2.00 |
|---|---|---|---|
| **Actual Dimensions (mm)** | 0.50 x 0.50 ± 0.01 | 0.50 x 1.00 ± 0.01 | 0.50 x 2.00 ± 0.03 |
| **Ideal GSA ($cm^2$)** | 0.0025 | 0.0050 | 0.0100 |
| **Actual GSA ($cm^2$)** | 0.0025 | 0.0050 | 0.0103 |
| **Impedance (1 kHz, kΩ)** | 5.54 ± 1.60 | 2.56 ± 0.60 | 1.06 ± 0.10 |
| **Measurements (n)** | 6 | 7 | 7 |

## 2.4 Results

### 2.4.1 Electrochemical characterization of electrodes

Electrochemical characterization of electrodes provides valuable information about the safety of stimulation waveforms with respect to tissue damage, electrode stability, and the response of electrodes to different stimulation waveforms. We performed CV measurements (Figure 12A) to quantify the cathodic CSC of each GSA with previously published potential limits (Cogan, 2008). Cyclic voltammograms for the 0.0025 $cm^2$ electrode demonstrated greater cycle-to-cycle variability. The cathodic CSCs decreased with increasing contact GSAs (Figure 12A). EIS measurements (Figure 12B-C) provide the frequency response of each electrode across a wide range of frequencies. Increasing the contact GSA decreases the electrical impedance magnitude at all frequencies greater than 100 Hz. At KES frequencies evaluated experimentally, the impedance was 505 $\pm$ 153 $\Omega$ for 20 kHz and 457 $\pm$ 122 $\Omega$ for 40 kHz.

### 2.4.2 Charge characteristics of KES waveforms

In addition to contact GSA, minimization of power consumption requires understanding the charge characteristics of typical KES waveforms. Cogan (Cogan, 2008) proposed charge per phase, charge density, and current density as informative metrics for characterizing neural stimulation electrodes and waveforms. We computationally characterized these metrics for a range of KES frequencies at a single amplitude (Figure 4). As the KES frequency increases, the period of the cathodic phase decreases (Figure 4A), resulting in a decreased charge per phase (Figure 4B). If the peak KES amplitude is increased, the absolute value of the charge per phase curve increases, however the exponential decrease as a function of KES frequency will remain. As the contact GSA increases, the magnitude of the current density decreases (Figure 4C).

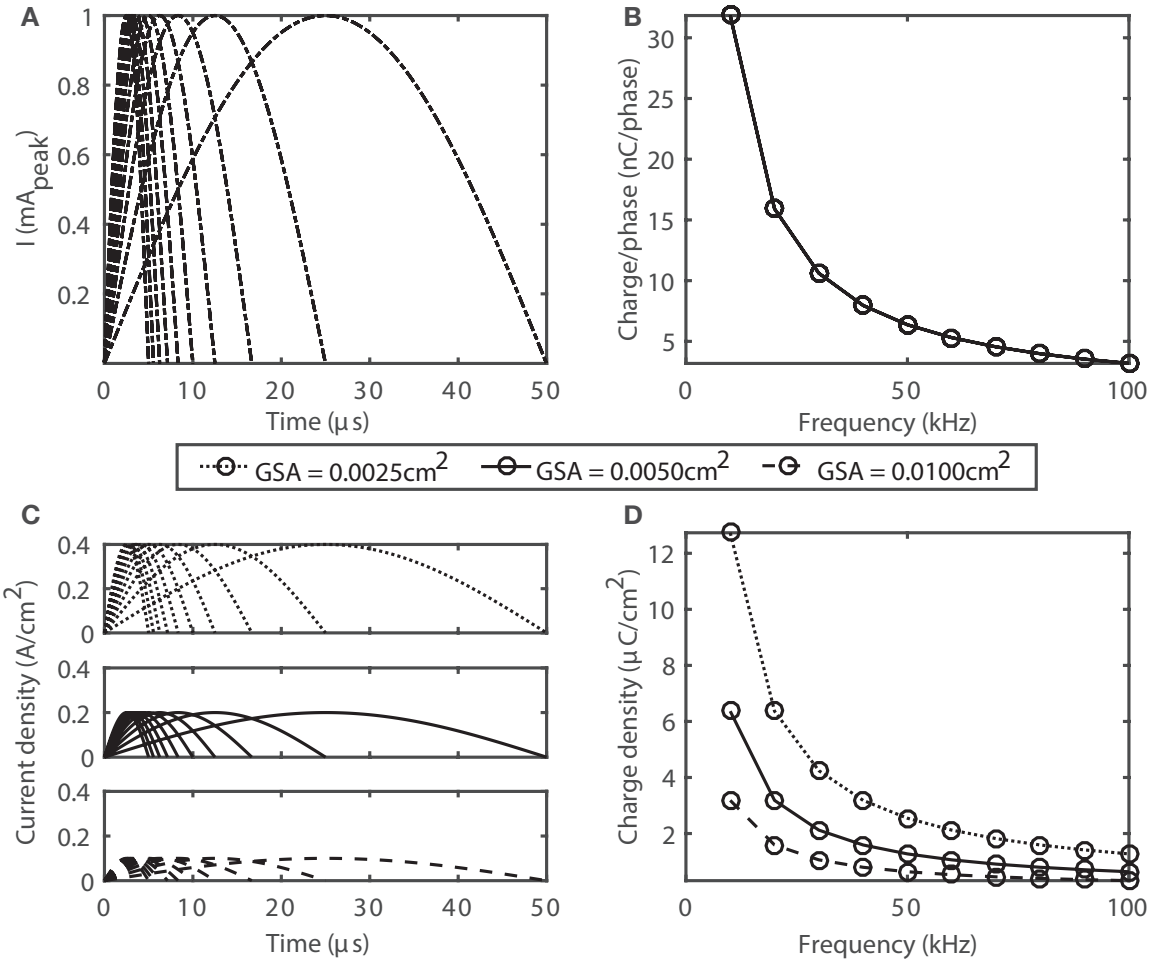


**Figure 4:** Waveform characteristics for a range of KES waveform frequencies (10-100 kHz, 10 kHz steps) with an amplitude of $1\text{mA}_{\text{peak}}$ as a function of contact GSAs. (A) Cathodic phase of each waveform used in computations. The x-axis is the period of a single cathodic cycle at a given KES frequency. (B) Charge per phase decreases exponentially as a function of KES frequency. (C) Current densities decrease as the contact GSA increases. (D) Charge densities decrease exponentially as a function of KES frequency and and linearly decrease with increasing contact GSA.

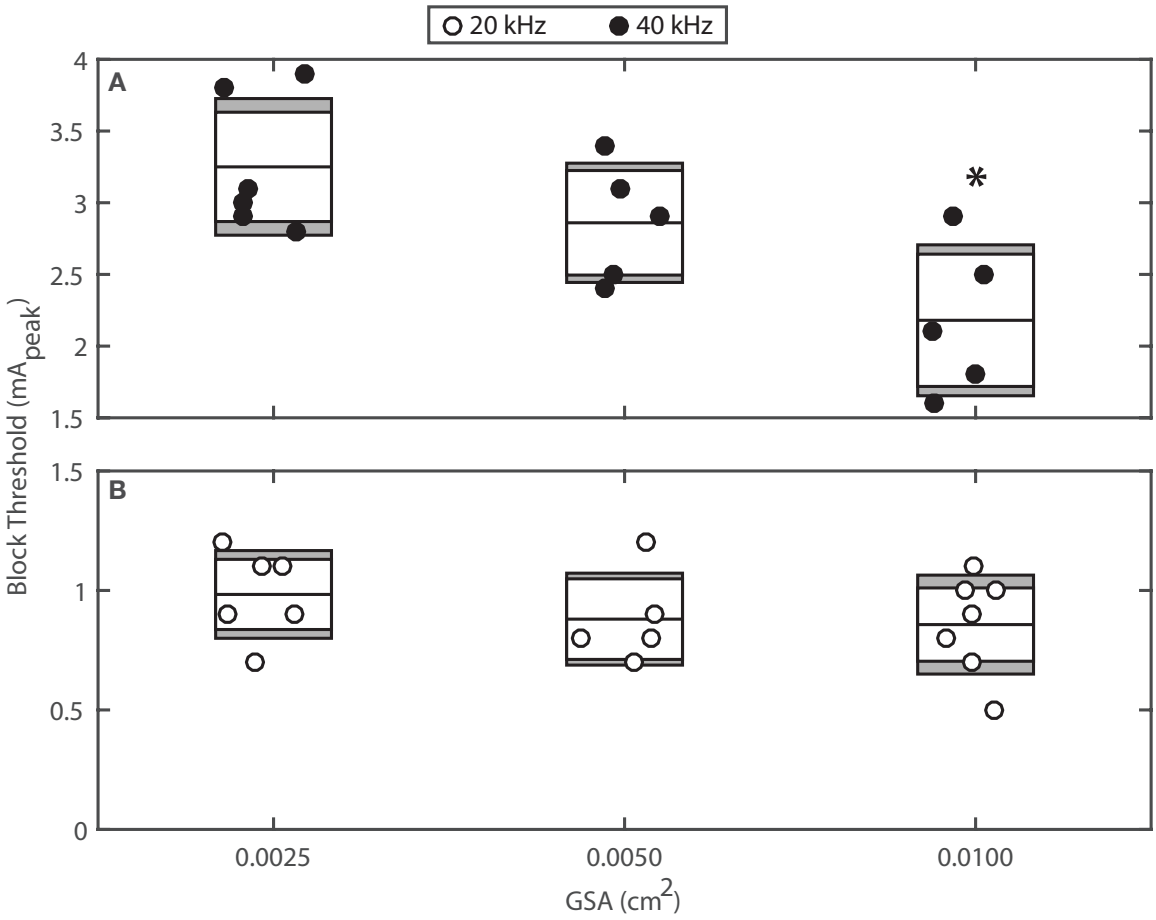


**Figure 5:** KES block thresholds as a function of contact GSA for 20 and 40 kHz KES nerve block. Each circle represents an individual trial at one KES frequency. Each contact GSA group was found to be normally distributed with the equal variances (Bartlett's statistic, $p_{20kHz} = 0.96$, $p_{40kHz} = 0.91$). A one-way analysis of variance revealed no significant difference between the mean 20 kHz block thresholds at all contact GSAs ($p < 0.05$), however did reveal a significant difference between the mean 40 kHz block thresholds for 0.0025 cm$^2$ and 0.0100 cm$^2$ contact GSAs ($p^* < 0.05$).

Charge densities (Figure 4D) exponentially decrease as a function of KES frequency, and decrease linearly as a function of contact GSA.

### *2.4.3 Increased GSA reduces KES block thresholds and power consumption*

Block thresholds are the primary metric reported by most KES nerve block studies. KES nerve block thresholds reported in this report (Figure 26) demonstrate an inverse relationship with contact GSA; block thresholds decrease as contact GSA increases. Decreases in mean block threshold were not significant with 20 kHz KES waveforms, in contrast to the significant decreases seen with 40 kHz KES waveforms (Figure 26). Average power consumption also decreased linearly as a function of contact GSA for both 20 kHz ($R^2 = 0.81$) and 40 kHz ($R^2 = 0.98$) KES waveforms.

### *2.4.4 Increased GSA does not alter post-KES nerve block characteristics*

In addition to power consumption, the clinical utility of KES nerve block may be affected by the onset response, changes in normal nerve conduction, as well as recovery of normal conduction after KES is turned off. The onset response durations (Figure 15) were quantified as a function of KES frequency and contact GSA. No consistent difference was observed in onset duration as a function of contact GSA. Changes in EMG activation (Figure 8) were used as a proxy to assess nerve conduction latencies pre- and post-KES nerve block. Although mean post-KES nerve block EMGs are reduced for all groups, significant variability exists, leading to no consistently identifiable change in EMG activation as a function of KES frequency or contact GSA. Nerve conduction latencies increased after delivery of KES nerve block but no consistent and reproducible change was observed. Mean post-KES latencies increase and

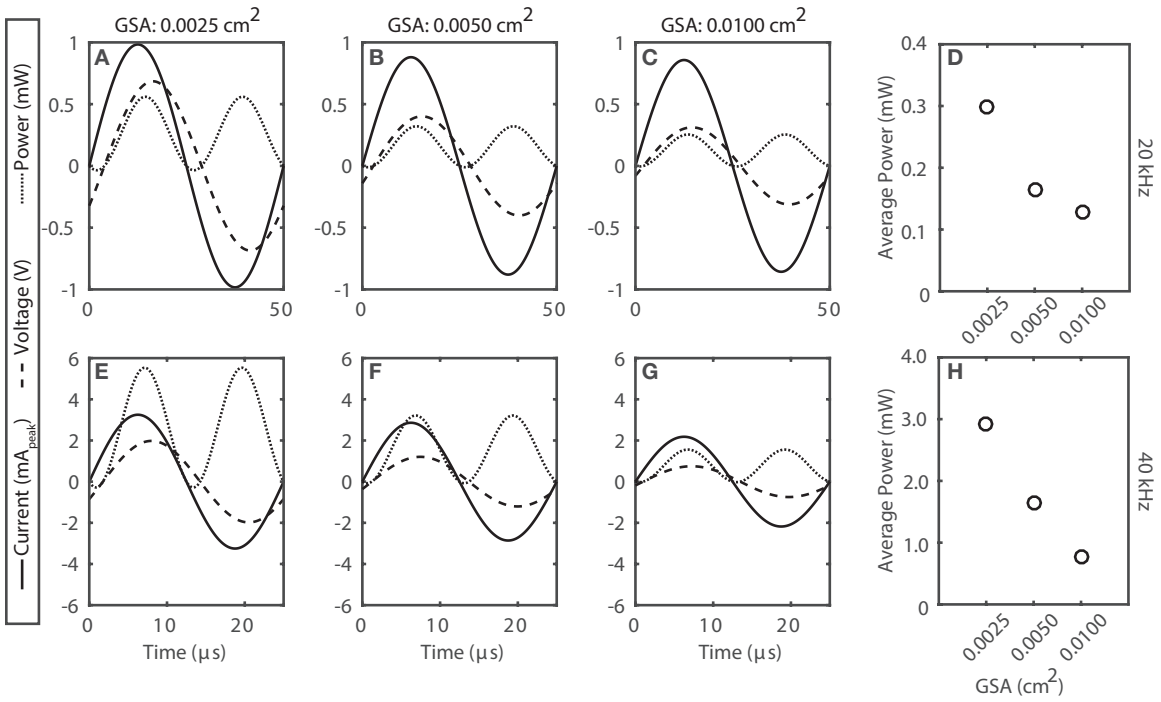


**Figure 6:** Increasing contact GSA reduces the power required for effective KES nerve block. The current ($mA_{peak}$, solid), voltage (V, dashed), and power (mW, dotted) are shown for each contact GSA. Voltage and power values are derived using the mean block thresholds and EIS measurements. The power is computed for each contact GSA at 20 kHz (D) and 40 kHz (H) for an application duration of 60 seconds. In both 20 and 40 kHz cases, the power required to achieve an effective KES nerve block decreases with increasing contact GSA.

demonstrate a wider distribution post-KES. There is no dependence upon contact GSA or KES frequency, however. Normalized EMG pre- and post-KES nerve block were used to quantify changes in the quality of recovered nerve activity after 60 seconds of complete and effective block (Figure 10). Finally, increasing contact GSAs decreased recovery times for 20 kHz KES trials. This effect, however, is not observed for 40 kHz KES trials.

## *2.5 Discussion*

Interest and clinical availability of bioelectronic medicines have significantly grown in the past decade mostly due to the initiatives started by for-profit and non-profit entities. At the root of many of these initiatives is the ability to interface with the nervous system - in particular with the peripheral nervous system with the goal of monitoring and treating a variety of clinical conditions. KES nerve block offers a promising new approach for bioelectronic medicines - providing both temporal and spatial control of peripheral nerve activity. A significant number of questions remain to be answered to ensure safe and effective implementation of KES nerve block in clinical therapies - including but not limited to the optimal electrode specifications and power requirements which are the focus of the present study.

In the present study, preparations of the anesthetized rat tibial nerve were used to evaluate the effects of increasing GSA on KES nerve block thresholds. Increasing GSA was achieved by increasing the length of the electrode contacts while the width was fixed. The effect of three different contact lengths (Table 4) on KES nerve block thresholds were evaluated with KES frequencies of 20 and 40 kHz. Electrode charge characteristics were computationally characterized as a function of increasing GSA and KES frequency (Figure 4). Finally, electrodes of different GSAs were electrochemically characterized (Figure 12) and paired with experimentally-derived KES

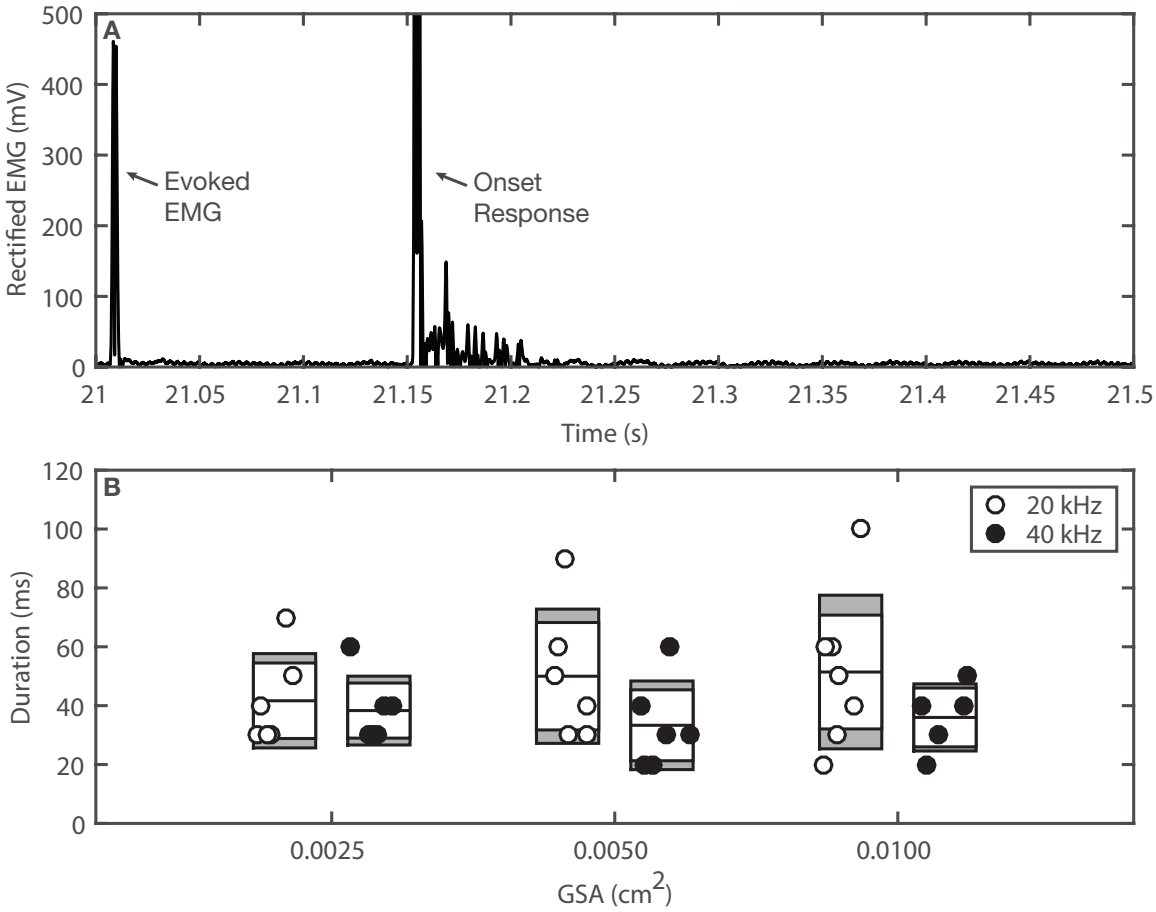


**Figure 7:** Rectified EMG onset artifact durations. (A) Rectified EMG onset artifacts always followed the 21st evoked-EMG response. The onset artifact consists of a large, high-frequency transient spike in measured EMG activity followed by a brief period of spontaneous activation, followed by complete KES nerve block. (B) The width of the windows rectified EMG onset artifact is used to represent the duration of the onset artifact as a function of contact GSA and KES frequency.

nerve block thresholds to estimate the power consumption of effective KES nerve block (Figure 6). Our results demonstrate that KES nerve block thresholds are inversely related to the electrode contact GSA (Figure 26), and that the magnitude of this inverse relationship increases at higher KES frequencies. As the KES nerve block threshold decreases, the estimated power for effective KES nerve block also decreases (Figure 6D and H). The inverse relationship between contact GSA and block thresholds is likely due to multiple factors - such as lower impedance magnitudes and increased electric field uniformity. Increasing GSA provides for a more power efficient KES nerve block but has no statistically significant and observable effect on the onset artifact duration, recovery, or the nerve conductivity (Figures 15, 8).

One observation of the experimental data presented here (Figures 26, 15, 8) is the wide range of variability in computed metrics. These experiments were performed with acute preparations which typically demonstrate a wide range of variability. This variability is inherently tied to acute experiments due to differences in the electrode-tissue interface resulting in different input-output relationships (Grill et al., 1998). It is speculated that this variability will decrease significantly in chronic experimental evaluation. For example, the KES block thresholds (Figure 26), although well within the published range of block thresholds at each KES frequency, might present a significantly tighter variance on a per-nerve basis once the electrode is encapsulated by fibrous tissue. It is also possible that the low levels of direct current contamination measured in our experiments contributed to the observed variability. For example, the reduction in post-KES EMG activity may be due to localized damage to axonal structures and requires histological examination. Previous investigations have been reported on the use of blocking capacitors and/or inductors to minimize direct current contamination of KES waveforms (Franke et al., 2014b). We did not employ these methods but did characterize the contamination. Our experience with blocking capacitors suggests that direct current contamination is reduced during delivery of

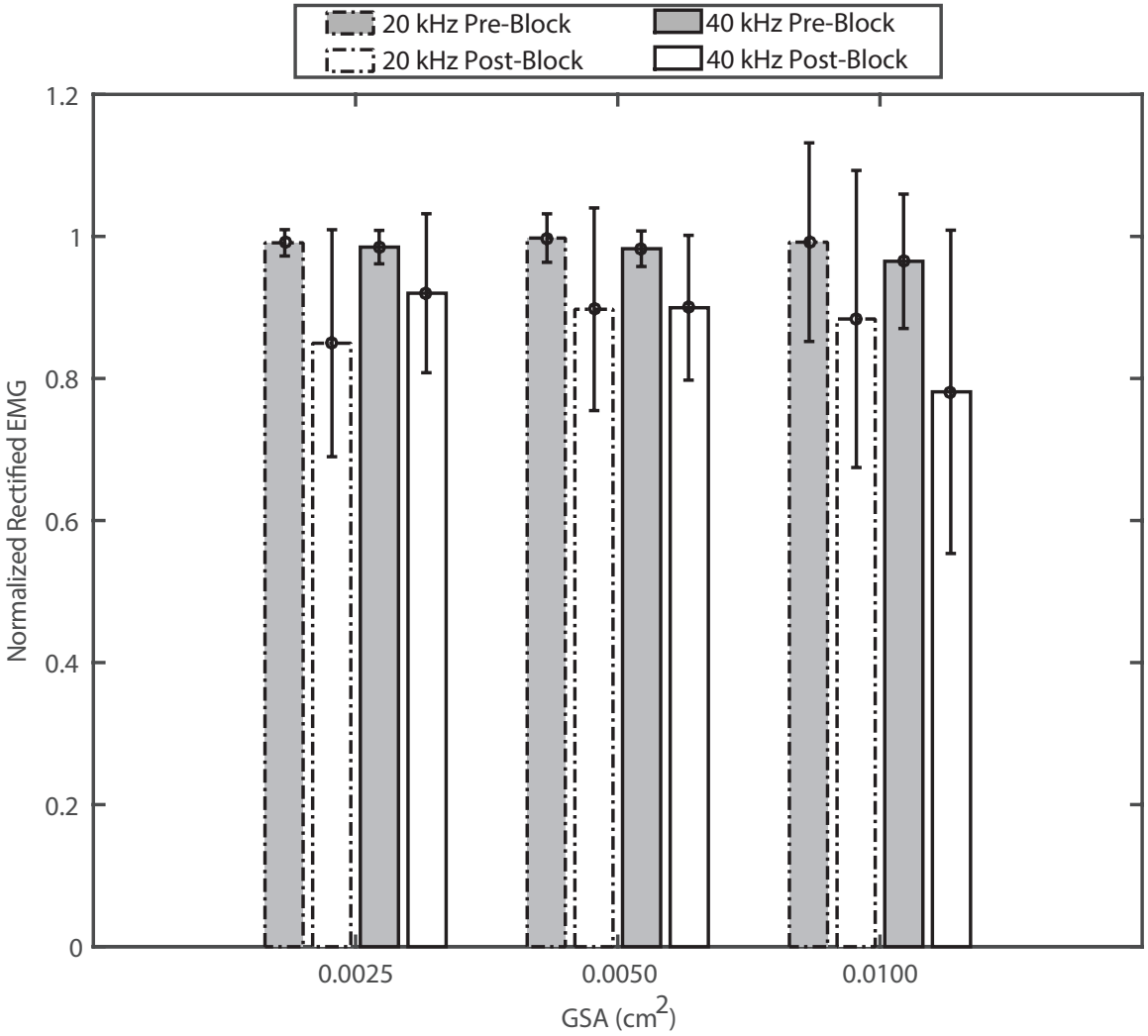


**Figure 8:** Normalized rectified EMG before and after delivery of KES nerve block. Gray and white bars represent pre- and post-KES nerve block EMG values. Dashed and solid line boxes represent trials using 20 kHz and 40 kHz, respectively. One-way analysis of variance demonstrated no significant difference in pre- and post-block EMG as a function of contact GSAs.

KES. However, the capacitors discharge through the neural tissue when KES delivery is turned off, significantly damaging the underlying neural tissues. Large inductors (>5 H) provide one solution to the discharging of blocking capacitors and direct current contamination (Franke et al., 2014b), but are clinically impractical.

Although not assessing contact GSA, other investigations have characterized the effects of electrode geometry, specifically spacing between electrode contacts on the KES nerve block threshold as well as the onset artifact. (Ackermann et al., 2009) investigated the effect of inter-pole distance on both KES nerve block thresholds and the onset response with results suggesting that 1 mm between poles is optimal. A number of follow-up investigations by the same group were carried out to reduce the onset response which can last up to 10 s after initiation of KES nerve block (Ackermann et al., 2010b; Ackermann et al., 2011a). However this onset artifact duration is in contrast to our findings which demonstrate (Figure 15) that the onset response never exceeded 120 ms (Patel et al., 2015). The longer duration onset artifacts published by others using the sciatic-gastrocnemius muscle complex preparation are likely a combination of both the neural onset (milliseconds) and physiological onset (seconds). In this case, the physiological onset is the passive relaxation properties of muscle fibers. The concept of neural vs physiological onset artifacts is an important factor that should be considered when evaluating the onset response in different neural circuits.

In addition to the short duration onset response, our experimental results demonstrate that recovery after 60 seconds of KES nerve block is nearly instantaneous with significant variability in terms of the magnitude of the recovered EMG response (Figure 8). The variability could be due to the extremely low levels of direct current measured in our experiments, however we stimulated the nerve distal to the KES nerve block cuff electrode to validate that KES block was local to the site of the block cuff electrode and not neuromuscular fatigue or depletion block (Kilgore et al., 2014). In all our trials, recovery of EMG activity was instantaneous with proxi-

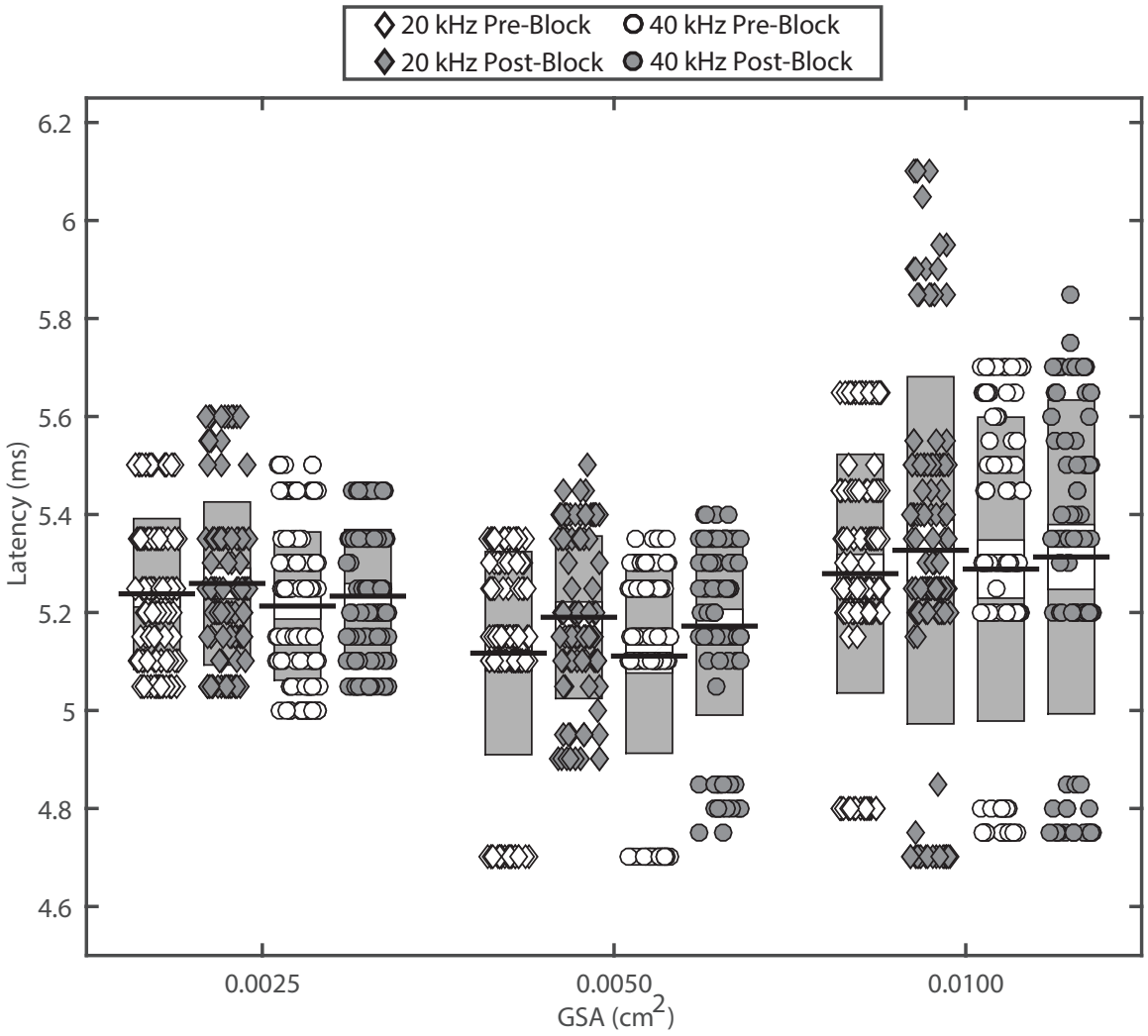


**Figure 9:** Evoked EMG latency values as a function of contact GSA and KES frequency. Each diamond/circle represents an individual stimulation-evoked EMG event. Center black bars representing group means have been extended for visualization purposes. The mean post-KES latencies are higher than mean pre-KES latencies for each pre- and post- pair, however no statistically significant difference could be determined.

mal stimulation evoked EMG measured within less than one second of turning off KES nerve block. Analysis of post-KES block EMG activity suggests that evoked EMG (resulting from nerve conduction recovery) returns to 90% of pre-KES EMG magnitude within an average of 10 seconds (Figure 10). These post-KES recovery characteristics are similar to previous reports (Liu et al., 2013), but in conflict with others (Yang et al., 2016). In the latter investigation, complete KES nerve block was observed up to 10 seconds after turning off KES. Although the study states the use of an electrode to stimulate the nerve distal to the block site, complete trials are not shown and twitches in response to distal stimulation are absent from force transducer measurements (Yang et al., 2016 Figures 2-4), suggesting that the results maybe an artifact of neuromuscular depletion or fatigue block, rather than a true conduction block localized to the KES electrode.

The results presented here demonstrate the ability of optimized electrode GSA to minimize the power consumption of KES nerve block. This data is based upon the tibial nerve, which is a mixed nerve containing both motor (4358 $\pm$ 513 axons, 2.0 - 12.0 $\mu$m diameter) and sensory (9077 $\pm$ 1600 axons, 0.5 - 1.0 $\mu$m diameter) (Schmalbruch, 1986). Efficacy of KES nerve block was assessed through measurements of supramaximal evoked EMG activity from the gastrocnemius muscle.

EMG activity can contain two identifiable waves - the M-wave and H-wave, which represent motor and sensor activity, respectively. Initial experiments attempted to measure both M- and H-wave activity to allow for assessment of both large (motor) and small (sensory) diameter axons. Unfortunately, a trade-off exists between using supramaximal stimulation to evoke maximal EMG and activation of a measurable H-reflex. With increasing stimulation intensities the M-wave increases, but the H-reflex amplitude decreases due to increased antidromic collisions (Aagaard et al., 2002).

For the purposes of this study, we opted for supramaximal activation of EMG activity (M-wave) to enable a thorough characterization of true, effective KES nerve

block thresholds as a function of contact GSA and the corresponding power consumption. However, it is important to note that KES nerve block of small diameter fibers has been shown with high amplitudes (at KES frequencies <30 kHz) and with lower KES amplitudes (at KES frequencies >30 kHz) (Joseph et al., 2011; Patel et al., 2015). In cases where KES nerve block of small diameter axons is desired, such as the cervical vagus (Patel et al., 2017b), optimization of contact GSA may provide significant reductions in power consumption.

Reduced power consumption of KES nerve block can significantly impact the design of clinical devices focused on effective KES nerve block. The data presented here demonstrate >2x reduction in power consumption when contact GSA is optimized and used with 20 kHz KES nerve block. Similarly, when contact GSAs are optimized for the nerve of interest, the power reductions are >3x for 40 kHz KES. In both cases the lifetime of an implanted device can be extended.

The mechanism of action of KES nerve block is unknown, with only computationally-derived hypotheses in the published literature. One computationally-derived hypothesis is that KES nerve block is achieved via inactivation of sodium channels by membrane depolarization (Kilgore et al., 2004; Bhadra et al., 2007; Williamson et al., 2005). In contrast, another computationally-derived hypothesis is that KES leads to elevated levels of potassium channel activation (Zhang, X, Tai, 2006; Tai et al., 2005; Liu et al., 2009). Neither of the hypothesized mechanisms have been experimentally investigated, primarily due to the difficulty associated with measurement of membrane characteristics under KES stimuli. The results from this investigation do not speak directly to the existing hypothesized mechanisms of KES nerve block, but do shed new light on appropriate computational approaches. For example, nearly all computational studies into the mechanism of KES nerve block have utilized single axon models with monopolar point sources for delivery of KES. This geometric configuration ignores the interactions between axonal elements, the electrode-tissue

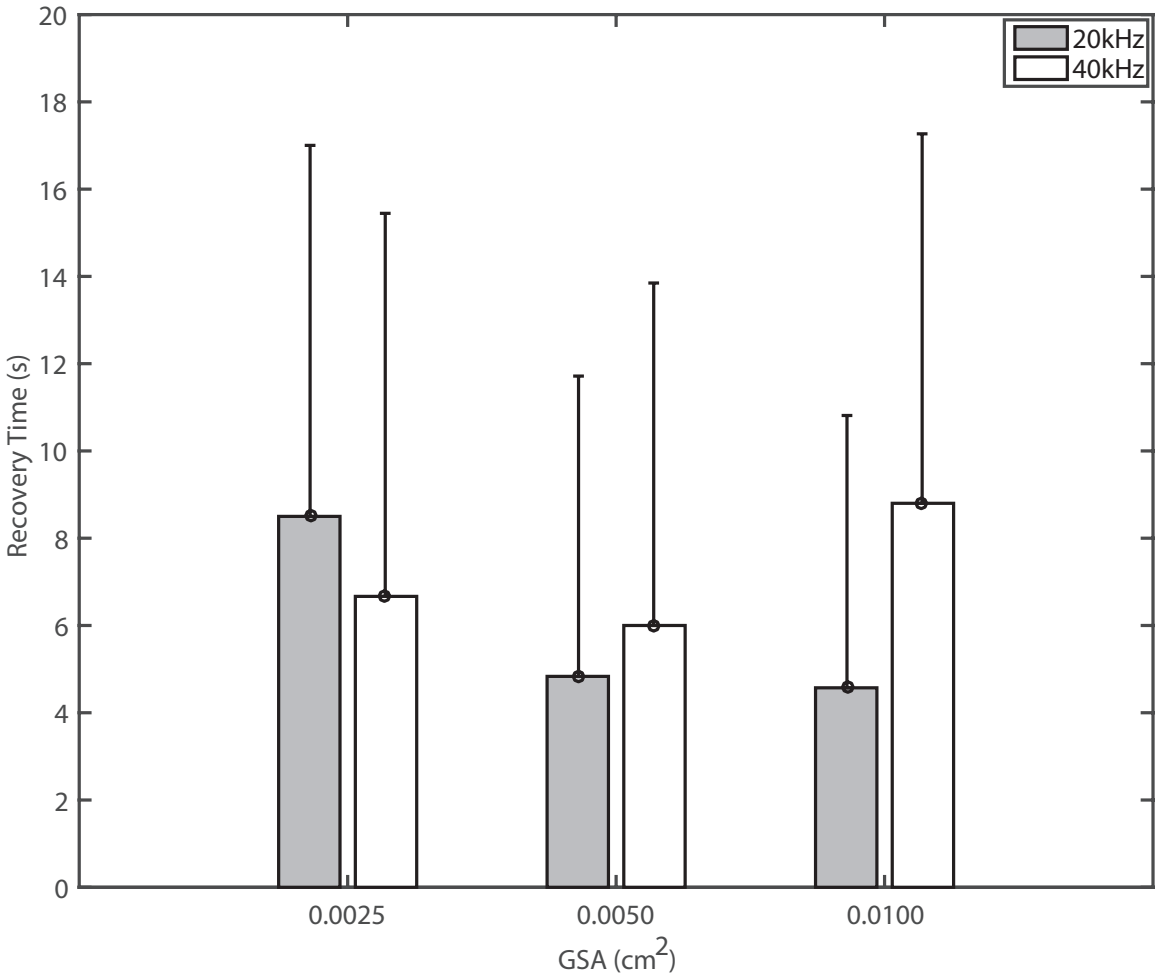


**Figure 10:** Post-KES recovery time of EMG activity. Gray and white boxes represent the duration between the end of KES block delivery and recovery of EMG activity to 90% of pre-KES block values. Mean recovery times decrease as a function of contact GSA for 20 kHz KES, however the standard deviation is large and the same behavior is not observed with 40 kHz trials. One-way analysis of variance demonstrated no significant difference in recovery times as a function of contact GSAs.

interface, and KES waveforms. The results from the present study suggest that geometry of the electrode plays a critical role in effective KES nerve block, and warrant the need for computational studies that include the appropriate scales, elements, and physics involved in achieving effective KES nerve block, as exemplified by recent investigations (Pelot et al., 2015; Howell et al., 2015; Martinek et al., 2008).

While the effects of electrode geometry have received some attention, other topics related to electrodes used for KES nerve block have not. The contacts used in this investigation were made of Pt/Ir, which has received significant attention by the neural stimulation community (Cogan et al., 2005; Brunton et al., 2015). Pt/Ir utilizes both faradaic (oxidation-reduction reactions) and capacitive (electrode-electrolyte double layer charging) mechanisms to inject charge into the target neural tissues, the contribution of each mechanism depending upon the current density and the pulse width. One question of significant interest is whether or not the use of materials with different charge injection mechanisms has an effect on KES nerve block thresholds and power consumption. For example, materials such as Titanium Nitride (TiN), which delivers charge through capacitive mechanisms (Meijs et al., 2015), has a high charge injection capacity, and reduced electrode polarization, may further reduce the power requirements of KES nerve block.

## *2.6 Conclusion*

KES nerve conduction block is a powerful technique capable of providing fast, effective, and robust block of nerve activity. The results presented in this manuscript demonstrates one approach for reducing the power consumption of KES nerve conduction block. A small but growing number of clinical products which utilize KES exist, such as Enteromedics VBLOC (Camilleri et al., 2008), Neuros Altius (Neuros Medical, Inc., Cleveland, OH, USA), and Nevro HF10 (Kapural et al., 2015). It is

unclear if any of these clinical products produce a true nerve conduction block via KES or if conduction block is the intended physiological response. These existing devices may be able to extend device battery life, however, and reduce or simplify recharging strategies by ensuring optimal contact GSAs and choice of KES frequency for the targets of interest.

# CHAPTER III

# EFFECTS OF ELECTRODE MATERIAL

## *3.1 Motivation*

Kilohertz electrical stimulation (KES) has enabled a novel new paradigm for spinal cord and peripheral nerve stimulation to treat a variety of neurological diseases. KES can excite or inhibit nerve activity and is used in many clinical devices today. However, the impact of different electrode materials on the efficacy of KES is unknown. We investigated the effect of different electrode materials and their respective charge injection mechanisms on KES nerve block thresholds using 20 and 40 kHz current-controlled sinusoidal KES waveforms. We evaluated the nerve block threshold and the power requirements for achieving an effective KES nerve block. In addition, we evaluated potential effects on the onset duration and recovery of normal conduction after delivery of KES. We found that thresholds and the onset and recovery of KES nerve block are not a function of the electrode material. In contrast, the power dissipation varies among electrode materials and are a function of the materials' properties at high frequencies. We conclude that materials with a proven track record of chronic stability, both for the tissue and electrode, are suitable for developing KES nerve block therapies.

Financial support for this work was provided by the National Institutes of Health (Grant 2R01EB016407-09A1).

## *3.2 Background*

Kilohertz electrical stimulation (KES) has garnered significant interest in the past decade for treatment of neurological disorders. KES spinal cord stimulation has been shown to treat chronic pain without significant paresthesia (Nevro Corp., Redwood City, CA, (Kapural et al., 2015; Bicket et al., 2016), while KES nerve stimulation has been demonstrated to reduce post-amputee pain (Neuros Medical Inc., Cleveland, OH, (Soin et al., 2015) and impact weight loss in obese patients (Enteromedics Inc., St. Paul, MN, (Camilleri et al., 2008). Outside the clinical, KES has been shown to induce repeatable and reversible conduction block of nerve activity (Patel et al., 2015; Patel et al., 2017b).

The ability to block nerve activity using KES has been demonstrated in a wide range of somatic and autonomic nerves using both mammalian (Patel et al., 2015; Patel et al., 2017b; Bhadra et al., 2005) and non-mammalian (Joseph et al., 2009; Joseph et al., 2011) animal models. The ability to achieve a safe, effective, and reversible block of nerve conduction is impacted by the electrode used to interface with the target tissue. Published results to date have highlighted the role of inter-pole distance (Ackermann et al., 2010b) and electrode contact geometry (Patel et al., 2017a), however we are unaware of any previous report (Table 3) investigating the effect of electrode material on KES outcomes. The goal of this investigation is to understand the impact of different electrode materials with different charge injection mechanisms on KES nerve block.

Two primary charge transfer mechanisms exist at the electrode/electrolyte interface - Faradaic and non-Faradaic. Faradaic charge transfer takes place by directly transferring electrons from the electrode to the electrolyte and reducing (electron transfer from electrode to electrolyte tissue) or oxidizing (electron transfer from electrolyte to electrode) chemical species in the electrolyte. Reversibility (or irreversibil-

ity) of the electrochemical reactions is dependent upon the electrode material, waveforms, and current densities and can be detrimental to the tissue, electrode, or both. In contrast, non-Faradaic reactions redistribute the charged electrochemical species present within the electrolyte, with no direct electron transfer into the electrolyte. Non-Faradaic reactions provide an entirely reversible charge transfer process with minimal to no tissue damage or electrode dissolution (Merrill et al., 2005).

Faradaic and non-Faradaic charge transfer mechanisms are often described as charge storing and charge dissipating mechanisms, respectively. These characteristics enable description of both charge transfer mechanisms with electrical circuit models represented by a parallel capacitance (non-Faradaic reactions) and resistance (Faradaic reactions). From this simple model, it can be understood that faradaic reactions mediate charge transfer with low frequencies, while non-Faradaic dominate at high frequencies. However both Faradaic and non-Faradaic mechanisms can be present when high stimulation currents are used, as is the case with KES nerve block. In addition, all real-world KES waveforms contain some level of direct current contamination, which may lead to an increase in Faradaic reactions.

We have recently studied the effect of electrode geometry on KES nerve block. The focus of the present study is to experimentally evaluate the effect of different electrode materials with different charge injection mechanisms on KES nerve block power requirements. Other goals of this study are to evaluate the effects of different materials on the onset artifact duration, nerve conduction, and recovery post-KES nerve block. The electrode materials investigated in this study include Stainless Steel (SS), Platinum (Pt), 90/10 Platinum-Iridium (Pt-Ir), and Titanium Nitride (TiN), enabling evaluation of materials using Faradaic (SS), non-Faradaic (TiN), and combined Faradaic/non-Faradaic (Pt, PtIr) charge injection mechanisms.

## 3.3 Experimental Methods

### 3.3.1 Animal Preparation

All animal research was approved by the Georgia Institute of Technology Institutional Animal Care and Use Committee. Experiments were conducted on tibial nerves from *in vivo* urethane-anesthetized male rats (384 ± 51g, n = 12). Animals were briefly anesthetized using isoflurane in oxygen (5%, 1 liter/min flow rate) prior to delivery of urethane (IP, 1.2 g/kg in 0.9% saline). Anesthetic depth was evaluated 60 - 90 minutes post-injection by pinching the rear footpad and supplemental urethane (0.12 mg/ml) was delivered as necessary until the reflex withdrawal was eliminated. After reaching surgical depth, the animal's back was shaved from the lumbar section down to the distal end of the gastrocnemius muscle. The animal's foot was magnetically clamped to the surgical table to minimize motion during experimental trial. An incision approximately 1 - 1.5 cm in length was made along the length of the biceps femoris muscle and the sciatic nerve exposed via blunt dissection. The tibial branch of the sciatic nerve was identified and isolated from the sciatic notch down to the gastrocnemius muscle under a high magnification dissection scope. The common peroneal, sural, and collateral branches of the sciatic were cut to minimize off-target stimulation. Normal rat ringer's solution (*Normal Rat Ringer's Solution*) was applied throughout the experiment to prevent muscle and nerve tissue dehydration. The animal's body temperature was monitored and maintained at 37 - 40 °C with a rectal temperature probe (Model BAT-12, Physitemp Instruments, Clifton, NJ) and warming pad (COM-11289, SparkFun Electronics, Niwot, CO). Preparations lasted 5 - 6 hours after which animals were euthanized via an IP injection of pentobarbital-based euthanasia drug (0.5 ml/kg, IP). All experiments were conducted at room temperature.

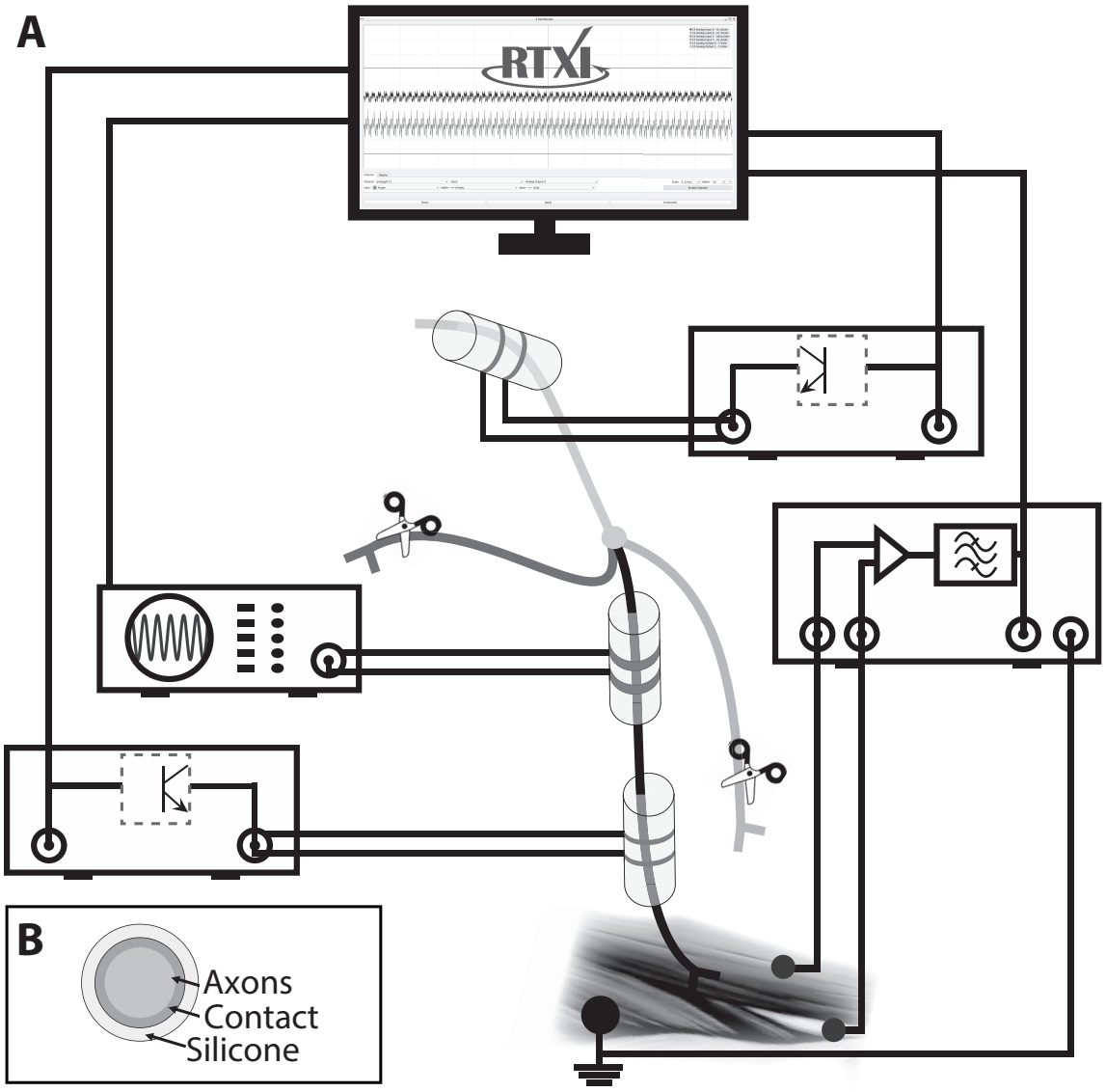


**Figure 11:** Electrophysiology setup and electrode configurations. (A) The nerve was electrically stimulated at the proximal and distal ends using bipolar cuff electrodes. EMG activity was measured from the gastrocnemius muscle using intramuscular fine wire electrodes. (B) Illustration of the circumferential electrode-tissue interface. Timing and duration of stimulation events, along with measurement of activity was achieved with RTXI.

### *3.3.2 Electrophysiology Setup*

The proximal end of the exposed sciatic nerve was stimulated using a bipolar cuff electrode made in-house. Two braided stainless steel wires (#793500, A-M Systems, Sequim, WA) separated by 1 mm were deinsulated and threaded through silicone tubing (#807600, A-M Systems, Sequim, WA). A second bipolar stimulation cuff electrode was placed approximately 0.2 cm distal to the block electrode in all experiments for delivery of distal test stimuli. Distal test stimuli verified that KES nerve block was localized to the site of the block electrode and did not cause neuromuscular fatigue or neurotransmitter depletion.

Spacing between the proximal stimulation and block electrodes was approximately 1 cm in all experiments. EMG activity was differentially measured from the gastrocnemius muscles using bipolar fine wire electrodes (Cooner Wire No. AS631, Chatsworth, CA). EMG measurements were filtered (100 - 300 Hz) and gained (1000x, Brownlee Precision Model 440, San Jose, CA) before being digitized at a rate of 20 kHz using The Real-Time eXperiment Interface (RTXI, `http://www.rtxi.org`) with a PCI-6036E data acquisition card (National Instruments, Austin, TX). A stainless steel wire was inserted into the contralateral gastrocnemius muscle and connected to the surgical air table to electrically ground the animal, with the surgical table grounded to the amplifier (building supply ground). Figure 23A shows the complete experiment setup.

### *3.3.3 Electrode fabrication*

Block of the tibial nerve was achieved using SS, Pt, PtIr (90/10), TiN-Pt, and TiN-PtIr (90/10) contact pads (25.4 $\mu$m thick, ESPI Metals, Ashland, OR). Each material was evaluated in random order in each experiment. The length and width of all contacts was 2.0 mm and 0.5 mm, respectively. Electrode contact geometric surface areas

(GSAs) were calculated to be 0.01 ± 0.0002 $cm^2$. This geometry provided complete circumferential coverage of the tibial nerve (Figure 23B, circumference 2.0 - 2.1 mm (Schmalbruch, 1986), which is critical for minimizing the KES nerve block threshold (Patel et al., 2017a). Contacts were cut and measured under a high resolution microscope with digital calipers (measurement error = 0.01 mm), spot welded to braided (7-strand) stainless steel wire, wrapped around the nerve under a dissection microscope, and insulated using silicone (Kwik-Cast, WPI, Sarasota, FL).

TiN coated electrodes were fabricated by adhering Pt and PtIr contacts to a 4 inch silicon wafer using parafilm tape. Leads were spot-welded to the contacts prior to TiN deposition and insulated with an additional layer of parafilm tape to prevent deposition of TiN onto lead wires. Porous TiN was sputtered (AJA Magnetron Sputter System, Scituate, MA) onto the exposed contact surfaces at a rate of 7.5 nm/min under a base pressure of $10^5$ Torr and Ar and $N_2$ gas flow rates of 180 and 240 sccm, respectively. These parameters provided a 200 nm layer of TiN on Pt and PtIr contacts.

### *3.3.4 Nerve Activation and KES Block*

Constant current pulses (0.3-0.5 $mA_{peak}$, 0.2 ms, 1 Hz) were generated using the RTXI signal generator module for proximal stimulation and an optically isolated constant current stimulator (DS3, Digitimer, Ft. Lauderdale, FL) for distal stimulation. Proximal stimulation pulses were optically-isolated using linear stimulus isolators (A395, WPI, Sarasota, FL). The KES waveform (current-controlled, continuous sinusoid) was generated using a floating current source function generator (Model 6221, Keithley Instruments, Inc, Clevelend, OH). The 2.1 $mA_{peak}$ and 21.0 $mA_{peak}$ ranges were used for the 20 kHz and 40 kHz KES trials, respectively. Direct current contamination of the KES waveform was measured to be 150 - 500 nA. All stimulus isolation units were calibrated prior to each experiment and output offsets zeroed by visualization

on an oscilloscope. Timing control of stimulation equipment was achieved by using digital I/O triggers generated from RTXI.

### *3.3.5 Experimental Protocols*

The first trial was conducted to determine the block threshold with a given electrode and KES frequency (as previously described in (Patel et al., 2015). The sciatic nerve was stimulated at 1 Hz using the proximal stimulation electrode to elicit supramaximal EMG activity in the gastrocnemius muscle. The threshold was found by increasing the amplitude of the KES waveform in 0.1 $mA_{peak}$ increments until complete block was achieved. Complete block was achieved only when the RMS voltage of the EMG measurement was equivalent to that of the measurement noise. The second trial was conducted at the empirically determined block threshold, with approximately 3 - 5 minutes between each trial. In each trial, a total of 100 stimulation pulses were delivered to the nerve (Figure 2A). The initial 21 stimulation pulses were delivered to the nerve to capture pre-KES EMG activity. KES was delivered to the nerve 150 ms after the $21^{st}$ stimulation pulse at either 20 or 40 kHz with the predetermined block threshold. Test pulses were delivered to the nerve while delivery of KES nerve block for continuous assessment of KES nerve block efficacy. The KES waveform was automatically turned off after 60 seconds (60 stimulation pulses) with continued nerve stimulation to measure post-KES EMG activity. Figure 2 provides a pictorial description of the experimental protocol for a single trial with representative data.

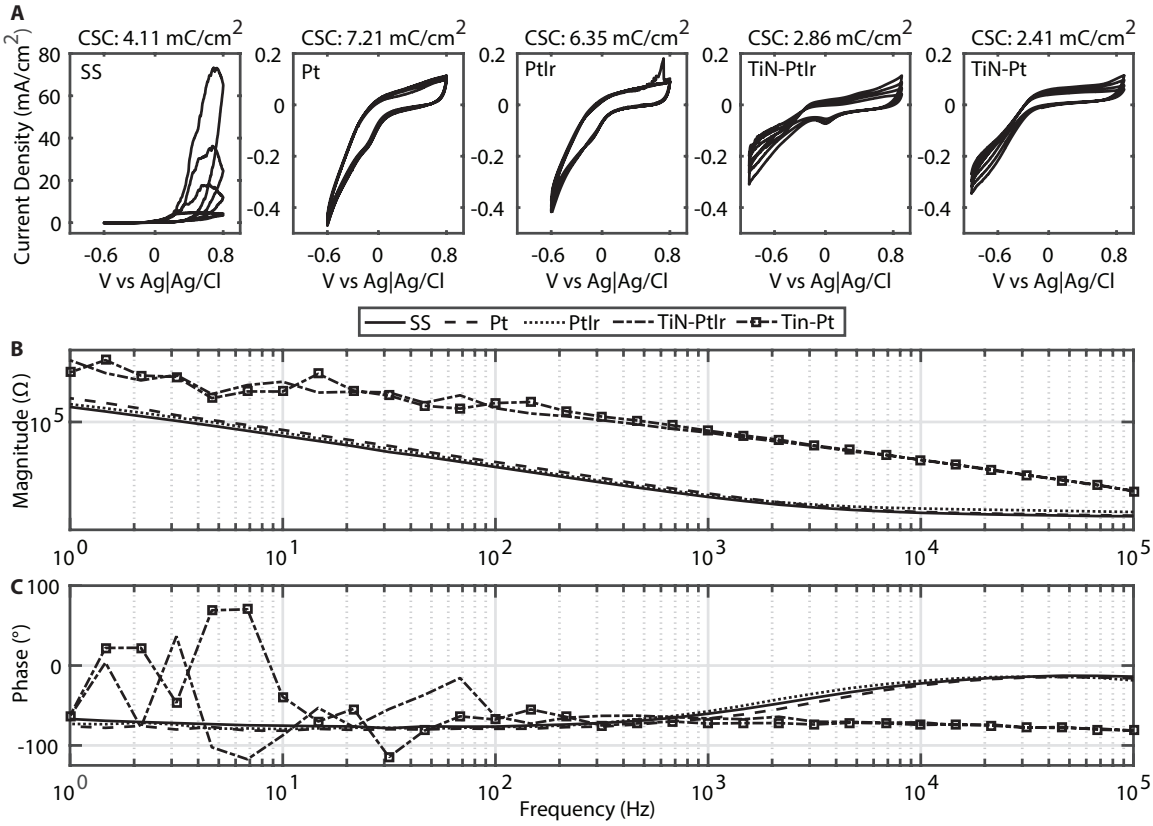


**Figure 12:** Electrochemical characterization of electrodes. (A) Five voltammograms and corresponding cathodic CSC are depicted for each contact material evaluated. Cathodic CSC is average of all five voltammograms per material were averaged to calculate the cathodic CSC. Representative electrochemical impedance magnitude (B) and phase angle (C) are shown for each material.

### *3.3.6 Electrochemical Measurements*

Monopolar cyclic voltammetry (CV) measurements were made for each electrode material to compute the cathodic charge storage capacity (CSC) (Figure 12A). Measurements were made using a three electrode setup with a Ag|AgCl reference electrode and a Pt counter electrode (surface area: 0.02 $cm^2$). A potentiostat (VMP3, Bio-Logic) was used to sweep the potential with a scan rate of 50 mV/sec while simultaneously measuring the current flow between the working (monopolar test electrode) and counter electrodes. The potential was swept between -0.6 V and 0.8 V for SS, Pt, and PtIr electrodes and between -1.0 V and 1.0 V for TiN coated contacts. The negative current time integrals were computed for each voltammogram and averaged to obtain the mean cathodic CSC for each contact material (Cogan, 2008).

Monopolar electrochemical impedance spectroscopy (EIS) measurements were made using the same three electrode setup to quantify frequency-dependent changes at the electrode/electrolyte interface (Figure 12B-C). Measurements were made by sweeping a 10 mV excitation waveform over a frequency range of 1 Hz - $10^5$ kHz. All electrochemical measurements were made in room temperature (25 °C) phosphate buffered saline (PBS, pH = 7.4, Sigma Aldrich, St. Louis, MO) stirred at a constant rate. The measured impedance magnitude and phase at experimentally tested KES frequencies were used for power computations. All measurements were made prior to use of electrodes in experiments.

### *3.3.7 Power Calculations*

We used EIS magnitude, phase, and mean KES block thresholds (Figure 26) to approximate the power required to achieve effective KES nerve conduction block with each contact material (Figure 26B-C). The mean KES block threshold ($mA_{peak}$) for each contact GSA was used to generate a single cycle of a 20 and 40 kHz KES cur-

rent waveform (Equation 1). The EIS magnitude and phase for 20 and 40 kHz were obtained by interpolating between the EIS measurements. The magnitude was used to generate an equivalent voltage waveform (Equation 7). The phase and generated voltage and current waveforms were then used to calculate the power (Equation 6).

$$V_{RMS} = I_{RMS} * |Z(Material, KES)| \tag{7}$$

### *3.3.8 Data Analysis*

All data were analyzed with MATLAB. EMG recordings were detrended and windowed (10 ms bins) to capture evoked EMG activity. The stimulus trigger was used to define the EMG window's left edge. An additional 10 ms window was used to capture baseline noise prior to stimulus delivery. The windowed data was full-wave rectified and the root mean square (RMS) voltage used as a metric for evaluating nerve and muscle activation as well as KES nerve block. The noise RMS voltage was subtracted from the EMG RMS voltage to reduce variance introduced by noise and differences in electrical coupling between experimental setups. Onset artifacts were identified by comparing the RMS voltage of a moving 10 ms window to pre-KES RMS noise values. All box plots show the population mean (center black bar), 95% confidence interval (white region), and one standard deviation (gray region).

## *3.4 Results*

### *3.4.1 Electrochemical characteristics of electrodes*

Electrochemical characterization of electrodes provides valuable information about the electrode stability and the response of electrodes to different stimulation wave-

forms. We performed CV measurements to quantify the cathodic CSC and EIS measurements to evaluate the frequency response and electrochemical reactions for each material. Figure 12A shows the cyclic voltammograms for each material evaluated.

With the exception of SS, all other electrode materials depict both Faradaic and non-Faradaic reactions as the potential is swept, with a greater Faradaic response by the Pt and PtIr electrodes and a greater non-Faradaic response displayed by the TiN electrodes. The voltammogram for SS depicts the presence of a developing oxide layer on the electrode surface and early stages of pitting, suggesting the onset of metal corrosion. In addition, SS presents increased water oxidation as observed by the significantly increased positive current.

The electrochemical spectra for all electrode materials are displayed in Figure 12B-C with mean and standard deviation values at relevant KES frequencies shown in Table 5. The access (or tissue) impedance for each material was taken at 100 kHz. The impedance magnitude decreases across the frequency spectrum for all materials. Interestingly, although the electrochemical surface area of TiN coated electrodes is greater, the impedance magnitude is significantly higher than planar, non-coated electrodes (discussed later). The decreased phase shift in the phase spectra of SS, Pt, and PtIr suggests that at high frequencies (>1 kHz), the solution (tissue) access resistance dominates. The nearly stationary phase shift observed for TiN coated electrodes suggests the presence of a double-layer and thus non-Faradaic charge injection mechanisms throughout the entire spectrum.

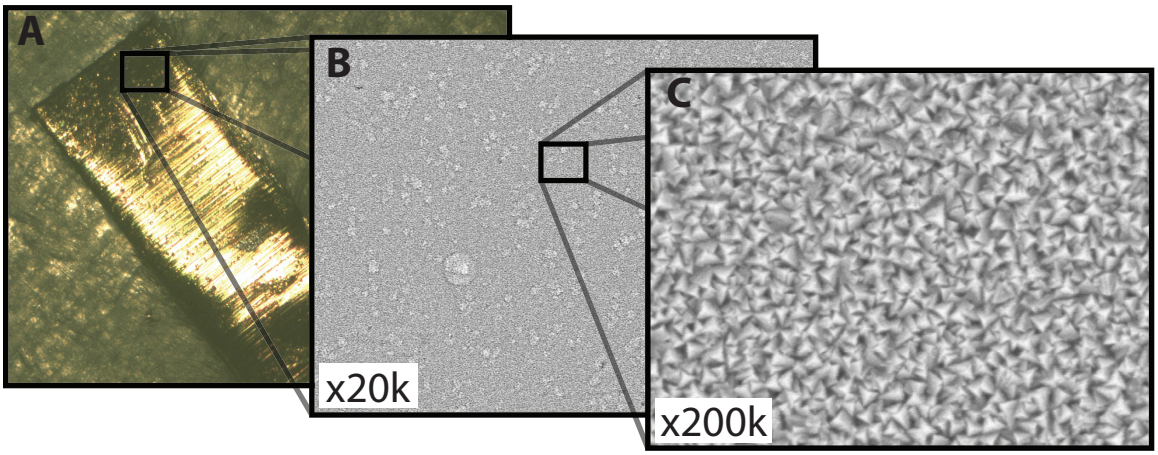


**Figure 13:** Surface composition of TiN coated electrodes prior to use. (A) Light microscope image of TiN-PtIr electrode. Scanning electron microscope images (B: x20k, C: x200k) of TiN-PtIr electrode surface. Increased electrochemical surface area of TiN coating is visible.

**Table 5:** Electrode impedance characteristics.

| Material | 20 kHz | 40 kHz | Access (100 kHz) |
|---|---|---|---|
| SS (Ω) | 267.5 ± 89.4 | 249.8 ± 53.1 | 238.3 ± 78.6 |
| Pt (Ω) | 282.7 ± 92.4 | 262.0 ± 72.4 | 248.2 ± 36.6 |
| PtIr (Ω) | 405.3 ± 62.6 | 375.6 ± 53.9 | 349.7 ± 52.1 |
| TiN-PtIr (Ω) | 4755.1 ± 432.5 | 2381.8 ± 395.6 | 1184.2 ± 119.5 |
| TiN-Pt (Ω) | 4236.6 ± 714.1 | 2259.1 ± 463.7 | 1120.9 ± 108.3 |

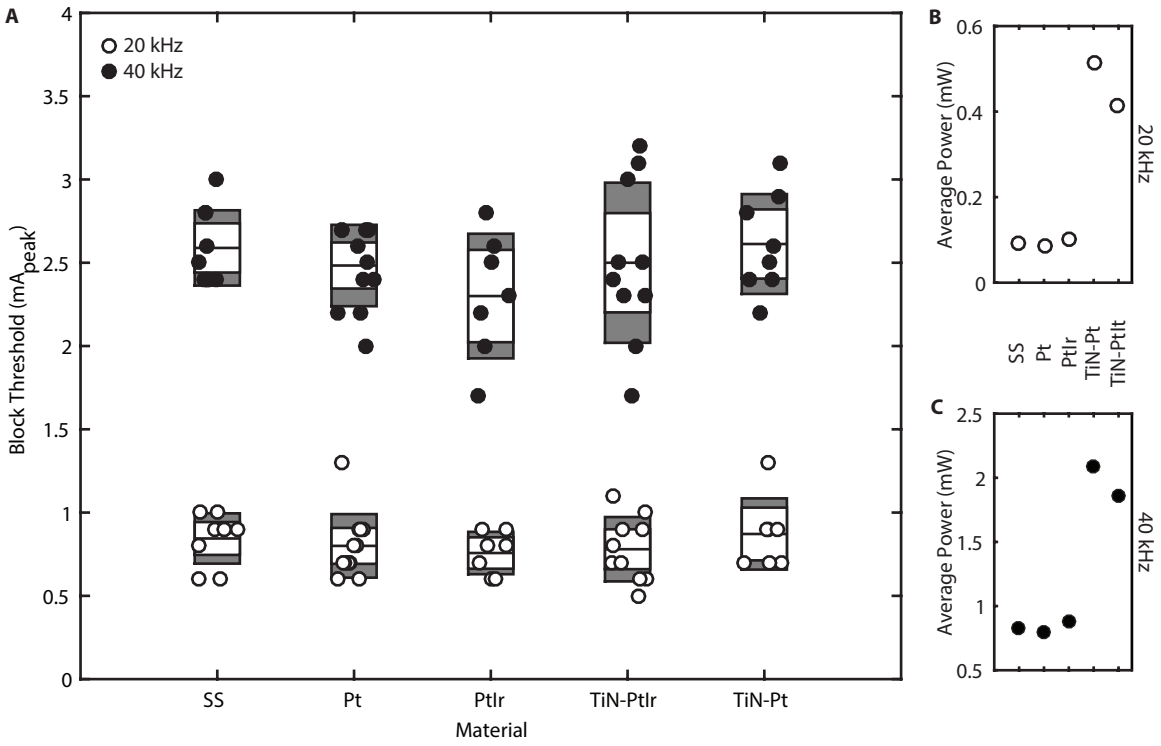


**Figure 14:** (A) KES block thresholds as a function of electrode contact material for 20 and 40 kHz KES nerve block. Each dot represents an individual trial. No statistically significant difference was observed between block thresholds with a given material at either 20 kHz or 40 kHz (Tukey-Kramer multiple comparison test, $\alpha = 0.05$). (B-C) Average power for each contact material computed at 20 kHz (B) and 40 kHz (C).

### *3.4.2 Electrode material does not impact KES nerve block thresholds*

KES nerve block thresholds (Figure 26) demonstrate no statistically significant dependence upon the electrode contact material at either frequency. In contrast, the average power consumption for TiN coated electrodes is higher with respect to non-coated electrodes, primarily due to the increased impedance magnitudes displayed in the EIS measurements (Figure 12B).

### *3.4.3 Electrode material does not alter post-KES nerve block characteristics*

The clinical utility of KES nerve block may be affected by the onset response, changes in normal nerve conduction, as well as recovery of normal conduction after KES is turned off. The onset response durations (Figure 15) were quantified as a function of KES frequency and contact material. No statistically significant difference was observed for the onset duration as a function of electrode contact material. Quantification of pre- and post-KES evoked EMG latencies (not shown) demonstrate no difference in nerve conduction from application of 60 s of KES.

## *3.5 Discussion*

KES nerve block holds great promise as a new approach for modulating the nervous system through peripheral and autonomic nerves. Successful translation of KES nerve block therapies requires investigation of a variety of unanswered questions. The present study evaluated the effect of different electrode materials, and thus different charge injection mechanisms, on KES nerve block characteristics. Electrochemical studies were conducted to understand the charge injection mechanisms and electrical

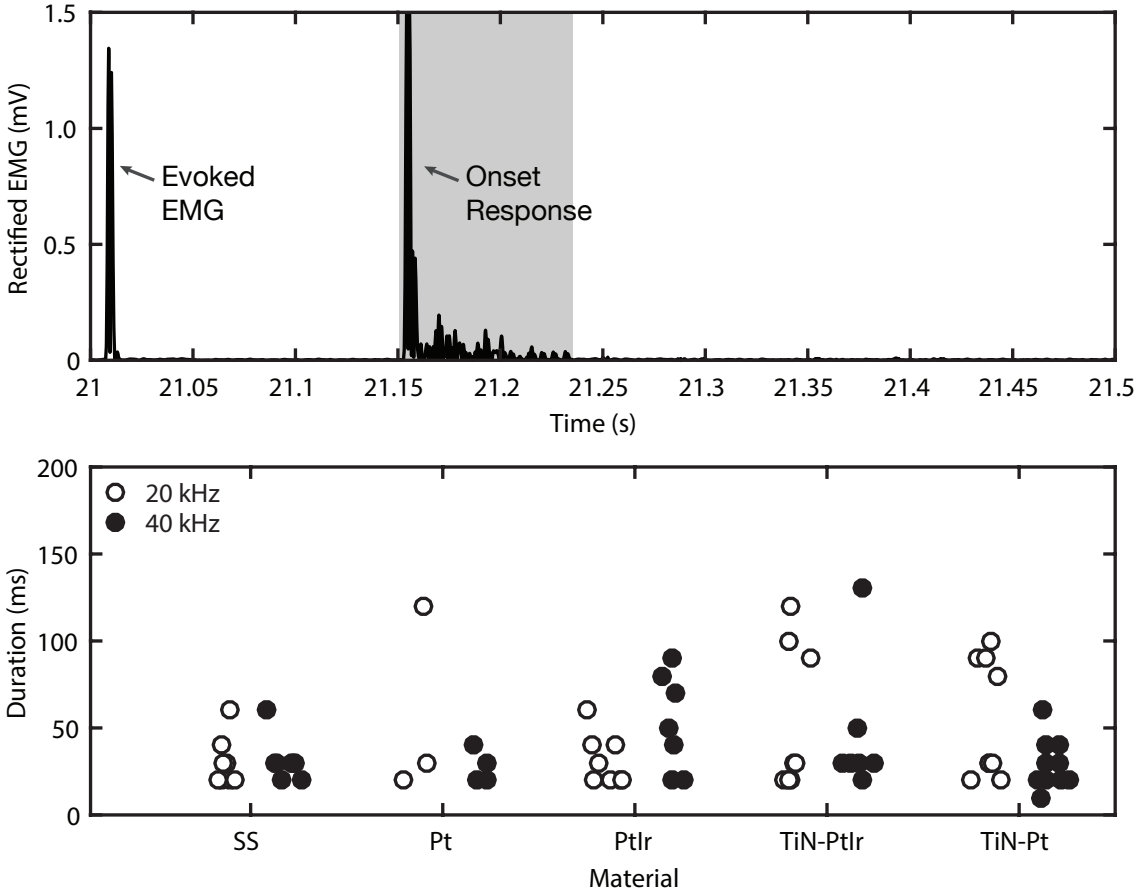


**Figure 15:** Rectified EMG onset artifact and durations. (A) Rectified EMG onset artifact consists of a large, high-frequency transient spike in measured EMG activity followed by a brief period of spontaneous activation, followed by complete KES nerve block. (B) The width of the windowed rectified EMG onset artifact is used to represent the duration of the onset artifact as a function of contact material and KES frequency. No statistically significant difference was observed between block thresholds with a given material at either 20 kHz or 40 kHz (Tukey-Kramer multiple comparison test, $\alpha = 0.05$)

characteristics of each material. *In vivo* experiments were conducted on the rat tibial nerve with gastrocnemius muscle EMG as a readout for KES nerve block.

Our results demonstrate that KES nerve block thresholds (Figure 26) and onset artifact duration (Figure 15) do not differ with different electrode materials. In contrast, the power consumption is increased by nearly 5-fold with the use of TiN-coated electrodes. These results further support findings by others suggesting that the electrode geometry (inter-pole distance) is the critical factor for minimizing the block threshold and onset response (Ackermann et al., 2009; Ackermann et al., 2010b).

A typical concern with KES nerve block is the initial asynchronous activation of the nerve called the onset response. Depending on the neural circuit being modulated, the onset response can be of great concern. In somatic nerves the onset typically represents itself as activation of the muscle and can last up to 10 s, with electrode configurations demonstrated to play a critical role in minimizing the onset response (Ackermann et al., 2010b; Ackermann et al., 2011a). The onset response characterized in our investigations typically lasted <200 ms (Figure 15). This disparity is likely due to differences in the true nerve onset measured from the nerve, lasting several milliseconds (Patel et al., 2015), versus the onset measured through force transduction, which includes the passive relaxation time of the muscle after being asynchronously activity. It remains to be thoroughly investigated how electrodes with penetrating features, such as minimally invasive microneedles (Patel et al., 2016), might impact the safety, efficacy, and characteristics of KES nerve block.

The contacts used in this investigation were made of Pt or PtIr, both of which have received significant attention by the neural stimulation community (Cogan et al., 2005; Brunton et al., 2015; Kumsa et al., 2016) and are used in clinically available KES devices. Pt and PtIr both utilize both faradaic and non-Faradaic charge injection mechanisms, with the contribution of each mechanism depending upon the current density and the pulse width. In the case of KES waveforms, where the pulse widths

are extremely short, the non-Faradaic mechanisms dominate. The lack of a significant effect of materials on KES nerve block characteristics is likely due to the dominating electrochemical mechanisms at high frequencies. All evaluated electrode materials show a dependence upon non-Faradaic charge transfer mechanisms at KES frequencies based upon the EIS data (Figure 12B-C).

Coating of Pt and PtIr electrodes with TiN, which has a high charge injection capacity (Meijs et al., 2015), can lead to a reduction in the polarization of the electrode during stimulation and thus the power requirements for neural stimulation therapies. Our results are in contrast to this and demonstrate a higher average power when using TiN-coated electrodes for KES nerve block (Figure 26B-C). These contrasting results are likely due to multiple factors including thickness and behavior of TiN at high frequencies. (Meijs et al., 2015) used TiN coatings 62.5-fold thicker (12.5$\mu$m) than our coatings (200 nm) to achieve substantial impedance magnitude reductions. Our attempts with thicker TiN layers were unsuccessful due to delamination and cracking of the TiN during implantation of the electrodes circumferentially around the nerve.

The fractal pattern of TiN (Figure 13C) increases the Electrochemical Surface Area (ESA) resulting in a greater number of sites for charge transfer to take place. Similar benefits are achieved with other materials and coatings, such as conducting polymer polypyrrole (PPy) doped with polystyrene sulfonate (PSS). However, utilization of the additional charge transfer sites has been shown to be frequency-dependent. Both modeling and experimental results suggest that the peaks and valleys on fractal pattern coatings are hidden from charge transfer at high frequencies (Cui et al., 2001), resembling an effective ESA closer to that of planar materials (Pt, PtIr, SS). Similar characteristics have been shown chronically *in vivo* with poly(3,4-ethylenedioxythiophene) (PEDOT) coated Michigan probes.

While this study focused on the acute effects of different electrode materials on KES nerve block, it is worth discussing the effects of chronic KES delivery (weeks to

months) and the impact that may have on electrodes. Electrodes are encapsulated in a fibrotic tissue within weeks of implantation. During this time, the distance between the electrode and the excitable tissue of interest changes and can increase the thresholds required to achieve the desired effect as well as decrease the charge injection and charge storage capacity of the electrode (Meijs et al., 2016). If the electrode is not sufficiently large in surface area, increases in thresholds can lead to electrode degradation or dissolution (Kumsa et al., 2016). It is also possible that a number of unspecified organic reactions and their byproducts take place and diffuse into nearby tissue. For example, oxidation of glucose at Pt-based electrodes may lead to protein aggregation on or around the electrode (Cogan et al., 2016). These post-implant changes at the electrode-electrolyte interface require further investigation of KES therapies, especially with existing clinical therapies and devices utilizing KES.

## *3.6 Conclusion*

KES nerve conduction block is a powerful neuromodulation technique capable of providing fast, effective, and robust block of nerve activity. The results presented in this manuscript demonstrate the independence of KES nerve block thresholds and post-KES nerve block characteristics on various electrode materials and charge injection mechanisms. However, the material of choice can substantially alter the power requirements based upon its behavior at high frequencies. These results suggest that the electrode material used for KES be selected based upon proven track records of chronic stability, long-term safety, and robust manufacturing methods. For example, PtIr alloys, which primarily utilize non-Faradaic charge injection mechanisms at KES frequencies, may provide chronic stability and safety for both the nerve and electrode.

# Part II

# Applications of Kilohertz Electrical Stimulation

# CHAPTER IV

# FIBER-SPECIFIC BLOCK OF NERVE CONDUCTION

## *4.1 Motivation*

Kilohertz Electrical Stimulation (KES) has been shown to induce repeatable and reversible nerve conduction block in animal models. In this study, we characterized the ability of KES stimuli to selectively block specific components of stimulated nerve activity using *in vivo* preparations of the rat sciatic and vagus nerves. KES stimuli in the frequency range of 5 - 70 kHz and amplitudes of 0.1 - 3.0 mA were applied. Compound action potentials were evoked using either electrical or sensory stimulation and block of components was assessed through direct nerve recordings and muscle force measurements. Distinct observable components of the compound action potential had unique conduction block thresholds as a function of frequency of KES. The fast component, which includes motor activity, had a monotonically increasing block threshold as a function of the KES frequency. The slow component, which includes sensory activity, showed a non-monotonic block threshold relationship with increasing KES frequency. The distinct trends with frequency of the two components enabled selective block of one component with an appropriate choice of frequency and amplitude. These trends in threshold of the two components were similar when studying electrical stimulation and responses of the sciatic nerve, electrical stimulation and responses of the vagus nerve, and sensorimotor stimulation and responses of the sciatic nerve. This differential blocking effect of KES on specific fibers can extend the applications of KES conduction block to selective block and stimulation of neural signals for neuromodulation as well as selective control of neural circuits underlying

sensorimotor function.

This work is published as Yogi A Patel et al. (2015). "Differential fiber-specific block of nerve conduction in mammalian peripheral nerves using kilohertz electrical stimulation." In: *Journal of Neurophysiology* 113.10, pp. 3923–9. Financial support for this work was provided by Georgia Tech and the National Institutes of Health (Grant 2R01EB016407-09A1).

## *4.2 Background*

Electrical stimulation for the modulation of peripheral nerve activity is utilized for the treatment of neuropathological diseases. In some cases, it is desirable to selectively inhibit specific fibers within a peripheral nerve. Various thermal (McMullan et al., 2004; Burgess et al., 1967), mechanical (Bentley et al., 1943), and pharmacological (Güven et al., 2005; Suzuki et al., 2009) methods have been used for selective blocking but are either slow acting, or not quickly reversible, rendering them unsuitable for chronic applications. Electrical stimulation with kilohertz frequency alternating current has been shown to be effective at blocking action potential conduction in peripheral nerves (Kilgore et al., 2004; Bhadra et al., 2005; Bhadra et al., 2006; Tai et al., 2005; Williamson et al., 2005; Zhang, X, Tai, 2006; Jensen et al., 2009). We refer to this as kilohertz electrical stimulation (KES) throughout this manuscript. The method is quick, reversible, and currently employed in a variety of clinical applications, including appetite control (Camilleri et al., 2008), bladder control (Boger et al., 2012), and post-amputation pain relief.

KES conduction block has been demonstrated in a variety of animal models and nerve diameters, including sea slugs (Joseph et al., 2011), frogs (Kilgore et al., 2004; Joseph et al., 2009), rats (Williamson et al., 2005; Bhadra et al., 2005), cats (Bhadra et al., 2006), dogs (Lin et al., 2007), goats (Cuellar et al., 2013), pigs (Camilleri et al.,

2008), and nonhuman primates (Ackermann et al., 2011c). All present implementations of KES inhibit all propagating electrical activity in the target peripheral nerve. Our *in vitro* study of the sciatic nerve of the leopard frog *Rana pipiens* demonstrated that KES stimuli can be selective towards fast and slow components of the Compound Action Potential (CAP) (Joseph et al., 2011), which we putatively associate with myelinated and unmyelinated nerve activity. Such selective block could enable new research protocols as well as new clinical applications.

The feasibility and evaluation of KES stimuli to selectively block fiber propagation has not been investigated in mammalian peripheral nerves, nor has it been investigated *in vivo*, nor functionally using sensory stimulation and motor output when appropriate. The objective of this study was to evaluate the feasibility of KES stimuli to selectively block conduction specific components of the CAP in mammalian peripheral nerves *in vivo* and characterize this specificity as a function of KES frequency. We characterized the ability of KES stimuli to selectively inhibit components of the CAP in the rat sciatic and vagus nerves. We utilized both electrical and sensory stimuli and measured CAP activity as well as motor output.

## *4.3 Experimental Methods*

### *4.3.1 Animal preparation*

*In vivo* acute experiments were performed on the left and right sciatic nerves of four Lewis rats as well as the vagus nerves of four additional Lewis rats. Rats were anesthetized with 5% isoflurane and fixed in the prone position prior to surgery. Anesthesia was maintained at 2 - 3% for the first 45 minutes and 1 - 1.5% for the remainder of the experiment using a nose cone. Ophthalmic ointment was applied to both eyes to prevent drying. The animal's toe pinch reflex was used to maintain surgical anesthetic depth throughout the experiment. Body temperature and circulation

were maintained via a heating pad at 37°C.

The right thigh of the animal was shaved and the biceps femoris muscle was separated for sciatic nerve preparations. The sciatic nerve was exposed from the top of the biceps femoris to the bottom of the gastrocnemius muscle in the ankle and cuff electrodes were placed around the nerve (Figure 16A). A total of 3 - 4 cm were exposed in all sciatic nerve preparations. Sterile rat ringer solution was applied throughout the experiment to prevent muscle and nerve tissue dehydration. After completing the experimental protocol on the animal's right side, the wound site was closed with surgical clips. The same procedure was executed on the animal's left sciatic nerve. The same sterile procedures were used to expose and experiment on the left cervical vagus nerve. Preparations lasted an average of 5 hours after which animals were euthanized via carbon dioxide. All experiments were conducted at room temperature. All animal experiment protocols were approved by the Georgia Tech Institutional Animal and Use Committee.

### *4.3.2 Electrophysiological configuration and measurement*

Recordings of CAP propagation along the nerve were used as an output measure to detect and monitor the status of selective conduction block in both sciatic and vagus nerves. A combination of hook and tripolar cuff electrodes were used to conduct these studies. A bipolar stainless steel hook electrode was used to electrically elicit CAPs. Tripolar cuff electrodes (Figure 16B) were used to record CAPs and deliver the KES block stimulus. The sampling rate of the data acquisition system (Digidata 1322, Molecular Devices, Foster City, CA, full scale range ±10.096V) was 50 kHz per channel. Nerve recordings were differentially amplified (Model 1700, A-M Systems, Sequim, WA) with a gain of 1000x, and filtered using a second-order bandpass (100 Hz - 5 kHz) filter. In some cases, an additional digital first-order bandpass (300 Hz - 3 kHz) filter was enabled in the acquisition system to enhance visualization of the

CAP during application of the KES stimuli. This experimental setup provided direct monitoring of the neural activity along the nerve and the status of selective KES conduction block. Figure 16 displays the experimental setup used for sciatic nerve studies. No significant modifications were made to this setup for the vagus nerve studies. Vagus nerve studies positioned the electrode on the cervical section of the vagus nerve.

### *4.3.3 Electrode design and fabrication*

Nerve recordings and application of the KES block stimulus were performed using custom-made, tripolar, longitudinally slit cuff electrodes as shown in Figure 16B. Cuff electrodes were made using silicone tubing, stainless steel wire, and platinum-iridium (Pt-Ir, 90/10) contacts (3 mm x 1 mm). Average cuff diameter and length for sciatic nerve studies were 1.25 - 1.5 mm and 5 mm, respectively, with 1 mm between Pt-Ir contacts. Average cuff diameter and length for vagus nerve studies were 1.0 - 1.2 mm and 3 mm, respectively, with 0.75 mm between Pt-Ir contacts. Impedance was characterized for all cuffs using an impedance conditioning module (FHC, Bowdoin, ME). The impedance range for the recording and KES stimuli cuffs were 1.6 - 2.0 kΩ and 1 - 1.2 kΩ, respectively at 1 kHz.

### *4.3.4 Electrical nerve stimulation*

Electrical stimulation was used to elicit CAPs in both sciatic and vagus nerves. Supra-maximal cathode-first biphasic electrical stimulus pulses (5 V, 0.2 ms) were generated by the data acquisition system to trigger CAPs in the nerve. Sensory stimulation in the form of a hot air gun was used to deliver a low flow, high heat noxious stimulus to the forepaw of the animal. The KES block stimulus (continuous sinusoidal waveform) was generated using a function generator (DS345, Stanford Research Systems, Sunnyvale, CA). Both the stimulation pulses and KES block stimulus were converted to

current sources (1 mA/V) by optically-isolated stimulus isolation units (Model 2200, A-M Systems, Sequim, WA). All stimulation equipment was calibrated and offsets were zeroed prior to experimentation to ensure no leakage of current from equipment.

Evoked CAPs have two visually distinguishable components that we refer to as the fast and slow responses, in reference to their time of appearance relative to the stimulus artifact that occurs when a nerve is electrically stimulated. The fast response is attributed to large diameter, predominantly (but not exclusively) myelinated fibers with fast conduction velocities (e.g., A$\alpha$, A$\beta$, A$\gamma$) and the slow response is attributed to small diameter, predominantly (but not exclusively) unmyelinated fibers with slow conduction velocities (e.g., C) (Gasser, 1941). Components with conduction velocities below 2 m/s were classified as slow and components with conduction velocities greater than 2 m/s were classified as fast. In addition, the waveforms associated with these two components were visually recognizable (Figure 17A-B). During experimentation, fast and slow components were identified by latencies between stimulus onset and the recording electrodes. Fast and slow components were associated with latencies in the range of 0.5-1.5 ms and 9-13 ms for electrode V1, respectively. In addition, fast and slow components were associated with latencies in the range of 3-5 ms and 15-20 ms for electrode V2, respectively.

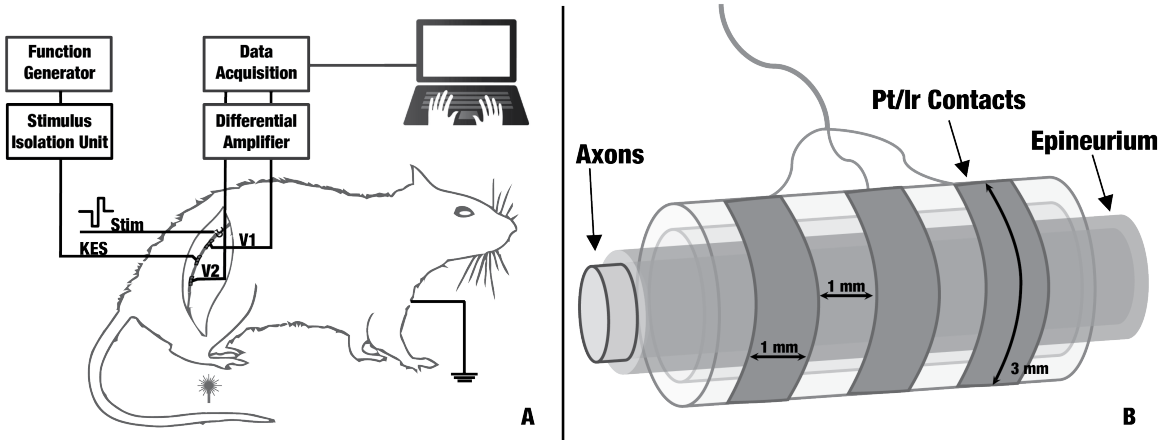


**Figure 16: A:** Experimental setup for selective KES conduction block in the rat sciatic nerve. All experiments were conducted in a faraday cage to minimize interference from external noise sources. A hook electrode is used to elicit CAPs at either the distal or proximal end of the nerve. Cuff electrodes are used to record nerve activity as well as deliver the KES stimulus. Sensory stimulation was delivered to the animal's hindleg using a convective heat source. **B:** Schematic of nerve cuff electrodes used for electrophysiology trials with exact dimensions (schematic not to scale).

### *4.3.5 Force transduction measurement*

Force transduction experiments were carried out to validate the functionality of selective block of the fast component. The posterior segment of the leg was shaved and the biceps femoris was exposed to allow dissection of the gastrocnemius-soleus muscle complex. The tibia was fixed to the experimental rig and the Achilles tendon was attached to a force transducer (Model 724490, Harvard Apparatus) using a hemostat.

### *4.3.6 KES conduction block trials*

Block (or no block) of the slow component was verified via visual classification. First, block was visually verified in-line during experimentation. Block did not occur when there was a repeatedly triggered and identifiable waveform in the latency window of the slow component. Block occurred when there was no identifiable and repeatable waveform in this latency window. This visual analysis was repeated during post-hoc data analysis.

Furthermore, we quantified the change in rectified and integrated area of both the fast and slow components of the CAP. Fast and slow components were identified using measured latencies and conduction velocities. The identified components were numerically integrated using Romberg's method for numerical integration (Burden et al., 2001). Romberg's method was chosen because of its simplicity and ability to eliminate error without the need for oversampling. Because of these qualities, Romberg's method is more suitable for integrating experimental data, which tends to be noisy.

### *4.3.7 Attenuation of stimulus isolation unit output at high frequencies*

Frequencies up to 50 kHz and 70 kHz were tested for the sciatic and vagus nerve experiments, respectively. These frequency ranges are beyond the rating (up to 40 kHz) of the stimulus isolation units (SIUs) driven by the waveform generator. The SIUs can provide outputs at frequencies higher than the ratings, however the output is of a lower amplitude than specified. We measured this attenuation and used this information to calculate the true current output at a given frequency. Attenuation of the KES waveform was characterized by measuring the current across varying resistances (1 kΩ, 10 kΩ, and 1 MΩ) in parallel with the output terminal of the SIU, as shown in Figure 18A. The resulting current across the resistor was calculated using voltage measurements made using an oscilloscope (HP 54602B, Hewlett Packard, Palo Alto, CA). The resulting calibration curves (Figure 18B) were used to calculate the true current provided by the KES. These adjusted values are reported in this manuscript. The same trends qualitatively reported are also evident in the non-adjusted data.

## *4.4 Results*

Each experimental preparation was tested for normal conduction properties prior to beginning selective KES trials. CAPs were triggered using supra-threshold electrical or sensory stimulation. Evoked nerve activity was recorded using cuff electrodes along the length of the nerve. The distance between stimulating and recording electrodes was used to determine conduction velocities for the CAP components.

Figure 19 shows single trial data from one experiment demonstrating selective KES block. The labels on the left correspond to the electrodes shown in Figure

16. Stimulus artifacts precede the fast component and occur earlier than the time traces shown in V1 and V2. Trial #1 shows the standard baseline trial conducted throughout every experiment to verify CAP initiation and propagation. A supra-threshold stimulation pulse is delivered to the nerve at the proximal end and the propagating CAP and associated muscle twitch are recorded. Trial #2 depicts the case where a CAP is triggered and the fast component is selectively blocked via KES. This block of the fast component led to an absence of the muscle twitch but maintained propagation of the slow component. Additional stimulation pulses were delivered to the nerve during selective block of the fast component to ensure true block had occurred. The additional stimulation pulses evoked the fast component response in the proximal recording electrode but not in the distal recording electrode, demonstrating the continued effects of the KES selective block. This resulted in continued absence of muscle force generation while maintaining propagation of the slow component. Trial #3 demonstrates a scenario where the slow component is selectively blocked, leaving the fast component and muscle force intact. Trial #4 shows the use of sensory stimulation (heat) to evoke the slow component only. The stimulus is applied to the hindleg of the animal, resulting in the CAP appearing on electrode V2 first and then being blocked (absent on V1). Individual trials, as shown in Figure 19, are aggregated to produce block threshold characterization curves (Figures 20-21).

The primary results from these studies are the block threshold characterization curves (Figures 20-21). These curves provide a visual representation of the frequency and amplitude pairs that allow for selective KES block of CAP components. Figure 20 depicts that KES amplitudes greater than or equal to the dark grey line but less than the light grey line provide for selective block of the fast component for frequencies up to 35 kHz. Similarly, KES amplitudes greater than or equal to the light grey line but less than the dark grey line provide for selective block of the slow component for

frequencies between 35 - 50 kHz. This interpretation applies to all the block threshold characterization curves presented here.

### *4.4.1 CAP components corresponding to sensory stimuli and motor output are selectively blocked*

We utilized selective KES block to demonstrate loss of either motor function or sensory evoked CAPs when either the fast or slow component was selectively blocked. Sensory stimulation was applied to the hindleg of the animal to evoke sensory CAPs and evaluate block of the slow component. Electrical stimulation was used to evoke motor output and evaluate block of the fast component. Motor block was verified by force measurements (Figure 19, Trial #2) and sensory CAP generation and block was verified by direct nerve recordings (Figure 19, Trial #4). The block threshold was characterized for both sensory evoked CAPs and motor output (Figure 20). The fast component block threshold increased with frequency while the slow component block threshold displayed a non-monotonic trend peaking around 30 kHz.

### *4.4.2 Selective block of fast and slow CAP components*

We achieved selective KES block of the fast (Figure 19, Trial #2) and slow (Figure 19, Trial #3) components of electrically triggered CAPs in 8 rat sciatic nerves. Figure 22 shows the block threshold characterization for KES stimuli up to 50 kHz. The non-monotonic block threshold trend peaked around 25 kHz.

### *4.4.3 Application to multiple nerves*

The robustness of selective KES conduction block was also examined in the rat vagus nerve preparation. The experimental setup (Figure 16) was modified by using smaller cuff electrodes for interfacing with the rat vagus nerve. Electrical stimulation was

used to evoke CAPs and nerve recordings were used to assess status of block (Figure 17B). Figure 21 shows the mean and standard deviation for selective KES block thresholds in the rat vagus nerve. The trends are similar to the sciatic nerve results in Figure 22. The fast component block threshold increases monotonically while the slow component block threshold displays a non-monotonic trend peaking around 30 kHz.

### *4.4.4 Changes in rectified and integrated CAP component areas*

We quantified the resolution of selective KES conduction block in the rat sciatic nerve by rectifying and integrating the fast and slow components. Table 6 depicts example data from two arbitrarily chosen frequencies and increasing amplitudes. The fast and slow components were rectified and integrated to quantify the percent reduction in the rectified and integrated area of each component compared to baseline (0% reduction) as a function of the block frequency and amplitude. It can be seen that the rectified and integrated area of the fast and slow components of the CAP decrease in a frequency and amplitude dependent manner. For example, the fast component area decreases significantly as the KES amplitude is increased at low frequencies (20 kHz). Simultaneously, the slow component demonstrates a decrease, until both are no longer identifiable by our classification method. The same trend is observed at high frequencies (40 kHz), in which the slow component rectified and integrated area significantly decreases with increasing amplitude.

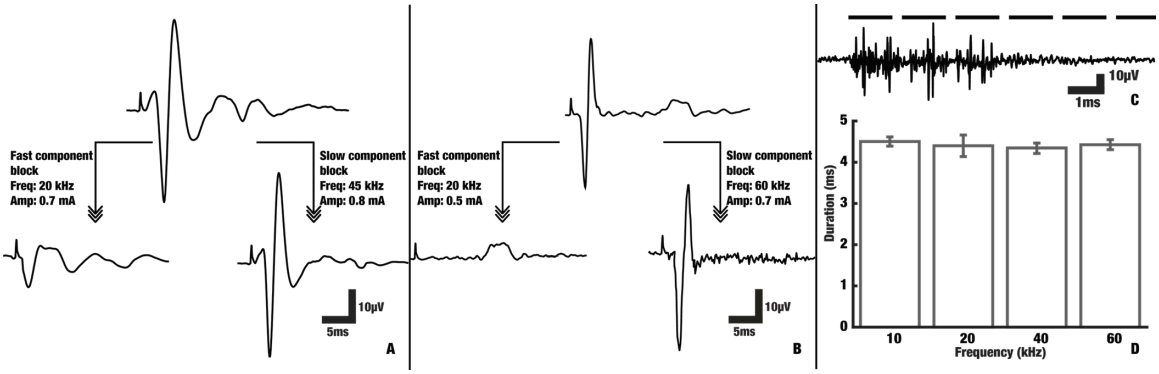


**Figure 17:** **A:** Selective KES block of electrically evoked fast and slow CAP components in rat sciatic nerve. The top trace is the raw evoked CAP (recorded with V1). The fast component block threshold (bottom left) was found to be 0.7 mA at 20 kHz and the slow component block threshold (bottom right) was found to be 0.8 mA at 45 kHz for this nerve. The bottom two traces correspond to recordings obtained with electrode V2. **B:** Selective KES block of electrically evoked fast and slow CAP components in the rat vagus nerve. The top trace is the raw evoked CAP (recorded with V1). The fast component block threshold (bottom left) was found to be 0.5 mA at 20 kHz and the slow component block threshold (bottom right) was found to be 0.7 mA at 60 kHz for this nerve. The bottom two traces correspond to recordings obtained with electrode V2. **C:** Example recording of the onset response as recorded by electrode V2 when KES (20 kHz at 1 mA) is delivered to the nerve with a bandpass (100 Hz - 10 kHz) filter. Dashed black bar above the recording depicts when KES was on. **D:** Onset response duration (mean and standard deviation, n=3) for select KES frequencies at 1 mA.

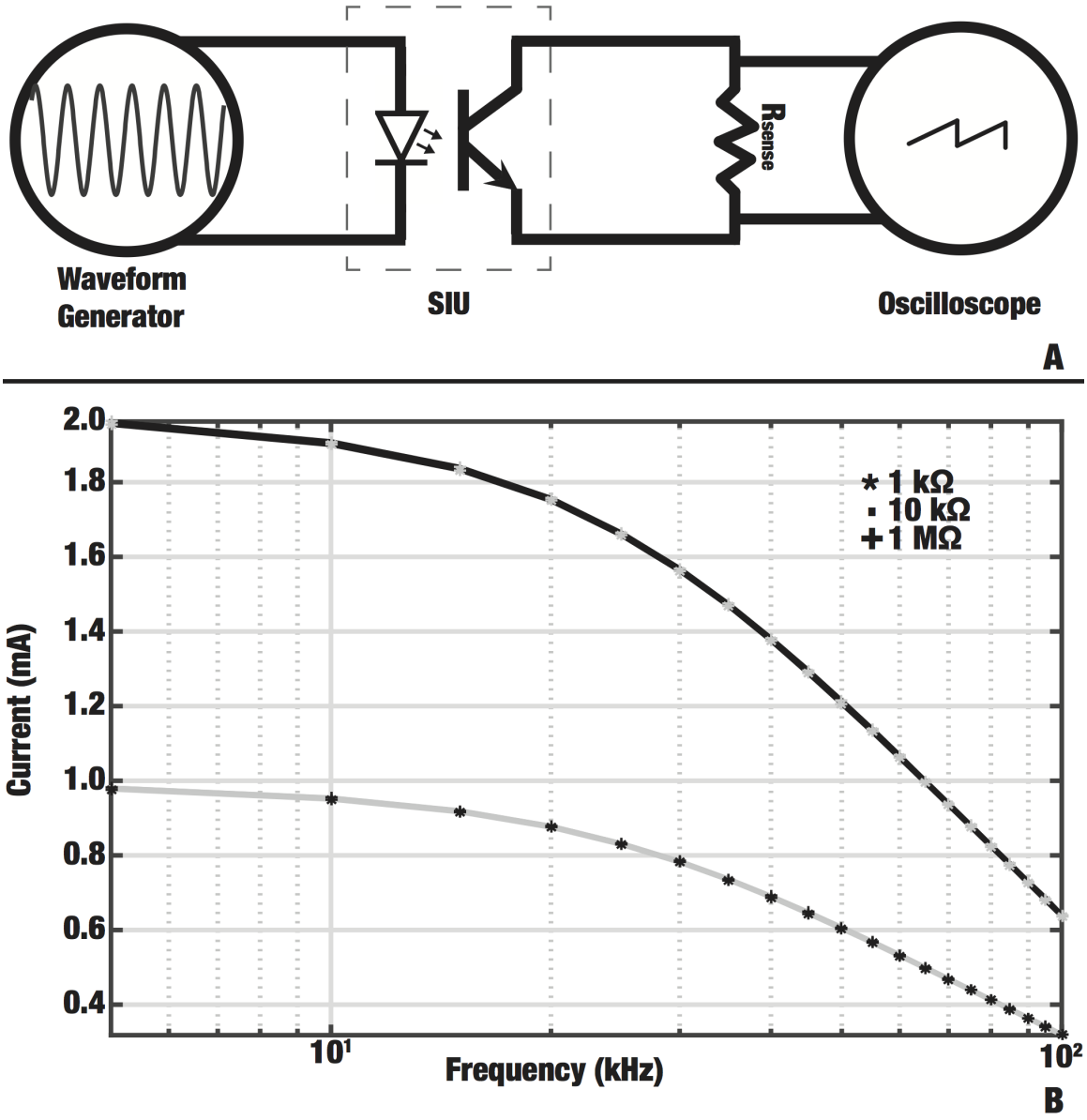


**Figure 18: A:** Setup for measuring attenuated output from optically-isolated SIUs. The function generator output was connected to the input of the SIU. The SIU was set to provide an output of 1 mA/V and the output was connected to varying loads ($R_{sense}$). **B:** Attenuation of current output by SIUs. The current across three different loads ($R_{sense}$) was measured at frequencies up to 100 kHz for input values of 1 V (grey) and 2 V (black). Curves for the three different loads at both input values overlap, showing that the attenuation is independent of the tested load and input value.

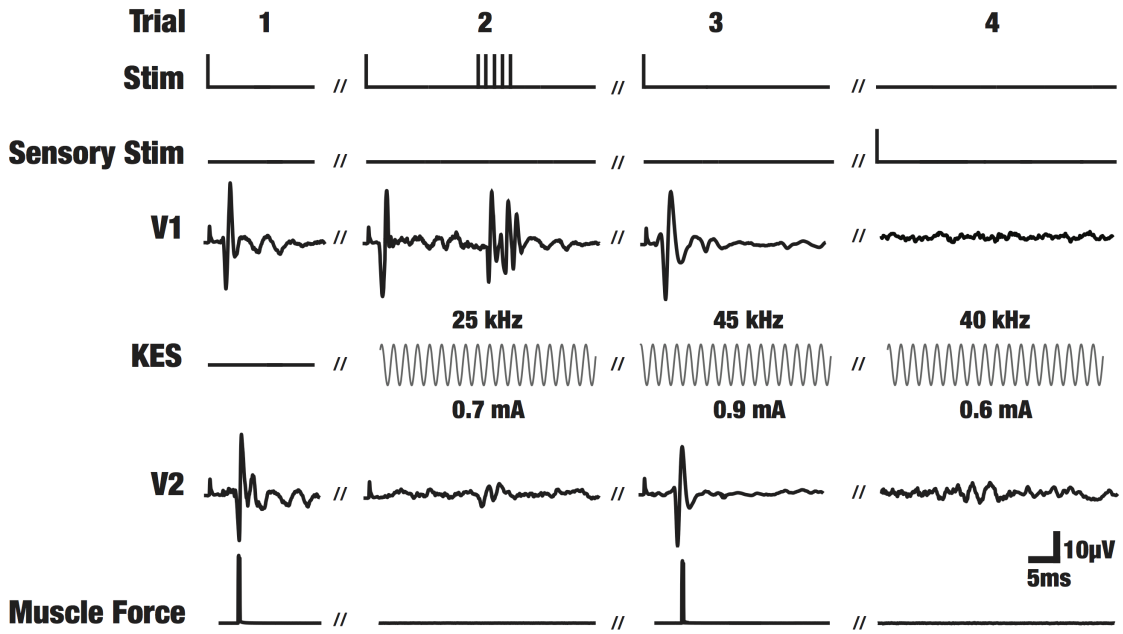


**Figure 19:** All data shown is from individual trials from one single experiment. The labels correspond to the electrodes in Figure 16. The *Stim* electrode was used to deliver electrical stimulation pulses to evoke CAPs. CAPs first show up on recording electrode *V1*. The *KES* trace shows the delivered KES block stimulus. The modulated CAP is then recorded by electrode *V2*. Simultaneous muscle force measurements were made using a force transducer. Sensory stimuli were also delivered to the hindleg of the animal to evoke sensory CAPs. In such cases the CAP appears on V2 before V1. The *Trial* numbers are arbitrarily labeled for referencing and do not represent the actual trial numbers from the experiment.

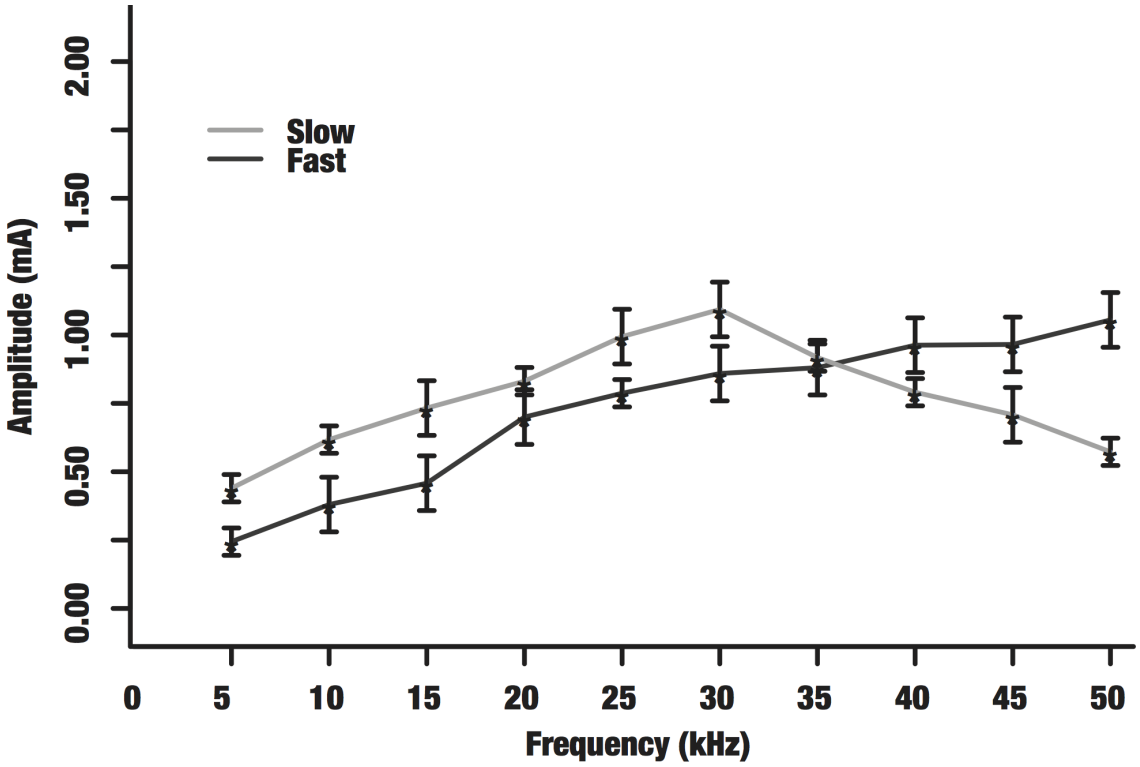


**Figure 20:** The mean block thresholds (denoted by asterisks) and their corresponding standard deviations are shown for 5 - 50 kHz. Only CAP measurements were used to determine block thresholds for the slow component (sensory evoked CAPs) and only motor output was used to determine block thresholds for the fast component (electrically evoked motor output).

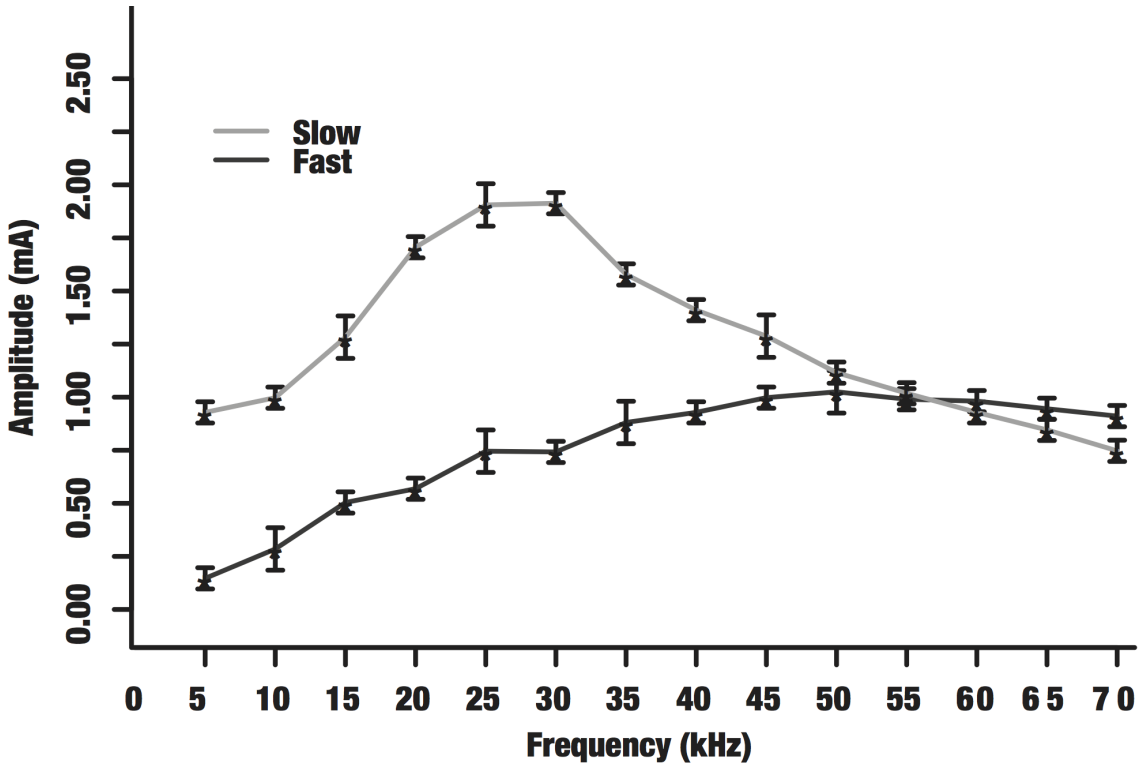


**Figure 21:** The mean block thresholds (denoted by asterisks) and their corresponding standard deviation are shown for 5 - 70 kHz. The fast component block threshold monotonically increases while the slow component displays a non-monotonic trend.

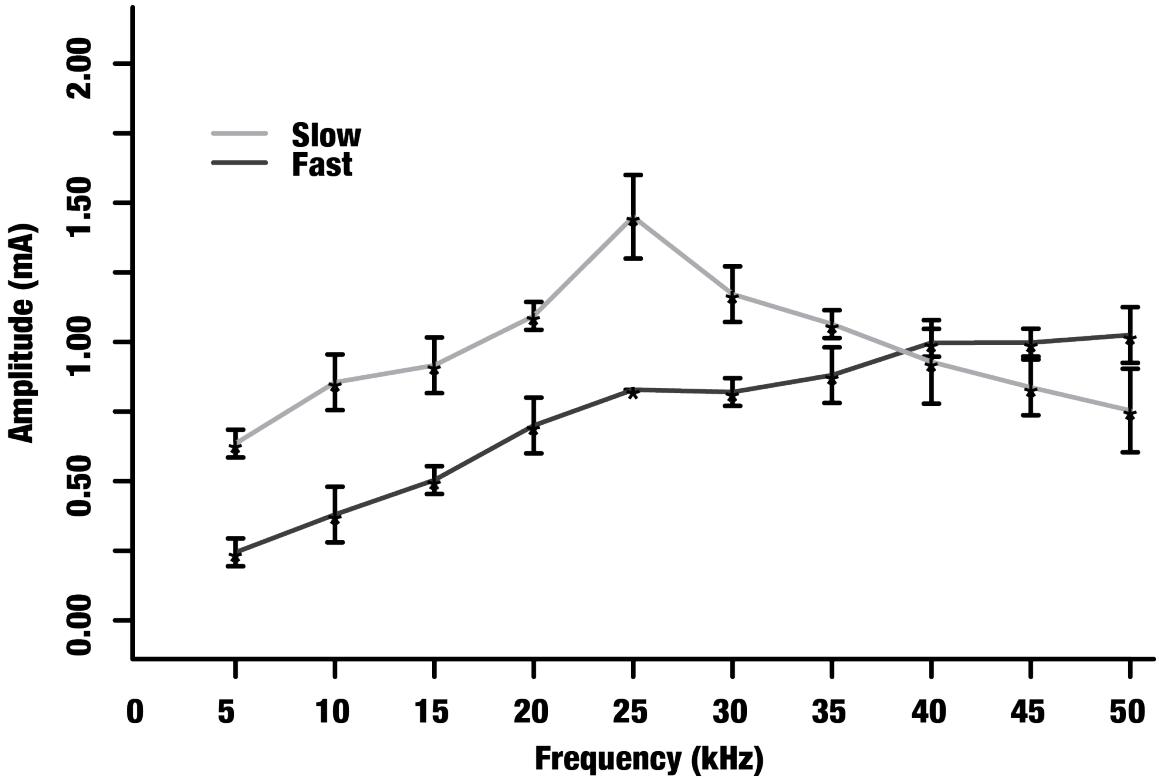


**Figure 22:** The mean block thresholds (denoted by asterisks) and their corresponding standard deviations are shown for 5 - 50 kHz. The light grey and dark grey data points correspond to the slow and fast components, respectively. The fast component block threshold monotonically increases while the slow component block threshold displays a non-monotonic trend. Labels 1-7 mark the frequency and amplitude pairs at which the fast and slow component rectified and integrated areas were quantified (Table 6).

## 4.5 Discussion

This investigation is the first to experimentally explore the frequency-amplitude relationship of the different components of the CAP of a mixed composition mammalian nerve to KES stimulation. The results show that KES stimulation can induce selective conduction block in whole nerves. This is also the first study to demonstrate the differential response of fast and slow mammalian nerve fibers to KES stimulation. In addition, it is also the first to demonstrate that the fast and slow components of CAPs can consistently and selectively be blocked in multiple different mammalian nerves. This was validated via electrical measurements in the sciatic and vagus nerves as well as in response to sensory stimuli and motor output in the sciatic nerve.

Our combined experimental setup, using direct measures of nerve activity through CAP recordings and muscle force output offers a powerful technique to investigate the effect of KES on different peripheral nerves and identify frequency-amplitude regions where specific fiber types may be selectively blocked. This setup enables direct observation and interpretation of the effects of KES stimuli on evoked CAPs and their distinct components.

Published work on KES conduction block shows that the block threshold increases with frequency for motor nerves (Ackermann et al., 2011c). Computational studies have shown similar relationships, that block threshold is inversely proportional to fiber diameter. They also suggest that small diameter unmyelinated fibers have a higher block threshold compared to large diameter myelinated fibers at all frequencies.

While block thresholds of larger diameter myelinated fibers continually increased with frequency, the block thresholds of the small diameter unmyelinated fibers decreased with frequencies above 25 kHz (sciatic) and 30 kHz (vagus). The fast component block thresholds showed a monotonic relationship with frequency, as suggested by previously published literature. The slow component block thresholds displayed

a non-monotonic relationship with frequency, consistent with previous experimental results conducted in purely unmyelinated nerves of *Aplysia californica* (Joseph et al., 2009) and our previous *in vitro* studies, which blocked the slow component in the sciatic nerve of the frog (Joseph et al., 2011).

While qualitatively similar, the block threshold curves between the sciatic and vagus nerve differed in their quantitative details. The slow component block thresholds were higher while fast component block thresholds were lower for the vagus nerve (Figure 21) compared to the sciatic nerve (Figure 22). We hypothesize that this occurs due to the differences in composition of the sciatic (Schmalbruch, 1986) and vagus (Yoo et al., 2013) nerves in terms of the number, types, and organization of fibers within the nerve. In addition, block threshold results from the sensory stimuli and motor output study (Figure 20) were lower compared to slow component block thresholds from the selective block study results (Figure 22). This is believed to be a result of the differences in fiber recruitment between electrical and sensory stimulation. Supra-maximal electrical pulses activate all the fibers within the nerve while sensory stimulation only activates a small subset of the fibers.

In addition to the trends shown in Figures 20, 22, and 21, changes in rectified and integrated area of each component of the CAP suggest that higher resolutions of selectivity may be feasible with KES. Figure 22 depicts changes in rectified and integrated area of both the fast and slow components of the CAP as a function of frequency and amplitude. Specific frequency and amplitude pairs demonstrate a preference for blocking specific components of the CAP. For example, labels 2, 3, 5, and 6 depict that there are individual changes in rectified and integrated area of either the fast or slow components with increasing amplitude. As the amplitude increased, the selectivity increased (as observed by increasing reduction in individual component areas). All fibers are blocked once the amplitude is above the threshold for both slow and fast fibers. While this investigation focused on the use of KES conduction block

for all-or-none inhibition, there may be applications in which reduction of specific components of the CAP may provide varying levels of neuromodulation. Continued investigations in our lab are aimed at understanding the resolution and sensitivity of KES conduction block.

Prior simulation studies have also indicated that numerous factors, including KES frequency, computational model of choice, and possible interactions between nodes of Ranvier, are key issues in achieving localized electrical nerve block and these factors may also affect the block threshold at each frequency (Bhadra et al., 2007; Joseph et al., 2007; Schnabel et al., 2001; Bédard et al., 2008; Rattay et al., 1993; Rattay, 1989). However, all of these computational studies suggest a monotonic relationship with frequency for all fiber types, including small diameter unmyelinated fibers. Our lab is currently investigating the biophysical mechanisms that may underlie the distinct block threshold plots through computational modeling and experimental approaches.

Block induction using KES waveforms is preceded with an onset response and a period of asynchronous firing (Figure 17C-D). This onset response is known to initially increase and then decrease as the KES amplitude or frequency are increased and has been investigated by others (Ackermann et al., 2011a; Miles et al., 2007; Gerges et al., 2010; Vrabec et al., 2013; Pyragas et al., 2013). In our current study, this onset response presented itself as rapid transients in the nerve response and as rapid muscle contractions.

The technique presented here may enable greater control of peripheral nerve stimulation for clinical and scientific purposes. While the work presented here demonstrates fiber specificity in the form of specific CAP components, we acknowledge that both the fast and slow components consist of activity from multiple different fiber types (e.g., A$\delta$, A$\beta$, C, etc). For example, A$\delta$ sensory fibers likely propagate with a velocity closer to what we associate with the fast component. The ability of KES to selectively block conduction in these specific fiber types is not clear and requires further

investigation using single fiber recordings. Present and ongoing studies are aimed at understanding this phenomenon in greater detail, as well as how KES stimuli affect physiological states. Present clinical implementations of KES conduction block are non-specific, blocking all activity in target nerves. In cases such as neuromodulation for diet control (Camilleri et al., 2008), systemic inflammation (Borovikova et al., 2000), pain, or motor inhibition in the central nervous system (Fisher et al., 2014), it is undesirable to modulate activity in all fibers of a target nerve, as this may lead to unknown long-term side-effects. The use of KES to selectively block conduction of specific fiber-types may enhance the efficacy of treatments while removing unnecessary side-effects. In addition, the use of KES to selectively block conduction may enable more controlled investigation of neural circuits underlying a variety of neural pathologies. For example, a KES-enabled reversible vagotomy would offer many advantages over irreversible vagotomy procedures presently used in both scientific and clinical applications.

**Table 6:** Average percent reduction in integrated electrically evoked CAP area. Percent changes were computed by normalizing each components area to baseline (0 kHz, 0 mA). In specific cases, such as 1.5 mA at both 20 kHz and 40 kHz, both components were no longer distinguishable. A reduction of 99.0% ±0.5 means that our classification methods were not able to detect those components.

| **Frequency (kHz)** | **Amplitude (mA)** | **Fast** | **Slow** |
|---|---|---|---|
| 0 | 0.0 | 0.0±0.0 | 0.0±0.0 |
| 20 | 0.5 | 13.6±1.5 | 2.0±0.3 |
| 20 | 1.0 | 99.0±0.5 | 12.3±0.8 |
| 20 | 1.5 | 99.0±0.5 | 99.0±0.5 |
| 40 | 0.5 | 8.7±2.4 | 24.1±3.6 |
| 40 | 0.9 | 18.2±5.3 | 99.0±0.5 |
| 40 | 1.5 | 99.0±0.5 | 99.0±0.5 |

# CHAPTER V

# DIRECTIONAL SELECTIVITY FOR DOWN-REGULATION OF SYSTEMIC INFLAMMATION

## *5.1 Motivation*

Efferent activation of the cervical Vagus Nerve (cVN) dampens systemic inflammatory processes (Borovikova et al., 2000), potentially modulating a wide-range of inflammatory pathological conditions. In contrast, afferent cVN activation amplifies systemic inflammatory processes (Hosoi et al., 2000), leading to activation of the hypothalamic-pituitary-adrenal (HPA) axis, the sympathetic nervous system through the Greater Splanchnic Nerve (GSN) (Martelli et al., 2014c), and elevation of pro-inflammatory cytokines. Ideally, to clinically implement anti-inflammatory therapy via intact cervical Vagus Nerve Stimulation (cVNS) one should selectively activate the efferent pathway. Unfortunately, current implementations, in animal and clinical investigations, activate both afferent and efferent pathways. We paired cVNS with kilohertz electrical stimulation (KES) nerve block to preferentially activate efferent pathways while blocking afferent pathways. Selective efferent cVNS enhanced the anti-inflammatory effects of cVNS. Our results demonstrate that: i) afferent, but not efferent, cVNS synchronously activates the GSN in a dose-dependent manner; ii) efferent cVNS enabled by complete afferent KES nerve block enhances the anti-inflammatory benefits of cVNS; and iii) incomplete afferent KES nerve block exacerbates systemic inflammation. Overall, these data demonstrate the utility of paired efferent cVNS and afferent KES nerve block for achieving selective efferent cVNS, specifically as it relates to neuromodulation of systemic inflammation.

This work is published as Yogi A Patel et al. (2017b). "Kilohertz frequency nerve block enhances anti-inflammatory effects of vagus nerve stimulation". In: *Scientific Reports* 7, p. 39810. Financial support for this work was provided by the National Institutes of Health (Grant 2R01EB016407-09A1), the Georgia Tech TI:GER program, Ian's Friends Foundation, The Georgia Research Alliance, and The Wallace H. Coulter Foundation.

## *5.2 Background*

Activation, inhibition, and control of the innate immune system is vital for maintenance of homeostasis in living organisms, and one in which both the Central Nervous System (CNS) and Peripheral Nervous System (PNS) play a critical role. The CNS actively responds to acute immune challenges by altering body temperature, stimulating the HPA axis, as well as up- and down-regulating specific sympathetic pathways, which are primarily involved in attenuating both cellular and humoral responses initiated by an immune challenge. The PNS enables modulation of the response to an immune challenge by allowing directional stimulation of nerves involved in signaling between the CNS and effector peripheral targets (ganglia, organs, tissues). Specifically, studies from over the last two decades have highlighted the ability to modulate the systemic response to an immune challenge, both in animal and clinical investigations, by electrical stimulation of the cVN.

Studies first conducted by Borovikova et al., 2000 demonstrated down regulation of the systemic response to lethal endotoxemia in rats by electrically stimulating the efferent pathways in the cVN (achieved by stimulating the distal end of the transected cVN). Their results demonstrated the direct influence of the response to an incoming and ongoing acute immune challenge via electrical stimulation. These initial findings led to a significant number of investigations aimed at the use of intact

cervical Vagus Nerve Stimulation (cVNS) for modulation of inflammation in a variety of clinical conditions (ClinicalTrials.gov Identifiers: NCT01552941,NCT02311660). Continued investigations by Rosas-Ballina et al., 2008 into the mechanism of action have engendered the cholinergic anti-inflammatory pathway. We refer the reader to Martelli et al., 2014b for a critical review of the cholinergic anti-inflammatory pathway.

Although the mechanism is unknown and requires significant inquiry, results from both animal and initial clinical investigations posit a potential benefit of efferent cVNS in ameliorating systemic and local inflammation. Many, if not all, cVNS investigations stimulate the intact cVN, leading to activation of both afferent and efferent pathways, or achieve stimulation of afferent or efferent pathways by transecting the nerve. While these approaches are sufficient for elucidating acute effects in animal investigations, clinical translation of selective afferent cervical Vagus Nerve Stimulation (acVNS) or efferent cervical Vagus Nerve Stimulation (ecVNS) requires a safe and effective alternative approach. Various studies have investigated the ability to selectively stimulate via custom electrode geometries and different stimulation waveforms. These approaches suffer from clinical challenges such as patient-to-patient variations in nerve anatomy as well as surgical placement and movement of electrodes. Furthermore, a cervical vagotomy is not desirable in clinical settings due to the fact that a significant amount of parasympathetic control is exerted on the viscero-motor systems through the vagi (Prechtl et al., 1990; Powley et al., 1983; Berthoud et al., 1993). A safe, effective, and reversible selective acVNS or ecVNS method is clearly necessary for controlling inflammation in humans.

We have previously shown that sinusoidal kilohertz electrical stimulation (KES) enables a safe, robust, and rapidly reversible block of nerve activity in the cVN (Patel et al., 2015). We thus hypothesized that KES nerve block could be utilized to achieve a quick, reliable, and temporary virtual vagotomy for inhibiting activation of afferent

pathways while delivering ecVNS. A KES-enabled virtual vagotomy has many advantages over uncontrollable and irreversible procedures such as nerve transection or pharmacological blockade presently used in both scientific and clinical applications. The investigation presented here demonstrates a paradigm for selective ecVNS and afferent KES nerve block for suppression of systemic inflammation in response to bacterial lipopolysaccharide (LPS)-induced endotoxemia in a rat animal model (Figure 23A-C). We quantified both nerve activation and inhibition through electrophysiological recordings of peripheral nerve activity along with biochemical changes induced by cVNS and KES nerve block.

Our results demonstrate that when the virtual vagotomy is successfully employed, the anti-inflammatory benefits of ecVNS are enhanced. In contrast, when the virtual vagotomy is incomplete, the beneficial effects of ecVNS are partial. Collectively, this acute study demonstrates i) the ability of KES nerve block to provide a method for virtually transecting nerves safely, robustly, and reversibly; ii) paired delivery of ecVNS and afferent KES nerve block for modulation of systemic inflammatory processes; and iii) quantitative criteria for evaluating the status of KES nerve block. This technique of paired delivery for achieving selective acVNS or ecVNS may benefit ongoing investigations utilizing cVNS, specifically when developing human bioelectronic medicines based upon laboratory findings.

## *5.3 Experimental Methods*

### *5.3.1 Animal preparation*

All animal care and procedures were reviewed and approved by the Institutional Animal Care and Use Committee at The Georgia Institute of Technology and all methods were performed in accordance with the relevant guidelines and regulations. *In vivo* experiments were carried out on the left cVN and GSN in adult male Sprague-

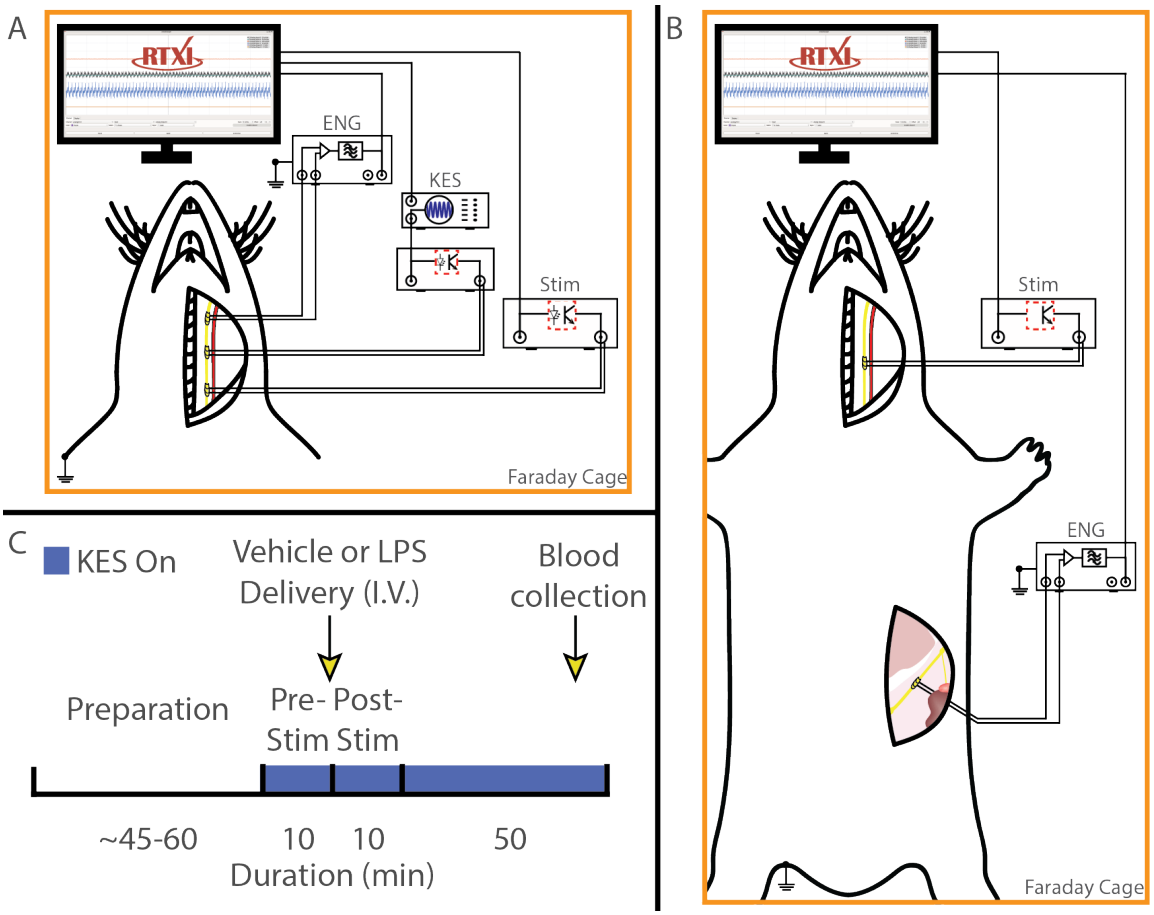


**Figure 23:** (A): Experiment setup and electrophysiological configuration. The left cVN was exposed and fitted with three cuff electrodes. ENG measurements were made from the cranial end of the exposed nerve. cVNS was delivered to the caudal end of the exposed nerve, with a KES delivering electrode located cranially. (B): Preparation used for to measure ENG from the GSN. (C): Experiment timeline. Nerve and electrode preparation were followed by a 10 minute stimulation (pre-stim) period, in which either cVNS or cVNS+KES were delivered to the nerve. Vehicle or LPS was injected through the lateral tail vein, followed by another 10 minute stimulation (post-stim) period. For nerve block experiments, KES was on for the entire 70 minutes. Blood was collected 50 minutes after the post-stim period for biochemical analysis.

Dawley rats (Charles River). Animals (311 ± 50 g, n = 65) were anesthetized in a chamber using 5% isoflurane (1 liter/min flow rate). Once recumbent, the animal was maintained at 2 - 3% isoflurane for 45 minutes, and then at 1.5% isoflurane for the remainder of the experiment. Body temperature was monitored and maintained at 37 - 40°C with a rectal temperature probe (TM-3, Warner Instruments, Hamden, CT) and warming pad (COM-11289, SparkFun Electronics, Niwot, CO). Depth of anesthesia was evaluated by pinching the rear footpad. When there was no response, the animals neck was shaved and depilated. A midline incision was made and the skin and subcutaneous muscles tissues were retracted via blunt dissection. The salivary glands, sternocleidomastoideus, and omohyoideus were repositioned to allow access to the carotid sheath. The cVN and the common carotid artery were separated using a dissection microscope providing a total exposed cVN length of 1.2 - 1.4 cm.

For studies requiring access to the GSN, the dorsal surface of the animal was prepared using the same preparation techniques above. An incision was made approximately 1 cm caudal to the 6th false rib and approximately 0.5 cm lateral to the spinous processes. The skin, underlying muscles, and *latissiumus dorsi* were blunt dissected and retracted. The suprarenal gland was identified and blunt dissected apart from the surrounding fat layers. The adrenal nerve was identified and followed proximally to the suprarenal ganglia, which is the proximal end of the greater splanchnic nerve. The greater splanchnic was isolated from surrounding fat and connective tissue. Electrodes (described below) were placed on the cVN for stimulation, block, and recording of nerve activity and, when desired, a recording electrode was placed on the GSN (Figure 23B). Nerves were not desheathed or dissected. Animals were euthanized at the end of the experiment by thoracotomy done to collect a cardiac blood sample.

### *5.3.2 Electrophysiology*

All experiments were conducted in a Faraday cage with an electrically floating setup powered by an uninterruptible power supply. A floating ground was established by a 20G needle inserted into the right gastrocnemius muscle and connected to the table. Control of experimental hardware, delivery of stimuli, and data acquisition were all achieved using The Real-Time eXperiment Interface (RTXI, Lin et al., 2010). Custom, bi-polar electrodes were made in-house to stimulate, record, and block activity from the cVN and GSN. In brief, braided stainless steel wires (#793500, A-M Systems, Sequim, WA) were threaded through silicone tubing (#807600, A-M Systems, Sequim, WA), spot-welded to platinum-iridium contact pads and the outer surface of the cuff coated with polydimethylsiloxane (PDMS) for electrical insulation. Electrode impedance ($1.2 \pm 0.6$ k$\Omega$) was characterized at 1 kHz using an impedance conditioning module (FHC Inc., Bowdoin, ME). Both electrical and mechanical characteristics were evaluated prior to electrode reuse. For cVN preparations, the electrode spacing was minimized between the stimulation and block electrodes ($0.2 \pm 0.1$ cm), and maximized between the recording and block electrodes ($1.0 \pm 0.1$ cm).

Electroneurogram (ENG) measurements were differentially measured and amplified with a gain of $10^4$x and filtered with a band-pass of $10^2$ - $10^4$ Hz (SR560, Stanford Research Systems, Sunnyvale, CA) prior to being digitized at 20 kHz (PCIe-6259, National Instruments, Austin, TX). Biphasic constant current pulses (1 $mA_{pp}$, 0.4 ms, 1 Hz) for nerve stimulation were generated using the RTXI signal generator module and optically-isolated using a linear stimulus isolator (A395, WPI, Sarasota, FL) prior to being delivered to the stimulation electrode. Block of nerve activity was achieved using kilohertz electrical stimuli (KES, Patel et al., 2015) generated by a function generator (AFG 3021, Tektronix, Beaverton, OR). The function generator output was optically-isolated using an analog stimulus isolator (Model 2200, A-M Systems,

Sequim, WA) prior delivery to the block electrode. KES frequencies and amplitudes were chosen based upon previously demonstrated values for complete block of cVN activity (Patel et al., 2015). Timing of KES delivery was controlled by gating the function generator output using RTXI. All stimulus isolation units used were calibrated prior to each experiment and output offsets zeroed by visualization on an oscilloscope. The complete cVN electrophysiological setups used in this study are shown in Figure 23.

### *5.3.3 Sample collection*

Approximately 5 ml of blood was collected from the left ventricle of the heart at the end of each experiment. Blood was allowed to clot at room temperature for 15 minutes prior to centrifugation at 2000 g for 20 minutes.

### *5.3.4 LPS-induced endotoxemic shock*

LPS (L2630, Sigma Aldrich) was freshly prepared the morning of each experiment by dissolving in sterile, deionized water followed by a 15 minute sonication at 37°C. Animals were injected intravenously via a 24G catheter inserted in the tail vein with a dose of 15 mg/kg in a total volume of 1 ml.

## *5.4 Experimental Protocols*

### *5.4.1 LPS-induced endotoxemic shock*

All experiments followed a standard protocol for induction of endotoxemic shock and delivery of paired efferent stimulation and block (Figure 23C). Animals first received 10 minutes of stimulation or paired stimulation and block (pre-stim). Upon completion, animals received either LPS or saline tail vein injections, and another

10 minutes of stimulation or paired stimulation and block were delivered (post-stim). KES block was continued through the duration of the experiment. Blood collection took place 50 minutes after the completion of the post-stim period. Recordings of cVN activity were made during the entire experiment to validate KES block of afferent activity.

### *5.4.2 Nerve transection studies*

The cVN was transected cVNx in a subset of studies to characterize the effects of afferent (n = 2, data not shown) and efferent (n = 6) cVNS on the systemic response to endotoxemic shock. A cuff electrode (described above) was placed around the cVN for stimulation prior to transection. Once the cuff was secured in place, the cranial or caudal end of the nerve were cut. The nerve was stimulated pre- and post-LPS injection, and blood was collected 50 minutes after the end of the post-stim period. In addition, GSN activity was measured while stimulating the cranial or caudal ends of the transected cVN.

### *5.4.3 Nerve block experiments*

We previously reported KES (sinusoidal) nerve block inhibited evoked potentials in the cVN, and characterized the response of the cVN to KES as a function of both KES frequency and amplitude. Based upon these findings, we used a KES frequency of 40 kHz with amplitudes in the range of 1.5 - 2.0 $mA_{peak}$. A calibration trial was conducted to determine the specific KES amplitude for use in each experiment. The nerve was stimulated at a rate of 1 Hz and online ENG measurements were used as a readout to assess the status of KES nerve block. KES amplitudes started at 1.5 $mA_{peak}$ and were increased in steps of 0.1 $mA_{peak}$ until the block threshold was identified. Both stimulation and block were turned off after identification of the block threshold. Calibration procedures lasted approximately 30 - 45 seconds in

each experiment. Post-experiment visualization and electrophysiological assessment of nerve viability were conducted by delivering 5 - 10 stimulating pulses and observing evoked CAPs, along with monitoring for nerve or electrode discoloration. From all experiments conducted, nerve discoloration, but not loss of nerve conduction, was observed in 2 animals with incomplete KES nerve block and have been removed from the data pool.

## *5.5 Data Analysis*

### *5.5.1 ENG Analysis*

We used ENG measurements to quantify cVNS activation and to validate the status of afferent block. All data processing and analysis was conducted in MATLAB (R2015b, MathWorks, Inc. Natick, MA). ENG recordings from the cVN and GSN were digitally band-pass filtered (100 to 3000 Hz) prior to being stimulus-triggered to generate average waveforms (20 runs per trial), resulting in a total of 210 trials per experiment. All waveforms shown in this report are averages of 20 runs unless stated otherwise. In the current experimental setup, only A and C components from stimulus-triggered average waveforms were distinguishable due to limitations in electrode-to-electrode distance. Time windows were computed using the electrode-to-electrode distance measured in the experimental setup and component-specific conduction velocities (A $>$ 2.0 m/s, C $<$ 2.0 m/s) for quantification of evoked components. Windows were calculated for the A and C fiber components, along with a 10 ms pre-stimulus noise window. Window bounds were set to exclude stimulus and amplifier artifacts. The root mean square (RMS) value of each window was computed using the MATLAB signal processing toolbox (rms function). The signal-to-noise ratio, represented by $\theta$, for each CAP component was calculated by taking the RMS value for a given component (A or C) and dividing by the RMS value of the noise window (Yoo et

al., 2013; Chu et al., 2012). The use of a windowed RMS metric, as opposed to peak analysis, incorporates the temporal dynamics of different CAP components and provides a more complete view of nerve activation or block. For example, small, slow-conducting fibers (e.g., C-fibers) appear as temporally dispersed waveforms which would not be captured by time of occurrence and magnitude of peaks alone.

### *5.5.2 Biochemical Analysis*

Serum TNF-$\alpha$ concentrations were quantified using commercially available ELISA kits (BD Biosciences). Calibration curves were generated and TNF-$\alpha$ concentrations were obtained by measuring absorbance at 450nm.

### *5.5.3 Statistical Analysis*

Analysis of variance and t-tests were performed using the MATLAB statistics toolbox (anova1, ttest2 functions). The Jarque-Bera tests (jbtest function) was used to evaluate normality of experimental groups. All statistical tests were carried out with $\alpha = 0.05$. All box plots show the 95% confidence interval (pink) for the mean (center bar) and 1 standard deviation (blue).

## *5.6 Results*

### *5.6.1 Afferent cVNS synchronously activates the greater splanchnic nerve*

Afferent activation of the cVN has been shown to up-regulate pro-inflammatory signaling via Interleukin-1 beta (IL-1$\beta$) expression and activation of the HPA axis through the GSN (Hosoi et al., 2000; Martelli et al., 2014c). Prior to conducting KES nerve block experiments, we conducted a small set of experiments (n = 3 rats)

to assess GSN activation as a function of cVNS as well as the effects of acVNS on inflammatory Tumor Necrosis Factor-$\alpha$ (TNF-$\alpha$) expression. cVNS was delivered to the left cVN and ENG measurements were made from the GSN with biphasic stimulation intensities of 1, 2, and 3 $mA_{pp}$ (1 Hz, 0.4 ms) (Figure 23B). A cVNx was performed afterwards on either the cranial or caudal end of the electrode for acVNS or ecVNS. A total of 1000 stimuli were delivered at each amplitude in each configuration to enable detection of the evoked GSN activity. Increasing amplitude evoked GSN potentials with latencies of 5-8 ms were measured during cVNS (Figure 24A-C). A linear fit of the $\theta$ calculations revealed a direct relationship between stimulation intensity and evoked GSN activity ($R^2 = 0.94$). Stimulus-triggered averages from either ecVNS (Figure 24D) or acVNS (Figure 24E), along with $\theta$ calculations, demonstrated that cVNS-induced activation of the GSN occurs during acVNS only. Biochemical analysis to quantify TNF-$\alpha$ expression (data not shown) and demonstrated an increase in serum TNF-$\alpha$ even without LPS delivery.

### *5.6.2 Paired efferent cVNS and complete afferent KES nerve block enhance anti-inflammatory effects*

cVNS of the intact cVN leads to bidirectional activation of the vagus, as shown through ENG measurements from locations both cranial and caudal to the stimulation electrode (Figure 25B-C). Cranial measurements depict two distinct components of the compound action potential (CAP) are measured, A and C, representing the set of A and C fibers respectively (Figure 25B). Characterization of $\theta$ for each component demonstrates substantial activation of both afferent and efferent pathways. cVNS alone did not demonstrate anti-inflammatory effects in all animals receiving LPS injections. No significant difference was determined between control animals (LPS only) and animals receiving LPS injections with cVNS. In contrast, as previously reported by others (Borovikova et al., 2000), cVNx+ecVNS resulted in a statistically

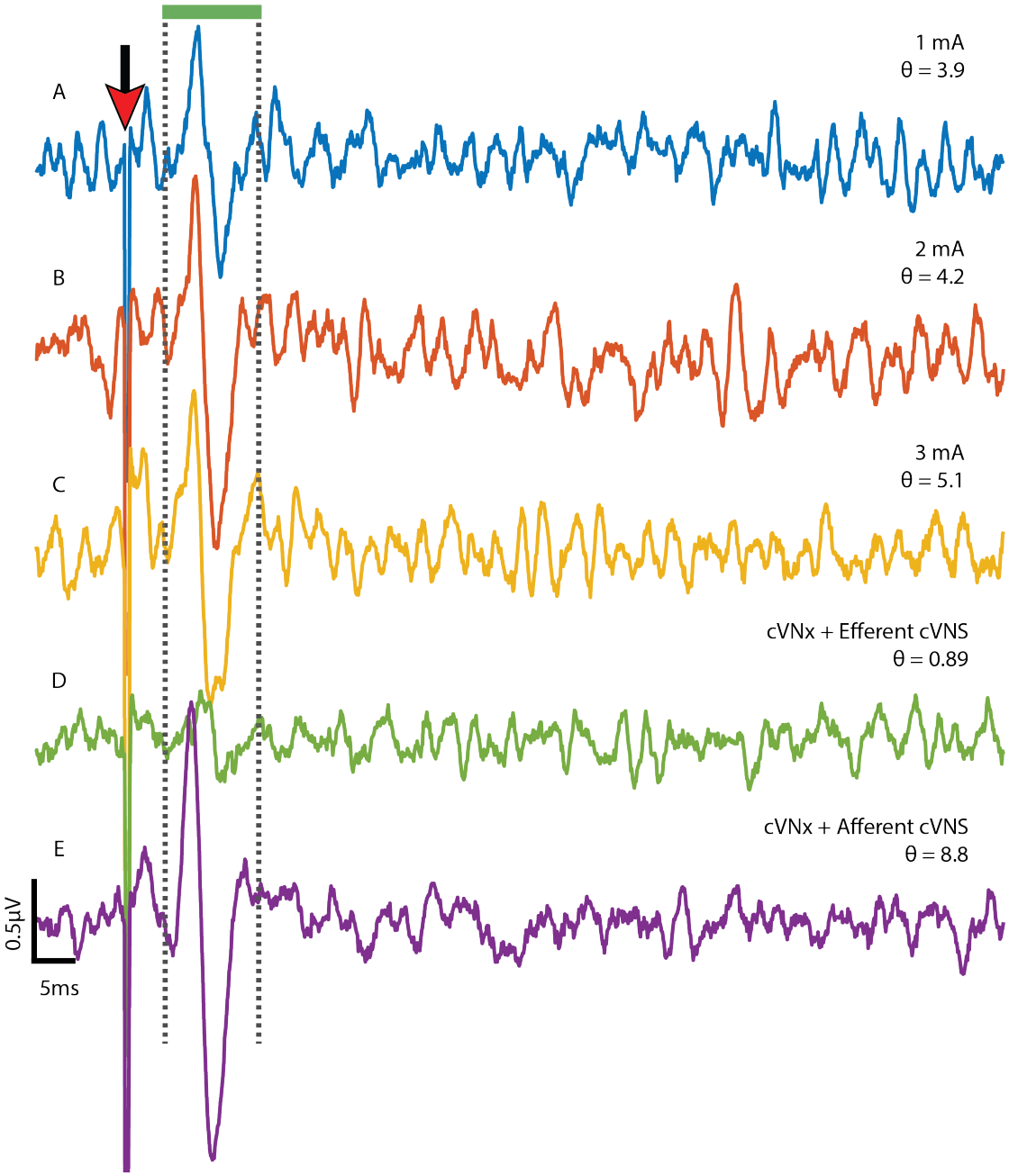


**Figure 24:** cVNS activates the GSN in a synchronous and dose-dependent manner. (A-C): increasing stimulus intensities are delivered to the intact left cVN. Simultaneous ENG measurements are made on the ipsilateral GSN. (D): The caudal end of the transected cVN is stimulated, activating efferent pathways alone. (E): A cVNx is performed and the cranial end of the cVN is stimulated, activating afferent pathways. Waveforms shown are stimulus-triggered averages from 1000 stimulation trials. The red arrow indicates stimulus artifact, and $\theta$ values are presented for each waveform.

significant decrease in TNF-$\alpha$ expression (Figure 25A).

We utilized KES nerve block with paired ecVNS of intact cVN to inhibit activation of afferent pathways while maintaining activation of efferent pathways. ENG measurements from the cranial end of the cVN and biochemical results are shown in Figure 25. Complete afferent KES nerve block+ecVNS significantly lowered TNF-$\alpha$ levels compared to control (LPS only), but not compared to cVNx+ecVNS (Figure 25A) suggesting the presence of a virtual vagotomy of the cVN with KES. ENG measurements from the cranial end of the cVN were used to calibrate and assess the status of afferent KES nerve block. Sample ENG measurements are shown in Figure 25B, along with the calculated $\theta$ values, which indicate complete block of both A and C fiber components. The values at which block was achieved in these experiments, referred to as block thresholds, are depicted in Figure 26A.

We further investigated $\theta$ by analyzing its status throughout the course of the experiment. ENG measurements from each experiment were parsed into 210 trials as previously described. $\theta$ was calculated for each trial for each experiment, resulting in a time series representation of $\theta$ with a sampling interval of 20 s. The $\theta$ mean $\pm$ one standard deviation for A and C fiber components across all complete KES nerve block experiments are shown in Figure 26B-C. For complete KES nerve block experiments, the $\theta$ criteria for highly efficacious and complete block was met. Post-experiment evaluation of nerve viability demonstrated components as seen in baseline measurements (Figure 25B).

### *5.6.3 Paired efferent cVNS and incomplete afferent KES block lead to pro-inflammatory effects*

Although the initial calibration tests were successful, a subset of experiments (n = 5 rats) were found to be incomplete with respect to afferent KES nerve block. Post hoc analysis revealed that the criteria for complete KES nerve block were not met in these

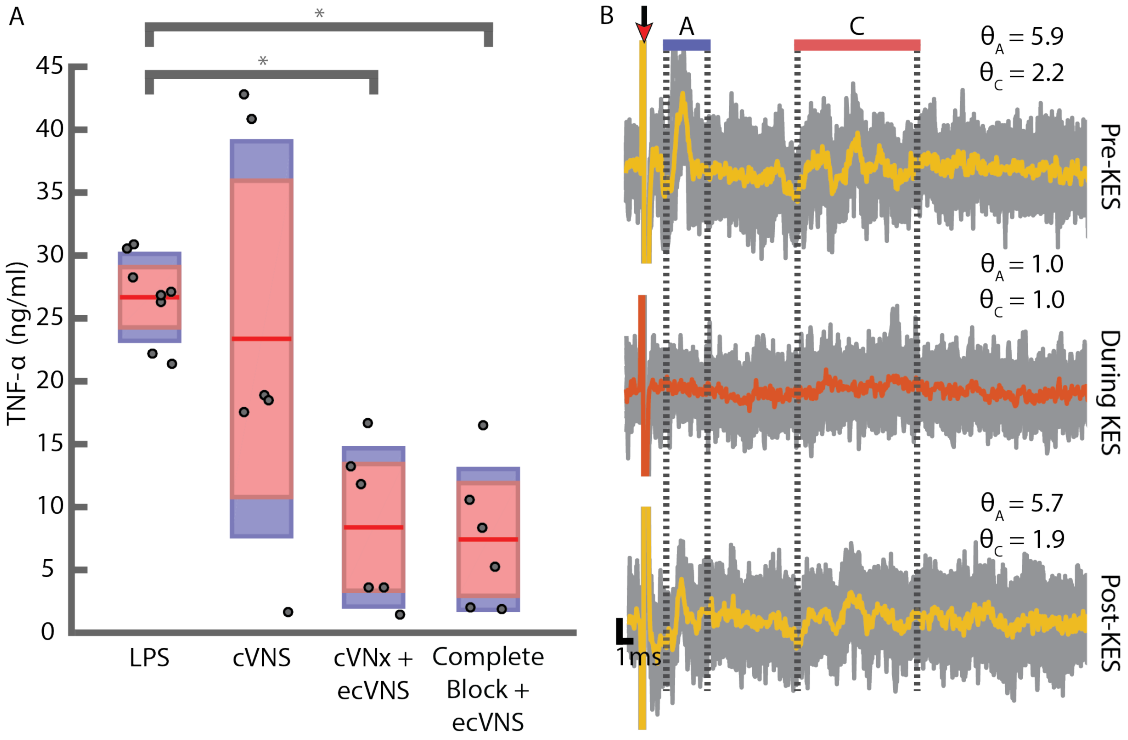


**Figure 25:** TNF-$\alpha$ expression and ENG data for baseline cVNS conditions. (A): TNF-$\alpha$ levels from animals receiving no stimulation (LPS, n = 8), stimulation of the intact cVN (cVNS, n = 6), vagotomized efferent cVNS (cVNx+ecVNS, n = 6), and complete afferent KES nerve block with paired efferent cVNS (Complete Block + ecVNS, n = 6). Asterisks denote significance between bracketed groups ($\alpha = 0.05$). (B): Representative recordings from the caudal end of the cVN pre-, during-, and post-KES delivery. Average measurements (yellow and orange) are superimposed upon individual runs (grey). A and C component regions depict the windows used for quantifying nerve activation ($\theta$) and block efficacy ($\theta$) for A and C components in the ENG measurements. Post-KES averages are from 10 runs only. Red arrow indicates stimulus artifact.

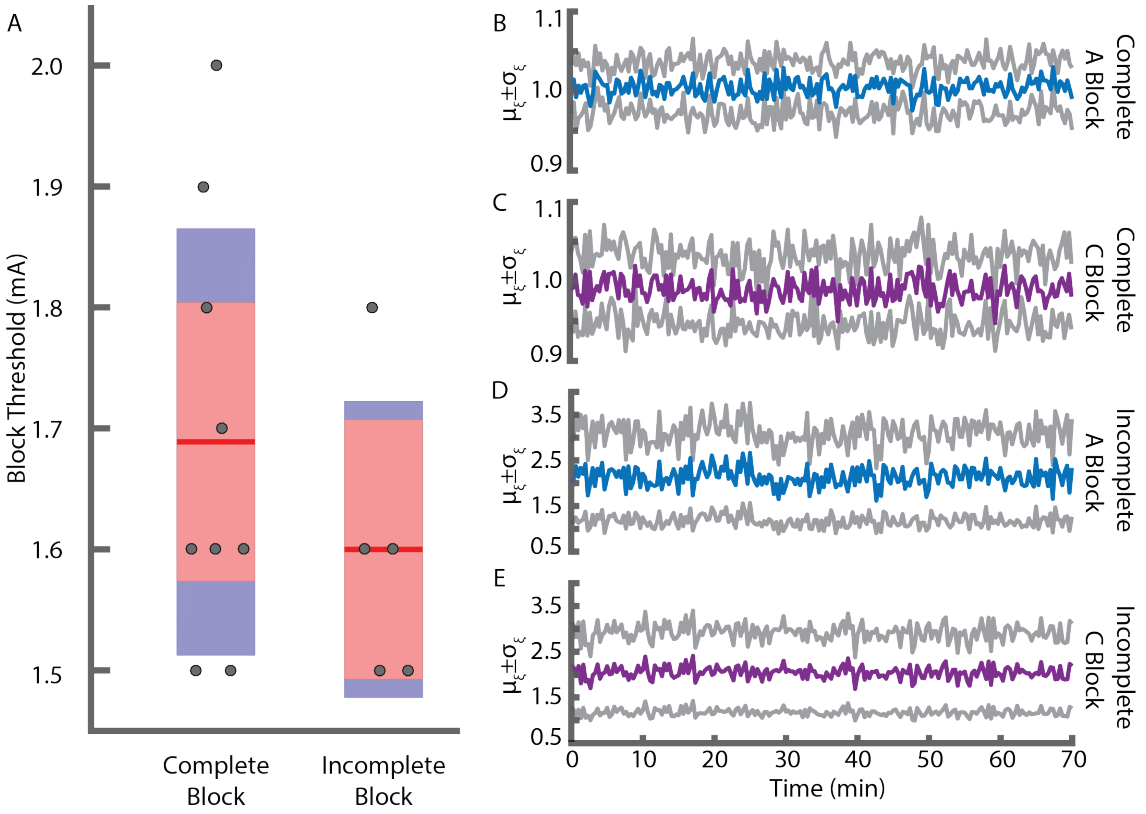


**Figure 26:** KES nerve block thresholds and $\theta$ computations. (A): KES block thresholds were determined during experimental preparation. Post-hoc analysis of ENG measurements and quantification of $\theta$ led to sorting of block thresholds into complete and incomplete block groups. Experiments with trials containing $\theta$ greater than the RMS noise floor during KES delivery were categorized as incomplete block for both biochemical and electrophysiological analysis. (B-E): Mean and standard deviation of $\theta$ throughout experiments with both complete afferent KES nerve block (B, C, n = 9 from all experiments) and incomplete afferent KES nerve block (D, E, n = 5 from all experiments). Recordings from the 70 minute experiments were parsed into 210 trials, each represented by a stimulus-triggered average waveform. Colored traces represent the mean from all experiments in each group, with the grey traces representing $\pm 1\sigma$. Experiments with complete afferent KES nerve block met the $\theta$ criteria, while incomplete block experiments did not.

animals, as represented in the sample ENG measurements and calculated $\theta$ values shown (Figure 27B). Both A and C components are present in stimulus-triggered average waveforms. Furthermore, TNF-$\alpha$ expression was elevated in the incomplete KES nerve block experiments to values similar to control (LPS only, Figure 27A). The block thresholds used in incomplete KES nerve block experiments are shown in Figure 26A. To investigate why KES nerve block was sometimes incomplete, we characterized $\theta$ over the 70 minute experiment period. Time series representations of $\theta$ for all incomplete KES nerve block experiments were generated. The $\theta$ mean $\pm$ one standard deviation for A and C fiber components across all incomplete KES nerve block experiments are shown in Figure 26D-E. Compared to complete KES nerve block, $\theta$ time series for incomplete KES nerve block presented a greater mean and standard deviation. No distinguishing features or events were observed suggesting why KES nerve block failed, however.

### *5.6.4 Virtual vagotomy alone does not provide anti-inflammatory benefits of cVNS.*

Previous reports (Borovikova et al., 2000) demonstrated that animals receiving cVNx and LPS, but not ecVNS, had elevated serum TNF-$\alpha$, similar to control animals (LPS only). For comparison, we characterized serum TNF-$\alpha$ in animals receiving complete KES nerve block and LPS, but no ecVNS. Complete KES nerve block was verified using the aforementioned procedures and the same experimental protocol (Figure 23C) was carried out. TNF-$\alpha$ ELISA (Figure 27A) showed elevated serum TNF-$\alpha$ levels, similar to those previously reported in cVNx animals (Borovikova et al., 2000).

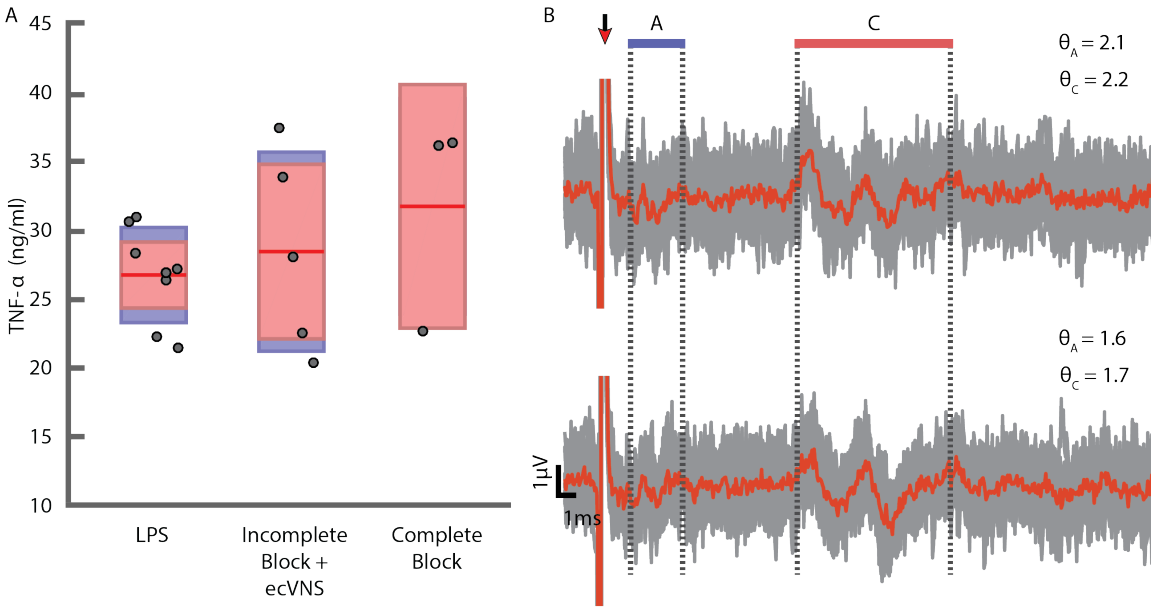


**Figure 27:** Incomplete afferent KES nerve block and KES nerve block alone are not sufficient for activating anti-inflammatory pathways. (A): TNF-$\alpha$ expression from control (LPS, n = 8), incomplete afferent KES nerve block and paired ecVNS (Incomplete Block+ecVNS, n = 5), and complete afferent KES nerve block only (Complete Block, n = 3). (B): Example ENG measurements from the caudal end of the cVN during incomplete afferent KES nerve block. Average waveforms (red) are superimposed upon individual runs (grey), with $\theta$ presented for each CAP component. Red arrow indicates stimulus artifact. This example is from an experiment in which the calibration period was successfully completed, however post-hoc analysis revealed that afferent KES nerve block was incomplete. The A fiber component is partially blocked, however not complete, and the C fiber component is unmodified compared to baseline measurements.

## *5.7 Discussion*

Suppression of systemic and local inflammation via eCVNS has the potential to be a powerful clinical strategy. When used on the bench top, investigations typically transect and stimulate the peripheral end of the vagus. In this report, we demonstrate the ability to conduct a virtual vagotomy via KES nerve block, which is feasible at the bedside. Our primary results are that 1) KES can block evoked nerve activity that is equivalent to nerve transection and 2) KES nerve block alone is insufficient for activating the vagal anti-inflammatory pathways. These results have important clinical implications, as it allows for unidirectional electrical activation of the vagus nerve without the need to transect the nerve.

Results from previous investigations have demonstrated activation of the GSN during cVNS as well as the role of the GSN in regulating inflammation (Bratton et al., 2012; Martelli et al., 2014c). However this report is qualitative and only demonstrates the presence of an event upon supramaximal stimulation (Martelli et al., 2014a). We quantified activation of the GSN during cVNS using stimulation intensities (1 $mA_{pp}$ vs 0.5-2.0 mA) that are commonly used in clinical applications of cVNS (Koopman et al., 2016). Our stimulation parameters differ from those use clinically with respect to pulse width (0.4 ms vs 0.25 ms) and frequency (1 Hz vs 10-20 Hz). A direct relationship was found between cVNS stimulation intensity and the resulting sympathetic activation. Transection of the nerve at either cranial or caudal ends of the stimulating electrode revealed that this activation is predominantly due to activation of afferent pathways (Figure 24). These results suggest that increased stimulation intensities result in greater activation of the GSN, which carries sympathetic activity to a majority of visceral organs responsible for maintenance of homeostasis. It has been shown that chronic SNS activity drives local persistent inflammation leading to deleterious side effects like cachexia and increased blood pressure (Laviano et al., 2008; Brooks et al.,

1981). Thus, while direct activation of the sympathetic splenic and splanchnic nerves can offset inflammation, chronic activation of the GSN in patients receiving cVNS is not a clinically viable strategy.

To the best of our knowledge, this is the first report applying KES nerve block as a tool for achieving a virtual vagotomy and selective efferent stimulation. Furthermore, we establish a robust method and criterion, called block efficacy, for evaluating the status of KES nerve block. This approach enables quantitative validation and evaluation of the effects of KES nerve block. Quantification of block efficacy throughout the experiment (Figure 26B-E) enables detection of changes in block efficacy and thresholds during application. No significant differences were observed in our experimental cases. It is possible that changes in block efficacy and thresholds may present themselves on longer timescales than those employed here.

In addition, although not evaluated here, it is possible that long-term delivery of KES may lead to physiological changes in nerve conduction, as well as excitability of the nerve. In the present study, a post-hoc assessment of nerve viability was conducted as a binary test for ensuring continued conduction of nerve activity post-KES delivery. Post-hoc assessment (described in Methods section) was conducted in each experiment but limited in time due to the need for blood collection. In each experiment, post-hoc assessment successfully resulted in ENG measurements not significantly different than baseline ENG measurements (Figure 25B).

We previously demonstrated the ability to use KES nerve block for selective block of A or C fiber components in mammalian (Patel et al., 2015) and amphibian (Joseph et al., 2011) animal models. The current investigation employed KES nerve block as an all-or-none technique. It is critical to note, however, that the use of selective KES nerve block may be useful in cases where selective block of A or C fiber activity is desired. Moreover, the mammalian cVN consists of fibers from A, B, and C fiber classes (Agostoni et al., 1957). Our experimental setup, limited by exposed nerve

length and electrode spacing, allowed investigation of only A and C fiber components at a macro scale. To validate block of all fiber classes and sub-types, along with selective KES nerve block, larger animal models in which a greater exposed nerve length is attainable is necessary.

In a subset of experiments (n = 5), post-hoc analysis revealed that block was incomplete (Figure 27), resulting in increased serum TNF-$\alpha$. Although calibration was conducted in each experiments to determine block threshold for each experiment (Figure 26A), and ENG measurements were visualized online, it is possible that failure to maintain block could have occurred from changes at the electrode-tissue interface or stimulation equipment. While it is possible for direct current (DC) to contaminate the effects of KES nerve block, it is unlikely because equipment was calibrated prior to starting KES nerve block. Furthermore, DC contamination leads to damage of nervous tissue and can result in uncontrolled and unwanted amounts of either DC stimulation or DC nerve block (Franke et al., 2014b).

The experimental methods and data analysis methods used in this study suggest one potential framework for clinical use of KES nerve conduction block. First, application of KES nerve conduction block requires a valid readout with temporal dynamics on the order of milliseconds. In our case, we used ENG measurements from the cVN to directly assess the effects of KES nerve conduction block on evoked cVN activity. Without such a readout, selection of the appropriate KES amplitudes and thresholds is difficult. Second, a baseline of what activity is to be blocked must be set. In the present investigation, we utilized the RMS voltage of evoked CAPs as the activity to block. Finally, the required duration of KES nerve block must be known for each nerve and physiological function of interest. These three elements may be incorporated into an implantable device for chronic use, or could be utilized acutely in patients through on-nerve electrodes with percutaneous leads.

One side-effect previously reported during application of KES nerve block is an

initial brief period of asynchronous activation of the nerve (Patel et al., 2015; Joseph et al., 2011; Miles et al., 2007). This response, coined the onset response, is typically short lived ($< 100$ ms) and occurs immediately after initiating KES nerve block. This asynchronous activation is removed from our recordings by the online filtering and post-hoc stimulus-triggered averaging of ENG measurements. Although not measured in our experiments, it is possible that the onset response was present in the form of laryngeal muscle activation. On-going investigations will attempt to quantify laryngeal activation during KES nerve block of the vagus.

Our studies and results presented here utilized the standard protocol for investigating neuromodulation of systemic inflammation on the left cVN. Additional pilot experiments (unpublished) were carried out to investigate the effects of bilateral cVNS and KES nerve block. These data suggest that no additional benefit could be achieved through bilateral neuromodulation similar to previous reports (Willemze et al., 2015). We also conducted a pilot study to investigate the necessity of the pre-stimulation period for down-regulation of systemic inflammation. Animals were subject to the same stimulation protocol described above, but without the pre-stimulation period. These additional data suggest that the pre-stimulation period has little to no effect on modulation of LPS-induced systemic inflammation. However, both pilot studies require additional experimentation to confirm significance to these findings.

It is clear that systemic inflammation can be modulated through cVNS, as shown by this report and others. How exactly the nervous system modulates systemic inflammation is a topic currently undergoing significant scientific inquiry. It is valuable to highlight knowns and unknowns about the mechanism of action for modulation of systemic inflammation through cVNS. The cholinergic anti-inflammatory pathway posits that the VN is the efferent arm of the inflammatory reflex. The hypothesized mechanism is that parasympathetic efferent fibers in the VN innervate post-ganglionic sympathetic splenic neurons in the celiac ganglia with axons in the splenic

nerve. Stimulation of efferent cVN pathways leads to modulation of the postganglionic splenic neurons and results in suppression of splenic TNF-$\alpha$ production. This mechanism of action has received significant debate due to evidence from anatomical investigations demonstrating little or no direct cholinergic vagal innervation of the spleen (Nance et al., 2007), from physiological studies demonstrating the need for intact GSN and splenic nerve (Huston et al., 2006), and electrophysiological studies, including this report (Figure 24), showing no measurable connection between ecVNS, the GSN, or the splenic branch of the GSN (Bratton et al., 2012).

Alternative hypotheses related to mechanism exist, such as the VN controls splenic nerve activity in an indirect manner through CNS reflex, but not by a direct efferent VN pathway (Bratton et al., 2012). In addition, we would be remiss to ignore the possibility that the effects of cVNS could be of non-physiological origin, and due to activation of afferent and efferent pathways in synchronous or asynchronous manners that drive physiological function to its limits. These contrasting mechanistic and functional results warrant the need for further investigation into the mechanism of action, especially as cVNS is utilized in clinical settings for long-term treatment of inflammatory conditions.

# CHAPTER VI

# MODULATION OF POSTPRANDIAL GLYCEMIA VIA SYMPATHETIC INHIBITION

## *6.1 Summary*

Mammalian blood glucose concentrations (i.e. glycemia) are maintained within well-defined biological limits despite considerable fluctuations in the rate at which glucose is obtained from food and utilized by tissues. Failure to achieve euglycemia (e.g., normal blood glucose levels) can result in significant physiological complications such as diabetes and hypertension, clinically referred to as metabolic syndrome. Glycemia is regulated by both hormonal and neural control mechanisms, with a majority of investigations focused on hormonal regulation. Recent investigations suggest that chronically increased sympathetic input to the visceral space contributes to the development of metabolic syndrome (Thorp et al., 2015; Schlaich et al., 2015). We investigated the role of sympathetic input to the visceral space through both denervation and Kilohertz Electrical Stimulation (KES) nerve block of the Greater Splanchnic Nerve (GSN).

This work was done in collaboration with Laura O'Farrell, Lian Sheng Liu, and Pankaj Jay Pasricha. Financial support for this work was provided by GlaxoSmithKline, National Institutes of Health (Grant 2R01EB016407-09A1), and the Georgia Tech TI:GER program.

## 6.2 Background

Glucose metabolism is controlled by multiple organs including liver, stomach, duodenum, and intestines which are themselves controlled by both neural and hormonal input (Wehrwein et al., 2016; Teff, 2008). Upon delivery of a stimulus (i.e., a candy bar), nerves and hormones coordinate to process the stimulus and restore glycemic homeostasis (i.e. normal blood glucose levels). The hormonal messaging system is well understood, unlike the neural messaging system. Hormonal messaging is predominately mediated by the pancreatic hormones insulin and glucagon, which have opposite effects on blood glucose levels. Similarly, the neural messaging system occurs via the sympathetic and parasympathetic pathways which might be predicted to also have opposite effects on blood glucose. These pathways originate in the hypothalamus and project to every organ in the visceral space, providing a mechanism through which organs can be modulated quickly and effectively.

Failure to sense or effectively regulate glucose metabolism can lead to the development of a variety of metabolic complications, such as type 2 diabetes, hypertension, and obesity. In addition, impaired glucose metabolism has been hypothesized to play a role in neurodegenerative diseases, such as Parkinson's and Alzheimer's. Recent investigations hypothesize that development of T2D may be due to chronically elevated sympathetic activity (Thorp et al., 2015; Schlaich et al., 2015). Various investigations have assessed the role of sympathetic control of individual visceral organs through denervation studies, in which the sympathetic input to the target organ is cut or chemically ablated.

The role of complete visceral sympathetic denervation, as opposed to organ-specific denervation, in regulating glycemia is unknown. The Greater Splanchnic Nerve (GSN) is the predominant source of sympathetic neural input to the viscera (Kuntz et al., 1957). In addition to efferent sympathetic fibers originating in the

hypothalamus, the GSN contains spinal afferents which are implicated in conveying information related to visceral pain, metabolite concentrations, and organ states (Celler et al., 1981; Furness et al., 2001; Barrett et al., 1985). Transection of the GSN has been assessed in humans for treatment of hypertension (Peet, 1935; Freyberg et al., 1937; Hoobler et al., 1951), but the effects of splanchnicectomy on glucose metabolism remain unclear. We investigated the role of sympathetic input to the viscera through chronic bilateral denervation studies of the GSN utilizing multiple animal models of T2D with the hypothesis that removal of visceral sympathetic input increase glucose tolerance, a clinical measure used to characterize the severity of T2D. We then assessed the utility of KES to block GSN activity in acute, anesthetized experiments.

## *6.3 Experimental Methods for Denervation Studies*

### *6.3.1 High Fat Diet (HFD)*

The High Fat Diet (HFD) model is an accepted model for diet-induced obesity in rats. After a few weeks of a high fat diet, animals develop obesity as well as T2D symptoms, including insulin sensitivity, glucose intolerance, and hypertension. Sprague-Dawley rats (Harlan Sprague Dawley Inc., IN, USA) were fed a ND (T.2014) or HFD (60%, TD.06414) for eight weeks prior to collection of baseline metabolic parameters and under-going bilateral denervation. Body weight was monitored weekly prior to surgery and every 4 weeks after. Serum insulin and urine Cuchulain measurements were made prior to bilateral GSNx. Glucose tolerance and blood pressure were measured every 4 weeks for up to 12 weeks. Figure 28A depicts the general study timeline.

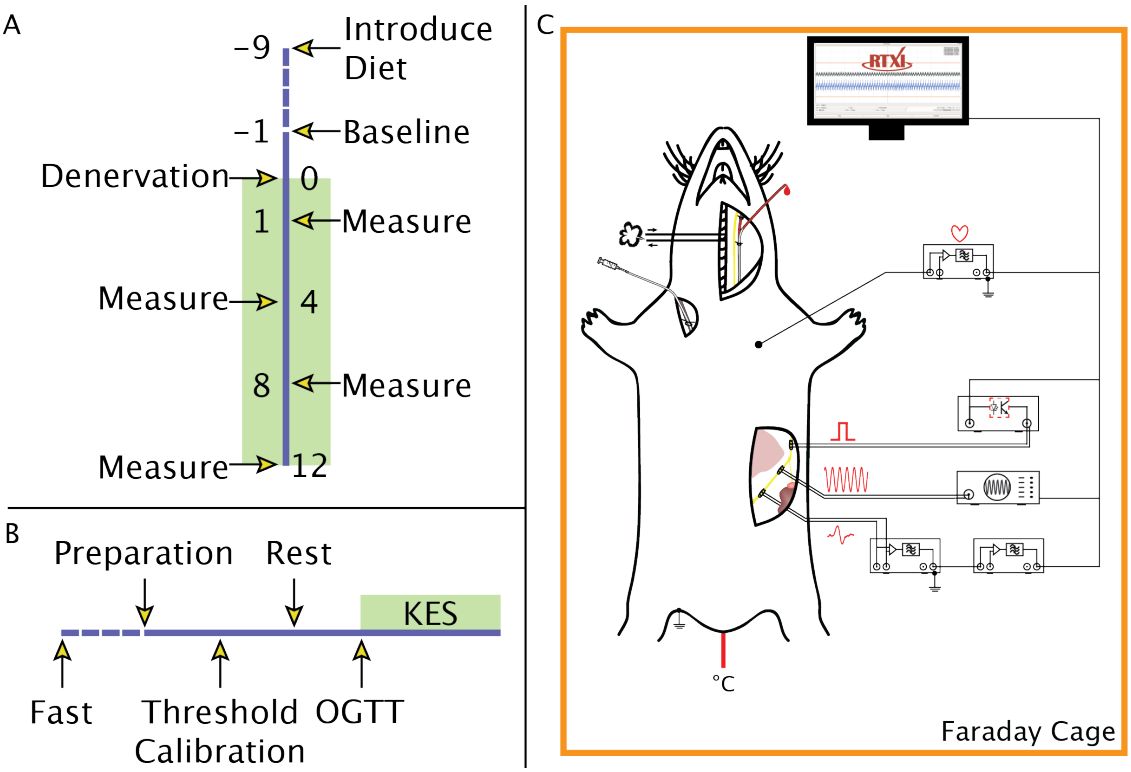


**Figure 28:** (A) Chronic denervation study timeline and protocol. Animals are randomly assigned to a diet group (normal or high fat) 9 weeks prior to bilateral denervation of the GSN. Animals remain on their respective diets throughout the study duration. Body weight is monitored weekly before denervation and then every 4 weeks after surgery. Baseline oral glucose tolerance tests and blood pressure measurements are made 1 week before surgery and used as a baseline for each animal. Animals are allowed to recover one week and then measurements are made every 4 weeks. Oral glucose tolerance tests, blood pressure, body weight, serum insulin, and fasting glucose are measured until the conclusion of the study (12 weeks). (B) Experimental protocol for acute KES nerve block studies. Animals are fasted overnight (approximately 12 hours). Animals are anesthetized and undergo surgical procedures for placement of catheters and electrodes. A threshold calibration trial is conducted in each animal, including Sham group animals. Animals are allowed to rest for a 30 minute period prior to start of the oral glucose tolerance tests. (C) Electrophysiology setup used for KES nerve block studies. The entire setup is configured to electrically float with the animal as the ground. Animals are ventilated and heart rate and core temperature are monitored.

### *6.3.2 Bilateral Greater Splanchnic Nerve transection (GSNx)*

All animal care and procedures were reviewed and approved by the Institutional Animal Care and Use Committee at The Johns Hopkins University and all methods were performed in accordance with National Institute of Health guidelines and regulations. Animals were anesthetized in a chamber using 5% isoflurane (1 liter/min flow rate). Once recumbent, the animal was maintained at 2% isoflurane for the remainder of the surgical procedure. The right GSN was exposed via a dorsolateral incision and subcostal muscle penetration. The post-suprarenal ganglia segment of the GSN was identified and transected with micro-scissors under a high magnification dissection microscope. The procedure was carried out on the contralateral side to identify and transect the left GSN. Both incision sites were sutured closed and the animal allowed to recover for one week. Animals in the sham groups received the exact same surgical procedure but nerves were not transected.

### *6.3.3 Oral Glucose Tolerance Test (OGTT)*

Oral glucose tolerance tests (OGTT) assess how fast a known amount of glucose is cleared by the body and identify the development of insulin sensitivity. Animals were fasted overnight with free access to water to deplete liver glycogen stores. The next morning, body weight and fasting glucose levels were measured via the tail using a handheld glucose meter (Bayer Hearthrug LLC). At same time, $\sim 50\mu$l of blood was collected and kept on ice for the serum insulin assay. A 10% glucose solution was then orally administered (1g/kg, 10ml/kg) and blood collected for glucose measurement and insulin assay 30, 60, 90 and 120 min after the gavage. OGTTs were performed 1, 4, 8, and 12 weeks post-surgery in conscious animals between the hours of 10AM and 2PM. Tail wounds were treated with Iodine after each procedure.

### *6.3.4 Non-invasive blood pressure measurement*

Blood pressure was measured in conscious animals using a non-invasive tail-cuff system (CODA, Kent Scientific, CT, USA). To reduce stress-induced variability, animal were trained by placing the animal in the measurement chamber for 15 minutes for 3 consecutive days prior to data collection. On the data collection day, animals were placed in the measurement chamber for 15 minutes prior to data collection. Measurements were made under a constant chamber temperature (32-35°C). The average of 20 pressure cycles were recorded as the mean, systolic, and diastolic pressures for each animal. All blood pressure measurements were made between 10AM-3PM.

### *6.3.5 Serum Insulin*

Blood samples were collected from conscious animals during OGTTs to assess changes in serum insulin levels resulting from GSNx. Serum (10 $\mu$l) was obtained by centrifuging blood collected during OGTTs and assayed using an ultra-sensitive enzyme-linked immunosorbent assay (ELISA, Crystal Chem #90060).

### *6.3.6 Urine Catecholamine*

Urine catecholamine can be used to evaluate tonic levels of sympathetic activation. Urine samples were collected over 24 hours before surgery, and 1 and 8 weeks after surgery from conscious animals. Urine epinephrine, norepinephrine, and dopamine were assayed using respective catecholamine ELISA kits (Rocky Mountain diagnostics Inc., CO, USA).

## 6.4 Experimental methods for acute KES block of the GSN

### 6.4.1 Animal preparation

All animal care and procedures were reviewed and approved by the Institutional Animal Care and Use Committee at The Georgia Institute of Technology and all methods were performed in accordance with the relevant guidelines and regulations. *In vivo* experiments were carried out on the left GSN of adult male Sprague-Dawley rats (Charles River Lab, MA, USA). Animals (378 $\pm$ 68 g, n = 20) were brought to the lab after an overnight fast and allowed to acclimate for approximately 30 minutes prior to being anesthetized with pentobarbital (50 mg/kg, IP). Animals were kept in their homecage under a heat source for approximately 20 minutes after delivery of pentobarbital to reach surgical anesthetic depth. Lidocaine (2%, 50$\mu$l) was injected subcutaneously on the ventral surface of the neck prior to shaving the ventral surface of the neck and abdomen.

The experimental protocol for all acute KES block studies is shown in Figure 28B. The animal was placed on the surgical table and body temperature was monitored and maintained at 36 - 38°C with a rectal temperature probe (TM-3, Warner Instruments, Hamden, CT) and recirculating water heater. Heart rate was monitored using subcutaneous fine wire EMG above the thoracic region and oxygen saturation monitored using a pulse oximeter (Physiosuite, Kent Scientific, CT, USA).

A midline incision was made at the neck and the skin and subcutaneous muscles tissues were retracted via blunt dissection to expose the trachea. A tracheotomy was performed to allow artificial ventilation of the animal (90 breaths per minute, MicroVent 1, Hallowell EMC, MA, USA). The salivary glands, sternocleidomastoideus, and omohyoideus were repositioned to allow access to the carotid sheath. The carotid

artery was isolated without perturbing the vagus or the cervical sympathetic chain and a heparin-filled polyethylene (PE-20) catheter inserted 23mm into the carotid artery for blood collection. A second incision was made below and lateral to the first incision to expose the right jugular vein. A silicone catheter was inserted approximately 8-10mm for continuous infusion of pentobarbital (10% in NaCl, 1.1ml/hour) to maintain anesthetic depth for the remainder of the experiment. Finally, a polyethylene (PE-20) tube was inserted into the esophagus approximately 9-10cm for delivery of the glucose bolus. An incision was made along the linea alba to allow access to the viscera. The right GSN was identified by retracting the visceral organs and identifying the right kidney and adrenal gland. Once identified, the adrenal gland was gently retracted to identify the suprarenal ganglia, which was then followed to identify and isolate the right GSN. The right GSN was cut in all KES and Sham group animals part of the acute KES study. The same procedure was repeated to identify and isolate the left GSN. The GSN was isolated from surrounding fat. Electrodes (described below) were placed along the length of the GSN for stimulation, block, and recording of nerve activity (Figure 28C). Nerves were not desheathed or dissected. Animals were euthanized at the end of the experiment with an overdose of pentobarbital.

### *6.4.2 Electrophysiology*

All experiments were conducted in a Faraday cage with an electrically floating setup. A floating ground was established by a 20G needle inserted into the right gastrocnemius muscle of the animal and connected to the table. Control of experimental hardware, delivery of stimuli, and data acquisition were all achieved using The Real-Time eXperiment Interface (RTXI, Lin et al., 2010). Custom, bi-polar electrodes were made in-house to stimulate, record, and block activity in the GSN. In brief, braided stainless steel wires (#793500, A-M Systems, Sequim, WA) were threaded through silicone tubing (#807600, A-M Systems, Sequim, WA), spot-welded to platinum-iridium con-

tact pads and the outer surface of the cuff coated with polydimethylsiloxane (PDMS) for electrical insulation. Electrode impedance (1.53 ± 0.83 kΩ) was characterized at 1 kHz using the RTXI Impedance Analysis module. Both electrical and mechanical characteristics were evaluated prior to electrode reuse.

ENG measurements were differentially measured and amplified with a gain of 10 and filtered with a low-pass of $10^4$ Hz (SR560, Stanford Research Systems, Sunnyvale, CA). The measurement is then gained ($10^2$), low-pass filtered (8000 Hz), and gained again ($10^2$) using a high-order, low-pass filter (SR640, Stanford Research Systems, Sunnyvale, CA) prior to being digitized at 20 kHz (PCIe-6259, National Instruments, Austin, TX) in RTXI.

Biphasic constant current pulses (1 $mA_{pp}$, 0.4 ms, 1 Hz) for nerve stimulation were generated by an isolated constant current stimulator (DS3, DigiTimer, FL, USA) triggered by RTXI. Block of nerve activity was achieved using a high frequency current source (6221, Keithley, OH, USA). Experimental timing for electrical stimulation, infusion, and measurement timing were controlled using RTXI. The complete electrophysiology setups used in this study are shown in Figure 28C.

### *6.4.3 Sample collection*

Blood was collected from acute KES studies at a total of 5 time points (0, 30, 60, 90, and 120 min) for glucose measurement and serum assays. A total of 400$\mu$l of blood were collected, centrifuged (2000g, 10 minutes), and serum collected and stored at -80°C for serum insulin assay. An equivalent volume of saline was used to replace the collected blood. An additional 2 measurements (150 and 180) were made for measurement of glucose only.

### *6.4.4 Nerve block experiments*

KES nerve block was utilized to mimic the effects of GSNx in acute preparations to determine if glycemic benefits could be achieved. Once surgical preparation was complete, a calibration trial was conducted to identify the specific KES amplitude for use in each experiment at 20 kHz. The nerve was stimulated at a rate of 1 Hz and single trial ENG measurements (Figure 29) were used to determine the KES threshold (amplitude). KES amplitudes started at 0.1 $mA_{peak}$ and were increased in steps of 0.1 $mA_{peak}$ until the block threshold was identified. Both stimulation and block were turned off after identification of the block threshold. Calibration procedures lasted approximately 120 seconds in each experiment. Post-experiment visualization and electrophysiological assessment of nerve viability were conducted by stimulating the nerve to evoke CAPs. Sham animals received the same surgery, the right GSN was transected, and the calibration trial performed, but the OGTT was performed without KES nerve block. A third control group was added which received bilateral GSNx and OGTTs under anesthesia for comparison against KES nerve block results.

### *6.4.5 Biochemical Analysis*

Serum insulin was assayed using commercially available ELISA kits (589501, Cayman Chemical, MI, USA). Blood glucose levels were measured using a handheld glucose meter (Contour Next, Bayer Healthcare, Berlin, Germany).

### *6.4.6 Data Analysis*

All data analysis was performed using standard MATLAB toolboxes (Mathworks, MA, USA). T-tests were performed using the MATLAB statistics toolbox (ttest2 function). All statistical tests were carried out with $\alpha = 0.05$. Glucose and insulin curves from OGTTs were integrated using the trapezoidal rule (trapz function).

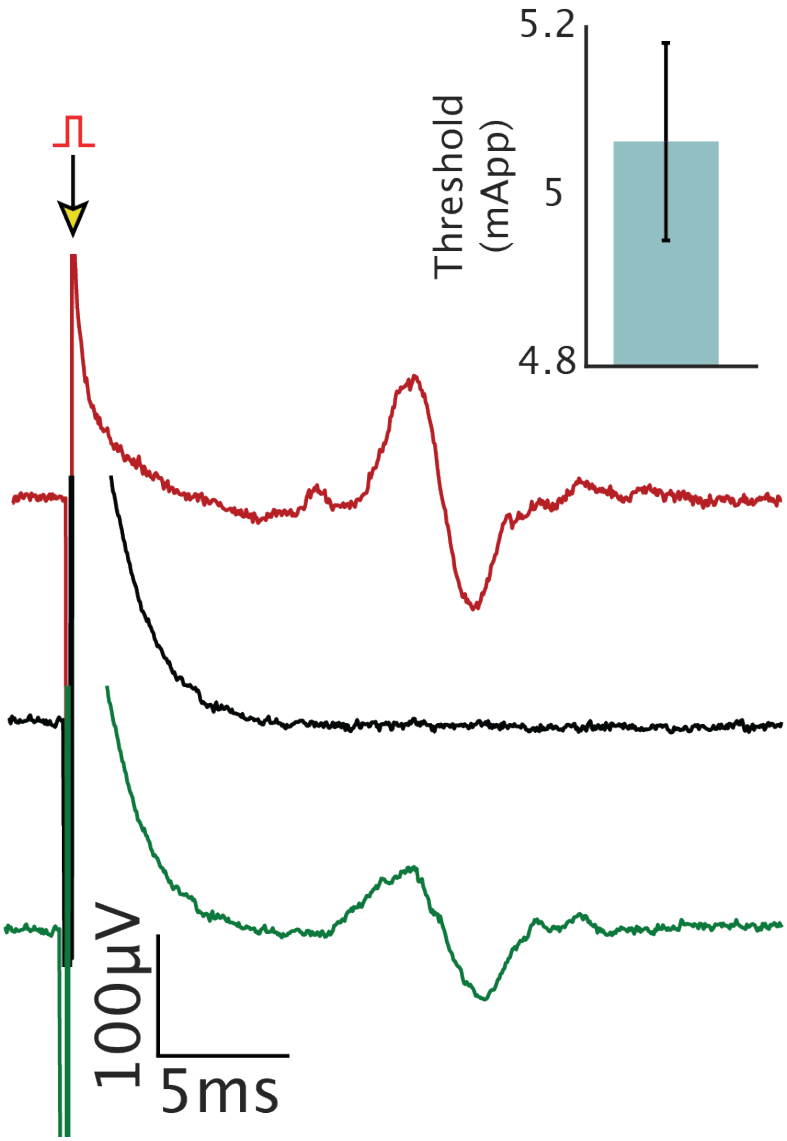


**Figure 29:** The red trace depicts a typical electrically evoked CAP from the left GSN. When KES nerve block is delivered at threshold, the evoked CAP is blocked (black trace). When KES nerve block is turned off, measurable CAP activity returns (green trace). Inset depicts the mean±standard error of the KES block thresholds determined during each calibration trial for animals in the KES and Sham groups.

## 6.5 Results

### 6.5.1 GSNx alters body weight profile of ND animals

Body weight provides is a gross and global measurement for metabolic function. We monitored the weight of both ND and HFD animals before and after surgery to evaluate development of HFD-induced obesity, glucose intolerance, and hypertension. Figure 30 depicts growth profiles of ND and HFD animals used in this study. Both HFD groups (Sham, GSNx) display identical growth curves, suggesting minimal to no effect of GSNx on the development of HFD-induced obesity. In contrast, ND animals that received GSNx displayed a decreased body weight profile and a statistically significant difference in weight 12 weeks post-GSNx compared to ND-Sham animals. Both ND-GSNx and ND-Sham animals displayed different profiles prior to GSNx. The transient decrease observed at week 1 in all animal groups represents typical post-surgical weight loss.

### 6.5.2 Fasting glucose levels reduced after GSNx

Fasting glucose levels are a standard clinical measure used to identify the presence of insulin sensitivity. We monitored fasting glucose levels over the course of the study duration to determine if GSNx altered baseline glycemia in ND and HFD animals. Fasting glucose levels are measured after an overnight fast and prior to initiation of the OGTT. Figure 31 shows fasting glucose levels over the course of the study duration in all animal groups. Both Sham and GSNx animals display a decrease in fasting glucose levels 1 week post-surgery. Sham animals from both diet groups present elevated glycemia after the surgery, while all GSNx animals demonstrate a sustained decrease in fasting glucose levels. Statistical significance is only evaluated between Sham and GSNx animals of the same diet.

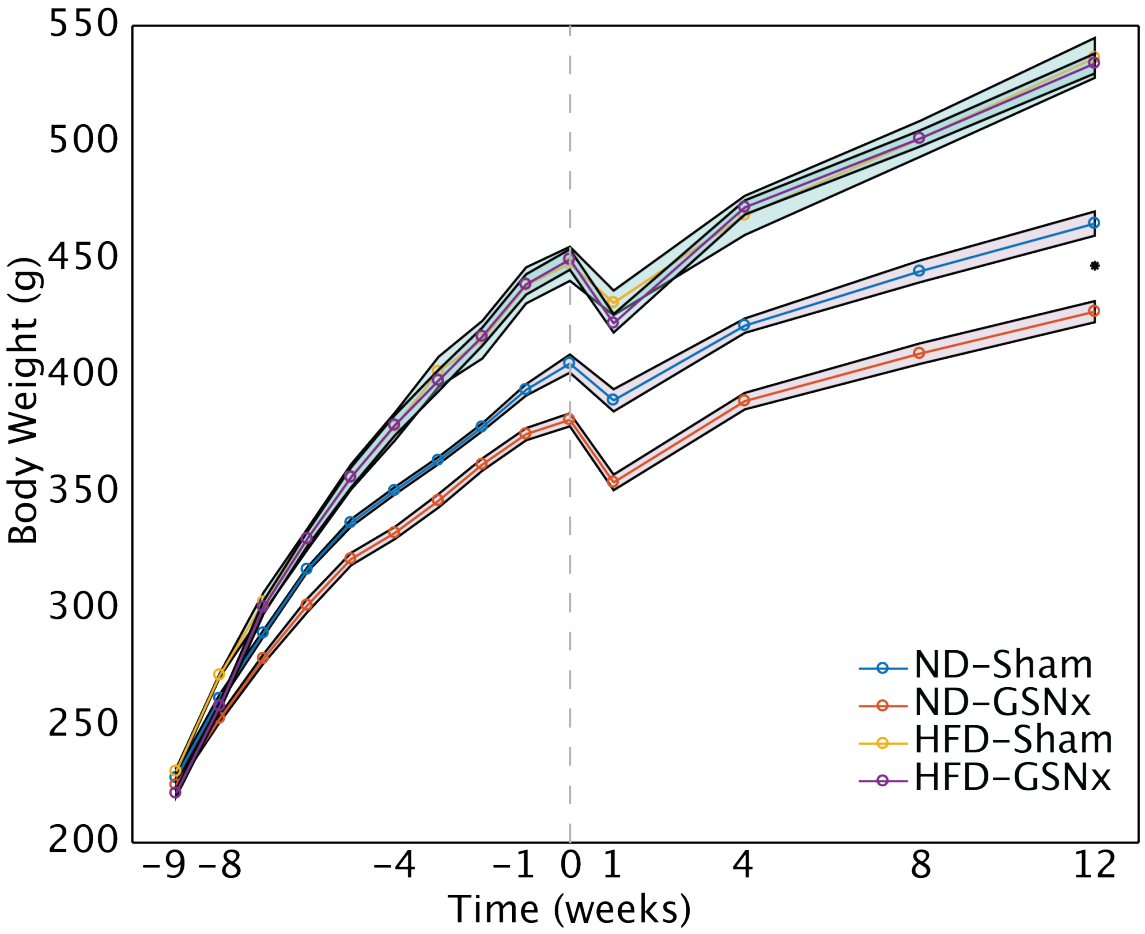


**Figure 30:** Weekly body weight measured in all animals over time. All HFD animals display increased body weight and development of HFD-induced obesity. In contrast, ND-GSNx animals display a shunted growth curve over time compared to sham ND animals, with a significant difference in body weight at 12 weeks post-GSNx. Mean±SE are shown. Grey line depicts surgical intervention. *Significant compared to corresponding animal from the same diet but different treatment.

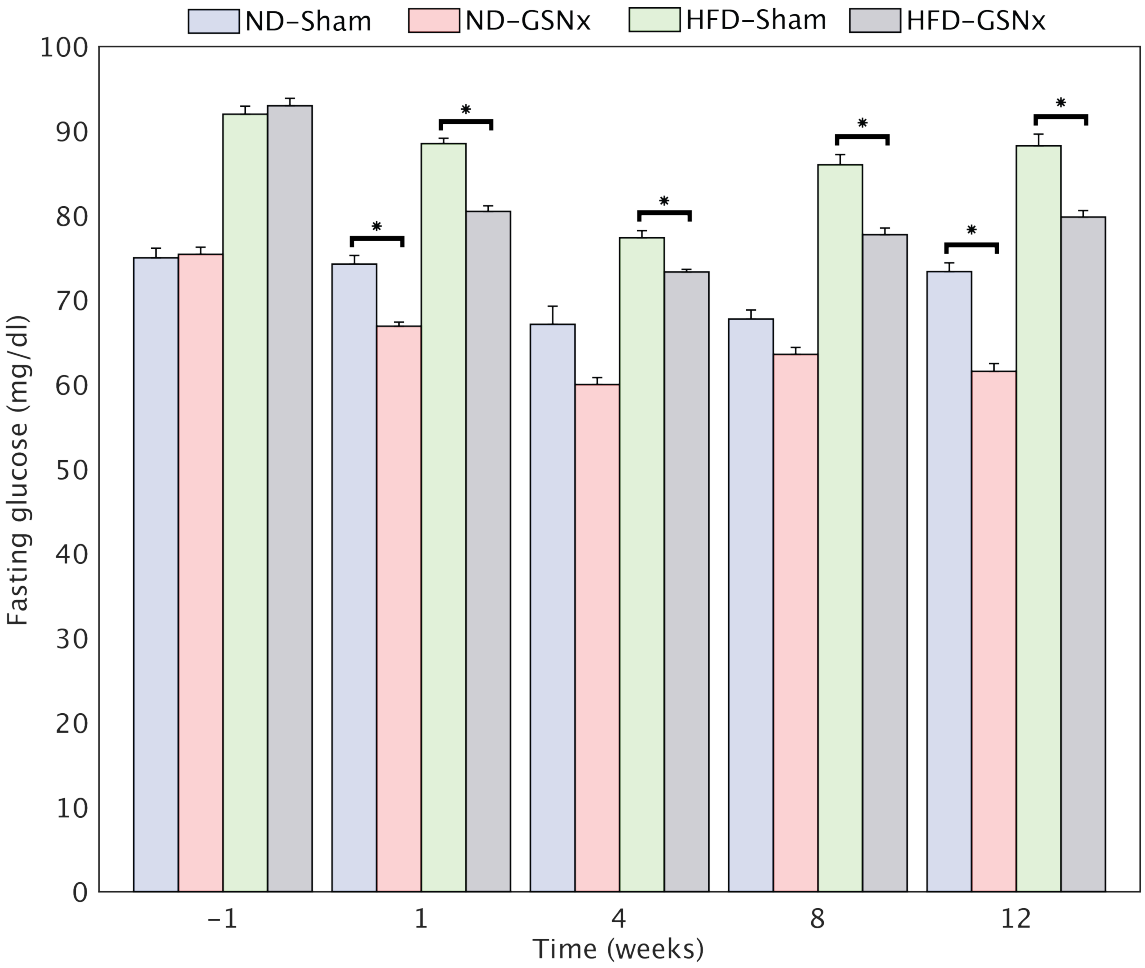


**Figure 31:** Fasting glucose levels over the course of the study duration. Glucose levels are measured prior to OGTT studies in conscious animals. *Significant compared to corresponding animal from the same diet but different treatment. Mean±SE are shown.

### *6.5.3 GSNx provides sustained increase in glucose tolerance*

Oral glucose tolerance tests allow characterization of the entire body's ability to respond to a known amount of glucose. Both ND and HFD animals were subject to routine OGTTs to determine the impact of GSNx over time. Figure 32 depicts glucose and insulin curves obtained from OGTTs in HFD-GSNx animals. The left panel of Figure 32 displays OGTT curves from before and after GSNx at multiple time points. A significant and sustained increase is observed in glucose tolerance after GSNx in HFD animals. Serum insulin levels 4 weeks are elevated in HFD-GSNx animals elevated relative to before GSNx, however do not show a significant difference compared to pre-GSNx.

Figure 33 shows glucose and insulin levels for all groups over time. Both glucose and insulin curves obtained from OGTTs are integrated with respect to time to obtain a scalar value that represents the total glucose or insulin in the blood or serum, respectively. Figures 33A-B show glucose and insulin for ND animals. ND-GSNx animals demonstrated a significant increase in glucose tolerance (i.e. reduced area under the curve) compared to ND-Sham animals for the duration of the study post-GSNx. In contrast, both ND groups present nearly identical insulin profiles at each timepoint.

Figure 33C-D show glucose and insulin data for HFD animals. Similar to ND animals, the HFD-GSNx animals present increased glucose tolerance, with significant differences up to 8 weeks post-GSNx. Serum insulin levels before and after GSNx are also nearly identical, but present continued development of HFD-induced obesity and insulin resistance as displayed by the increasing serum insulin levels between at 4 weeks post-GSNx.

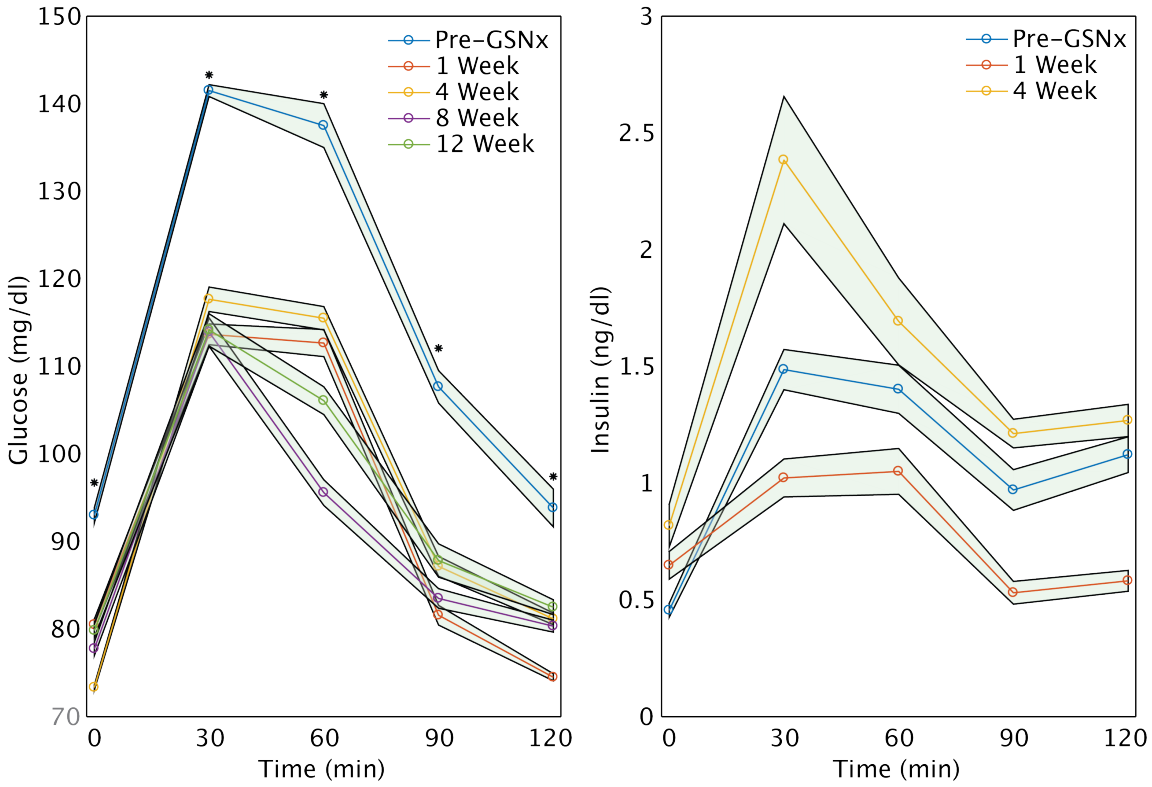


**Figure 32:** Mean±SE of glucose (left) and serum insulin (right) from oral glucose tolerance tests in HFD-GSNx animals. *Significant compared to corresponding time value in all other tolerance tests.

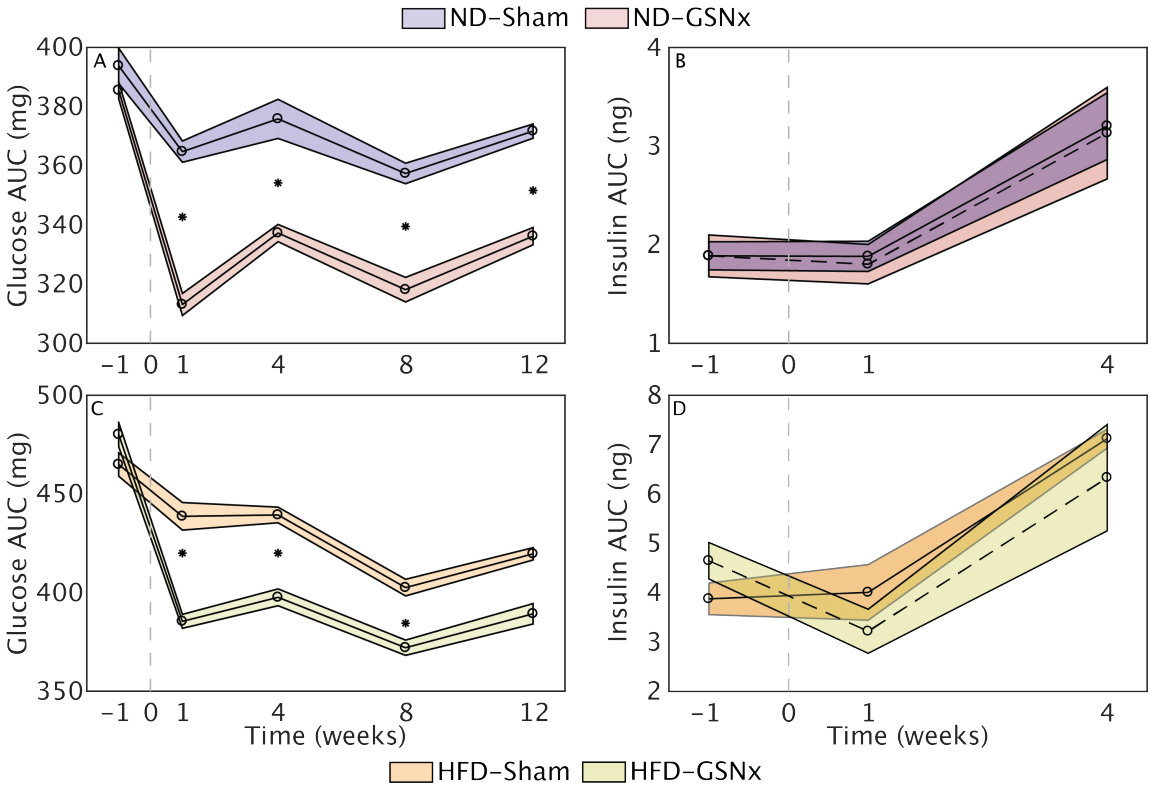


**Figure 33:** Area under the OGTT and insulin curves over multiple weeks in ND (A-B) and HFD (C-D) rats. GSNx significantly increases glucose tolerance with no significant difference in measured serum insulin levels for the study duration in both ND and HFD groups. Grey line depicts surgical intervention. Black line and corresponding shaded region represent mean±standard error. *Significant compared to corresponding animal from the same diet but different treatment.

### *6.5.4 Systemic blood pressure is reduced after GSNx*

The GSN contains a small population of efferent axons that play a critical role in modulating visceral and systemic blood pressure (Hoobler et al., 1951). Non-invasive measurement blood pressure measurements were made to characterize the effects of GSNx on blood pressure. Figure 34A-B show the routine systemic blood pressure measurements made in conscious animals and Figure 34C-E depicts the 4 week systemic blood pressure measurements in all groups.

Both ND-GSNx and HFD-GSNx animals demonstrated attenuated systemic blood pressure levels post-GSNx compared to their respective shams. The ND-GSNx animals displayed a sharp transient drop in systemic blood pressure 4 weeks post-GSNx but quickly returned to baseline (1 week post-GSNx) levels. HFD-GSNx animals showed a decrease in systemic blood pressure post-GSNx but return to HFD-Sham levels within the duration of the study. Figure 32C-E provide a snapshot systemic blood pressure in all groups at 4 weeks post-GSNx. Although not statistically significant, GSNx substantially reduced the diastolic, systolic, and mean blood pressure in ND-GSNx and HFD-GSNx animals.

### *6.5.5 Decreased systemic catecholamines contribute to physiological benefits of GSNx*

Upon activation, sympathetic neurons stimulate synthesis and release of epinephrine, norepinephrine, and dopamine in various visceral tissues. We collected and measured urine catecholamine levels to determine if denervation of the GSN, which is a sympathetic nerve, alters circulating catecholamine levels. Figure 35 depicts the changes in catecholamines observed in ND and HFD animals. Bilateral GSNx results in epinephrine levels below the detection limit of the assay and a substantial reduction in circulating norepinephrine and dopamine levels. In contrast, GSNx in HFD

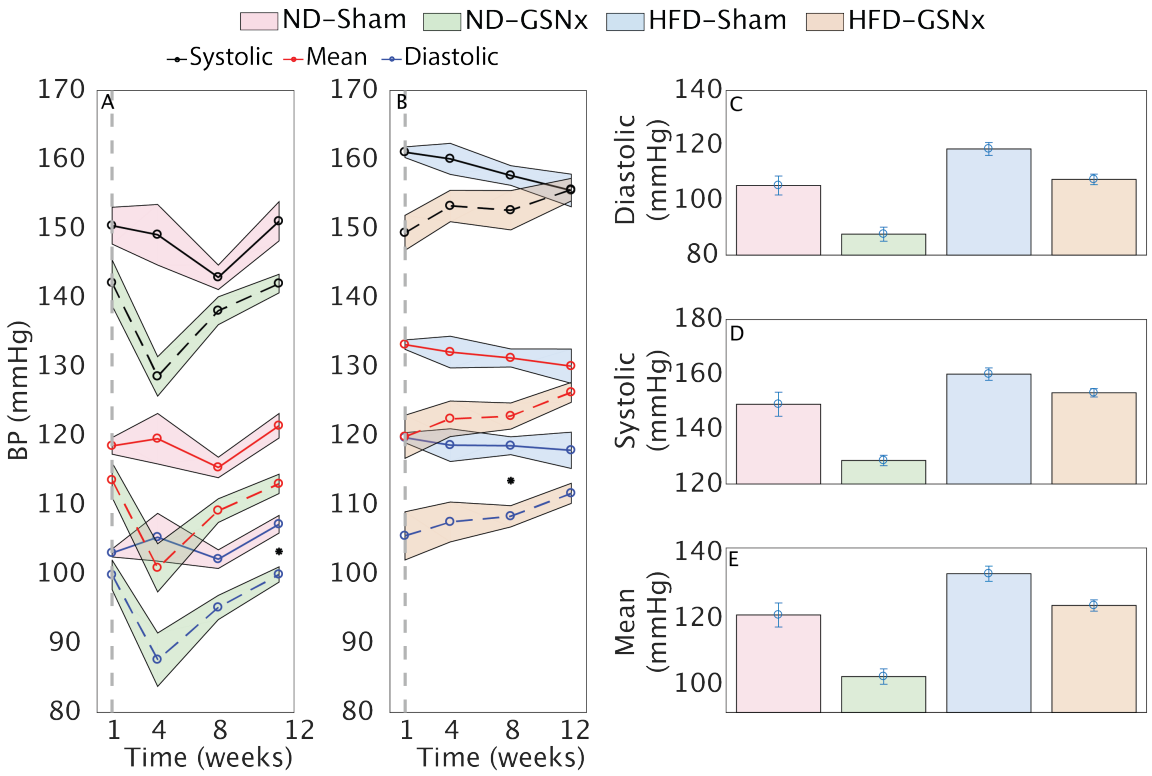


**Figure 34:** (A-B) Weekly systemic blood pressure measurements in all animals. Diastolic (C), systolic (D), and mean (E) pressure are shown 4 weeks post-surgery to depict differences across animal groups. *Significant compared to corresponding animal from the same diet but different treatment. Mean±standard error are shown in all cases.

animals reduced only epinephrine levels, with minimal impact on norepinephrine and dopamine.

### *6.5.6 KES nerve block of the GSN increases glucose tolerance*

Although clinically viable, denervation of nerves is challenging due to variable and uncontrollable regeneration of transected nerves. KES nerve block, which enables a local, reversible, and reliable block of nerve activity, is a clinically feasible modality for virtually transecting nerves in a controllable manner. We conducted acute experiments in ND Sprague-Dawley rats to determine if block of the left GSN, with right GSNx), enabled the same glycemic benefits as GSNx.

Figure 36 shows the glucose tolerance and serum insulin measurements obtained from anesthetized experiments using KES to block the left GSN. Sham animals, which underwent the OGTT without KES nerve block, presented lower levels of glucose tolerance compared to animals receiving either bilateral GSNx or left GSN KES nerve block. Animals receiving left GSN KES nerve block demonstrated identical glucose tolerance profiles to bilateral GSNx animals, with both groups having a glucose tolerance significantly higher than Sham animals. Serum insulin results from Sham, KES, and GSNx groups demonstrated no significant change.

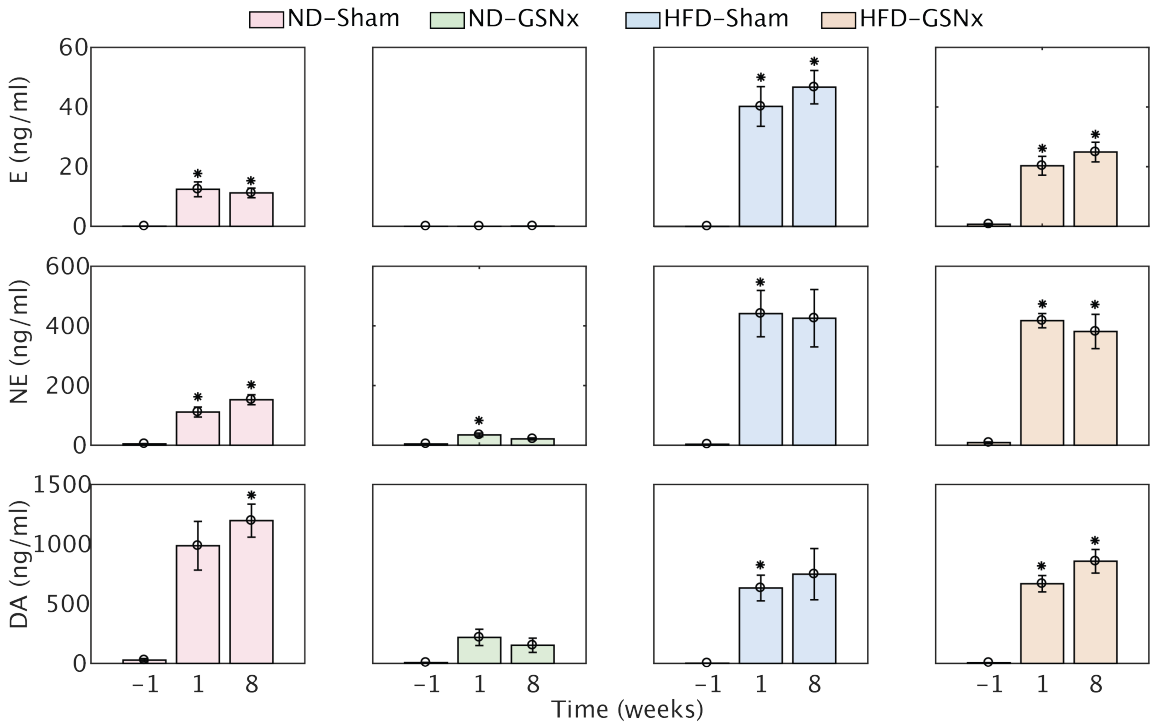


**Figure 35:** Urine (systemic) Epinephrine (E), Norepinephrine (NE), and Dopamine (DA) are shown along the rows for each animal group (columns). Each subplot represents measurements made before (-1) and after (1 and 8 weeks) GSNx. *Significant compared to pre-GSNx levels. Mean±standard error are shown for each catecholamine.

## 6.6 Discussion

Sympathetic hyperactivity is hypothesized to play a critical role in the development of metabolic syndrome. This work investigated the role of sympathetic input to the visceral organs by conducting both denervation and electrical stimulation-based studies, with the objective of understanding neural control and methods for obtaining therapeutic benefit.

In this report, we show the physiological impact of sympathetic denervation, particularly as it relates to the visceral organs in ND and HFD animals. Results from the long-term denervation studies suggest that removal of sympathetic input to the visceral organs can significantly increase glucose tolerance in both ND and HFD animals. Furthermore, we demonstrate that KES nerve block can mimic the metabolic effects provided by GSNx.

In long-term GSNx studies, we monitored body weight before and after GSNx. No significant difference was observed between HFD groups, however a significant difference was observed between ND-Sham and ND-GSNx groups 12 weeks post-GSNx. It is unclear if the significance at 12 weeks post-GSNx is truly significant due to the different body weight trends in both ND groups prior to GSNx. Regardless, all animal groups displayed typical growth curves, which is further exemplified by the elevated serum insulin levels measured 4 weeks after GSNx in both ND and HFD animals(Figure 33B and D).

One important distinction to be made is the effect of GSNx in normal (ND) vs disease (HFD) states. Characterization of fasting glucose (Figure 31) and glucose tolerance (Figure 33A) in ND animals suggests that the GSN plays a critical role in homeostatic regulation of glucose metabolism and that in disease states (Figure 33C), GSN activity is altered and contributes to the on-going development of disease symptoms. This baseline role of the GSN in glucose metabolism is also demonstrated by

the observation that the metabolic benefits of GSNx can be achieved instantaneously with KES in acute studies in ND animals. If the benefits to glucose tolerance were attributed to other neural or physiological modifications, then KES nerve block might not increased glucose tolerance in acute anesthetized studies.

We utilized KES nerve block unilaterally to increase glucose tolerance in ND anesthetized animals. One critical challenge for translation of KES nerve block is how it will be implemented in clinical therapies where it is necessary to interface with both left and right nerves. One potential solution is to implant two individual devices, however this increases the surgery time, increases the chances of failure and infection, and significantly increases the cost of the therapy. Alternatively, it may be feasible to achieve therapeutic benefit through unilateral modulation, however this remains to be evaluated.

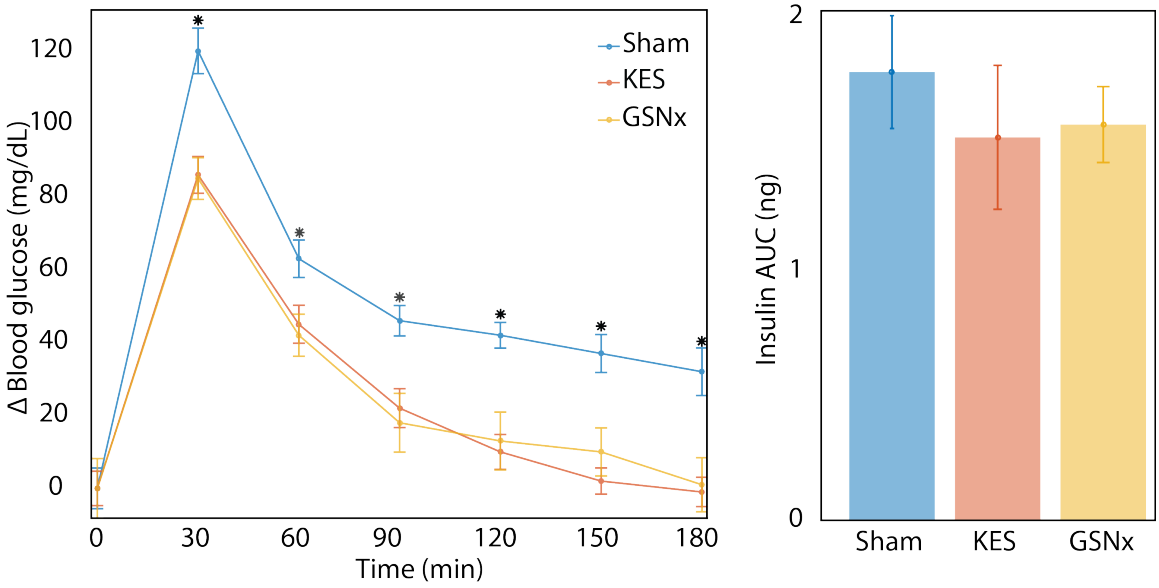


**Figure 36:** Oral glucose tolerance (left), insulin (middle), and mean arterial pressure (right) are shown from acute GSN KES nerve block studies. Glucose values are shown as the difference between the first and each subsequent measurement glucose measurement. Mean±standard error are shown in all figures with each group consisting of 6 animals. *Significant compared to glucose values at the same timepoint from other treatment groups.

# CHAPTER VII

# CONCLUSIONS

In this dissertation, I investigate and apply kilohertz electrical stimulation (KES) nerve block to autonomic neural circuits with the goal of understanding and modulating neural activity to restore homeostasis.

In part one of this thesis, I focus on different electrode characteristics as they pertain to KES nerve block. I demonstrate the role of electrode geometries in reducing electrical power required by KES nerve block therapies. My results demonstrate the importance of a proper electrode-tissue interface and the effect it can have on reducing the electrode-tissue impedance, and ultimately the power. I then evaluate the electrochemical behavior of electrode materials used in existing neural stimulation therapies at kilohertz frequencies. Results from these studies suggest that fractal coatings are identical to planar electrode materials such as Platinum-alloys at kilohertz frequencies. This identical behavior is predominately due to the fractal nature effectively being invisible to charge carriers at kilohertz frequencies.

In part two of this thesis, I use KES nerve block in multiple somatic and autonomic neural circuits to modulate nerve activity and restore homeostasis. I demonstrate the ability of KES nerve block to be selective towards fast (myelinated) and slow (unmyelinated) conducting axons in both the cervical vagus and sciatic nerves. Then I demonstrate the utility of KES nerve block to achieve directionality-specific stimulation of the cervical vagus nerve for upregulation of anti-inflammatory pathways. In the last chapter of this thesis, I demonstrate the ability of KES nerve block to enable robust and reversible denervation of the greater splanchnic nerve for increasing glucose tolerance.

Altogether, this thesis provides a case for further investigating KES nerve block as a potential bioelectronic therapy for modulating autonomic circuits involved in regulation of homeostasis.

# Appendices

# APPENDIX A.1
# HARD REAL-TIME CLOSED-LOOP ELECTROPHYSIOLOGY WITH THE REAL-TIME EXPERIMENT INTERFACE (RTXI)

## *1.1 Motivation*

The ability to experimentally perturb biological systems has traditionally been limited to static pre-programmed or operator-controlled protocols. In contrast, real-time control allows dynamic probing of biological systems with perturbations that are computed on-the-fly during experimentation. Real-time control applications for biological research are available; however, these systems are costly and often restrict the flexibility and customization of experimental protocols. The Real-Time eXperiment Interface (RTXI) is an open source software platform for achieving hard real-time data acquisition and closed-loop control in biological experiments while retaining the flexibility needed for experimental settings. RTXI has enabled users to implement complex custom closed-loop protocols in single cell, cell network, animal, and human electrophysiology studies. RTXI is also used as a free and open source, customizable electrophysiology platform in open-loop studies requiring online data acquisition, processing, and visualization. RTXI is easy to install, can be used with an extensive range of external experimentation and data acquisition hardware, and includes standard modules for implementing common electrophysiology protocols.

All the work presented in this manuscript is a result of the effort put in by many individuals. First, we would like to thank Calin Culianu, Jonathan Bettencourt, Risa Lin, and Francis Ortega for their significant and valuable contributions to the develop-

ment of RTXI that continue to be a part of its core. Next, we would like to thank authors of the highlighted use cases, Michale Skocik, Romuald Nargeot, Michael Boyle, Caroline Lustenberger, Sankar Alagapan, and Flavio Frohlich for openly providing data, figures, and feedback on this manuscript. In addition, the authors also thank Laura O'Farrell, Brian Kim, and Will Rountree for comments on the manuscript and how to communicate highly technical concepts in a simpler and effective manner. Most importantly, the authors would like to thank the RTXI user-community and greater open-source hardware/software communities for continued feedback, interest, and use of RTXI. Their contributions have helped develop a long-term, stable product that enables new paradigms of scientific investigations. Finally, we would like to thank the National Institutes of Health, which has financially supported the development and continued maintenance of RTXI for over 10 years (NIH grants R01RR020115 and R01EB016407, to DJC).

## *1.2 Introduction and Background*

Advances in stimulation (electrical, optical, biochemical) and measurement (electrical, biochemical, optical) techniques have increased the spatial and temporal resolution with which researchers can monitor or perturb biological activity. Using such tools and techniques in a closed-loop paradigm, where an acquired signal is used to compute the system output, can enable observation of physiological function, development and validation of computational models, as well as investigation of causal relationships in biological systems. This requires closed-loop control that operates on timescales that are physiologically relevant, which span tens of microseconds at the ion channel level to minutes at the behavioral level. Furthermore, the closed-loop control needs to be hard real-time (RT) - operating on a strict schedule for acquisition, processing, and yielding a computationally determined output with guaranteed performance bounds

appropriate for the timescales of interest. Such hard RT, closed-loop control is implemented in industrial applications (e.g, aerospace, robotics, stock markets); however its use in biological research is stymied due to the relative high cost of commercial systems, and lack of flexibility in customizing closed-loop protocols, performance, and features.

The Real-Time eXperiment Interface (RTXI) (RTXI, Figure 37) is an open source software platform for hard RT, closed-loop Data Acquisition (DAQ) and experimental control in biological experiments used by over 70 labs worldwide. RTXI is based on Xenomai, a Real-Time Linux framework (Barabanov et al., 1996; Gerum, 2004) and can be run or installed on any desktop PC by using the Live CD or by manually compiling the source code. RTXI can interface with an extensive range of external experimentation and data acquisition hardware, and includes standard modules for implementing commonly used electrophysiology protocols. Modules contain function-specific code that can be used in combinations to build custom workflows, experimental protocols, and interfaces, thereby eliminating the need to code all aspects of each experiment protocol from scratch. The power, flexibility, and stability of RTXI has made it possible for users to implement complex custom closed-loop protocols in a variety of cardiac (Groenendaal et al., 2014; Groenendaal et al., 2015; Brown et al., 2016; Devenyi et al., 2016; Bartolucci et al., 2015) and neuronal systems at the single cell (Idoux et al., 2011; Nabi et al., 2013), cell network (Wilson et al., 2014), animal, and human electrophysiology (Lustenberger et al., 2016) levels. Dozens of publications (Supplement 3H]) have used RTXI. Examples include investigation of the contribution of specific ion channels or synaptic receptors to spiking and bursting activity in a variety of neuronal cell types, oscillatory behavior of pacemaker neurons (Norman et al., 2016), the effect of network topology and intrinsic neuronal properties on population activity in a hybrid network (Kispersky et al., 2011), and effects of Transcranial Alternating Current Stimulation (tACS) on cortical activity

(Boyle et al., 2013; Lustenberger et al., 2016). Each example utilized RTXI to create a custom, hard RT closed-loop protocol with the goal of dynamically probing the target system.

This manuscript provides a technical and practical overview of RTXI's architecture and features, as well as highlights select novel applications. Functionality of RTXI's architecture and features has been validated both computationally through load testing and performance characterization, and experimentally in multiple setups of different biological systems and varying time scales.

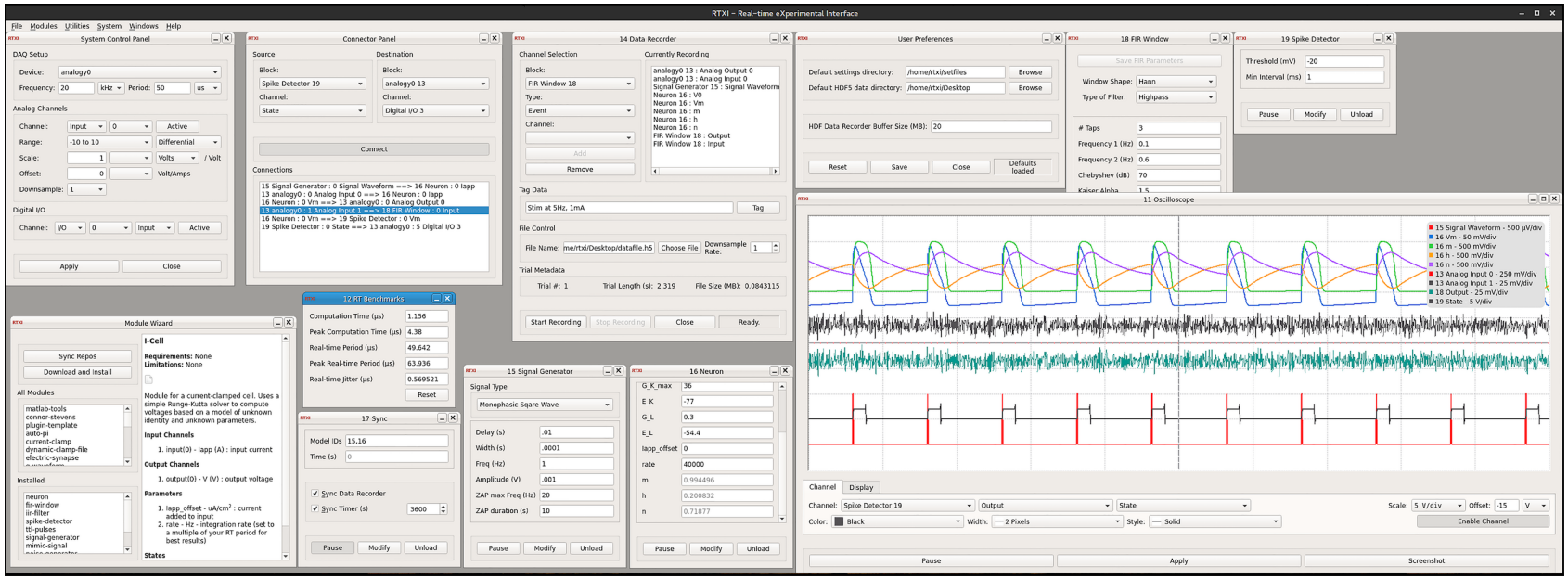


**Figure 37:** Screenshot of arbitrary RTXI workspace with core and custom modules. The workspace is intended to demonstrate the level of user-configurability provided by RTXI, such as channel configurations, combinations of data I/O connections, and saving virtually every programmed element of each module. Additional custom modules are shown (e.g., Spike Detector, FIR Filter, Signal Generator, Neuron Model, etc) to demonstrate the versatility of RTXI's API system for creation of any utility or model to be used in hard RT, closed-loop experiments. We refer the reader to the up-to-date user manual (Supplement 3D) and tutorials (Supplement 3E) available online for more information on how to navigate the RTXI workspace.

## 1.3 Design and Implementation of the Real-Time eXperiment Interface

### 1.3.1 System architecture

An RT control system for closed-loop control typically runs in an iterative computational loop with the smallest possible nominal cycle period, a minimum amount of cycle-to-cycle variation (jitter) in the actual period, and the shortest possible system latency (delay from input to computed output). Standard desktop computer operating systems, including Linux, are built upon a monolithic kernel whose scheduler is engineered to balance distribution of resources amongst the various active threads and respond to hardware and software triggered interrupts in a resource-efficient manner. This results in standard desktop operating systems providing only soft real-time performance. In soft RT systems, occurrence and timing of data acquisition, processing, and output generation events is neither guaranteed nor bounded. A lack of such guarantees can lead to substantial, yet often unnoticed, effects in experimental control (Economo et al., 2010; Butera et al., 2001; Raikov et al., 2004). For example, in the case of dynamic clamp (Bettencourt et al., 2008; Dorval et al., 2001; Prinz et al., 2004; Sharp et al., 1993), a soft RT system may occasionally wait so long to compute the injected current that the actual value of the membrane potential has changed significantly in the meantime. The resulting experimental dynamics may look acceptable but still be wrong, since they are based on incorrect assumptions about the state of the cell. In practice, this means that phase-dependent stimulation may be delayed or occur at the incorrect physiologically-relevant time.

To achieve hard real-time performance, RTXI uses a Real-Time Operating System (RTOS). An RTOS enables hard RT performance by modifying the operating system's native kernel architecture to enable priority-based pre-emption of processes,

allocation of memory, and communication with on-board hardware for data and file Input/Output (I/O). To enable hard RT control, RTXI uses Xenomai, a real-time framework, which installs a micro-kernel alongside the standard Linux kernel. The micro-kernel consists of its own scheduler and interrupt handler and places the standard Linux kernel in a low-priority state, allowing dedicated processes to be prioritized. For example, Xenomai's prioritization of RTXI enables hard RT control of periodic tasks such as sampling from experimental equipment, performing computations, and generating output signals. The use of an RTOS also minimizes system and hardware latencies, resulting in faster sampling rates, computation times, and file I/O. For some experimental designs with closed-loop feedback, a higher sampling rate also improves the stability of the protocol (Preyer et al., 2009).

### *1.3.2 Application architecture*

RTXI is written in C/C++ and utilizes three threads to process: 1) hard RT data acquisition and experimental control, 2) user interactions, and 3) data storage. Figure 38 provides an overview of the complete system architecture. The RT thread is instantiated with the highest system priority and controlled by the micro-kernel. The second user interface and experience (UI/UX) thread, powered by the Qt (*Qt*) and Qwt (*Qwt - Qt Widgets for Technical Applications*) Graphical User Interface (GUI) frameworks, processes user inputs to RTXI and online data visualization in soft RT. The final soft RT thread continuously reads and writes data to disk. With the advent of multi-core desktop computers, users are also able to instantiate additional soft RT threads for online data processing. All threads run in the same process address space, making it easy to share data for processing, updating visualizations, and data storage. RTXI's architecture allows it to be used as an open-loop experimental control and data acquisition system, or even as a simulation environment.

The RT thread wakes on each clock cycle and executes all DAQ operations, mod-

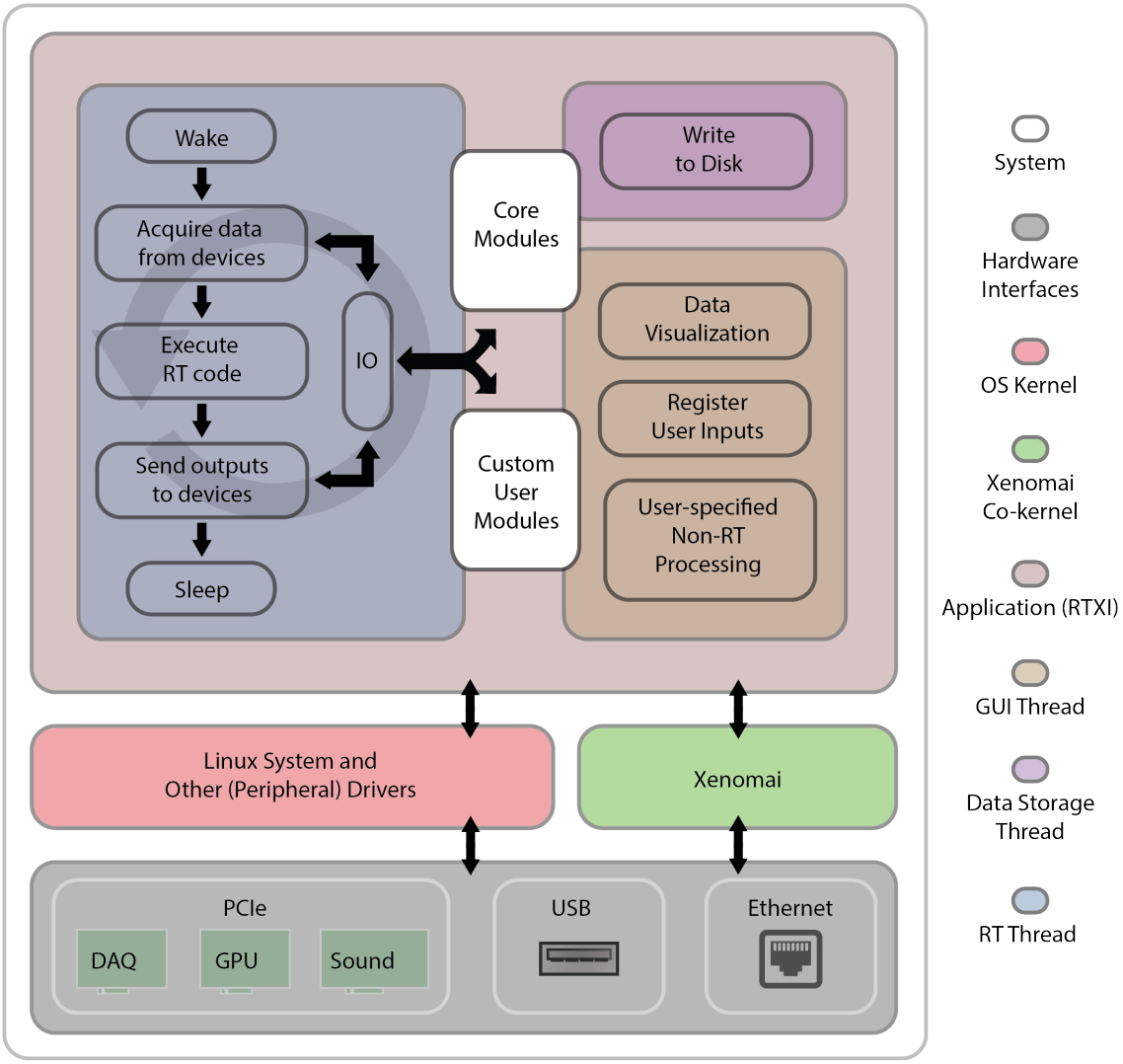


**Figure 38:** System architecture. The bottom block depicts the hardware layer with which RTXI interfaces. RTXI is capable of interfacing with DAQs using either PCI/PCIe, USB, or Ethernet interfaces (see Compatible hardware for more information). Hard RT communication with hardware devices is achieved through Analogy, a set of drivers within the Xenomai framework. The top block of the diagram illustrates the core architecture of RTXI. On each cycle of the RT period, the RT Thread wakes up, acquires new data, executes instructions defined within the hard RT function of both core and user modules (see Custom modules and Application Programming Interface (API)), outputs data to the DAQ, and returns to sleep (idle). Transmission of data to/from different modules is handled by the `IO` class. When the RT Thread is idle, resources are made available to other system applications and functions. The GUI and Data Storage Threads continuously run with a static period to provide a stable balance between hard RT performance and handling of user input, updating of visualizations, and data storage.

ule functions, and RT system functions. Module functions refer to both base system operations, such as transmitting data across modules and writing data to system buffers, and all RT operations implemented within custom modules. During this step, modules can post RT events - which notify other modules about state changes and user-initiated events, e.g., unloading or loading of new modules - to queue. These events are then executed by the RT thread once all module computations are complete.

An important advantage of this modular application architecture is the ability to load and unload both core system and user-created modules, change parameters, and modify any system variable online without halting closed-loop execution or affecting hard RT performance. Commercial systems, such as Simulink (MathWorks, Natick, MA), Signal (Cambridge Electronic Design, Cambridge, England), LabVIEW (National Instruments, Austin, TX), Tucker David Technologies (Alachua, FL) typically require halting execution and recompiling the modified loop prior to being able to continue execution. Open-source platforms, such as NeuroRighter (Newman et al., 2013), MANTA (Englitz et al., 2013), PLDAPS (Eastman et al., 2012), and the Open Ephys GUI (Siegle et al., 2015), provide closed-loop control with varying degrees of flexibility, but none enable hard RT closed-loop control. Such limitations are not ideal for investigation of causal relationships in biological systems.

### *1.3.3 Compatible hardware*

RTXI interfaces with experiments through a variety of hardware interfaces, including PCI/PCIe based DAQs, Ethernet based devices such as cameras and commercial amplifiers, as well as USB-based acquisition devices (Supplement 3C). The hardware used with RTXI should be chosen based upon the hard RT needs of the custom protocol. Devices interfacing through the PCI/PCIe and Ethernet interfaces are capable of providing hard RT closed-loop performance with the appropriate drivers.

PCI/PCIe hardware can achieve sub-millisecond latencies, while Ethernet devices can provide millisecond latencies. USB devices can provide closed-loop functionality with the appropriate driver, but the non-deterministic bounds of the USB protocol prevent hard RT control.

### *1.3.4 Portability and sharing*

RTXI allows users to move developed and tested modules, algorithms, and entire closed-loop protocols from one computer to another without significant overhead. Once the workflow and protocol have been set up, the entire workspace can be saved to an XML-based workspace settings file. This file saves all core system specifications set by the user, loaded modules along with their parameter and state values, and connections between modules. The settings file can then be used on any other computer with RTXI and the appropriate modules installed to restore the workspace. Furthermore, existing workspace settings files can be used as a starting point for creating new experimental protocols. This reduces the chances of errors when setting up a complex protocol with many modules and provides an easy mechanism for sharing custom protocols.

### *1.3.5 Core modules*

RTXI's base functionality (data acquisition, processing, and visualization) is achieved through core modules designed to provide hard RT closed-loop performance. A set of core modules with minimal computational overhead are compiled as shared object libraries during the RTXI installation process and linked to RTXI at run-time. This approach leads to lower system overhead and thus greater flexibility for users to define custom protocols that may require greater computational resources.

**System Control Panel.** The System Control Panel shown in Figure 37 is the primary interface for configuring RT system settings and DAQ I/O channels. The detected on-board DAQs are listed in the Devices drop-down menu (e.g., analogy0). Users can set the Frequency or Period of the RT system, which is used as the data acquisition and processing speed. All available Analog Input (AI), Analog Output (AO), and Digital Input/Output (DIO) channels are automatically detected from the installed DAQ and listed for the user to enable and configure. For example, users can configure the measurement mode (Ground-referenced, Differential, etc), scale the input measurements to account for hardware gains, change the measurement range, and add or remove offset to each channel individually. Users can also configure available Digital I/O channels through this panel. When the channel configurations are "applied", an event is registered on the system stack, notifying all open modules of the changes. Users can respond to these changes through the update function of their custom modules (see Figure 39B).

**Data Recorder and HDF5 Files.** The Data Recorder module shown in Figure 37 allows saving of virtually anything within RTXI. Users first select the module of interest, and then have the option of saving any module element specified within the `DefaultGUIModel::vars` struct (see Figure 39B). Parameters for all modules are automatically registered at the beginning of a recording session. If modified during execution, the updated value is registered to the data file with a timestamp. Users can also "tag" various time points throughout their experiment to note relevant events. Events are timestamped and registered as a list of tags within the specified data file. A global downsampling option is available to reduce output file sizes. In between active recording sessions, the size and number of trials present in the specified data file, and length of the previous trial are displayed in the metadata section. If a user chooses an existing file to write data to, the option is presented to either overwrite

A

```
// Create a new class by abstracting from
// DefaultGUIModel which provides access to
// hard- and soft-realtime elements
#include <default_gui_model.h>

class PluginTemplate : public DefaultGUIModel
{
 // Macro required for creation of custom Qt events
 Q_OBJECT

public:
 // Function declarations
 PluginTemplate();
 virtual ~PluginTemplate();

 // Hard real-time execution code
 void execute();

 // Instantiate GUI elements, events, etc
 void createGUI(DefaultGUIModel::variable_t*, int);
 void customizeGUI();

protected:
 // Switch-based system for updating
 // system states, variables, and parameters
 virtual void update(DefaultGUIModel::update_flags_t);

private:
 // Variables, parameters, and functions
 double some_parameter;
 double some_state;
 double system_period;
 void initParameters();

private slots:
 // Example custom functions that can also be
 // onnected to GUI elements through the Qt API.
 void aBttn_event();
 void bBttn_event();
};
```

B

```
// Each entry into this struct represents an
// element within the module
static DefaultGUIModel::variable_t vars[] = {
 // This entry creates a PARAMETER of type DOUBLE
 // and will be called "GUI label" in the module GUI
 {
  "GUI label", "Description of parameter",
  DefaultGUIModel::PARAMETER | DefaultGUIModel::DOUBLE,
 },
 // This entry creates a STATE of type INTEGER
 // and will be called "A State" in the module GUI
 {
  "A State", "Description of state",
  DefaultGUIModel::STATE | DefaultGUIModel::INTEGER,
 },
};
```

C

```
// All hard real-time code goes in this function
void PluginTemplate::execute()
{
 return;
}
```

D

```
// All code in this function is executed in hard
// real-time by the hard real-time thread
void PluginTemplate::
 update(DefaultGUIModel::update_flags_t flag)
{
 switch (flag) {
  // Code executed when module is loaded into RTXI
  case INIT:
   period = RT::System::getInstance()->getPeriod();
   setParameter("GUI label", some_parameter);
   setState("A State", some_state);
   break;

  // Code executed when the "Modify" button is pressed
  case MODIFY:
   some_parameter = getParameter("GUI label").toDouble();
   break;

  // Code executed when the "Pause" button is depressed
  case UNPAUSE:
   break;

  // Code executed when the "Pause" button is pressed
  case PAUSE:
   break;

  // Code executed when the system frequency is modified
  case PERIOD:
   period = RT::System::getInstance()->getPeriod();
   break;

  // Code executed if valid state is not specified
  default:
   break;
 }
}
```

E

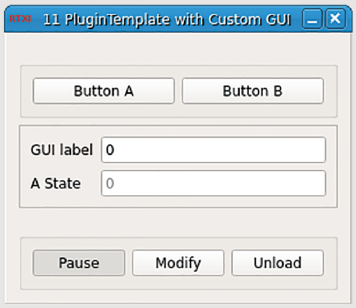


**Figure 39:** Example template code available (Supplement 3F) to users for writing custom modules, and corresponding module loaded within RTXI. (A) Basic C++ header (`plugin_template.h`) for an RTXI module. (B) Users can declare inputs, outputs, states, parameters, and events for custom modules through the DefaultGUIModel struct and (C) implement hard RT code within the execute function. (D) The `update` function allows execution of state-specific code for the module. (E) The module after it is compiled with the provided Makefile and loaded into RTXI. Each element of the module GUI is tied to a specific line of code. For example, when "Button A" is clicked, the `aBttn_event()` (line 35, A) code is executed. Similarly, the "GUI label" (lines 5-6, B) and "A State" (lines 11-13, B) components of the GUI are created by the `vars` struct and their values are initialized from the `INIT` block of the `update()` function (lines 8-9, C). Visit the GitHub repository (Supplement 3F) for complete corresponding C++ implementation (`plugin_template.cpp`) file.

or append the data file.

Experiment data and metadata saved by the Data Recorder are stored in the Hierarchical Data Format (HDF). HDF5 (*HDF5*) is an open data model that is increasingly popular for representing large and complex data, data relationships, and their associated metadata. HDF5 file read and write operations are supported by many common analysis frameworks and languages (e.g., MATLAB, Python, Julia, R, etc). Acquired raw and processed data, module states and parameters, system configurations, and almost any other value can be synchronously saved to a single HDF5 file by simply selecting the appropriate signal and adding it to the list of active recording channels. In addition, any computed value or intermediate signal can easily be captured for offline debugging or validation of RT algorithms and processing. When a parameter value is modified on-the-fly during data acquisition, the new value is automatically time stamped and stored into the data file. The Data Recorder also includes the ability to timestamp data with tags to experimental events or making notes and includes DAQ channel configuration details for all active channels. For precise control of data recorder start and stop times, the Data Recorder can easily be coupled with the Sync module, shown in Figure 37, which can be used to control the state of numerous modules and the data recorder all at once.

Figure 40 depicts the structure of an RTXI-generated HDF5 file. Scripts and analysis tools are provided for importing RTXI-generated HDF5 files into a single MATLAB structure for post-hoc analysis. RTXI-generated HDF5 files are compatible with many commercial and free software applications for a variety of platforms. There is no required proprietary software for viewing or analyzing data stored in RTXI-generated HDF5 files. Much of the available software also supports editing data in place within the HDF5 file or appending new data to an existing file. This allows users to add associated data such as images, post-processed data, or additional notes.

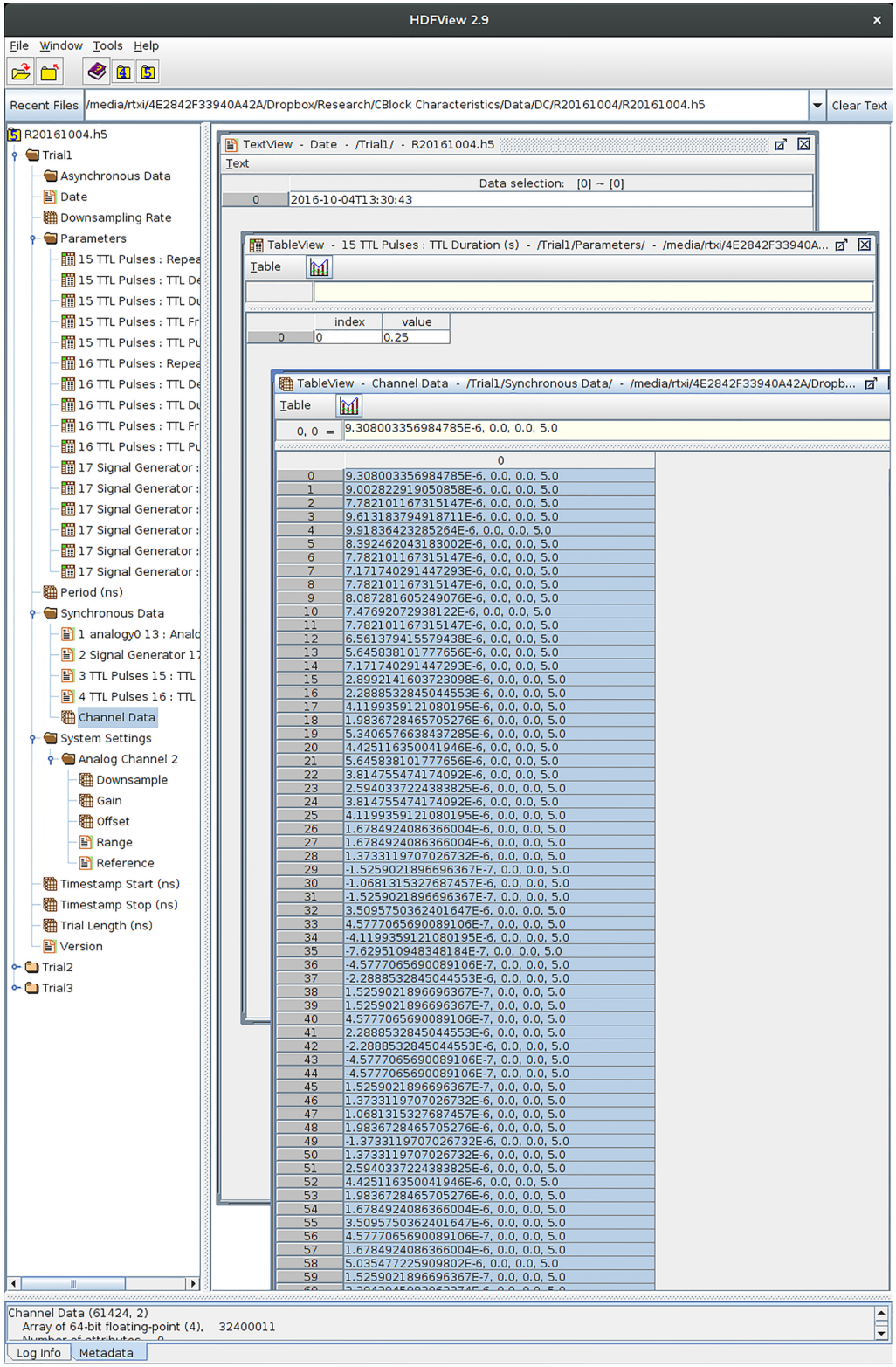


**Figure 40:** Hierarchical Data Format data file generated by RTXI. Each trial is represented as an ordered group of data and metadata objects. By default, RTXI saves parameter values from all modules when recording is started into the "Parameters" group. All enabled DAQ AI channel configuration settings are also saved into the "System Settings" group. HDF5 files can be opened, modified, and appended to from a variety of post-hoc analysis frameworks (e.g., HDFView, MATLAB, R, Python).

**Connector.** Passing of data between core and custom modules within the RTXI workspace takes place through the Connector module shown in Figure 37. The module's simple interface allows mapping of outputs from a module or DAQ AI channel to the input of another module in various configurations (one-to-one, one-to-many, many-to-one, etc). The specific input and output signals available to a module are defined in the module's code (see Figure 39). In cases where a many-to-one connection is formed, the inputs are summed prior to passing the data to the specified input. For example, Figure 37 shows the data from DAQ AI channel 0 and the output of the Signal Generator module connected to the input of the Neuron module. Simultaneously, the output of the Neuron module is sent to the Spike Detector module as well as out to hardware via DAQ AO channel 0.

**Oscilloscope.** RTXI's built-in real-time, high-speed, fully configurable Oscilloscope shown in Figure 37 module allows visualization of signals, parameters, states, and events from any loaded core or custom module. Similar to the Data Recorder and other system modules, the Oscilloscope can access data of any kind from any loaded module within the workspace. To visualize the signal, the user selects the block of interest on the "Channel" tab, which provides a list of available streams along with options to customize the color, style, and vertical scale (per division) of the selected signal. Once the modifications are "applied", the enabled signal is visualized with the configured settings and a legend entry is created listing the enabled channels by name along with their respective vertical scale. A second tab, titled "Display" allows configuration of the time scale (per division), the Oscilloscope's refresh rate, and specify trigger settings. Screenshots can be saved online during experiments for quick figure generation.

**Real-Time Benchmarks.** Online evaluation of system performance is useful when designing RT algorithms, debugging experimental setups, and even during experi-

ments. The RT Benchmarks module shown in Figure 37 (pane with blue top bar) provides key statistics about the RT performance of the system - including the computational time, real-time period, and the RT period's jitter - by using timestamps directly from the real-time system's clock. These benchmarks have been shown to be critical in evaluating hard real-time performance (Raikov et al., 2004). The computational time is inclusive of all system and custom modules loaded into the workspace, enabling evaluation of the full hard RT closed-loop execution time of each custom protocol. The RT period and RT period's jitter provide a means for viewing the actual period of the closed-loop system. *The RT period should never exceed twice the desired RT period, otherwise hard RT behavior is compromised.* Furthermore, each statistic reported by the RT Benchmarks module can be saved to an HDF5 file through the Data Recorder for post-hoc validation and verification of hard RT performance during the experiment. As described in the RTXI documentation (Supplement 3D), end users are strongly advised to benchmark their hardware and modules to ensure that the performance they require is actually being delivered.

**Module Wizard.** There are over 50 modules available to RTXI users through the RTXI GitHub repositories (Supplement 3F). The Module Wizard shown in Figure 37 was created to ease the process of downloading, installing, and updating new and existing modules. Users can quickly synchronize with the GitHub repositories and view details about each module, including the specific functions, how it works, and its development status. If a specific module is of interest, the user can download and install the module directly from within the Module Wizard and within seconds load the new module into their workspace.

**Users Preferences.** The User Preferences module shown in Figure 37 enables customization of default file locations for various file I/O operations. Users can specify folder locations for workspace setfiles and HDF5 data files. In addition, users can

specify buffer sizes for the Data Recorder, which can be beneficial when acquiring large amounts of data at high sampling rates. All settings specified within the User Preferences module are set as the default values and saved to the global RTXI configuration file.

### *1.3.6 Custom modules and Application Programming Interface (API)*

One core strength of RTXI is the ability to create custom RT modules without being restricted to hardware and software-defined boundaries, which is a common obstacle with commercial systems. RTXI users implement custom experimental protocols by writing all aspects of their RT protocol in C++-based modules. The use of C++ as the language of choice allows users to incorporate a variety of established libraries, such as LAPACK, Boost, and GNU Scientific Library for processing and data visualization, while capitalizing upon the strengths of C++ such as recursion, object-oriented programming, and abstraction. This system for creating custom closed-loop protocols enables complete freedom with respect to customization of closed-loop RT protocols without any virtual limit on what can be implemented.

To get started, users are encouraged to reference the Plugin Template, which provides the critical elements required for creating a custom RTXI module. Figure 39 provides an overview of the Plugin Template files and code. The Plugin Template files include a Makefile, which is used to define compilation rules on how files should be compiled, which external libraries are to be included, and how to package the individual pieces together to form a shared library object that is RTXI-compatible. In addition, one header (`plugin_template.h`, Figure 39A) and implementation (`plugin_template.cpp`) file are included as examples that can be built upon.

All custom modules are abstracted from the `DefaultGUIModel` class, which includes all elements necessary for interfacing with both the RT and GUI threads.

When creating a new module, users create the various I/O elements for that module through the `vars` structure (Figure 39B). To run specific code in RT, the code is placed in the `execute()` function (Figure 39C), which is common to all system and custom modules and processed at each time step. Functions called from within the `execute` function are also run in RT, while all code that is not in or called by the `DefaultGUIModel::execute` function is run on the soft RT GUI thread. This enables a simple mechanism for separating hard RT and soft RT tasks without significant programming overhead for the end user.

Users are able to customize the GUI of the module by including a variety of labels for model parameter and state variables, buttons and other elements for module control, as well as plotting elements for online analysis and visualization through the `customizeGUI()` function. By default, each module consists of three automatically generated buttons for starting or pausing execution, updating user-set parameters, and unloading itself from the workspace. Customization of the GUI is achieved by using the Qt framework, which provides a variety of GUI elements such as buttons, lists, text boxes, etc. Users can include signals and slots, which is a mechanism for calling specific functions based upon the occurrence of an event (e.g., button press $\rightarrow$ meet threshold criteria $\rightarrow$ specific animal behavior). For example, users can include a radio button in their module that has a signal-slot connection to a plot. When a user clicks the radio button, a signal is emitted and tells the module to display a scatter plot of data, which is otherwise hidden. The same signal-slot mechanism can be used to create buttons that drive outputs via the DAQ, call specific protocol functions, or generate notifications when an event occurs. Users are also encouraged to check the listing of available modules on the RTXI GitHub page for examples or potentially suitable modules that can easily be adapted to meet individual needs.

Updates to module variables, responding to changes in RT system settings applied through the system control panel, and controlling the state of each module takes

place through the `update()` function (Figure 39D). Each module can be in one of five states - which are responsible for initializing all module elements (`INIT`), registering UI/UX commands to the module (`MODIFY`), responding to changes in the RT system frequency (`PERIOD`), and controlling whether or not the module is running (`UNPAUSED`) or not (`PAUSED`). Users can customize any state for experiment-specific needs.

## *1.4 Results and Discussion*

### *1.4.1 System Characterization and Load Testing*

We evaluated RTXI's performance in different I/O configurations and computational loads (Figure 41). Tests were performed by providing a randomly triggered input signal (square wave, 50% duty cycle, 5 Vpp) to one of the DAQ AI channels. Each test case was run for 30 minutes (1800 total input events). In Case 1 (top), 1 AI channel was used to measure the input signal, and 1 AO channel was used to output the same signal, with no processing in the loop to evaluate system performance in a Single-Input Single-Output (SISO) configuration. Case 2 (middle) used the same configuration as Case 1, but included 2 AI and 2 AO channels. Only one AI channel received the input signal. The other AI channel was left floating and directly connected to the second AO channel, allowing characterization of system performance in a Multiple-Input Multiple-Output (MIMO) configuration. Case 3 used the same configuration as Case 2, but with added processing within the loop. The Hodgkin-Huxley Neuron model was configured to receive the test input signal and the output of the Neuron model (membrane potential, $V_m$) was connected to the Spike Detector module. The Spike Detector module determines if an action potential has occurred by checking for a threshold-crossing event. When an action potential is detected, the Spike Detector outputs a TTL pulse that is then sent out via the AO channel.

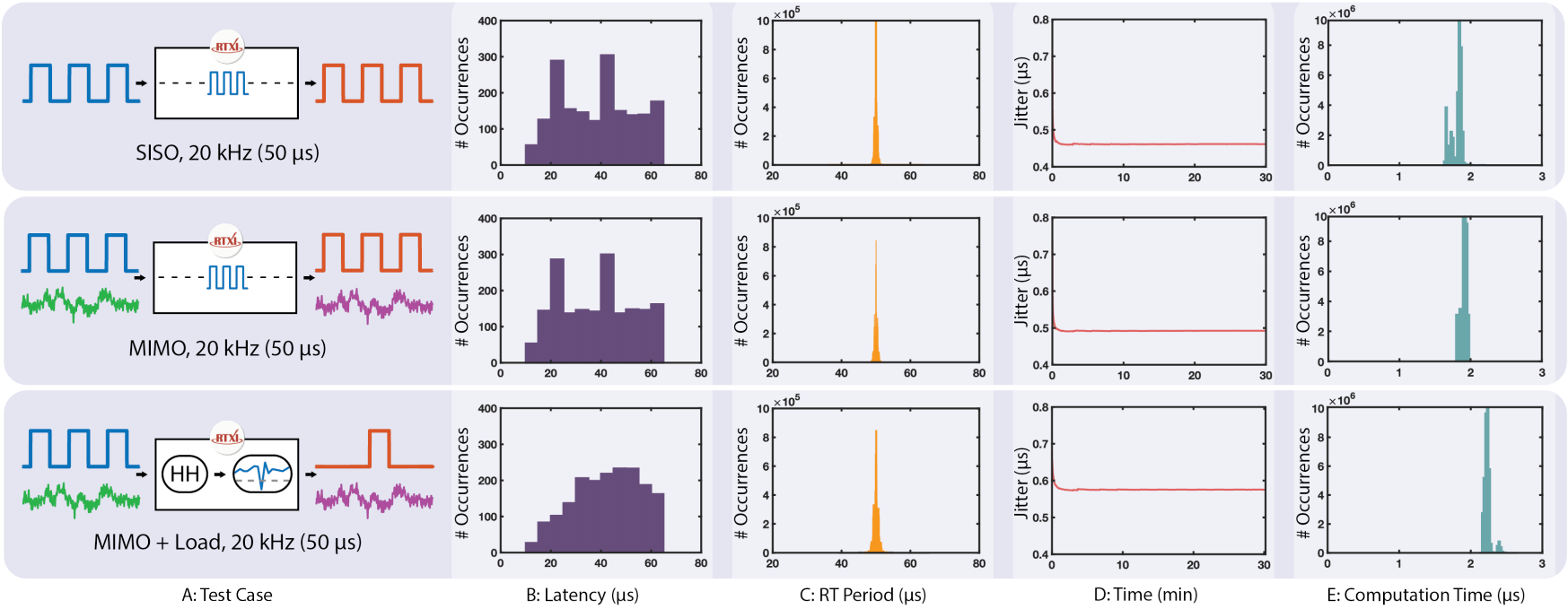


**Figure 41:** System performance under different computational loads and closed-loop configurations. System I/O latency does not exceed twice the system period (50 $\mu$s) nor are I/O events missed in all test cases, demonstrating hard RT performance and a delay of no more than one sample. The second column depicts the distribution of measured RT periods in each tests case by the Real-Time Benchmarks module. The RT period should never exceed twice the desired RT period, otherwise hard RT behavior is compromised. The increase in RT period variability with increasing computational loads is predominantly from the initial time frame after which a protocol starts execution. This is represented by the RT period jitter data, which demonstrates the RT period stabilizing within the first few minutes of execution. The final column provides an overview of the time spent processing the `execute()` function of each loaded module on each RT loop cycle.

A separate data acquisition system (MATLAB, NI USB-6341) was used to sample (250 kHz) the AI and AO signals from each case to quantify the I/O latency with each configuration. The RT period, RT period jitter, and computation time are measured with the Real-Time Benchmarks module and recorded with the Data Recorder. All tests were performed with an RTXI (v2.1) system frequency of 20 KHz on a desktop computer with an Intel Core i5 Quad Core Processor (3.40 GHz), 32GB of physical RAM, 10,000 RPM hard drive, Radeon HD 8570 graphics card, and an NI PCIe-6259 DAQ. All system and application daemons were killed prior to performance evaluation (recommended) because such background processes can prevent resource allocation or occupy significant amounts of Central Processing Unit (CPU) time. All analysis was performed using MATLAB 2016 (MathWorks, Natick, MA, USA). Data shown in Figure 41 is from one RTXI installation, however additional performance characterization results are available online from different installations A. Each test case demonstrates I/O processing of 1800 events with the desired RT period, demonstrating hard RT performance and a delay of no more than one sample.

### *1.4.2 Use Cases*

#### ***Use Case 1: Replication and suppression of learning-induced membrane and synaptic plasticity***

RTXI's most common application is for the dynamic-clamp technique (of the many examples, some include: (Prinz et al., 2004; Sharp et al., 1993; Dorval et al., 2001; Lin et al., 2010). This has led to significant advances in fundamental concepts in neuroscience and related fields.

Feeding behavior in the mollusk Aplysia is modified by various forms of associative learning, including classical and operant conditioning, and alter the central decision-making processes related to feeding actions. Experimental modification of intrinsic

excitability and electrical synapses of neurons in the Aplysia feeding central pattern-generating network have been shown to correlate with compulsive-like motor output expressions induced by *in vivo* operant conditioning. Despite this correlation between plasticity and operant conditioning-induced changes, a causal relationship was not shown.

Using RTXI, (Sieling et al., 2014) used the dynamic-clamp technique, in which simulated membrane and synaptic currents are artificially added or subtracted from neurons, to examine whether selective changes in single conductances governing cell excitability and electrical coupling are responsible for the associative modification of feeding circuit output and behavior (Figure 42). Using *in vitro* preparations of buccal ganglia isolated from naive and operantly trained animals, Sieling et al either enhanced or diminished neuronal excitability and coupling strengths in RT to test for causation and determine respective contributions of synaptic and non-synaptic processes by which associative learning leads to expression of compulsive behavior.

### *Use Case 2: Real-time distorted auditory feedback for control of song bird timing*

In addition to the widely used dynamic clamp, RTXI's flexibility and robustness are useful for a variety of investigations testing causal relationships. One such area is Distorted Auditory Feedback (DAF), which is routinely used to assess the effects of auditory input on vocal production and underlying neural activity in songbirds. Some bird species' songs have been shown to be highly sensitive to acoustic input, showing immediate effects on the timing and acoustic structure of the produced song. Investigation of immediate changes taking place after DAF presentation often requires having a system capable of providing RT acoustic processing and feedback. Commercial systems for RT acoustic processing are available but are expensive and contain a significant number of constraints that must be considered during experimental design.

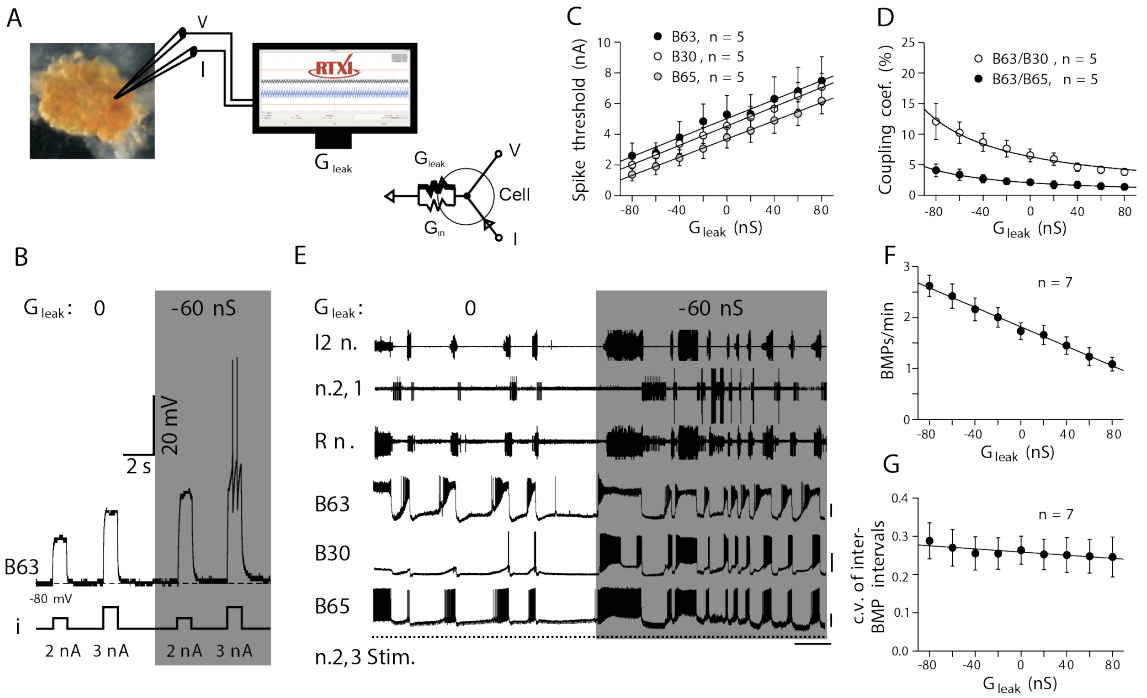


**Figure 42:** Artificially modulating neuronal excitability mimics learning-induced increase in frequency, but not the regularity, of buccal motor pattern (BMP) genesis. (A) Experimental protocol and equivalent electrical circuit for the addition of a dynamic-clamp-defined leak conductance ($G_{leak}$) to the natural input conductance ($G_{in}$) of an individual neuron using RTXI. (B) Introduction of an artificial $G_{leak}$ of -60 nS (shaded panel) increased the excitability of a target B63 neuron (indicated by a decrease in spike threshold) compared with that arising from the natural leak conductance alone (i.e., $G_{leak}$: 0 nS). Horizontal and vertical scale bars represent 2 s and 20 mV, respectively. In (C), $G_{leak}$ was introduced into one of B63, B30, or B65. In (D), $G_{leak}$ was introduced into a B63 and current pulses for measuring coupling coefficients were injected into either postjunctional B30 or B65. (For details, see (Sieling et al., 2014 Figure S1.) (E) In a control preparation, the frequency, but not the regularity, of spontaneous BMP genesis and associated spike bursts in B63/B30/B65 increased in response to a dynamic-clamp-defined $G_{leak}$ of -60 nS (shaded panel) introduced simultaneously into the three neurons. Horizontal and vertical scale bars represent 30 s and 25 mV, respectively. (F and G) Quantification of changes in frequency (F), but not irregularity (G), of BMP generation for different values of artificial $G_{leak}$ added simultaneously to the three neurons. Group data show means ± SEM and individual sample sizes. All figures obtained and modified with permission from (Sieling et al., 2014).

Furthermore, typical experiments using acoustic feedback use detection of a certain template signal, either a certain frequency or more complex combination or sweeps of frequencies, and feedback is delivered upon template detection. Template detection tasks are computationally intensive, requiring spectrogram-based or feature-based techniques (Tchernichovski et al., 2000; Leonardo et al., 2005), comparison across detected elements and templates, and if successful, generate the appropriate feedback signal. These computations have to be done fast enough to enable RT performance while not interfering with other processes such as data acquisition, storage, and visualization.

Skocik and Kozhevinokov (Skocik et al., 2012) capitalized on the strengths of RTXI and modified it for experimental use in RT acoustic signal processing and feedback. Acoustic measurements were made by interfacing a microphone and amplifier to the analog inputs present on a National Instruments PCIe-6251 DAQ with a system frequency of 30 KHz. Acoustic feedback was generated by custom RTXI modules and delivered via the analog outputs on the DAQ. To minimize processing latency, the Data Recorder module was customized to provide two high-speed modes of operations  triggered (active) and non-triggered (idle). The complete process flow for the customized Data Recorder is shown in Figure 43. A circular buffer is inserted into the Data Recorder's processing loop to enable buffering of acquired acoustic signals. The root mean square (RMS) is continuously quantified for the last 10ms of acquire data at a rate of 1 KHz. When the RMS exceeds the user-specified threshold, the system automatically switches to triggered mode operation.

Performance was also evaluated in experiments to detect specific syllables in the song of Bengalese finches. The finch song consists of a sequence of syllables separated by silences (inter-syllable gaps) (Figure 43), with variability introduced by the specific sequence of syllables in each song. Experiments were conducted to detect specific target syllables, with successful crossing of the correlation coefficient result-

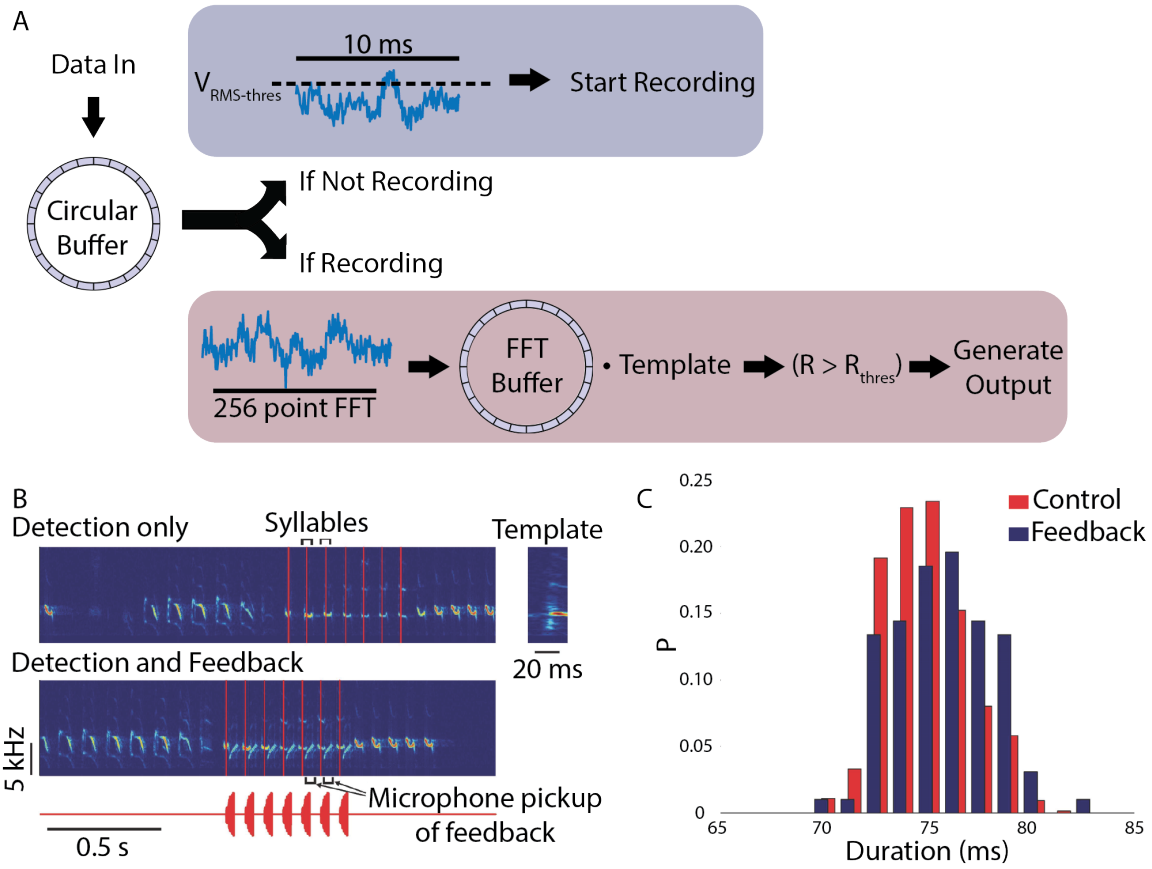


**Figure 43:** Hard RT distorted auditory feedback system. (A) Simplified diagram of the acoustic feedback system. When not triggered (top), the system computes the root mean square (RMS) of the input signal. When the RMS exceeds the threshold, the system is triggered. When triggered (bottom), the system computes the spectrogram of the most recent 20ms of signal and computes the correlation coefficient of this spectrogram with the spectrogram of the template sound (e.g., song syllable). The template sound is detected when the correlation coefficient exceeds a threshold value; in this case, acoustic feedback can be generated. Both the input and the acoustic output are saved to the computer hard drive. (B) Spectrogram of the song of a Bengalese finch and the times of occurrence of one of the song syllables. The system was programmed to only detect the occurrences of the target syllable in real time, no acoustic feedback was generated. The detection times are shown as vertical red lines. Bottom: the system is detecting the target syllables (vertical red lines) and is generating acoustic feedback after detection. The acoustic feedback waveform is shown below. The feedback signal is one of the birdsong syllables; the acoustic feedback pickup by the microphone is visible on the spectrogram. The zoomed-in spectrogram of the template is shown on the right. (C) DAF increases the duration of the time interval between Bengalese finch song syllables. Histogram depicts the time intervals between two subsequent syllables in the song in the presence of DAF (blue) and without DAF (red). The means are: $\Delta t_{mean}$ = 74.8ms (control, $N$ = 637 syllables) and $\Delta t_{mean}$ = 75.7ms (feedback, $N$ = 97 syllables), the difference is statistically significant ($p$ = 0.001, two-way KolmogorovSmirnov test). All figures obtained and modified with permission from (Skocik et al., 2012).

ing in generation of acoustic feedback (either white noise or the song syllable). Figure 43B provides sample data demonstrating RTXI's performance in both open-loop (detection only) and closed-loop modes (detection and feedback). System performance was characterized by comparing online syllable detection to off-line detection using spectrogram-based techniques. Over 92% of the target syllables (n = 659) were correctly identified by RTXI, with zero false positives. The undetected 8% are believed to be due to natural variability in acoustic structure that are not accounted for by the detection algorithm. Additional tests in Zebra finches resulted in a detection rate up to 96%(n = 756), with less than 1% false positives. In a final round of experiments, detection of target syllables was followed by DAF for modulation of timing between song syllables. Without DAF, the mean interval is 74.8 ms (n = 637), while with DAF the mean interval increases to 75.7 ms (n = 97).

These observations are consistent with previously published observations on the effects of RT feedback on song structure(Sakata et al., 2006). Moreover, they demonstrate the robust hard-RT capabilities of RTXI and the advantages of open-source software. Using RTXI enabled the authors to set up interfaces with different I/O hardware and modify the RTXI source code to run custom RT protocols.

### *Use Case 3: EEG feedback-controlled transcranial Alternating Current Stimulation*

In addition to *in vitro* and *in vivo* closed-loop hard RT electrophysiology, RTXI's flexibility, customizability, and hard RT performance has been utilized to investigate the effects of feedback-driven tACS. Brain stimulation using transcranial Alternating Current Stimulation (tACS) has gained significant momentum as an alternative to pharmacological methods for treatment of neurological and psychiatric disorders. By electrically stimulating the brain, aberrant network dynamics can be targeted with potentially higher efficacy, increasing therapeutic efficacy while minimizing undesired

off-target effects (Fröhlich, 2014; Fröhlich, 2015). Unfortunately, most clinical investigations using tACS are conducted in a feedforward, open-loop manner. Given the success of feedback (closed-loop) control in a variety of engineering and neuroscience applications, (Boyle et al., 2013) investigated the ability of Electroencephalography (EEG) measurement driven delivery of tACS to provide better control of cerebral cortex dynamics, which is implicated in several psychiatric illnesses.

tACS applies a weak sinusoidal electrical current to the scalp, resulting in a change in polarization of a large number of neurons, thus effectively altering neuronal network activity. Evidence from previous studies suggests that sinusoidal stimulation waveforms can be used to selectively modulate cortical oscillations at different frequencies commonly associated with different cognitive states. In their study, Boyle et al combined 40 Hz tACS with EEG measurements to control visual cortex state dynamics and modulate high- and low-alpha states induced by opening and closing the eyes.

RTXI was used in this investigation to measure and process incoming EEG activity, compute the appropriate output stimulation waveform in RT, and control timing of the experimental protocol. EEG measurements were made by interfacing with a Biopac EEG amplifier connected to a National Instruments PCI-6221 DAQ with a system frequency of 2 KHz. Measured EEG activity was processed online with custom C++ modules. Stimulation timing and waveforms were generated by RTXI and delivered to an isolation unit through the DAQ's analog output channel. Figure 44 depicts the custom closed-loop, RT protocol engineered for this investigation.

All data processing and analysis was conducted in RT with custom modules written in C++. The incoming EEG data was filtered with a $6^{\text{th}}$ order Butterworth band-pass filter with a bandwidth of 8  12 Hz to isolate the alpha band. Power was then computed for the alpha band as the mean oscillation power with a 1 second window width. During the calibration period in each experiment, the module built

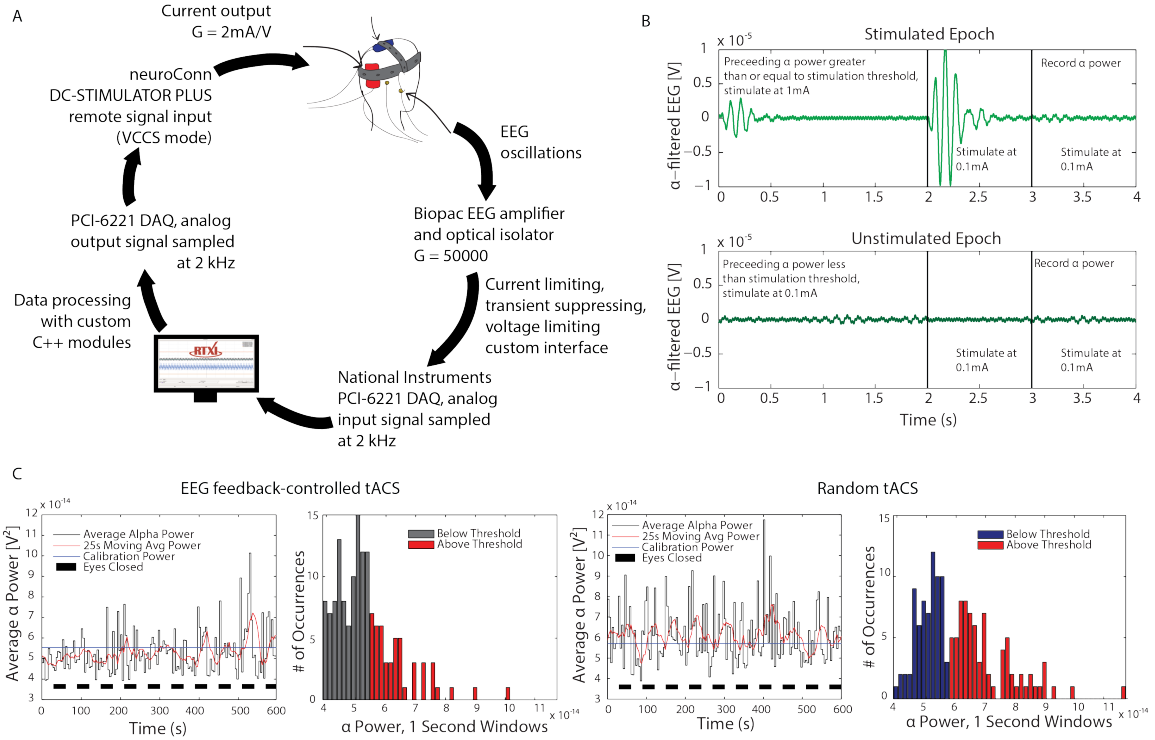


**Figure 44:** Optimization of therapeutic benefit of tACS via closed-loop EEG feedback-controlled tACS. (A) Hard real-time closed-loop protocol used for feedback-controlled delivery of tACS. EEG are measured and amplified prior to sampling with RTXI while the subject opens and closes their eyes every 30 seconds. EEG data from international 10-20 system sites O2, A1, and A2 are processed in hard RT using a custom module written to measure the alpha band power within a one second window. The computed power is validated against a threshold criteria, which determines the tACS amplitude to be delivered. The output from RTXI is connected to an external current-controlled stimulation and isolation unit. Sample alpha-filtered EEG traces with and without feedback-controlled tACS are shown in (B). Feedback-controlled tACS (C) almost completely suppressed alpha band power in a targeted way (Ratio $EC_\alpha$ to $EO_\alpha$ = 1.03, $p = 0.041$). Dose-matched random tACS (D) also suppressed alpha band power (normalized random-No Stim = -0.31, $p = 0.0183$), but was less effective than feedback-controlled tACS (normalized $feedback_\alpha$ - $random_\alpha$ = -0.10, $p = 0.0145$). All figures obtained and modified with permission from (Boyle et al., 2013).

a distribution with the computed alpha power values to determine the mean alpha power for both eyes-open and eyes-closed conditions. Stimulation thresholds were set to 1.05 of the average of the two mean alpha power values. The protocol then continued to assess mean alpha power at a rate of 0.25 Hz and modulated the stimulation depending on the measured alpha power. If alpha power was higher than the stimulation threshold, tACS was delivered to the subject for the first 2 seconds of the next epoch, otherwise stimulation was turned off. Each subject completed a total of four 12 minute recording sessions. Each recording started with a 2 minute calibration period. For the first 60 seconds, the subjects were asked to relax and be still with their eyes open. For the next 60 seconds, the subjects were asked to relax, be still, and close their eyes. After calibration, two recordings were conducted in each subject. First, subjects were asked to keep their eyes open (EO) and received EEG feedback-controlled tACS. For the second recording, subjects were asked to open and close their eyes when told by the experimenter every 30 seconds (EOEC) while receiving EEG-feedback driven tACS. These two recordings were repeated, however subjects received dose-matched randomly administered tACS.

The results of this investigation found that EEG feedback-controlled tACS can successfully suppress alpha power as well as state transitions caused by opening and closing of eyes. Subsequent investigations by the same group using RTXI have also demonstrated the ability of closed-loop tACS to boost sleep spindle activity and sleep-dependent motor memory consolidation (Lustenberger et al., 2016). These results demonstrate the customizability, modularity, and robust closed-loop RT performance of RTXI.

## 1.5 Availability

RTXI is available under the GNU GPLv3 license and is publicly accessible online via GitHub (Supplement 3B) along with over 50 custom modules contributed by the RTXI community. This repository enables tracking of user-submitted bugs and requests, and makes the continued development of RTXI publicly viewable. GitHub also allows users to watch the progress and development of RTXI, receive notifications as new updates or patches are submitted, and easily share custom modules built by any RTXI user. Users are encouraged to use this platform to communicate with the RTXI team with questions, comments, feature requests, and troubleshooting advice.

In addition to GitHub, a website (Supplement 3A) is maintained and routinely updated with new troubleshooting tips and FAQs (Supplement 3E) as well as a user manual and documentation (Supplement 3D). Publications utilizing RTXI are indexed and listed for users to access key details associated with experimental setups, module use, and system parameters - enabling greater reproducibility of shared data. The RTXI team is dedicated to helping users with any aspect of RTXI whether it is installation, creating custom modules, or integration of addition experimental hardware.

## 1.6 Future Directions

Advances in measurement and stimulation technologies over the last decade have increased both the spatial and temporal resolution at which scientists can investigate biological systems. Enhancements in micro-fabrication technologies have enabled development of high density silicon probes (Scholvin et al., 2016; Frey et al., 2010), allowing large-scale spatial and temporal over-sampling of biological activity (Buzsáki, 2004). Development of Application Specific Integrated Circuit (ASIC)s has led to

wide adoption of systems such as the low-cost and easy-to-use Intan headstages (Harrison, 2007; Harrison et al., 2015). Furthermore, recent developments in imaging technologies have made it possible to consider closed-loop applications in which the measured signal is an image representative of underlying electrical activity, rather than direct measurement of electrical potentials.

On-going development efforts within RTXI are focused on incorporating new measurement modalities (e.g., imaging) and acquiring from high channel count interfaces – all with hard RT closed-loop performance. For example, a image acquisition and processing module (GenICam) and a Ethernet-based data acquisition module (EthernetAcq) are now available for use within RTXI (Supplement 3F). In many cases, hard RT closed-loop control with image or high channel count data processing can require more computation time than is available per cycle. On-going RTXI development efforts are also focused on providing API calls for distributing computational loads across dedicated CPU cores and Graphics Processing Unit (GPU)s, with the goal of requiring little to no technical know-how on the user's end.

The advent of optogenetics has enabled tight spatial and temporal control of stimulation of biological tissues (Zhang et al., 2006a; Yizhar et al., 2011; Arrenberg et al., 2010). These developments have spawned a significant interest in closed-loop control of biological systems (Grosenick et al., 2015), such as optical clamping of network activity (Newman et al., 2015) and optical shortening of cardiac action potential durations (Govorunova et al., 2016). In most cases, delivery of optogenetic stimuli via a laser or diode is controlled and modulated by a voltage signal. For example, users can generate a standard stimulus waveform using the Signal Generator module or a custom stimulus waveform by providing an ASCII file to the Waveform Maker module and use it to control a laser or diode to achieve hard RT optogenetic stimulation. Such re-utilization of existing code and custom modules simplifies the transition to hard RT closed-loop control.

### *1.6.0 Useful Links*

A Website: `https://rtxi.org`

B Source code: `https://github.com/RTXI/rtxi`

C Compatible Hardware: `http://rtxi.org/docs/manual/#daqs`

D User manual: `http://rtxi.org/docs/manual`

E Tutorials and FAQs: `http://rtxi.org/docs/`

F User contributed modules: `http://rtxi.org/modules/`

G Support: `http://rtxi.org/contact/`

H Publications using RTXI: `http://rtxi.org/papers/`

# APPENDIX A.2

# MICRONEEDLE CUFF ELECTRODES

## *2.1 Motivation*

*Objective.* The work presented here describes a new tool for peripheral nerve interfacing, called the microneedle cuff ($\mu$N-cuff) electrode. *Approach.* $\mu$N arrays are designed and integrated into cuff electrodes for penetrating superficial tissues while remaining non-invasive to delicate axonal tracts. *Main results.* In acute testing, the presence of 75 $\mu$m height $\mu$Ns decreased the electrode-tissue interface impedance by 0.34 k$\Omega$, resulting in a 0.9 mA reduction in functional stimulation thresholds and increased the signal-to-noise ratio by 9.1 dB compared to standard (needle-less) nerve cuff electrodes. Preliminary acute characterization suggests that $\mu$N-cuff electrodes provide the stability and ease of use of standard cuff electrodes while enhancing electrical interfacing characteristics. *Significance.* The ability to stimulate, block, and record peripheral nerve activity with greater specificity, resolution, and fidelity can enable more precise spatiotemporal control and measurement of neural circuits.

## *2.2 Introduction*

Cuff electrodes are commonly used for interfacing with peripheral nerves (Polasek et al., 2007; Schuettler et al., 2013) because they are stable, easy to customize, and easy to implant. However, major challenges associated with cuff electrodes include minimizing the amount of electrical charge delivered to the nerve, improving sensitivity and resolution of recordings, increased selectivity, as well as maintaining the position of the cuff electrode on the nerve post-implantation (Goodall et al., 1996; Grill et al.,

1998). Standard (needle-less) cuff electrodes consist of a conductive pad either soldered or spot-welded to a lead wire and adhered to the inner wall of a silicone tube. Attempts have been made to optimize the geometry, electrical characteristics, and robustness of standard cuff electrodes (Loeb et al., 1996). Although effective, many of these optimizations do not address the electrical characteristics of the outer tissue layers, which are composed of fatty tissue, connective sheaths, and the epineurium. Epineurial tissue is mainly comprised of collagen fibers, elastin fibers, and small blood vessels (Thomas, 1963) and is electrically-insulating. This outer layer can range in thickness from 100 $\mu$m in the rat (Islam et al., 2012) to over 1 mm in canines (Yoo et al., 2013) and humans (Gamble et al., 1964).

Previous studies have shown that the selective stimulation and/or recording capabilities of a peripheral nerve interface can be significantly enhanced by placing the electrodes within the fascicles of the nerve (Branner et al., 2001; Zheng et al., 2003). Such interfaces are classified as intrafascicular and provide selectivity but require penetrating the perineurium. In all cases, the long-term efficacy and safety of electrodes are heavily dependent upon surgical technique and ease of use, and are prone to substantial damage from motion in chronic studies. Thus, a neural interface that maintains the benefits of standard cuff electrodes while providing enhanced stimulation and recording capabilities is desirable.

In this paper, we present a minimally invasive neural interface, called the microneedle cuff electrode ($\mu$N-cuff), where $\mu$Ns minimally penetrate the outer tissue layers for enhanced peripheral nerve interfacing. We characterized the electrode-tissue interface impedance, motor stimulation thresholds, and Signal to Noise Ratio (SNR) of varying height $\mu$N-cuffs.

## 2.3 Methods

### 2.3.1 Fabrication of $\mu$N-cuff electrodes

$\mu$N electrode arrays were fabricated through a multistep process (Figure 46). Arrays were designed in AutoCAD (Autodesk Inc., San Rafael, CA) with the desired $\mu$N electrode dimensions in a planar (2-D) orientation. The $\mu$Ns varied in dimensions from 75 $\mu$m to 200 $\mu$m in height with a consistent width of 75 $\mu$m and a pitch of 150 $\mu$m in X and 230-440 $\mu$m in Y. The overall size of a single $\mu$N electrode array (of any height) was 1 mm (width) by 3 mm (height) (Figure 46A). $\mu$Ns were designed to be 20 $\mu$m greater than the desired height to accommodate for laser beam width variability.

Additional features, such as release lines and alignment guides were added to the designs to assist in the handling of arrays (Figures 46A-D). $\mu$N electrode arrays were laser micromachined (Micron Laser Technology, Hillsboro, OR) from a square platinum-iridium foil (Pt-Ir, 90/10, 25.4 $\mu$m thick, ESPI Metals, Ashland, OR, see Figure 46B). The foil was subsequently ultra-sonically cleaned for 60 seconds in acetone to remove laser micromachining debris prior to imaging, assembly, and characterization. The resulting lasered foil was spot-welded (Figure 46D) to an insulated braided stainless steel wire (#793500 A-M Systems, Sequim, WA). $\mu$N arrays were placed on a square inch of polydimethylsiloxane (PDMS) and two fine forceps (Dumont #5 Fine Science Tools, Foster City, CA) were used to individually bend the $\mu$Ns out of the foil plane. Figure 46D shows an illustration of the foil with the lead spot-welded and $\mu$Ns bent out of plane.

Two $\mu$N arrays were used to create bipolar $\mu$N-cuff electrodes (Figure 46E). The arrays were adhered onto a square inch of parafilm tape (Parafilm M and Dispenser, SPI Supplies, West Chester, PA) to insulate the back plane of the contacts. A second

square inch of parafilm tape was used to cover the front plane of the contacts. An opening of 1 mm x 1 mm was made on the front plane to deinsulate the contacts for interfacing with the nerve. The cuff was placed in a 60°C oven for 60 seconds to adhere the two layers of parafilm tape together. Upon removal, excess parafilm tape was cut to obtain $\mu$N-cuff electrodes with an average diameter and length of 1.5 mm and 5 mm, respectively, and 1 mm between contacts. Standard cuff electrodes used as a control were also fabricated by laser micromachining standard pads (previously described in (Patel et al., 2015). $\mu$N-cuffs were imaged between experiments under a high magnification microscope to assess damage or deformation of $\mu$Ns.

**Experimental preparation** *In vivo* acute experiments were performed on the left and right sciatic nerves of four anesthetized Lewis rats (n=8 nerves, 250-300 g). The right sciatic nerve was exposed for a total exposed length of 3-4 cm. Sterile rat Ringer's solution was applied throughout the experiment. The foot of the animal was tied to the experimental rig to minimize motion artifacts. The animal was kept on a warming pad (body temperature 37-38°C and euthanized upon completion of the experiment. All protocols were approved by the Georgia Tech Institutional Animal Care and Use Committee.

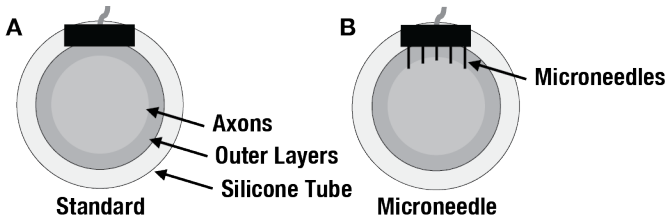


**Figure 45:** Illustration showing the physical difference between standard and $\mu$N-cuff electrodes. (A:) Standard cuff electrodes enable stimulation and recording of neural activity from outside the outer layers. (B:) $\mu$N-cuffs penetrate the outer layers and provide measurement and recording from within the nerve bundle.

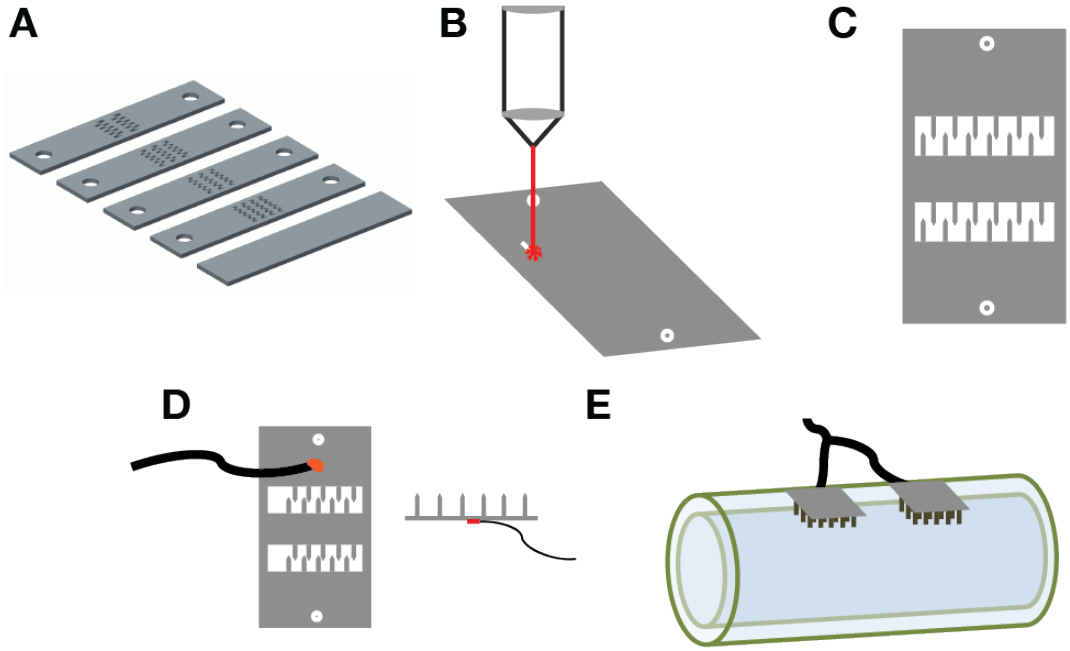


**Figure 46:** $\mu$N-cuff fabrication process. (A) $\mu$Ns are designed in AutoCAD. (B) $\mu$Ns are laser micromachined out of Pt/Ir foil. (C) Resulting foil with $\mu$Ns. (D) Braided stainless steel wire is spot-welded to the array on one side of the $\mu$Ns. $\mu$Ns are then bent out of plane by hand under a high magnification scope. (E) $\mu$N arrays are embedded in parafilm tape to create $\mu$N-cuffs.

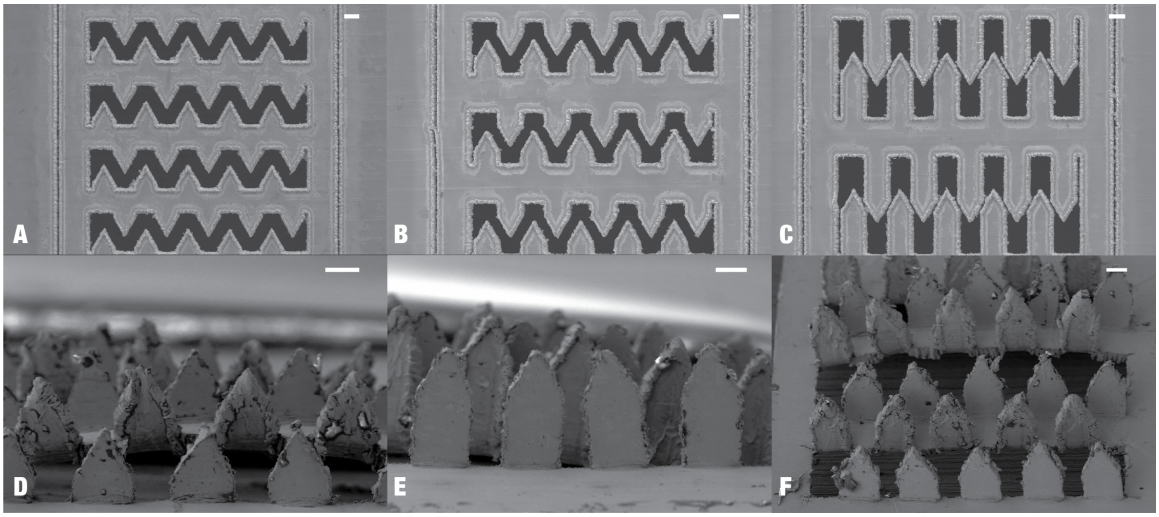


**Figure 47:** Scanning electron microscope images of $\mu$N arrays at different stages of fabrication. Scale bars are 100 $\mu$m for all images. (A-C) Laser micromachined $\mu$N arrays of different heights prior to being bent out of plane. Heights shown are 75 $\mu$m (A), 100 $\mu$m (B), and 200 $\mu$m (C). (D-F) Arrays after being bent out of plane $\mu$Ns and prior to ultra-sonication.

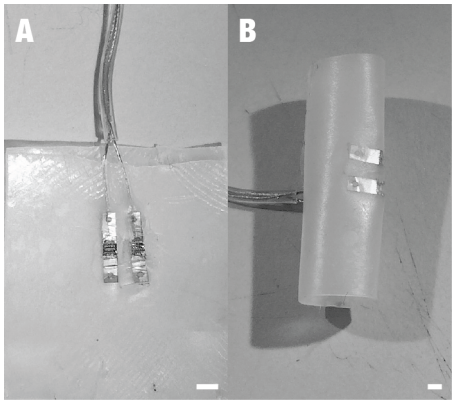


**Figure 48:** Images of $\mu$N-cuff fabrication. (A:) $\mu$N arrays adhered between two layers of parafilm tape with contact windows cut open. (B:) Top view of fully fabricated $\mu$N-cuff prior to being cut to desired specifications. (C:) Side view of fully fabricated $\mu$N-cuff with $\mu$N arrays visible prior to being cut to desired specifications. Scale bars are 1 mm.

### 2.3.2 Electrophysiology setup and procedures

$\mu$N-cuffs were compared with standard nerve cuffs in terms of electrode-tissue interface impedance, motor stimulation thresholds, and SNR. $\mu$Ns ranging in height from 75-200 $\mu$m were experimentally evaluated in random order. In each experiment, the electrode-tissue interface was observed under a dissection microscope for proper electrode-nerve contact. All data presented here is mean $\pm$ standard deviation.

### 2.3.3 Electrode-tissue interface impedance

Electrode-tissue interface impedance was characterized at 1 kHz using a Bode 100 Impedance Meter (Omicron Labs, Klaus, Austria). Impedance was characterized between the contacts of bipolar $\mu$N-cuff and standard cuff electrodes. Impedance for each electrode was also characterized by placing a single $\mu$N array in physiological saline (0.9% NaCl) at room temperature.

### 2.3.4 Motor stimulation thresholds

Motor stimulation thresholds were characterized for $\mu$N-cuff and standard cuff electrodes. The tibia was fixed to the experimental rig and the Achilles tendon was attached to a force transducer (Model 724490, Harvard Apparatus, Holliston, MA) using a hemostat. The force transducer output was acquired by the data acquisition system at a rate of 50 kHz (Digidata 1322, Molecular Devices). Cathodic stimulus pulses (0.2 ms pulse width) were generated by the data acquisition system, isolated using a constant current source (1 mA/V, Model 2200, A-M Systems, Sequim, WA) to evoke compound action potentials (CAPs) from the nerve. Stimulus pulses were applied to the proximal end of the exposed nerve with either a $\mu$N-cuff or a standard cuff electrode. The stimulus amplitude was increased until 5 Newtons of force was exerted and measured by the transducer. A set force value was used as opposed to

twitch force to overcome variabilities induced by the location of the electrode along the length and circumference of the nerve.

### *2.3.5 Nerve activity recordings*

Neural activity was recorded from the sciatic nerve to characterize SNR. Supra-threshold cathodic pulses (1-2 mA) were applied to the proximal end of the nerve via a hook electrode. Evoked CAPs were differentially recorded with both $\mu$N-cuff and standard cuff electrodes from the distal end of the nerve with a distance of 1-2 cm between stimulating and recording electrodes. Recordings were amplified (10,000x, Model 1700, A-M Systems) and band-pass filtered (100-5000 Hz) before digitization at a rate of 50 kHz (Digidata 1322, Molecular Devices). SNR was calculated using the sum of the largest peak-to-peak amplitudes of each measured CAP component and noise in the window prior to stimulation. All data analysis was conducted in MATLAB (MathWorks, Natick, MA).

**Table 7:** $\mu$N Characteristics.

| **$\mu$N height ($\mu$m)** | **0** | **75** | **100** | **150** | **200** |
|---|---|---|---|---|---|
| **$\mu$N count** | 0 | 40 | 30 | 30 | 20 |
| **Desired height ($\mu$m)** | 0 | 75 | 100 | 150 | 200 |
| **Designed height ($\mu$m)** | 0 | 95 | 120 | 170 | 220 |
| **Fabricated height ($\mu$m)** | 0 | 87 | 111 | 163 | 217 |
| **Standard Deviation ($\mu$m)** | 0 | $\pm$2.0 | $\pm$1.3 | $\pm$0.49 | $\pm$5.1 |
| **Surface area ($mm^2$)** | 1.0 | 1.2 | 1.3 | 1.5 | 1.4 |

## 2.4 Results

### 2.4.1 Characterization of $\mu$N arrays

We evaluated $\mu$N definition and released areas (where Pt/Ir has been removed due to laser micromachining) under a high resolution scanning electron microscope (SEM, Hitachi S-3700 VP SEM, Hitachi High Technologies America, Dallas, TX). Figure 47 depicts SEM images of various $\mu$N electrode arrays in their planar and 3-D configurations. Figure 47E provides a close up view of a $\mu$N tip. Figure 47F shows an array with a wide range of $\mu$N heights. Inspection of $\mu$N arrays between trials and experiments did not show significant signs of damage.

The height (key characteristic for this study) and the sharpness (width) of the $\mu$N tips were evaluated post-machining. The findings are summarized in Table 7, along with the number of $\mu$Ns on each contact, and the contact surface area. The $\mu$N heights were found to be approximately 11-17 $\mu$m longer than the design specification. The average measured tip width was 10.62 $\mu$m. The surface area in contact with the nerve is increased by the presence of the $\mu$Ns (Table 7).

### 2.4.2 Decreased electrode-tissue interface impedance

The electrode-tissue interface impedance of $\mu$N-cuff and standard cuff electrodes was measured and compared. Figure 50 summarizes the measured impedance values in saline and on nerve. The impedance is significantly reduced ($0.34\pm0.06$ k$\Omega$) with the shortest $\mu$N heights (75 $\mu$m) compared to standard cuff electrodes. Increasing $\mu$N heights provided further reductions in the interface impedance (up to 42%) compared to standard cuff electrodes. $\mu$N arrays had a higher impedance (Figure 50, bottom) in saline compared to standard pads. However, the $\mu$N arrays decreased the impedance at the electrode-tissue interface. In addition, all electrode-tissue interface impedances

with the $\mu$N-cuff were lower than the measured impedance in saline, but followed a different trend.

### *2.4.3 Reduced motor activation thresholds*

Motor thresholds were characterized as the minimum stimulus amplitude required for the gastrocnemius muscle to exert 5 Newtons of force as measured by the force transducer. Figure 50 (middle) shows average stimulation thresholds from all 8 experiments. Increasing $\mu$N height is inversely related to the stimulus threshold. 75 $\mu$m height $\mu$Ns decreased the stimulus threshold 0.92$\pm$0.41 mA, with continued reductions in stimulus threshold for increasing $\mu$N heights. A maximum reduction of 1.7 mA (39%) was observed for $\mu$Ns of 200 $\mu$m height.

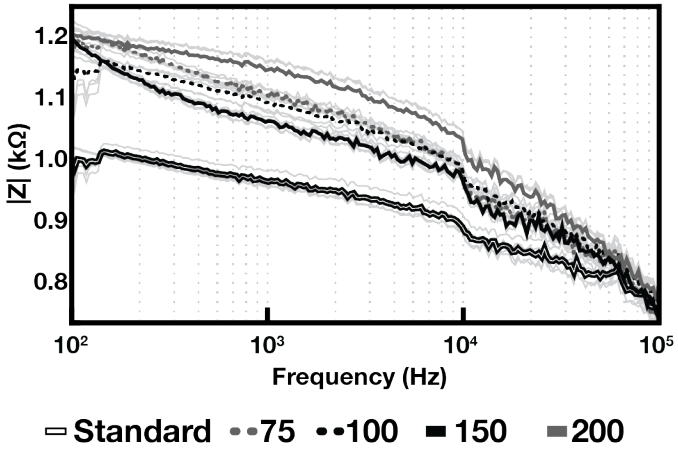


**Figure 49:** Impedance characterization of $\mu$N arrays in saline at room temperature. The averages of five measurements with each $\mu$N height are shown along with individual traces. All trials were conducted in random order.

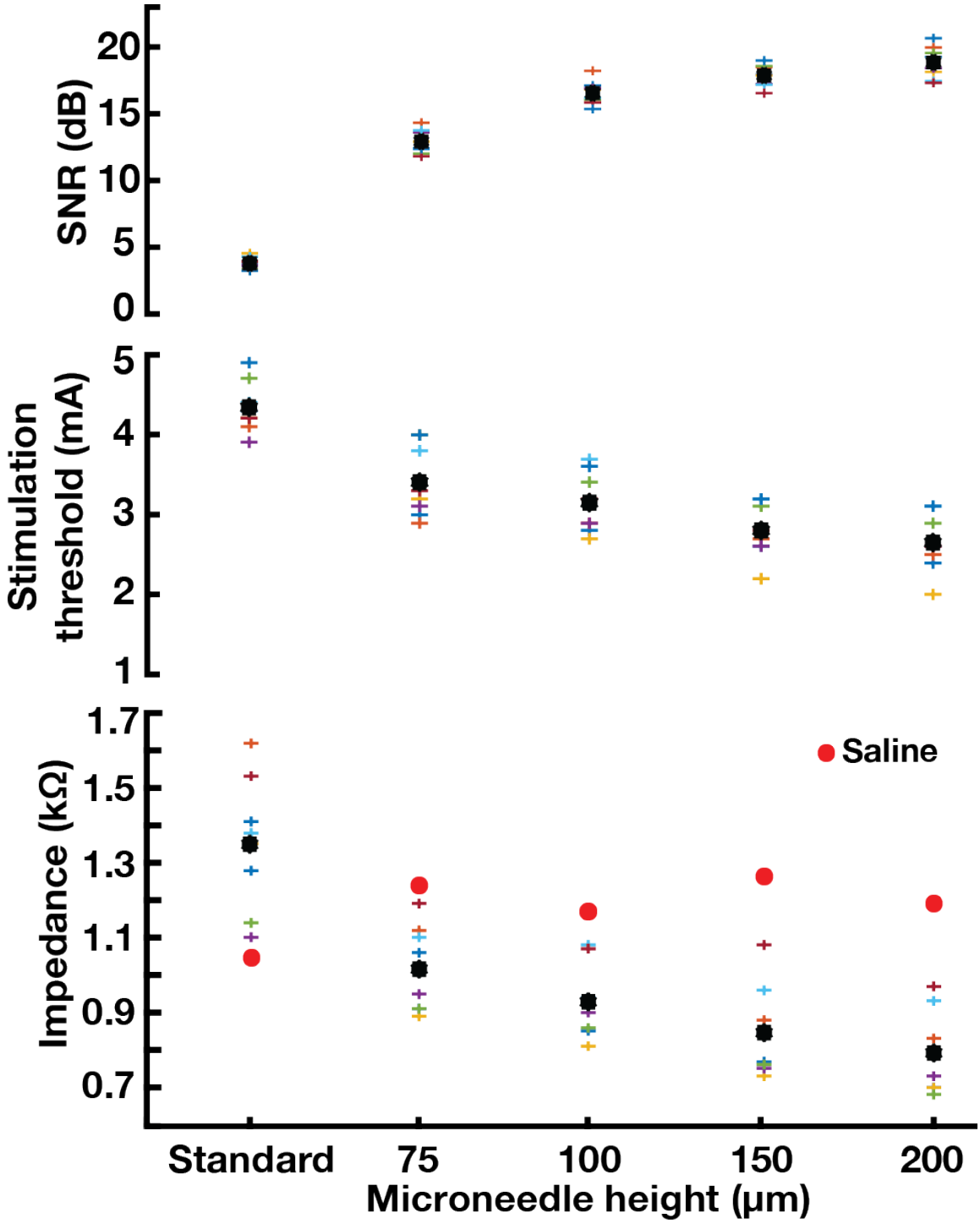


**Figure 50:** Increases in SNR (top), decreases in motor stimulation thresholds (middle), and decreases in electrode-tissue interface impedance (1 kHz) enabled by $\mu$N arrays. Experimental averages (cross marks) and population mean (black dots) are shown. Each cross mark represents the average SNR from 3 trials in a distinct experiment.

### *2.4.4 Increased SNR nerve activity recordings*

A direct relationship was observed between $\mu$N height and SNR of the recordings (Figure 50, top). Example traces of nerve activity recorded using standard and $\mu$N-cuff electrodes are shown in Figure 52. The use of $\mu$Ns enabled measurement of CAP components that are difficult to detect or discriminate using standard cuff electrodes. A maximum gain of 15 dB in SNR was observed with $\mu$N-cuffs with $\mu$Ns of height 200 $\mu$m. Compared to standard cuffs, the presence of 75 $\mu$m $\mu$Ns increased the SNR by 9.1 dB.

### *2.4.5 In vivo Biocompatibility*

$\mu$N-cuffs were implanted onto the right sciatic nerve of two Lewis rats for evaluation of chronic biocompatibility. Nerves with intact $\mu$N-cuffs were excised 14-days post-implantation for histological evaluation. No excessive inflammatory response was observed Figure 51.

## *2.5 Discussion*

Electrical stimulation and recording of peripheral nerve activity in the rat sciatic nerve enabled evaluation of the $\mu$N-cuff electrode compared to standard cuff electrodes. The results presented here demonstrate the $\mu$N-cuff's ability to lower the electrode-tissue interface impedance, lower motor stimulation thresholds, and increase the SNR.

Our data (Figure 50, bottom) shows that an indirect non-linear relationship exists between $\mu$N height and the measured reduction in interface impedance. Saline impedance measurements demonstrated higher impedances for all $\mu$N arrays compared to standards. $\mu$N arrays suffer a loss of bulk material from the laser micromachining process, which can explain increased saline impedances. All average

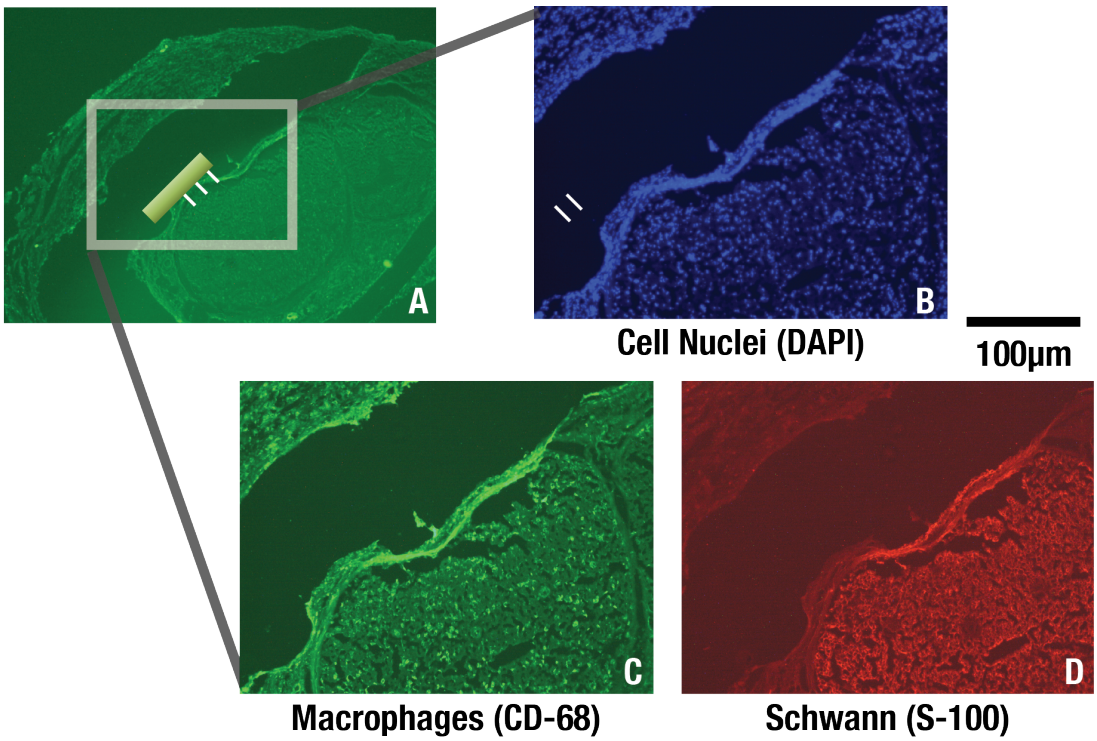


**Figure 51:** Radial cross section of a sciatic nerve with $\mu$N-cuff implants in place (A) stained for Nuclei (B), Macrophages (C), and Schwann cells (D).

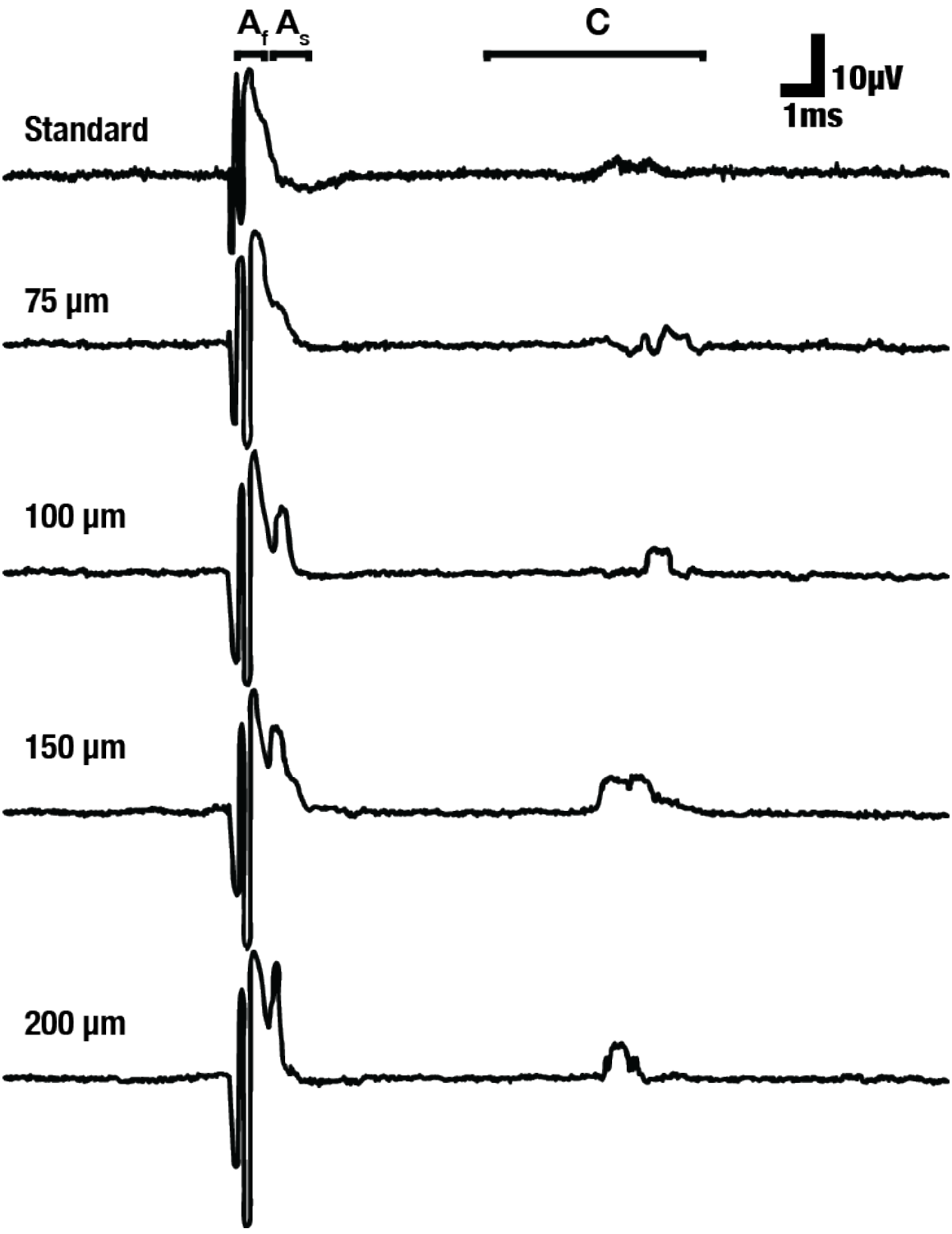


**Figure 52:** Single trial evoked CAP recordings from the rat sciatic nerve (same animal). Time windows for each measured component are shown at the top. $A_f$ and $A_s$ represent A-fast and A-slow fiber activity, respectively. C represents the time window for C-fiber activity. Time windows were computed using physiologically accepted conduction velocities. Stimulus artifacts precede the $A_f$ time window.

electrode-nerve interface impedance values measured with $\mu$N-cuffs were lower than corresponding measurements in saline (Figure 50, bottom), suggesting penetration of the outer layers.

Although our current study did not evaluate the extent to which $\mu$Ns penetrated the outer layers, the results presented here (Figure 50, middle) demonstrate the effectiveness of $\mu$Ns to also reduce motor stimulation thresholds. These benefits may be attributed to the fact that $\mu$Ns change the current distribution on the electrode surface, as well as stimulate directly inside of the nerve rather than through the outer layers. In addition, the presence of $\mu$Ns may provide localized regions of charge, providing greater selectivity and recruitment and an approach for maintaining cuff location post-implantation.

Previous studies have shown that desheathing the outer layers of the canine vagus nerve provides significant SNR increases and enables measurement of multiple fiber-types (Yoo et al., 2013). Our results (Figures 50, top and 52) suggest an alternative approach to desheathing that provides similar benefits. Figure 52 shows that the use of 75 $\mu$m $\mu$Ns leads to identification of different types of A-fibers, which could not be achieved with standard cuff electrodes (Figure 52, top trace). In addition, $\mu$Ns increased the resolution of C-fiber activity measurements.

Furthermore, there is no guarantee that electrodes were placed at exactly the same location or that $\mu$N penetration depth was consistent between trials or experiments. The nerve used in these investigations is multi-fascicular, and although attention was given to ensure consistent placement of electrodes, it is possible that the presented results may be enhanced when interfacing with individual nerves.

In conclusion, $\mu$N-cuffs are well suited for peripheral nerve interfacing, enabling sensitive recording and efficient stimulation of nerve activity. Ultimately, the ability to measure high resolution peripheral nerve activity and stimulate at lower thresholds will enable optimization of stimulation parameters and neural stimulation therapies.

# BIBLIOGRAPHY


Aagaard, Per, Erik B Simonsen, Jesper L Andersen, Peter Magnusson, and Poul Dyhre-Poulsen (2002). "Neural adaptation to resistance training: changes in evoked V-wave and H-reflex responses." In: *Journal of Applied Physiology* 92.6, pp. 2309–2318.

Ackermann, D Michael, Emily L Foldes, Niloy Bhadra, and Kevin L Kilgore (2009). "Effect of bipolar cuff electrode design on block thresholds in high-frequency electrical neural conduction block". In: *IEEE Transactions on Neural Systems and Rehabilitation Engineering* 17.5, pp. 469–477.

Ackermann, D. Michael, Emily L. Foldes, Niloy Bhadra, and Kevin L. Kilgore (2010a). "Conduction block of peripheral nerve using high-frequency alternating currents delivered through an intrafascicular electrode". In: *Muscle & Nerve* 41.1, pp. 117–119.

Ackermann, D. Michael, Niloy Bhadra, Emily L. Foldes, Xiao Feng Wang, and Kevin L. Kilgore (2010b). "Effect of nerve cuff electrode geometry on onset response firing in high-frequency nerve conduction block". In: *IEEE Transactions on Neural Systems and Rehabilitation Engineering* 18.6, pp. 658–665.

Ackermann, D. Michael, Emily L. Foldes, Niloy Bhadra, and Kevin L. Kilgore (2010c). "Nerve conduction block using combined thermoelectric cooling and high frequency electrical stimulation". In: *Journal of Neuroscience Methods* 193.1, pp. 72–76.

Ackermann, D. Michael, Niloy Bhadra, Emily L Foldes, and Kevin L Kilgore (2011a). "Conduction block of whole nerve without onset firing using combined high frequency and direct current". In: *Medical & Biological Engineering & Computing* 49.2, pp. 241–251.

Ackermann, D Michael, Niloy Bhadra, Meana Gerges, and Peter J Thomas (2011b). "Dynamics and sensitivity analysis of high-frequency conduction block." In: *Journal of Neural Engineering* 8.6, p. 065007.

Ackermann, Michael D., Christian Ethier, Emily L. Foldes, Emily R. Oby, Dustin Tyler, Matt Bauman, Niloy Bhadra, Lee Miller, and Kevin L. Kilgore (2011c). "Electrical conduction block in large nerves: High frequency current delivery in the nonhuman primate". In: *Muscle & Nerve* 43.6, pp. 897–899.

Ackermann, Michael D, Niloy Bhadra, Emily L. Foldes, and Kevin L. Kilgore (2011d). "Separated Interface Nerve Electrode Prevents Direct Current Induced Nerve Damage". In: *Journal of Neuroscience Methods* 201.1, pp. 173–176.

Agostoni, E, J E Chinnock, M. De Burgh Daly, and J G Murray (1957). "Functional and histological studies of the vagus nerve and its branches to the heart, lungs and abdominal viscera in the cat". In: *The Journal of Physiology* 135.1, pp. 182–205.

Apovian, Caroline M., Sajani N. Shah, Bruce M. Wolfe, Sayeed Ikramuddin, Christopher J. Miller, Katherine S. Tweden, Charles J. Billington, and Scott A. Shikora (2016). "Two-Year Outcomes of Vagal Nerve Blocking (vBloc) for the Treatment of Obesity in the ReCharge Trial". In: *Obesity Surgery*.

Arrenberg, Aristides B, Didier YR Stainier, Herwig Baier, and Jan Huisken (2010). "Optogenetic control of cardiac function". In: *Science* 330.6006, pp. 971–974.

Barabanov, Michael and Victor Yodaiken (1996). "Real-time linux". In: *Linux Journal* 23.4.2, p. 1.

Baratta, R, M Ichie, S K Hwang, and M Solomonow (1989). "Orderly stimulation of skeletal muscle motor units with tripolar nerve cuff electrode." In: *IEEE Transactions on Biomedical Engineering* 36.8, pp. 836–843.

Barrett, Eugene J., Eleuterio Ferrannini, Richard Gusberg, Stefano Bevilacqua, and Ralph A. DeFronzo (1985). "Hepatic and extrahepatic splanchnic glucose metabolism in the postabsorptive and glucose fed dog". In: *Metabolism* 34.5, pp. 410–420.

Bartolucci, Chiara, Claudia Altomare, Marco Bennati, Simone Furini, Antonio Zaza, and Stefano Severi (2015). "Combined action potential- and dynamic-clamp for accurate computational modelling of the cardiac IKr current". In: *Journal of Molecular and Cellular Cardiology* 79.2014, pp. 187–194.

Beard, SM, Amanda Hunn, and Jeremy Wight (2003). "Treatments for spasticity and pain in multiple sclerosis: a systematic review". In:

Bédard, Claude and Alain Destexhe (2008). "A modified cable formalism for modeling neuronal membranes at high frequencies." In: *Biophysical Journal* 94.4, pp. 1133–1143.

Bentley, Frederic H and W Schlapp (1943). "The effects of pressure on conduction in peripheral nerve". In: *The Journal of Physiology* 102.1, pp. 72–82.

Berthoud, Hans Rudolf and Terry L. Powley (1993). "Characterization of vagal innervation to the rat celiac, suprarenal and mesenteric ganglia". In: *Journal of the Autonomic Nervous System* 42.2, pp. 153–169.

Bettencourt, Jonathan C, Kyle P Lillis, Laura R Stupin, and John A White (2008). "Effects of imperfect dynamic clamp: computational and experimental results". In: *Journal of neuroscience methods* 169.2, pp. 282–289.

Bhadra, Narendra, Niloy Bhadra, Kevin Kilgore, and Kenneth J Gustafson (2006). "High frequency electrical conduction block of the pudendal nerve". In: *Journal of Neural Engineering* 3.2, pp. 180–187.

Bhadra, Niloy and Kevin L Kilgore (2005). "High-frequency electrical conduction block of mammalian peripheral motor nerve". In: *Muscle & Nerve* 32.6, pp. 782–790.

Bhadra, Niloy, Emily A Lahowetz, Stephen T Foldes, and Kevin L Kilgore (2007). "Simulation of high-frequency sinusoidal electrical block of mammalian myelinated axons". In: *Journal of Computational Neuroscience* 22.3, pp. 313–326.

Bicket, Mark C., Roger Y. Dunn, and Shihab U. Ahmed (2016). "High-Frequency Spinal Cord Stimulation for Chronic Pain: Pre-Clinical Overview and Systematic Review of Controlled Trials". In: *Pain Medicine*, pnw156.

Boger, Adam, Narendra Bhadra, and Kenneth J. Gustafson (2008). "Bladder voiding by combined high frequency electrical pudendal nerve block and sacral root stimulation". In: *Neurourology and Urodynamics* 27.5, pp. 435–439.

Boger, Adam, Narendra Bhadra, and Kenneth J Gustafson (2013). "Different clinical electrodes achieve similar electrical nerve conduction block." In: *Journal of Neural Engineering* 10.5, p. 056016.

Boger, Adam S, Narendra Bhadra, and Kenneth J Gustafson (2012). "High frequency sacral root nerve block allows bladder voiding." In: *Neurourology and Urodynamics* 31.5, pp. 677–682.

Borovikova, Lyudmila V, Svetlana Ivanova, Minghuang Zhang, Huan Yang, Galina I Botchkina, Linda R Watkins, Haichao Wang, Naji Abumrad, John W Eaton, and Kevin J Tracey (2000). "Vagus nerve stimulation attenuates the systemic inflammatory response to endotoxin." In: *Nature* 405.6785, pp. 458–462.

Bowman, Bruce R and Donald R McNeal (1987). "Response of single alpha motoneurons to high-frequency pulse trains". In: *Stereotactic and Functional Neurosurgery* 49.3, pp. 121–138.

Boyle, Michael R and Flavio Frohlich (2013). "EEG feedback-controlled transcranial alternating current stimulation". In: *International IEEE/EMBS Conference on Neural Engineering, NER*, pp. 140–143.

Branner, Almut, Richard B Stein, and Richard A Normann (2001). "Selective stimulation of cat sciatic nerve using an array of varying-length microelectrodes." In: *Journal of Neurophysiology* 85.4, pp. 1585–94.

Bratton, B O, D Martelli, M J McKinley, D Trevaks, C R Anderson, and R M McAllen (2012). "Neural regulation of inflammation: no neural connection from the vagus to splenic sympathetic neurons." In: *Experimental Physiology* 97.11, pp. 1180–5.

Brooks, S. L., A. M. Neville, N. J. Rothwell, M. J. Stock, and S. Wilson (1981). "Sympathetic activation of brown-adipose-tissue thermogenesis in cachexia". In: *Bioscience Reports* 1.6, pp. 509–517.

Brown, Tashalee R, Trine Krogh-Madsen, and David J Christini (2016). "Illuminating Myocyte-Fibroblast Homotypic and Heterotypic Gap Junction Dynamics Using Dynamic Clamp". In: *Biophysical Journal* 111.4, pp. 785–797.

Brunton, Emma Kate, Bjorn Winther-Jensen, Chun Wang, Edwin Bingbing Yan, Saman Hagh Gooie, Arthur James Lowery, and Ramesh Rajan (2015). "In vivo comparison of the charge densities required to evoke motor responses using novel annular penetrating microelectrodes." In: *Frontiers in Neuroscience* 9.May, p. 265.

Buckley, Una, Ray W Chiu, Pradeep S Rajendran, Tina S Vrabec, Kalyanam Shivkumar, and Jeffrey L Ardell (2017). "Bioelectronic neuromodulation of the paravertebral cardiac efferent sympathetic outflow and its effect on ventricular electrical indices". In: *Heart Rhythm* 17.)30215-1, S1547–5271.

Burden, Richard L and J Douglas Faires (2001). *Numerical Analysis.* Wadsworth Group.

Burgess, PR and ER Perl (1967). "Myelinated afferent fibres responding specificaly to noxious stimulation of the skin". In: *The Journal of Physiology* 190.3, pp. 541–562.

Butera, Robert J, Christopher G Wilson, Christopher A DelNegro, and Jeffrey C Smith (2001). "A methodology for achieving high-speed rates for artificial conductance injection in electrically excitable biological cells". In: *IEEE Transactions on Biomedical Engineering* 48.12, pp. 1460–1470.

Buzsáki, György (2004). "Large-scale recording of neuronal ensembles". In: *Nature Neuroscience* 7.5, pp. 446–451.

Camilleri, M, J Toouli, M F F. Herrera, B Kulseng, L Kow, J P Pantoja, R Marvik, G Johnsen, C J Billington, F G Moody, M B Knudson, K S Tweden, M Vollmer, R R Wilson, and M Anvari (2008). "Intra-abdominal vagal blocking (VBLOC

therapy): clinical results with a new implantable medical device". In: *Surgery* 143.6, pp. 723–731.

Cattell, M and R W Gerard (1935). "The "inhibitory" effect of high-frequency stimulation and the excitation state of nerve." In: *The Journal of Physiology* 83.4, pp. 407–15.

Celler, B G and L P Schramm (1981). "Pre- and postganglionic sympathetic activity in splanchnic nerves of rats". In: *Am.J.Physiol* 241.1, R55–R61.

Chu, Jun-Uk, Kang-Il Song, Sungmin Han, Soo Hyun Lee, Jinseok Kim, Ji Yoon Kang, Dosik Hwang, Jun-Kyo Francis Suh, Kuiwon Choi, and Inchan Youn (2012). "Improvement of signal-to-interference ratio and signal-to-noise ratio in nerve cuff electrode systems." In: *Physiological Measurement* 33.6, pp. 943–67.

Cogan, Stuart F (2008). "Neural stimulation and recording electrodes." In: *Annual Review of Biomedical Engineering* 10, pp. 275–309.

Cogan, Stuart F, Philip R Troyk, Julia Ehrlich, and Timothy D Plante (2005). "In Vitro Comparison of the Charge-Injection Limits of Activated Irirdium Oxide (AIROF) and Platimum-Irirdium Microelectrodes". In: *IEEE Transactions on Biomedical Engineering* 52.9, pp. 1612–1613.

Cogan, Stuart F, Kip A Ludwig, Cristin G Welle, and Pavel Takmakov (2016). "Tissue damage thresholds during therapeutic electrical stimulation". In: *Journal of Neural Engineering* 13.2, p. 021001.

Cuellar, Jason M, Konstantinos Alataris, Andre Walker, David C Yeomans, and Joseph F Antognini (2013). "Effect of high-frequency alternating current on spinal afferent nociceptive transmission." In: *Neuromodulation: Technology at the Neural Interface* 16.4, pp. 318–327.

Cui, Xinyan, Jamille F Hetke, James a Wiler, David J Anderson, and David C Martin (2001). "Electrochemical deposition and characterization of conducting polymer polypyrrole / PSS on multichannel neural probes". In: *Sensors and actuators* 93, pp. 8–18.

Devenyi, Ryan A., Francis A. Ortega, Willemijn Groenendaal, Trine Krogh-Madsen, David J. Christini, and Eric A. Sobie (2016). "Differential roles of two delayed rectifier potassium currents in regulation of ventricular action potential duration and arrhythmia susceptibility". In: *The Journal of Physiology*, 10.1113/JP273191.

Dorval, A. D., D. J. Christini, and J. A. White (2001). "Real-time linux dynamic clamp: A fast and flexible way to construct virtual ion channels in living cells". In: *Annals of Biomedical Engineering* 29.10, pp. 897–907.

Eastman, Kyler M and Alexander C Huk (2012). "PLDAPS: a hardware architecture and software toolbox for neurophysiology requiring complex visual stimuli and online behavioral control". In: *Frontiers in Neuroinformatics* 6.

Economo, Michael N, Fernando R Fernandez, and John A White (2010). "Dynamic clamp: alteration of response properties and creation of virtual realities in neurophysiology". In: *The Journal of Neuroscience* 30.7, pp. 2407–2413.

Englitz, Bernhard, Stephen V David, Mike D Sorenson, and Shihab A Shamma (2013). "MANTAan open-source, high density electrophysiology recording suite for MATLAB". In: *Frontiers in Neural Circuits* 7, p. 69.

Fisher, Karen M, Ngalla E Jillani, George O Oluoch, and Stuart N Baker (2014). "Blocking central pathways in the primate motor system using high frequency sinusoidal current". In: *Journal of Neurophysiology*, p. 00347.

Flett, Peter J (2003). "Rehabilitation of spasticity and related problems in childhood cerebral palsy". In: *Journal of Paediatrics and child health* 39.1, pp. 6–14.

Franke, Manfred, Tina Vrabec, Jesse Wainright, Niloy Bhadra, Narendra Bhadra, and Kevin Kilgore (2014a). "Combined KHFAC + DC nerve block without onset or reduced nerve conductivity after block." In: *Journal of Neural Engineering* 11.5, p. 056012.

Franke, Manfred, Niloy Bhadra, Narendra Bhadra, and Kevin Kilgore (2014b). "Direct current contamination of kilohertz frequency alternating current waveforms". In: *Journal of Neuroscience Methods* 232.2014, pp. 74–83.

Frey, Urs, Jan Sedivy, Flavio Heer, Rene Pedron, Marco Ballini, Jan Mueller, Douglas Bakkum, Sadik Hafizovic, Francesca D Faraci, Frauke Greve, et al. (2010). "Switch-matrix-based high-density microelectrode array in CMOS technology". In: *IEEE Journal of Solid-State Circuits* 45.2, pp. 467–482.

Freyberg, R H and M M Peet (1937). "The effect on the kidney of bilateral splanchnicectomy in patients with hypertension". In: *The Journal of Clinical Investigation* 16.1, pp. 49–65.

Fröhlich, Flavio (2014). "Endogenous and exogenous electric fields as modifiers of brain activity: rational design of noninvasive brain stimulation with transcranial alternating current stimulation". In: *Dialogues in Clinical Neuroscience* 16.1, pp. 93–102.

Fröhlich, Flavio (2015). "Experiments and models of cortical oscillations as a target for noninvasive brain stimulation". In: *Progress in Brain Research* 222, pp. 41–73.

Furness, J. B., H. S. Koopmans, H. L. Robbins, N. Clerc, J. M. Tobin, and M. J. Morris (2001). "Effects of vagal and splanchnic section on food intake, weight, serum leptin and hypothalamic neuropeptide Y in rat". In: *Autonomic Neuroscience: Basic and Clinical* 92.1-2, pp. 28–36.

Gamble, H. J. and Rosemary A Eames (1964). "An electron microscope study of the connective tissues of the human peripheral nerve". In: *Journal of Anatomy* 98.1964, pp. 655–663.

Gasser, HS (1941). "The classification of nerve fibers." In: *Ohio Journal of Science* 41.3, pp. 145–159.

Gerges, Meana, Emily L Foldes, Michael D Ackermann, Narendra Bhadra, Niloy Bhadra, and Kevin L Kilgore (2010). "Frequency- and amplitude-transitioned waveforms mitigate the onset response in high-frequency nerve block." In: *Journal of Neural Engineering* 7.6, p. 066003.

Gerum, Philippe (2004). "Xenomai - Implementing a RTOS emulation framework on GNU/Linux". In: *White Paper, Xenomai*, pp. 1–12.

Goodall, E V, J F de Breij, and J Holsheimer (1996). "Position-selective activation of peripheral nerve fibers with a cuff electrode." In: *IEEE Transactions on Biomedical Engineering* 43.8, pp. 851–6.

Govorunova, Elena G, Shane R Cunha, Oleg A Sineshchekov, and John L Spudich (2016). "Anion channelrhodopsins for inhibitory cardiac optogenetics". In: *Scientific Reports* 6.

Grill, W. M. and J. T. Mortimer (1998). "Stability of the input-output properties of chronically implanted multiple contact nerve cuff stimulating electrodes". In: *IEEE Transactions on Rehabilitation Engineering* 6.4, pp. 364–373.

Groenendaal, Willemijn, Francis A Ortega, Trine Krogh-Madsen, and David J Christini (2014). "Voltage and calcium dynamics both underlie cellular alternans in cardiac myocytes". In: *Biophysical Journal* 106.10, pp. 2222–2232.

Groenendaal, Willemijn, Francis A Ortega, Armen R Kherlopian, Andrew C Zygmunt, Trine Krogh-Madsen, and David J Christini (2015). "Cell-specific cardiac electrophysiology models". In: *PLoS Computational Biology* 11.4, e1004242.

Grosenick, Logan, James H Marshel, and Karl Deisseroth (2015). "Closed-loop and activity-guided optogenetic control". In: *Neuron* 86.1, pp. 106–139.

Güven, Mustafa, Kerem Ozgünen, and Ismail Günay (2005). "Conduction blocks of lidocaine on crushed rat sciatic nerve: an in-vitro study." In: *International Journal of Neuroscience* 115.5, pp. 725–734.

Harrison, Reid R (2007). "A versatile integrated circuit for the acquisition of biopotentials". In: *2007 IEEE Custom Integrated Circuits Conference*. IEEE, pp. 115–122.

Harrison, Reid R, Ilya Kolb, Suhasa B Kodandaramaiah, Alexander A Chubykin, Aimei Yang, Mark F Bear, Edward S Boyden, and Craig R Forest (2015). "Microchip amplifier for in vitro, in vivo, and automated whole cell patch-clamp recording". In: *Journal of Neurophysiology* 113.4, pp. 1275–1282.

*HDF5*.

Hines, Michael (1993). "NEURON - A Program for Simulation of Nerve Equations". In: *Neural Systems: Analysis and modeling*, pp. 127–136.

Hoobler, S W, J T Manning, W G Paine, S G McClellan, P O Helcher, H Renfert, M M Peet, and E a Kahn (1951). "The effects of splanchnicectomy on the blood pressure in hypertension; a controlled study." In: *Circulation* 4.2, pp. 173–183.

Hosoi, T, Y Okuma, and Y Nomura (2000). "Electrical stimulation of afferent vagus nerve induces IL-1beta expression in the brain and activates HPA axis." In: *American Journal of Physiology. Regulatory, Integrative and Comparative Physiology* 279.1, R141–R147.

Howell, Bryan, Leonel E Medina, and Warren M Grill (2015). "Effects of frequency-dependent membrane capacitance on neural excitability". In: *Journal of Neural Engineering* 12.5, pp. 1–17.

Huston, Jared M, Mahendar Ochani, Mauricio Rosas-Ballina, Hong Liao, Kanta Ochani, Valentin A Pavlov, Margot Gallowitsch-Puerta, Mala Ashok, Christopher J Czura, Brian Foxwell, Kevin J Tracey, and Luis Ulloa (2006). "Splenectomy inactivates the cholinergic antiinflammatory pathway during lethal endotoxemia and polymicrobial sepsis." In: *The Journal of Experimental Medicine* 203.7, pp. 1623–8.

Idoux, Erwin and Jerome Mertz (2011). "Control of local intracellular calcium concentration with dynamic-clamp controlled 2-photon uncaging". In: *PLoS ONE* 6.12, e28685.

Islam, M Shahidul, Michael C Oliveira, Yan Wang, Francis P Henry, Mark A Randolph, B Hyle Park, and Johannes F de Boer (2012). "Extracting structural fea-

tures of rat sciatic nerve using polarization-sensitive spectral domain optical coherence tomography". In: *Journal of Biomedical Optics* 17.5, p. 56012.

Jensen, Alicia L and Dominique M Durand (2009). "High frequency stimulation can block axonal conduction". In: *Experimental Neurology* 220.1, pp. 57–70.

Joseph, Laveeta, Benjamin D Haeffele, and Robert J Butera (2007). "Conduction block induced by high frequency AC stimulation in unmyelinated nerves." In: *Annual International Conference of the IEEE Engineering in Medicine and Biology Society*, pp. 1719–1722.

Joseph, Laveeta and Robert J Butera (2009). "Unmyelinated Aplysia nerves exhibit a nonmonotonic blocking response to high-frequency stimulation." In: *IEEE Transactions on Neural Systems and Rehabilitation Engineering* 17.6, pp. 537–544.

Joseph, Laveeta and Robert J Butera (2011). "High-frequency stimulation selectively blocks different types of fibers in frog sciatic nerve". In: *IEEE Transactions on Neural Systems and Rehabilitation Engineering* 19.5, pp. 550–557.

Kapural, Leonardo, Cong Yu, Matthew W Doust, Bradford E Gliner, Ricardo Vallejo, B Todd Sitzman, Kasra Amirdelfan, Donna M Morgan, Lora L Brown, Thomas L Yearwood, Richard Bundschu, Allen W Burton, Thomas Yang, Ramsin Benyamin, and Abram H Burgher (2015). "Novel 10-kHz High-frequency Therapy (HF10 Therapy) Is Superior to Traditional Low-frequency Spinal Cord Stimulation for the Treatment of Chronic Back and Leg Pain: The SENZA-RCT Randomized Controlled Trial". In: *Anesthesiology* 123.4, pp. 851–60.

Kilgore, Kevin L. and N. Bhadra (2004). "Nerve conduction block utilising high-frequency alternating current". In: *Medical & Biological Engineering & Computing* 42.3, pp. 394–406.

Kilgore, Kevin L and Niloy Bhadra (2014). "Reversible nerve conduction block using kilohertz frequency alternating current". In: *Neuromodulation: Technology at the Neural Interface* 17.3, pp. 242–254.

Kispersky, Tilman J, Michael N Economo, Pratik Randeria, and John a White (2011). "GenNet: A Platform for Hybrid Network Experiments." In: *Frontiers in Neuroinformatics* 5.July, p. 11.

Koopman, Frieda A, Sangeeta S Chavan, Sanda Miljko, Simeon Grazio, Sekib Sokolovic, P Richard Schuurman, Ashesh D Mehta, Yaakov A Levine, Michael Faltys, Ralph Zitnik, and Others (2016). "Vagus nerve stimulation inhibits cytokine production and attenuates disease severity in rheumatoid arthritis". In: *Proceedings of the National Academy of Sciences* 113.29, pp. 8284–8289.

Kumsa, Doe, Eric M Hudak, Fred W Montague, Shawn C Kelley, Darrel F Untereker, Benjamin P Hahn, Chris Condit, Martin Cholette, Hyowon Lee, Dawn Bardot, and Pavel Takmakov (2016). "Electrical neurostimulation with imbalanced waveform mitigates dissolution of platinum electrodes". In: *Journal of Neural Engineering* 13.5, p. 054001.

Kuntz, A, H Hoffman, and E M Schaeffer (1957). "Fiber components of the splanchnic nerves." In: *The Anatomical Record* 128.1, pp. 139–146.

Laviano, Alessandro, Akio Inui, Daniel L Marks, Michael M Meguid, Claude Pichard, Filippo Rossi Fanelli, and Marilia Seelaender (2008). "Neural control of the anorexia-cachexia syndrome". In: *American Journal of Physiology. Endocrinology And Metabolism* 295.5, pp. 1000–1008.

Leonardo, Anthony and Michale S Fee (2005). "Ensemble coding of vocal control in birdsong". In: *The Journal of Neuroscience* 25.3, pp. 652–661.

Lin, E, Kevin L Kilgore, Niloy Bhadra, and Emily A Lahowetz (2007). "Chronic high-frequency nerve block with an implanted waveform generator". In: *International Functional Electrical Stimulation Society Conference*, p. 1.

Lin, Risa J., Jonathan Bettencourt, John A. White, David J. Christini, and Robert J Butera (2010). "Real-time Experiment Interface for biological control applications". In: *2010 Annual International Conference of the IEEE Engineering in Medicine and Biology Society, EMBC'10*, pp. 4160–4163.

Liu, Hailong, James R. Roppolo, William C. De Groat, and Changfeng Tai (2009). "The role of slow potassium current in nerve conduction block induced by high-frequency biphasic electrical current". In: *IEEE Transactions on Biomedical Engineering* 56.1, pp. 137–146.

Liu, Hailong, Linlin Zhu, Shulei Sheng, Lifei Sun, Hongmin Zhou, Hong Tang, and Tianshuang Qiu (2013). "Post stimulus effects of high frequency biphasic electrical current on a fibre's conductibility in isolated frog nerves." In: *Journal of Neural Engineering* 10.3, p. 036024.

Loeb, G E and R A Peck (1996). "Cuff electrodes for chronic stimulation and recording of peripheral nerve activity." In: *Journal of Neuroscience Methods* 64.1, pp. 95–103.

Lustenberger, Caroline, Michael R. Boyle, Sankaraleengam Alagapan, Juliann M. Mellin, Bradley V. Vaughn, and Flavio Frohlich (2016). "Feedback-Controlled Transcranial Alternating Current Stimulation Reveals a Functional Role of Sleep Spindles in Motor Memory Consolidation". In: *Current Biology* 26, pp. 1–10.

Martelli, D, S T Yao, M J McKinley, and R M McAllen (2014a). "Reflex control of inflammation by sympathetic nerves, not the vagus." In: *The Journal of Physiology* 592.Pt 7, pp. 1677–86.

Martelli, D., M.J. McKinley, and R.M. McAllen (2014b). "The cholinergic anti-inflammatory pathway: A critical review". In: *Autonomic Neuroscience: Basic and Clinical* 182.2014, pp. 65–69.

Martelli, Davide, Song T Yao, Michael J McKinley, and Robin M McAllen (2014c). "Neural control of inflammation by the greater splanchnic nerves". In: *Temperature* 1.1, pp. 14–15.

Martinek, Johannes, Yvonne Stickler, Martin Reichel, Winfried Mayr, and Frank Rattay (2008). "A novel approach to simulate Hodgkin-Huxley-like excitation with COMSOL Multiphysics". In: *Artificial Organs* 32.8, pp. 614–619.

McMullan, Simon, Daniel A Simpson, and Bridget M Lumb (2004). "A reliable method for the preferential activation of C- or A-fibre heat nociceptors". In: *Journal of Neuroscience Methods* 138.1, pp. 133–139.

Meijs, Suzan, Morten Fjorback, Carina Jensen, and Søren Sørensen (2015). "Electrochemical properties of titanium nitride nerve stimulation electrodes: an in vitro and in vivo study". In: *Frontiers in Neuroscience* 9.268, pp. 1–11.

Meijs, Suzan, Morten Fjorback, Carina Jensen, Søren Sørensen, Kristian Rechendorff, and Nico J M Rijkhoff (2016). "Influence of fibrous encapsulation on electrochemical properties of TiN electrodes". In: *Medical Engineering and Physics* 38.5, pp. 468–476.

Merrill, Daniel R, Marom Bikson, and John G R Jefferys (2005). "Electrical stimulation of excitable tissue: design of efficacious and safe protocols." In: *Journal of Neuroscience Methods* 141.2, pp. 171–98.

Miles, J D, Kevin L Kilgore, Niloy Bhadra, and Emily Lahowetz (2007). "Effects of ramped amplitude waveforms on the onset response of high-frequency mammalian nerve block." In: *Journal of Neural Engineering* 4.4, pp. 390–398.

Miller, Jonathan P., Sam Eldabe, Eric Buchser, Lisa M. Johanek, Yun Guan, and Bengt Linderoth (2016). "Parameters of Spinal Cord Stimulation and Their Role in Electrical Charge Delivery: A Review". In: *Neuromodulation: Technology at the Neural Interface* 2016.

Nabi, Ali, Tyler Stigen, Jeff Moehlis, and Theoden Netoff (2013). "Corrigendum: Minimum energy control for in vitro neurons". In: *Journal of Neural Engineering* 10.4, p. 049501.

Nance, Dwight M. and Virginia M. Sanders (2007). "Autonomic Innervation and Regulation of the Immune System (1987-2007)". In: *Brain, Behavior, and Immunity* 21.6, pp. 736–745.

Newman, Jonathan P, Riley Zeller-Townson, Ming-Fai Fong, Sharanya Arcot Desai, Robert E Gross, and Steve M Potter (2013). "Closed-Loop, Multichannel Experimentation Using the Open-Source NeuroRighter Electrophysiology Platform". In: *Frontiers in Neural Circuits* 6, p. 98.

Newman, Jonathan P, Ming-fai Fong, Daniel C Millard, Clarissa J Whitmire, Garrett B Stanley, and Steve M Potter (2015). "Optogenetic feedback control of neural activity". In: *eLife* 4, e07192.

*Normal Rat Ringer's Solution.*

Norman, Sharon E, Robert J Butera, and Carmen C Canavier (2016). "Stochastic Slowly Adapting Ionic Currents May Provide a Decorrelation Mechanism For Neural Oscillators by Causing Wander in the Intrinsic Period". In: *Journal of Neurophysiology*, jn–00193.

O'dwyer, NJ, L Ada, and PD Neilson (1996). "Spasticity and muscle contracture following stroke". In: *Brain* 119.5, pp. 1737–1749.

Patel, Yogi A and Robert J Butera (2015). "Differential fiber-specific block of nerve conduction in mammalian peripheral nerves using kilohertz electrical stimulation." In: *Journal of Neurophysiology* 113.10, pp. 3923–9.

Patel, Yogi A, Andrew Willsie, Isaac P Clements, Ricardo Aguilar, Swaminathan Rajaraman, and Robert J Butera (2016). "Microneedle cuff electrodes for extrafascicular peripheral nerve interfacing". In: *38th Annual International Conference of the IEEE Engineering in Medicine and Biology Society*, pp. 1741–1744.

Patel, Yogi A., Brian S. Kim, William S. Rountree, and Robert J. Butera (2017a). "Kilohertz Electrical Stimulation Nerve Conduction Block: Effects of Electrode Surface Area". In: *IEEE Transactions on Neural Systems and Rehabilitation Engineering*.

Patel, Yogi A, Tarun Saxena, Ravi V Bellamkonda, and Robert J Butera (2017b). "Kilohertz frequency nerve block enhances anti-inflammatory effects of vagus nerve stimulation". In: *Scientific Reports* 7, p. 39810.

Peet, Max M (1935). "Splanchnic section for hypertension: A preliminary report". In: *Univ. Hosp. Bull., Ann Arbor* 1.June, p. 17.

Pelot, Nicole A, Christina E Behrend, and Warren M Grill (2015). "Modeling the response of small myelinated and unmyelinated axons to kilohertz frequency signals". In: *International IEEE/EMBS Conference on Neural Engineering, NER*, pp. 406–409.

Polasek, Katharine H., Harry A. Hoyen, Michael W. Keith, and Dustin J. Tyler (2007). "Human nerve stimulation thresholds and selectivity using a multi-contact nerve cuff electrode". In: *IEEE Transactions on Neural Systems and Rehabilitation Engineering* 15.1, pp. 76–82.

Powley, T L, J C Prechtl, E A Fox, and H R Berthoud (1983). "Anatomical considerations for surgery of the rat abdominal vagus: distribution, paraganglia and regeneration." In: *Journal of the Autonomic Nervous System* 9.1, pp. 79–97.

Prechtl, JC and TL Powley (1990). "The fiber composition of the abdominal vagus of the rat". In: *Anatomy and Embryology* 181, pp. 101–115.

Preyer, Amanda J and Robert J Butera (2009). "Causes of transient instabilities in the dynamic clamp". In: *IEEE Transactions on Neural Systems and Rehabilitation Engineering* 17.2, pp. 190–198.

Prinz, Astrid A, L F Abbott, and Eve Marder (2004). "The dynamic clamp comes of age". In: *Trends in Neurosciences* 27.4, pp. 218–224.

Pyragas, Kestutis, Viktor Novičenko, and Peter Alexander Tass (2013). "Mechanism of suppression of sustained neuronal spiking under high-frequency stimulation". In: *Biological Cybernetics* 107.6, pp. 669–684.

*Qt*.

*Qwt - Qt Widgets for Technical Applications*.

Raikov, Ivan, Amanda Preyer, and Robert J Butera (2004). "MRCI: a flexible real-time dynamic clamp system for electrophysiology experiments". In: *Journal of Neuroscience Methods* 132.2, pp. 109–123.

Rattay, Frank (1989). "Analysis of models for extracellular fiber stimulation." In: *IEEE Transactions on Biomedical Engineering* 36.7, pp. 676–682.

Rattay, Frank and Matthias Aberham (1993). "Modeling Axon Membranes for Functional Electrical Stimulation". In: *IEEE Transactions on Biomedical Engineering* 40.12, pp. 1201–1209.

Reboul, J and A Rosenblueth (1939). "The action of alternating currents upon the electrical excitability of nerve". In: *American Journal of Physiology. Legacy Content* 125.2, pp. 205–215.

Rosas-Ballina, Mauricio, Mahendar Ochani, William R Parrish, Kanta Ochani, Yael T Harris, Jared M Huston, Sangeeta Chavan, and Kevin J Tracey (2008). "Splenic nerve is required for cholinergic antiinflammatory pathway control of TNF in endotoxemia." In: *Proceedings of the National Academy of Sciences of the United States of America* 105.31, pp. 11008–13.

Rosenblueth, Arturo and J Reboul (1939). "The blocking and deblocking effects of alternating currents on nerve". In: *American Journal of Physiology. Legacy Content* 125.2, pp. 251–264.

Sakata, J T and Brainard M S (2006). "Real-time contributions of auditory feedback to avian vocal motor control". In: *The Journal of Neuroscience* 26, 9619–9628.

Schlaich, Markus, Nora Straznicky, Elisabeth Lambert, and Gavin Lambert (2015). "Metabolic syndrome: A sympathetic disease?" In: *The Lancet Diabetes and Endocrinology* 3.2, pp. 148–158.

Schmalbruch, H (1986). "Fiber composition of the rat sciatic nerve". In: *The Anatomical Record* 215.1, pp. 71–81.

Schnabel, V and J J Struijk (2001). "Evaluation of the cable model for electrical stimulation of unmyelinated nerve fibers". In: *IEEE Transactions on Biomedical Engineering* 48.9, pp. 1027–1033.

Scholvin, Jörg, Justin P Kinney, Jacob G Bernstein, Caroline Moore-Kochlacs, Nancy Kopell, Clifton G Fonstad, and Edward S Boyden (2016). "Close-packed silicon microelectrodes for scalable spatially oversampled neural recording". In: *IEEE Transactions on Biomedical Engineering* 63.1, pp. 120–130.

Schuettler, Martin, Nick Donaldson, Vipin Seetohul, and John Taylor (2013). "Fibre-selective recording from the peripheral nerves of frogs using a multi-electrode cuff". In: *Journal of Neural Engineering* 10.3, p. 036016.

Sharp, Andrew A., Michael B O'Neil, L F Abbott, and Eve Marder (1993). "The dynamic clamp: artificial conductances in biological neurons". In: *Trends in Neurosciences* 16.10, pp. 389–394.

Siegle, Joshua H., Gregory J. Hale, Jonathan P. Newman, and Jakob Voigts (2015). "Neural ensemble communities: Open-source approaches to hardware for large-scale electrophysiology". In: *Current Opinion in Neurobiology* 32, pp. 53–59.

Sieling, Fred, Alexis Bédécarrats, John Simmers, Astrid A Prinz, and Romuald Nargeot (2014). "Differential roles of nonsynaptic and synaptic plasticity in operant reward learning-induced compulsive behavior". In: *Current Biology* 24.9, pp. 941–950.

Skocik, Mike and Alexay Kozhevnikov (2012). "Real-time system for studies of the effects of acoustic feedback on animal vocalizations." In: *Frontiers in Neural Circuits* 6, p. 111.

Sköld, Camilla, Richard Levi, and Åke Seiger (1999). "Spasticity after traumatic spinal cord injury: nature, severity, and location". In: *Archives of Physical Medicine and Rehabilitation* 80.12, pp. 1548–1557.

Soin, Amol, Nemath Syed Shah, and Zi-Ping Fang (2015). "High-Frequency Electrical Nerve Block for Postamputation Pain: A Pilot Study". In: *Neuromodulation: Technology at the Neural Interface* 18.3, pp. 197–206.

Suzuki, Suzuko, Peter Gerner, Anna C Colvin, and Alexander M Binshtok (2009). "C-fiber-selective peripheral nerve blockade". In: *The Open Pain Journal* 2.1, pp. 24–29.

Tai, Changfeng, James R Roppolo, and William C de Groat (2004). "Block of external urethral sphincter contraction by high frequency electrical stimulation of pudendal nerve". In: *The Journal of urology* 172.5, pp. 2069–2072.

Tai, Changfeng, William C. De Groat, and James R Roppolo (2005). "Simulation analysis of conduction block in unmyelinated axons induced by high-frequency biphasic electrical currents." In: *IEEE Transactions on Biomedical Engineering* 52.7, pp. 1323–1332.

Tai, Changfeng, Dong Guo, Jicheng Wang, James R Roppolo, and William C de Groat (2011). "Mechanism of conduction block in amphibian myelinated axon induced by biphasic electrical current at ultra-high frequency." In: *Journal of Computational Neuroscience* 31.3, pp. 615–23.

Tanner, J. A. (1962). "Reversible blocking of nerve conduction by alternating-current excitation." In: *Nature* 195.4842, pp. 712–713.

Tchernichovski, Ofer, Fernando Nottebohm, Ching Elizabeth Ho, Bijan Pesaran, and Partha Pratim Mitra (2000). "A procedure for an automated measurement of song similarity". In: *Animal Behaviour* 59.6, pp. 1167–1176.

Teff, Karen L (2008). "Visceral nerves: vagal and sympathetic innervation." In: *Journal of Parenteral and Enteral Nutrition* 32.5, pp. 569–571.

Thomas, P K (1963). "The connective tissue of peripheral nerve: an electron microscope study." In: *Journal of Anatomy* 97.1963, pp. 35–44.

Thorp, Alicia A and Markus P Schlaich (2015). "Review Article Relevance of Sympathetic Nervous System Activation in Obesity and Metabolic Syndrome". In: 2015.

Vrabec, Tina L and Narendra Bhadra (2013). "A novel waveform for no-onset nerve block combining direct current and kilohertz frequency alternating current". In: *Neural Engineering (NER), 2013 6th International IEEE EMBS Conference on Neural Engineering*, pp. 283–286.

Wehrwein, Erica A., Hakan S. Orer, and Susan M. Barman (2016). "Overview of the Anatomy, Physiology, and Pharmacology of the Autonomic Nervous System". In: *Comprehensive Physiology* 6.July, pp. 1239–1278.

Willemze, Rose A, Misha D Luyer, Wim A Buurman, and Wouter J de Jonge (2015). "Neural reflex pathways in intestinal inflammation: hypotheses to viable therapy." In: *Nature Reviews. Gastroenterology & Hepatology* 12.6, pp. 353–362.

Williamson, Richard P and Brian J Andrews (2005). "Localized electrical nerve blocking". In: *IEEE Transactions on Biomedical Engineering* 52.3, pp. 362–370.

Wilson, Charles J., David Barraza, Todd Troyer, and Michael A. Farries (2014). "Predicting the Responses of Repetitively Firing Neurons to Current Noise". In: *PLoS Computational Biology* 10.5, pp. 1–17.

Woo, MY and B Campbell (1964). "Asynchronous Firing and Block of Peripheral Nerve Conduction by 20 Kc Alternating Current". In: *Bulletin of the Los Angeles Neurological Society* 29, p. 87.

Yang, Guangning, Zhiying Xiao, Jicheng Wang, Bing Shen, James R. Roppolo, William C. de Groat, and Changfeng Tai (2016). "Post-stimulation block of frog sciatic nerve by high-frequency (kHz) biphasic stimulation". In: *Medical & Biological Engineering & Computing*, pp. 1–9.

Yizhar, Ofer, Lief E Fenno, Thomas J Davidson, Murtaza Mogri, and Karl Deisseroth (2011). "Optogenetics in neural systems." In: *Neuron* 71.1, pp. 9–34.

Yoo, Paul B, Nathan B. Lubock, Juan G. Hincapie, Stephen B. Ruble, Jason J. Hamann, and Warren M. Grill (2013). "High-resolution measurement of electrically-evoked vagus nerve activity in the anesthetized dog". In: *Journal of Neural Engineering* 10.2, pp. 1–9.

Zhang, Feng, Li-Ping Wang, Edward S Boyden, and Karl Deisseroth (2006a). "Channelrhodopsin-2 and optical control of excitable cells". In: *Nature Methods* 3.10, pp. 785–792.

Zhang, Xu, James R. Roppolo, William C. De Groat, and Changfeng Tai (2006b). "Simulation analysis of conduction block in myelinated axons induced by high-frequency biphasic rectangular pulses". In: *IEEE Transactions on Biomedical Engineering* 53.7, pp. 673–676.

Zhang, X, Tai, Changfeng (2006). "Mechanism of nerve conduction block induced by high-frequency biphasic electrical currents". In: *IEEE Transactions on Biomedical Engineering* 53.12, pp. 1–19.

Zheng, Xiujun, Jian Zhang, Tongyi Chen, and Zhongwei Chen (2003). "Longitudinally implanted intrafascicular electrodes for stimulating and recording fascicular physioelectrical signals in the sciatic nerve of rabbits". In: *Microsurgery* 23.3, pp. 268–273.

# VITA

Yogi A. Patel was born in Philadelphia, PA in 1989. He has lived in India and the United States for extended periods of time. He completed Bachelor of Science degrees in Biochemistry and Molecular Biology and in Computational Science from Mercer University, Macon, GA, in 2011. He joined the Interdisciplinary Bioengineering Graduate Program at the Georgia Institute of Technology, Atlanta, GA in 2012.

During his PhD, Yogi presented his work at several international engineering as well as scientific conferences and has been awarded multiple poster and presentation awards, in addition to the BRAIN Grand Challenges Young Investigator Award from IEEE's Engineering in Medicine and Biology (EMBS) society. Yogi's research and publications have quickly turned him into a leader in the field of neuromodulation, specifically the use of kilohertz frequency electrical stimulation to inihibt activity in neural circuits.

Yogi approaches scientific problems with translation in mind. He has received multiple awards highlighting his translational research, including the Georgia Tech Edison Prize, which recognizes innovation driven by scientific results. Yogi received the Outstanding Entrepreneurship award by the Georgia Tech Biomedical Engineering Department and is a graduate of the joint Georgia Tech-Emory Technological Innovation: Generating Economic Results (TI:GER) program.

Yogi is a member of the IEEE Engineering in Medicine and Biology Society, the American Physiology Society, and Society for Neuroscience. His current research interests include real-time control systems, neuromodulation, autonomic neurophysiology, and neural control. In the near future, he hopes to establish an independent lab that studies autonomic physiology and control, and engineer physiologically-driven neuromodulation therapies.